Current-Induced Dynamics
of Chiral Magnetic Structures

Skyrmions, Emergent Electrodynamics
and Spin-Transfer Torques

Inaugural-Dissertation

zur

Erlangung des Doktorgrades

der Mathematisch-Naturwissenschaftlichen Fakultät

der Universität zu Köln

vorgelegt von

Karin Everschor

aus

Köln

Köln 2012

Abstract

In magnets without inversion symmetry weak spin-orbit coupling leads to the formation of smooth twisted magnetic structures like helices with a long period. In 2009, a new chiral magnetic phase was observed in the helimagnet manganese silicide (MnSi) within a certain temperature and magnetic field range. It turned out that this phase is a lattice of skyrmions which are topologically stable whirl-lines.

In the first Part of this Thesis, we review the discovery of the skyrmion lattice in MnSi, its manifestation in other chiral magnets and in thin films. Furthermore, we review the Ginzburg-Landau theory for chiral magnetic structures describing their equilibrium properties, followed by a discussion of additional terms that orient and distort the skyrmion lattice. Finally, we analyze the crystalline nature of the skyrmion lattice.

In the second Part of this Thesis, we investigate the interplay of electric currents and magnetic structures in bulk materials, in particular the skyrmion phase. Electrons traversing a spatially or temporally inhomogeneous magnetization configuration pick up a Berry phase which, rewritten as an Aharonov-Bohm phase arising from emergent magnetic and electric fields, leads to an effective Lorentz force acting on the electrons. For the skyrmion lattice these emergent fields are particularly interesting as the emergent magnetic field is quantized due to the topology of the skyrmions. On the other hand, the electric current induces forces on the magnetic texture via spin-tranfer torques, describing the transfer of angular momentum from the conduction electrons to the local magnetic structure. We show that skyrmions act very sensitively to electric currents, and we study their current-induced dynamics, *i.e.* the translational motion as well as rotations of the topologically stable knots.

This research was, is and will be done in cooperation with recent experiments performed by the group of Prof. Dr. Christian Pfleiderer from the Technical University of Munich. The very efficient coupling of skyrmions to electric currents was experimentally confirmed by an ultra-low threshold current density of about 10^6 A/m^2 above which spin-transfer torque effects were observed. It is about five order of magnitude smaller compared to that of other present-day spin-torque effects like domain wall motion. Hence, skyrmions are expected to be excellent systems to study the interplay of magnetism and electric currents, thereby advancing the general understanding of spin-transfer torque effects. We further think that the gained knowledge from such studies might be useful for future spintronic devices.
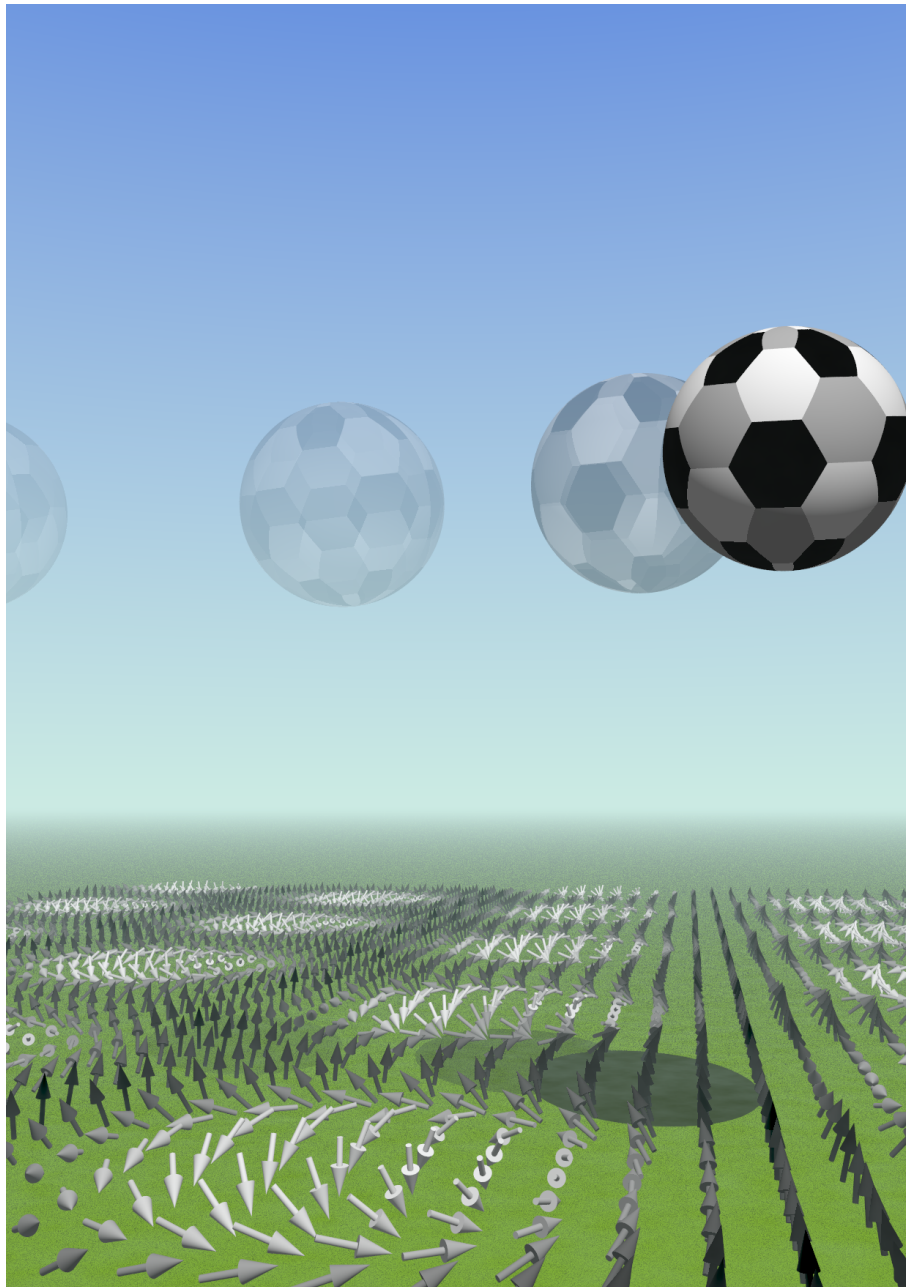
Kurzzusammenfassung

In chiralen, magnetischen Materialien bilden sich auf Grund der schwachen Spin-Bahn-kopplung getwistete magnetische Strukturen, wie zum Beispiel magnetische Helizes mit einer langen Periodenlänge aus. Im Jahre 2009 wurde eine neue magnetische Struktur bestehend aus topologisch stabilen „Wirbel-Linien", das sogenannte Skyrmiongitter, in Mangansilizium (MnSi) in einem gewissen Temperatur- und Magnetfeldbereich entdeckt.

Im ersten Teil dieser Arbeit werden wir uns mit der Entdeckung des Skyrmiongitters in MnSi sowie dessen Beobachtung in weiteren Materialien und in dünnen Filmen befassen. Zudem erläutern wir die Ginzburg-Landau-Theorie für chirale magnetische Strukturen im Gleichgewicht und erweitern diese um Terme, die für eine Ausrichtung und Verzerrung des Skyrmiongitters sorgen. Im letzten Kapitel dieses Teils analysieren wir den kristallinen Charakter des Skyrmiongitters.

Im zweiten Teil der vorliegenden Arbeit untersuchen wir die wechselseitige Beeinflussung zwischen magnetischen Strukturen, insbesondere dem Skyrmiongitter, und elektrischen Strömen. Leitungselektronen, die sich durch eine räumlich oder zeitlich inhomogene Magnetisierungsanordnung bewegen, erhalten eine Berry-Phase. Diese lässt sich als Aharonov-Bohm-Phase, hervorgerufen durch emergente elektrische und magnetische Felder, interpretieren und führt zu einer effektiven Lorentz-Kraft auf die Elektronen. Für Skyrmionen sind diese emergenten Felder besonders interessant, da sich zum Beispiel herausstellt, dass in diesem Fall das emergente magnetische Feld quantisiert ist. Im Gegenzug übt auch der elektrische Strom Kräfte auf das Skyrmiongitter durch Übertragung von Drehmomenten der Leitungselektronen auf die lokale magnetische Textur aus. Wir zeigen, dass Skyrmionen sehr leicht auf elektrische Ströme reagieren und studieren deren strominduzierte Dynamik, d.h. wir betrachten die translatorische Bewegung sowie die Rotation der topologisch stabilen Wirbel.

Diese Arbeit war, ist und wird in Zusammenarbeit mit Experimenten erfolgen, die von der Arbeitsgruppe von Herrn Prof. Dr. Christian Pfleiderer von der Technischen Universität München durchgeführt wurden bzw. werden. Die sehr effektive Kopplung von Skyrmionen und elektrischen Strömen wurde experimentell durch eine sehr niedrige Stromdichte von 10^6 A/m^2 bestätigt, oberhalb derer die wechselseitigen Beeinflussungen beobachtbar sind. Diese ist ca. fünf Größenordnungen kleiner als es in bisherigen Experimenten mit anderen magnetischen Anordnungen der Fall war. Daher stellen Skyrmionen exzellente Systeme dar, um das Wechselspiel zwischen Magnetismus und elektrischen Strömen zu untersuchen. Desweiteren denken wir, dass die aus solchen Studien gewonnenen Erkenntnisse in der Zukunft für die Spintronik-Technologie von Nutzen sein könnten.

... aus zwei werden drei ...

Contents

1 Introduction

The electromagnetic interaction is one of the four fundamental interactions in nature and is responsible for phenomena like electricity and magnetism. Both of them are omnipresent in our daily life, ranging from rather old-fashioned inventions like light bulbs or magnetic compasses to modern applications such as light-emitting diodes and magnetic sensors in smartphones.

Magnetic orders like ferromagnetism and antiferromagnetism are well known. Moreover, helimagnets with spiral magnetic structures, where, for example, the magnetization twists around a certain axis, are established for more than 30 years. In 2009, the discovery of a novel magnetic structure called skyrmion lattice, shown in Fig. 3.5, has spurred a lot of interest [1]. This peculiar magnetic configuration consists of magnetic whirl-lines that are topologically stable, similar to the vortex lattice in a type-II superconductor. Since skyrmions do not only occur in chiral magnets we first briefly review their emergence in other areas of physics. In the first Part of this Thesis, we focus on the skyrmions in chiral magnets. We describe their experimental discovery and analyze their equilibrium configuration within a Ginzburg-Landau theory. Furthermore, we discuss additional terms that pin the orientation of the skyrmion lattice. Finally, we focus on the crystalline nature of the skyrmion lattice.

In 1865, James Clerk Maxwell showed that electricity and magnetism are coupled and also interact with electric charges and currents [2]. About 40 years earlier, in 1826, William Sturgeon constructed the first electromagnet which exploits the phenomenon that a current-carrying conductor induces a magnetic field. A modern range of applications for the interplay of magnetism and currents are, *e.g.*, data storage devices based on the giant magnetoresistance (GMR) effect. In 1988, Peter Grünberg and Albert Fert independently discovered this effect which allows to manipulate magnetically the current flow [3, 4]. In 2007, they were awarded the Nobel prize in Physics for their discovery of the GMR effect.

John Slonczewski and Luc Berger proposed in 1996 the opposite mechanism [5, 6], where an electric current is used to influence the local magnetization of a material. This mechanism is called spin-transfer torque, because during this process a torque is exerted on the local magnetization by the spin of the conduction electron. The spin-transfer torque effect allows, for example, to move ferromagnetic domain walls with applied currents. In terms of applications, spin torques might be useful, for example, for non-volatile memory devices like racetrack memories as suggested by Stuart Parkin *et al.* [7]. However, all of these traditional spintronic applications like domain wall motion have in common that very high current densities are needed to induce observable spin-torque effects. The threshold current density above which the magnetic textures get unpinned from disorder is of the order of $j \sim 10^{11}$ A/m^2. A spin-torque effect, however, only occurs if the local magnetization changes in space or time. In the case of the moving domain wall, the torque affects only the region of the domain wall, where the magnetic structure is canted.

Therefore, the skyrmion lattice as novel magnetic order seems to be ideally suited to study spin-torque effects as the magnetic structure is smooth, but varies gradually in space. Actually, it turns out that skyrmions couple very efficiently to electric currents which manifests itself in an ultra-low threshold current density of about $j \sim 10^6$ A/m^2 being five orders of magnitude smaller compared to traditional spin-torque effects. In the second Part of this Thesis, we consider the interplay of the skyrmion lattice with an electric current. First, we focus on the physics of the conduction electrons which collect Berry phases while traversing non-collinear magnetic structures. In Chapter 7, we discuss that this Berry phase physics can be translated into emergent magnetic and electric fields felt by the conduction electrons which lead to experimentally observable effects. These emergent fields are particularly interesting for the skyrmion lattice, because, for example, the topology of the skyrmions causes the emergent magnetic field to be quantized. Afterwards, we analyze the effect of the current on the magnetic texture. To describe the response of the skyrmion lattice with respect to an applied current we use the standard Landau-Lifshitz-Gilbert equation extended by a recently suggested new damping mechanism for non-collinear magnetic textures [8, 9]. In particular, we examine the current-induced forces on the skyrmion lattice. Above a critical threshold current density determined by the strength of pinning by disorder those forces lead to a motion of the skyrmion lattice. We derive an equation for the acting forces from which one can infer the drift velocity within the so-called Thiele method where we include pinning physics phenomenologically. In Chapter 10, we focus on a current-induced rotation of the skyrmion lattice and discuss different rotation mechanisms. Technically, we present a generalization of the Thiele approach which is applicable for the rotational degree of freedom. A rotation by a finite angle has already been observed experimentally [10]. In the last section of Chapter 10 we predict a continuous rotation of the skyrmion lattice which will be analyzed experimentally in the near future.

Finally, we compare the properties of the skyrmion lattice to the vortex lattice in type-II superconductors. We will see that despite their analogies their dynamics behave different. We end with a conclusion in Chapter 12.

2

2 Skyrmions

In the sense the word "skyrmion" is used nowadays it is a mathematical object, which is realized in different parts of physics. In this Chapter, we will first briefly discuss the historical origin of skyrmions and their nomenclature. Then we give a definition of a skyrmion, and discuss its properties. This is followed by some facts, where skyrmions do occur in nature. Finally, we focus on skyrmions in chiral magnets being the main objects of this Thesis.

A "skyrmion" is named after the nuclear physicist Tony Skyrme. He studied a certain nonlinear field theory for interacting pions, *i.e.* mesons, and showed in the early 1960's that quantized and topologically stable field configurations do occur as solutions of such field theories [11, 12]. He also showed that those localized particle-like solutions can be interpreted as baryons, *i.e.* they have a fermionic character, although pions are described by bosonic fields.

In the original work, Tony Skyrme considered three-dimensional versions of skyrmions. Later, the notion of a "skyrmion" was generalized in the following way. A skyrmion is a smooth, topologically stable field configuration which defines a non-trivial surjective mapping from real space (or momentum space) to an order parameter space with a non-trivial topology. Here, we will restrict the target manifold to a d-dimensional sphere S_d. Furthermore, a skyrmion is everywhere non-singular, finite and trivial at infinity, *i.e.* it has no winding at infinity. As an example, let us consider $d = 2$, where one can obtain a skyrmion by taking a hedgehog configuration and projecting it onto the plane, as shown in Fig. 2.1. The reverse process immediately indicates this mapping. The color code in the following Figures is chosen such that arrows pointing to the north pole are plotted in red, to the south pole in blue, and along the equator in green, and so on. Another example of a skyrmion configuration is shown in the lowest panel of Fig. 2.2. It is obtained by a similar recipe as the previous one, but with one step in between, where the hedgehog was "combed", which leads to a chiral, *i.e.* non-inversion symmetric skyrmion. Since the latter will be the main object of this Thesis, there is another plot of it shown in Fig. 2.3 which, for clarity, also contains a projection from above.

Skyrmions can be classified according to their integer-quantized winding number. It counts how many times the field configuration covers the whole sphere. It is given by the integrated skyrmion density $\mathbf{\Phi}$. In $d = 2$, the skyrmion density is given by

$$\Phi_\mu = \frac{1}{8\pi}\epsilon_{\mu\nu\lambda}\hat{\mathbf{\Omega}} \cdot (\partial_\nu\hat{\mathbf{\Omega}} \times \partial_\lambda\hat{\mathbf{\Omega}}) \tag{2.1}$$

where $\epsilon_{\mu\nu\lambda}$ is the totally antisymmetric unit tensor, and $\hat{\mathbf{\Omega}}$ denotes the normalized field configuration, $|\hat{\mathbf{\Omega}}| = 1$. For the examples shown in the following Figures, the skyrmion is restricted to the xy-plane, such that the winding number is given by

$$W = \int \frac{dx\,dy}{4\pi}\,\hat{\mathbf{\Omega}} \cdot (\partial_x\hat{\mathbf{\Omega}} \times \partial_y\hat{\mathbf{\Omega}}). \tag{2.2}$$
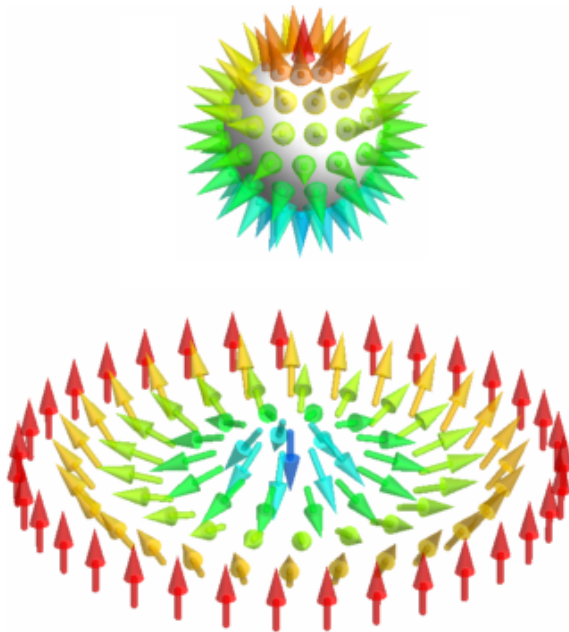
Figure 2.1: From a hedgehog to a skyrmion configuration

Note that, in contrast to a skyrmion configuration, a vortex does not cover the whole sphere, it has a non-trivial winding at infinity, and it is singular at its center.

Besides the "original" skyrmions predicted by Tony Skyrme, skyrmions and related structures have also been considered in many other areas of physics ranging from nuclear and particle physics over high-energy physics to condensed matter physics. Here, we will mention just a few examples. For instance, three-dimensional lattices of skyrmions were proposed to occur in the dense nuclear matter of neutron stars [13–15].

Moreover, skyrmions were predicted to occur in quantum Hall systems close to (or at) the Landau level filling factor $\nu = 1$. For example, in a ferromagnetic quantum Hall system with small Zeeman splitting, excitations can be modeled as two-dimensional skyrmions [16]. Here, $\hat{\mathbf{\Omega}}$ corresponds to the spin density, and the quantized winding number is correlated to the charge νe of the skyrmion. Furthermore, in these systems also lattices of skyrmions were theoretically proposed [17–19]. However, so far these predictions have been experimentally confirmed only indirectly via nuclear magnetic resonance measurements [20, 21] or via inelastic light scattering experiments [22]. Furthermore, skyrmions are discussed to occur as topological excitations in multi-component ferromagnetic Bose-Einstein condensates [23, 24]. In addition, skyrmion textures have been considered in cholesteric liquid crystals [25, 26] as well as in thin films in the form of bubble domains [27, 28].

In the late 1980's and early 1990's, A. N. Bogdanov and collaborators showed that skyrmion textures also occur as mean-field ground states for models of anisotropic non-centrosymmetric magnetic materials with chiral spin-orbit interactions subjected to a magnetic field [29–31]. In these systems, they are predicted to form crystalline structures. Moreover, A. N. Bogdanov and collaborators pointed out that within their mean-field analysis a skyrmion lattice is only a thermodynamical metastable solution for cubic materials like manganese silicide (MnSi) and that the energy of a conical state is always lower than the one of a skyrmion lattice. Since then, many further theoretical works on skyrmion and skyrmion-like textures in magnets appeared [32–35], where also other
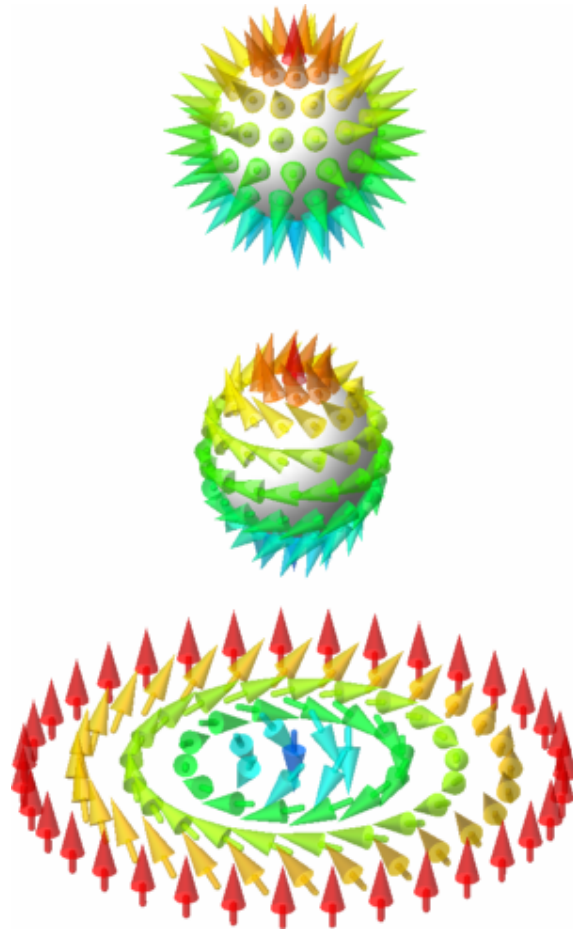
Figure 2.2: From a combed hedgehog to a chiral skyrmion configuration
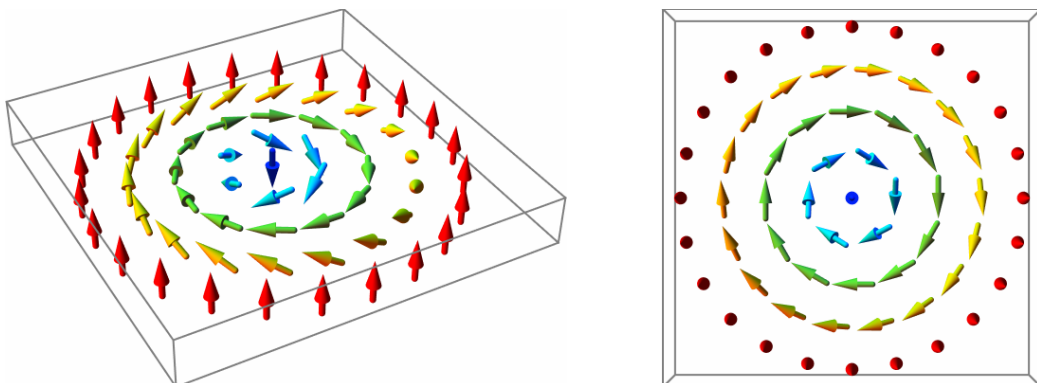
Figure 2.3: Single chiral skyrmion. Left panel: Three-dimensional sideview illustrating the doubly twisted field configuration around the skyrmion center. Right panel: Projection from above.

stabilization mechanisms like long-ranged interactions [36, 37] or extra phenomenological parameters [38] were suggested.

Concerning magnetic skyrmions, the real breakthrough, however, was in 2009 when in the presence of a finite external magnetic field a lattice of skyrmions was experimentally discovered in MnSi [1]. Here, the lattice consists of two-dimensional skyrmions as sketched in Fig. 2.3, where in this case the arrows correspond to the local magnetization direction. In this new type of magnetic order, the skyrmions are arranged on a hexagonal lattice perpendicular to the applied magnetic field (an illustration of a skyrmion lattice can be found in the next Chapter). The three-dimensional magnetic structure is translationally invariant along the direction of the magnetic field, so that the magnetic texture is actually made of hexagonal skyrmion tubes, similar to vortices in an Abrikosov vortex lattice of a type-II superconductor. We will see that this skyrmion lattice has even more features in common with the Abrikosov vortex lattice, and therefore pursue this point after having derived all results for the skyrmion lattice in Chapter 11.

In short, in this novel skyrmion lattice phase, the magnetization remains always finite and its direction winds once around a unit sphere per skyrmion in the plane perpendicular to the external magnetic field. In Eq. (2.1) $\hat{\mathbf{\Omega}}$ corresponds to the magnetization direction and $\hat{\mathbf{\Omega}} = \mathbf{M}/|M|$.

Since 2009 this new type of magnetic order has been observed also in other chiral magnetic bulk materials as well as in thin films. In the next Chapter, we discuss this magnetic skyrmion lattice, its experimental discovery as well as further experimental observations in more detail. Furthermore, when we mention skyrmions in the following Chapters, we will always refer to the skyrmions which occur in chiral magnets, if not stated otherwise.

Part I

Chiral Magnetic Structures, the Skyrmion Lattice

3 Experiments and Materials

The first experimental observation of the skyrmion lattice as a new type of magnetic order was in the chiral magnet manganese silicide (MnSi) in 2009 [1]. Since then it has been observed also in other bulk materials as well as in thin films.

In the first Section of this Chapter, we review the experimental discovery of the skyrmion lattice in MnSi, where we first introduce the different magnetic phases of MnSi with one of them being the skyrmion lattice phase. This is followed by a discussion of the first seminal neutron scattering measurements for the skyrmion lattice phase which provided the crucial hints for a new type of magnetic order. Later, in Chapter 5, we analyze more recent neutron scattering data and consider the crystalline character of the skyrmion lattice. Finally, we discuss briefly indications for the skyrmion lattice phase in MnSi in other measurements like susceptibility data.

As expected from the theoretical considerations [1], which will be discussed in Chapter 4, the skyrmion lattice is a rather general phase which occurs in many so-called B20 compounds. In Section 3.2, we briefly discuss other B20 compounds, where the skyrmion lattice, since 2009, has already been detected by neutron scattering measurements [39–41]. Note that, so far, the skyrmion lattice has not only been observed in metals like MnSi, but also in semiconductors, and recently also in an insulating, multiferroic material [42, 43]. Another essential progress concerning experiments is that the skyrmion lattice cannot only be observed in momentum space by neutron scattering, but since 2010 also in real space using Lorentz transmission electron microscopy in thin films. For example, the skyrmion lattice was confirmed to exist using Lorentz transmission electron microscopy for thin films of $Fe_{1-x}Co_xSi$ ($x = 0.5$) [44], FeGe [45] and also MnSi [46].

3.1   Discovery of the Skyrmion Lattice in MnSi

The skyrmion lattice in a magnetic material has first been observed in 2009 by Mühlbauer *et al.* [1]. They used neutron scattering to observe the spontaneous formation of this novel type of magnetic order in MnSi.

3.1.1   Properties of Manganese silicide

Manganese silicide (MnSi) is an itinerant, chiral weak ferromagnet, with a fluctuating magnetic moment of 2.2 μ_B and a saturated magnetic moment of 0.4 μ_B per Mn atom. The Bravais lattice is cubic, and MnSi crystallizes in the B20 structure that lacks inversion symmetry. The space group of MnSi is given by P2$_1$3 which consists of threefold rotations around $\langle 111 \rangle$ axes and of screw axes. The latter consist of a twofold rotation around cubic $\langle 100 \rangle$ axes followed by a translation by half a lattice vector along the same axis. Fig. 3.1 shows a sketch of the atomic unit cell of MnSi. It comprises four Mn and four Si atoms at
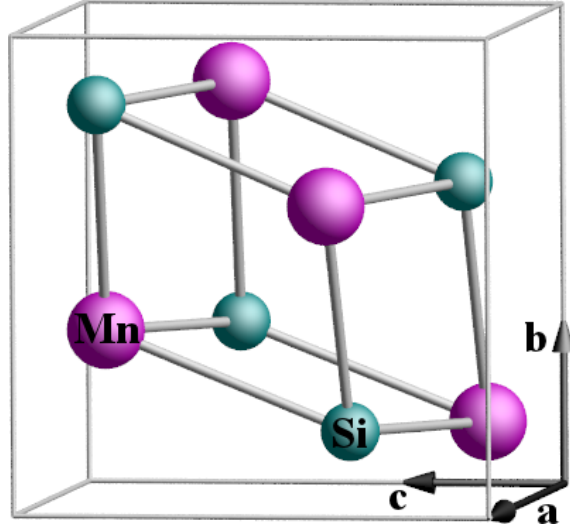
Figure 3.1: The atomic unit cell of MnSi comprising four Mn and four Si atoms.

the positions (u, u, u), $(\frac{1}{2} + u, \frac{1}{2} - u, \bar{u})$, $(\frac{1}{2} - u, \bar{u}, \frac{1}{2} + u)$, $(\bar{u}, \frac{1}{2} + u, \frac{1}{2} - u)$ with $u_{\text{Mn}} = 0.138$ and $u_{\text{Si}} = 0.845$. MnSi can be produced in ultra-pure form with a mean free path of about up to 5000 Å. At ambient pressure, it can be described very well by Fermi-liquid theory. However, MnSi attracted attention since above a critical pressure of about $p_c \approx 14.6$ kbar a non-Fermi liquid phase was observed [47–50]. In this phase, the temperature dependence of the resistivity is proportional to $T^{3/2}$, in contrast to the typical T^2 behavior for Fermi-liquids. Furthermore, in an intermediate pressure region (12 kbar $\lesssim p \lesssim$ 20 kbar) a state with a partial magnetic order was observed in neutron scattering [51].

Concerning the magnetic properties of MnSi, note that due to the lack of inversion symmetry of the atomic crystalline structure also non-inversion symmetric magnetic structures are allowed. Quite recently also the magnetic properties of MnSi caused sensation [1], as it was the first material where the new magnetic order, the skyrmion lattice, was observed.

3.1.2 Magnetic Phase Diagram of MnSi

MnSi is a material with a dominating ferromagnetic exchange interaction. In the field-polarized phase, the spontaneous magnetic moment per Mn atom is given by 0.4 μ_{B}. Aside from the usual paramagnetic phase above the Curie temperature T_c and a field-polarized phase for large magnetic fields, the absence of inversion symmetry of the atomic lattice also allows for additional chiral magnetic structures. Fig. 3.2 shows the different magnetic phases in the form of a temperature T versus applied magnetic field B phase diagram at ambient pressure [1, 52, 53]. In particular, it shows the three occuring chiral phases – the helical, the conical, and the skyrmion phase. In Fig. 3.2 the skyrmion phase is still denoted by its previous name "A-phase" which was assigned to this phase before it was found out to be a skyrmion lattice phase [52, 54]. These three phases are described in the following. All of them do occur due to the interplay of three hierarchical energy scales controlled by the strength of spin-orbit coupling $\lambda_{\text{so}} \sim 10^{-2}$. The strongest energy scale is ferromagnetic, which favors a uniform magnetization configuration. It is followed by the weaker chiral spin-orbit interactions originating from relativistic effects that occur due to the lack of inversion symmetry of the atomic structure [55–58]. The lowest-order chiral spin-orbit interaction is called Dzyaloshinskii-Moriya interaction [59, 60]. It circumvents the forma-
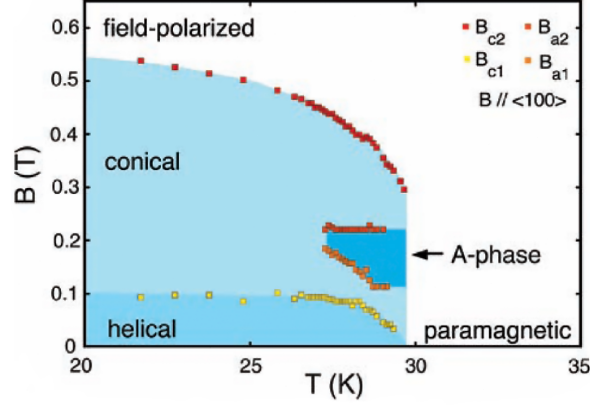
Figure 3.2: Magnetic phase diagram of MnSi as a function of temperature T and applied magnetic field strength B. The magnetic field was applied along a $\langle 100 \rangle$ direction. The phase diagram is taken from Ref. [1]
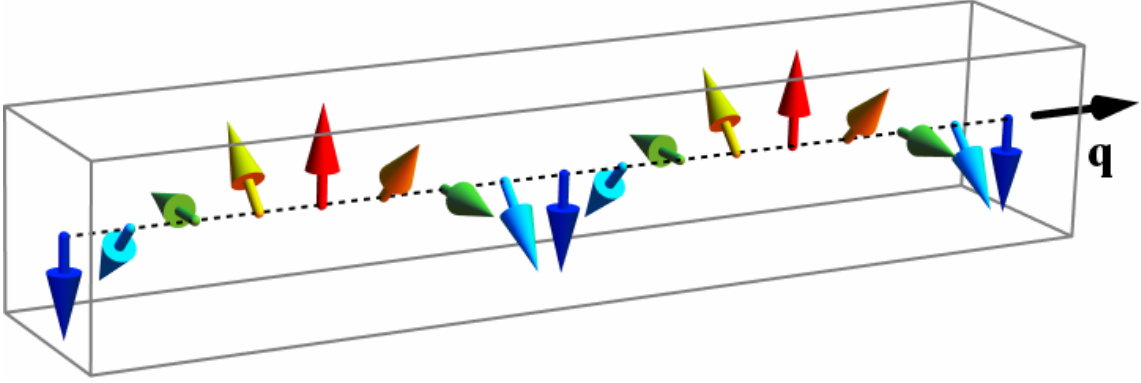
Figure 3.3: In the helical phase, the magnetization winds around $\boldsymbol{q}$, the propagation vector denoted by the black arrow in the Figure, and is perpendicular to it.

tion of a ferromagnetic ground state, because the Dzyaloshinskii-Moriya interaction favors twisted magnetic structures typically by forming spiral-like magnetization configurations. Besides the ferromagnetic and the Dzyaloshinskii-Moriya interaction, there are very weak crystalline field interactions which break the rotational symmetry [55, 56]. For example, they orient the magnetic structures according to crystal axes.

Helical phase: Below the critical temperature $T_c \approx 29\,\mathrm{K}$ and at zero or only small applied magnetic field, MnSi exhibits helical magnetic order [55, 57, 61, 62]. In this phase, the magnetization twists around an axis denoted as the propagation vector $\boldsymbol{q}$ of the helix, as shown in Fig. 3.3. The local magnetic moment $\boldsymbol{M}$ is perpendicular to $\boldsymbol{q}$ for $\boldsymbol{B} = 0$. The period or wavelength of the helix, denoted by λ_{helix}, is determined by the interplay of the ferromagnetic exchange interaction and the Dzyaloshinskii-Moriya interaction. It is about $\lambda_{\mathrm{helix}} \sim 180\,\text{Å}$ [56, 61]. This is huge compared to the atomic lattice constant of MnSi of $a \approx 4.56\,\text{Å}$. Due to the two different length scales, the magnetic structure couples only very weakly to the underlying atomic structure. In MnSi, the helices are weakly aligned along the cubic space diagonal $\langle 111 \rangle$ due to tiny crystalline field interactions which break the rotational symmetry [55, 56, 61]. This effect occurs only in fourth order in the small
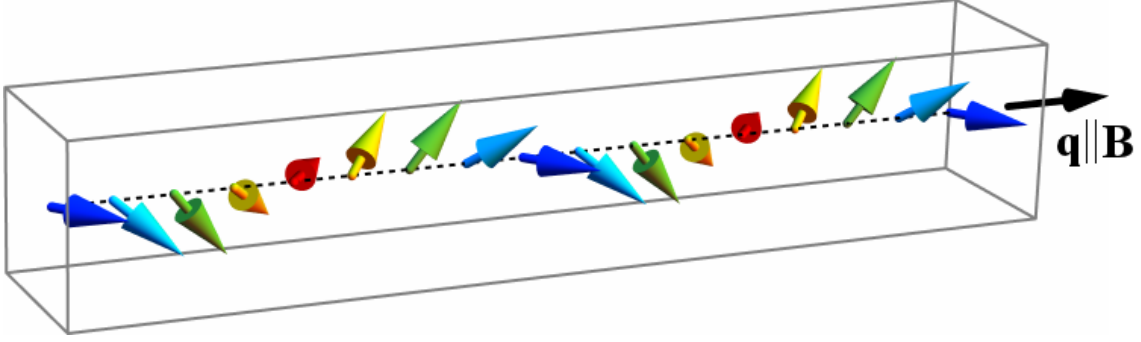
Figure 3.4: In the conical phase, the spiral wave vector q (black arrow) aligns along the direction of the magnetic field. The magnetization still winds around q, but it also has a uniform magnetic component in the direction of the magnetic field B.

spin-orbit coupling strength, λ_{so}^4. The correlation length of the zero-field helical state is about 10^4 Å. This was obtained by measuring the Gaussian rocking width in typical small angle neutron scattering experiments, (see Refs. [63, 64] and references therein).

Conical phase: Increasing the magnetic field above a critical magnetic field $B_{c1} \approx 0.1$ T and keeping the temperature below T_c, it is more favorable for the local magnetization to build up a net ferromagnetic component. But before reaching the fully polarized ferromagnetic state above a magnetic field of $B_{c2} \approx 0.6$ T, where the effects of the Dzyaloshinskii-Moriya interaction are suppressed, the system prefers a state that is called conical phase. In this phase, the q vector aligns along the direction of the magnetic field B [54, 65, 66], and the local magnetization is no longer perpendicular to q, but has also a component in the direction of the magnetic field which leads to a uniform magnetization. A sketch of a conical order is shown in Fig. 3.4. The line separating the helical and the conical phase is in general expected to be a crossover where the direction of the q vector changes continuously (but hysteretic) from a $\langle 111 \rangle$ direction to the direction of the magnetic field. Only if the magnetic field is applied along certain special directions like for example one of the high symmetry directions as [100], it might possibly be a second order phase transition. The cone angle, *i.e.* the angle between the local magnetization and the direction of the magnetic field, smoothly decreases to zero at the field strength $B_{c2} \approx 0.6$ T. For a magnetic field above B_{c2}, the effects of the Dzyaloshinskii-Moriya interaction are negligible compared to the ferromagnetic interaction, and the field-polarized state is the ground state.

Skyrmion phase: In a small pocket of the phase diagram, for temperatures just below T_c and finite magnetic field, a two-dimensional hexagonal lattice of anti-skyrmions oriented perpendicular to the applied magnetic field is the ground state. The corresponding phase transition from the skyrmion lattice phase to the conical phase is first order [1, 40]. The lattice constant of the skyrmion lattice is given by $2\lambda_{\mathrm{helix}}/\sqrt{3}$. The magnetization texture of the skyrmion lattice is shown in Fig. 3.5, illustrating the doubly twisted magnetic structure around an anti-skyrmion center. The skyrmion lattice decouples very efficiently from the atomic crystal lattice, such that the plane of the skyrmion lattice orients perpendicular to the applied magnetic field B independent of the underlying atomic orientation. Only the orientation of the hexagonal lattice within the plane is determined by crystalline field
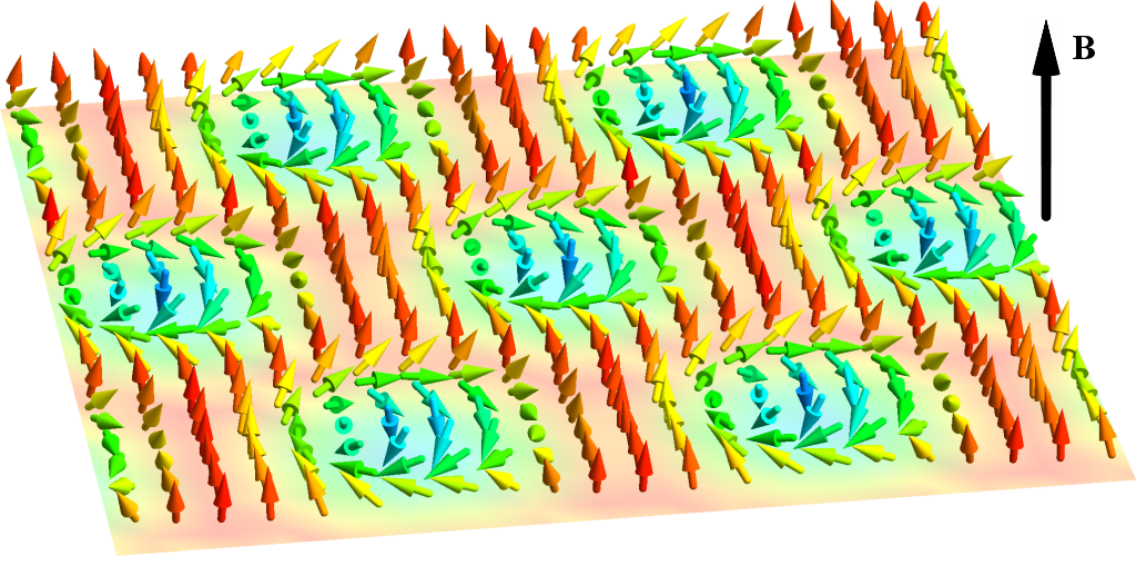
Figure 3.5: Illustration of the magnetic order in the skyrmion lattice phase which was pre-viously denoted as "A-phase". The magnetic structure forms a two-dimensional hexagonal lattice of anti-skyrmions that is translationally invariant in the direction of the magnetic field being perpendicular to the skyrmion lattice plane. The color code from red to blue is chosen according to the alignment with the magnetic field. A red (blue) arrow indicates that the magnetization is parallel (antiparallel) to the applied magnetic field.

interactions. For example, for a magnetic field that is perpendicular to a ⟨110⟩ direction of the atomic crystal, the skyrmion lattice pins very weakly in this ⟨110⟩ direction of the atomic crystal. Along the direction of the magnetic field, the magnetic structure is trans-lationally invariant, implying that the three-dimensional magnetic structure assumes the form of skyrmion lines or skyrmion tubes, as shown in the right panel of Fig. 11.1. The winded magnetic building blocks are called anti-skyrmions since the winding number W per two-dimensional unit cell is quantized to $W = -1$, implying that the magnetization in the center of a skyrmion is antiparallel to the applied magnetic field and the uniform magnetic component. Previously, this phase was also referred to as the "A-phase" [54, 65], because the magnetization texture of this phase was not properly understood. Before the discovery of the skyrmion lattice it had been believed that the A-phase was just a single helix with a spiral wave vector q aligned perpendicular to the applied field [65, 66]. This interpretation can be clearly ruled out by the corresponding neutron scattering data disussed below.

3.1.3 Neutron scattering: setups and results for the different chiral magnetic phases

Neutron scattering is a very good technique to analyze magnetic structures. Since neu-trons have a magnetic moment they scatter at the magnetic structure. In general, the contributing modes of a periodic magnetic texture can be observed in neutron scattering experiments in the form of Bragg peaks in reciprocal space. Via Fourier transformation,

$$\boldsymbol{M}(\boldsymbol{r}) = \sum_{\boldsymbol{q}} \boldsymbol{m_q} e^{i\boldsymbol{q} \cdot \boldsymbol{r}} \tag{3.1}$$
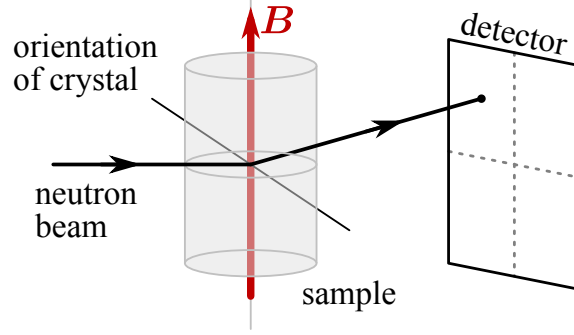
Figure 3.6: Neutron scattering setup, where the applied magnetic field $\boldsymbol{B}$ is perpendicular to the incident neutron beam.

one can then, in principle, obtain information about the real space picture of the magnetization configuration.

A basic neutron scattering setup is shown in Fig. 3.6. The incident neutron beam interacts with the sample and its signal can then be observed on the detector. For a given periodic structure and for every $\boldsymbol{q}$ with $\boldsymbol{m_q} \neq 0$ in Eq. (3.1) we expect to observe a neutron scattering spot in the direction of $\boldsymbol{q}$ located on a sphere in reciprocal phase with a radius of $q = |\boldsymbol{q}|$.

There are several reasons why one cannot immediately translate the momentum space picture obtained from the neutron scattering result into a real space picture. First of all, experimental neutron scattering peaks are not delta peaks, but the spot size is representative for the resolution limit of the measurement. Second, with this particular technique it is not possible to adress the $\boldsymbol{q} = 0$ mode, *i.e.* the uniform component of the magnetic structure is not accessible. This is due to the fact that one is not able to distinguish between neutrons that don't interact with the sample and those that do interact, but are scattered to the origin of reciprocal space, $\boldsymbol{q} = 0$. Therefore, in most experimental data the intensity at the origin is removed. Nonetheless, the uniform magnetic moment can be measured with other experimental techniques like, *e.g.*, vibrating sample magnetometry. Furthermore, in almost all data shown a substraction of the noisy background signal was performed already to better observe the scattering spots from the magnetic structure. A more challenging problem is that the neutron penetrates the whole sample. In the usual case, where the magnetic texture consists of different domains, the observed data contains the accumulated signal of all penetrated domains. Furthermore, experimentally it is quite tricky to distinguish between higher-order scattering and multiple scattering peaks. Concerning the skyrmion phase, it was possible to detect the first higher-order peaks and differentiate between the doubly scattered neutrons [67], thereby emphasizing the long-range crystalline nature of the skyrmion lattice. This will be further discussed in Chapter 5. Another important reason why a direct Fourier transformation is not possible is that the neutron scattering data do not allow to determine complex phases. For a helical or conical magnetic structure, a change in the phase corresponds only to a translation of the full texture along the spiral wave vector. However, for a multi-$\boldsymbol{q}$ structure like the skyrmion lattice these phases play an important role, as will be discussed further in Section 4.3. Despite these rather fundamental problems, there is also a practical problem. Within a single measurement one cannot map out the full reciprocal space. One is rather limited to a part of the Ewald-sphere, namely to those modes that can be measured due to the size limitations of the detector. Since neutron scattering experiments are quite
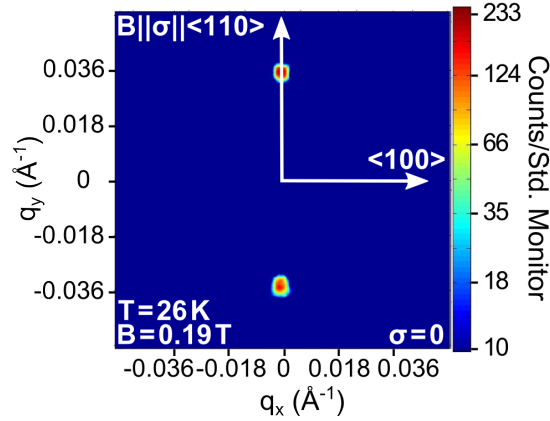
Figure 3.7: Neutron scattering data for the conical phase in MnSi at ambient pressure for $T = 26$ K and $B = 0.19$ T measured by Alfonso Chacón Roldán of the group of Prof. Dr. Christian Pfleiderer. The propagation vector of the conical phase aligns clearly with the direction of the magnetic field.

expensive and beam time is limited, before doing the experiment one has to adjust the experimental setup such that the spots one is interested in are measureable.

Conical phase: A conical phase is characterized by three real numbers, namely the strength of the uniform magnetization M_f, the amplitude $\sqrt{2}\Phi$ of the helix, and the pitch of the helix q. The direction of the spiral wave vector is fixed since it is aligned with the magnetic field $\boldsymbol{q} = q\hat{\boldsymbol{B}}$. For a magnetic field in z direction the local magnetization is given by

$$\boldsymbol{M}(\boldsymbol{r}) = \begin{pmatrix} \sqrt{2}\Phi\cos(qz) \\ \sqrt{2}\Phi\sin(qz) \\ M_f \end{pmatrix} = \begin{pmatrix} \Phi/\sqrt{2} \\ -i\Phi/\sqrt{2} \\ 0 \end{pmatrix} e^{i\boldsymbol{q}\cdot\boldsymbol{r}} + \begin{pmatrix} \Phi/\sqrt{2} \\ i\Phi/\sqrt{2} \\ 0 \end{pmatrix} e^{-i\boldsymbol{q}\cdot\boldsymbol{r}} + \begin{pmatrix} 0 \\ 0 \\ M_f \end{pmatrix} \quad (3.2)$$

with $\boldsymbol{q} = (0,0,q)^T$ parallel to $\boldsymbol{B}$. From this Fourier decomposition one expects to see exactly two spots (besides the $\boldsymbol{q} = 0$ spot) in neutron scattering, one in the direction of the magnetic field $\boldsymbol{B}$, and the other one in $-\boldsymbol{B}$ direction. The radius q of the sphere in momentum space is proportional to the inverse pitch of the helix, and Φ^2 is the weight of the peaks. To observe both spots on the detector it is neccessary to apply the magnetic field in the direction perpendicular to the neutron beam, *i.e.* in a direction of the measuring plane, as shown in Fig. 3.6.

The first neutron scattering experiments for MnSi to study the conical and helical phase were performed in 1976 by Ishikawa *et al.* [61]. Fig. 3.7 shows a more recent typical neutron scattering pattern of the conical phase in MnSi at $T = 26$ K and $B = 0.19$ T, measured at ambient pressure in the setup of Fig. 3.6. As expected, one clearly observes the two spots of high neutron intensity along the direction of the magnetic field. This is the reason why in the conical phase in general neutron scattering measurements were performed in the setup of Fig. 3.6, where the magnetic field is perpendicular to the indicent neutron beam [54, 65, 66]. However, it turned out that this is not the best way to get informations about the skyrmion lattice, as discussed below.
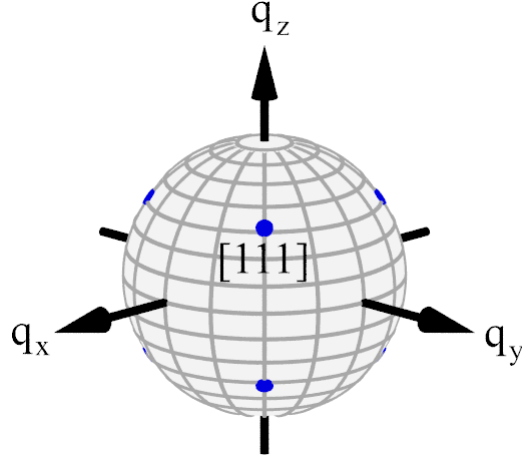
Figure 3.8: Equivalent $\langle 111 \rangle$ orientations for the helical propagation vector.

Helical phase: In the helical phase, the interpretation of the neutron scattering data is a little bit more complex than in the conical phase. In MnSi, the prefered direction for the helical wavevector q due to crystalline field interactions is along a $\langle 111 \rangle$ direction [55, 61]. Since there are four equivalent threefold axes of the cubic structure $q_1 \parallel [111]$, $q_2 \parallel [11\bar{1}]$, $q_3 \parallel [\bar{1}1\bar{1}]$, and $q_4 \parallel [\bar{1}\bar{1}1]$, in general, the magnetic material consists of domains with different orientations of their magnetic propagation vectors. Hence, performing the measurement with unpolarized neutrons there are eight magnetic peaks around each nuclear Bragg peak, corresponding to $\pm q_k$ $(k = 1, \ldots, 4)$, as shown in Fig. 3.8. Nonetheless, due to the restriction of the reception range of the detector one does not see all of them at the same time. A typical result of the scattering intensity in the helical phase is shown in panel (A) and (D) of Fig. 3.10. Both are measured in a zero-field-cooled state and at zero magnetic field $|\boldsymbol{B}| = 0$ for a $\langle 110 \rangle$ scattering plane. Panel (A) is measured at temperature of $T = 27$ K and (D) at $T = 16$ K. The intense spots shown are all aligned along a $\langle 111 \rangle$ direction, and one observes helical magnetic order along $\langle 111 \rangle$ directions. With polarized neutron scattering one can also demonstrate that the chirality of the magnetic structure is single-handed, meaning that there are no chiral domains. The same helix is observed at q and $-q$.

Skyrmion phase: As mentioned above, most neutron scattering experiments in the presence of a magnetic field where performed such that the magnetic field is perpendicular to the indicent neutron beam (setup of Fig. 3.6). However, in the skyrmion lattice phase it turned out to be much more beneficial to apply the magnetic field in the direction of the incident neutron beam, as shown in Fig. 3.9. The work reviewed in this part has been published in Ref. [1]. Mühlbauer *et al.* performed neutron scattering experiments at the diffractometer MIRA [68] at FRM II at the Technische Universität München[1] and used an incident neutron wavelength of $\lambda = 9.6$ Å with a 5% full-width half-maximum (FWHM) wavelength spread. The most important results of their small-angle neutron scattering (SANS) experiments are summarized in Fig. 3.10. Panels (A) and (D) represent data for the helical phase as discussed above. Panels (B), (C), (E) and (F) show data for the skyrmion phase. All data for the skyrmion phase except the one shown in panel (F) are measured in the setup of Fig. 3.9, where the magnetic field is aligned in the direction of

---

[1]FRM: Forschungsreaktor München
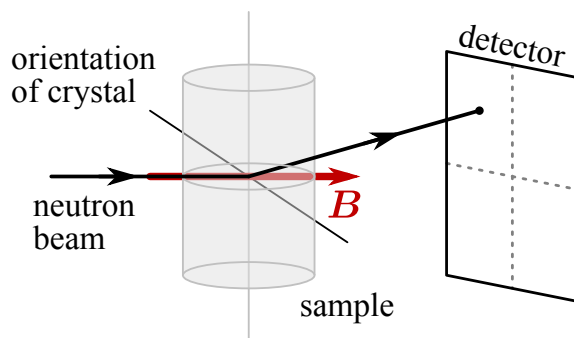
Figure 3.9: Neutron scattering setup, where the applied magnetic field $\boldsymbol{B}$ is parallel to the incident neutron beam.

the incident neutron beam. Only the data of panel (F) has been measured in the usual setup for the conical phase, as sketched in Fig. 3.6. The measurements shown in panels (A) to (F) are performed for two different single-crystal MnSi samples. The data on the left hand side of Fig. 3.10 show measurements of sample 1, and the ones on the right hand side belong to sample 2. Sample 1 has the shape of a disk, where the normal vector of the disc was slightly misaligned with respect to a $\langle 110 \rangle$ axis, and sample 2 is a small parallelepiped, where a $\langle 110 \rangle$ axis corresponds to the long axis. Both are of the size of a few millimeters (for further details see Ref. [1]). The data shown were measured by performing a sum over rocking scans with respect to the vertical axis through the sample. The measurements with a finite magnetic field were performed such that Mühlbauer *et al.* first cooled to the desired temperature and then turned on the magnetic field. However, they have also tested that the neutron scattering results for the skyrmion lattice phase do not depend on the specific way how the skyrmion phase is reached, zero-field cooled or field cooled [1].

Panels (B), (C) and (E) of Fig. 3.10 show the first published intensity measurements in the skyrmion phase that were performed in the setup of Fig. 3.9. All of these three pictures and all other measurements that were performed in the skyrmion phase, but are not shown, have in common that one observes six spots on a regular hexagon, independent of the particular sample and the orientation of the sample. Panel (B) was measured for a $\langle 110 \rangle$ scattering plane at a temperature of $T = 26.45$ K and a magnetic field of $B = 0.164$ T. In panel (E), the temperature is $T = 27.7$ K, and the magnetic field is $B = 0.162$ T. It was measured with the same orientation as in panel (D). In (B) and (E) the scattering plane contained a $\langle 110 \rangle$ direction and one observes that two of the six peaks coincide with this direction. In panel (C) the orientation of the sample was random. In particular, it did not contain a $\langle 110 \rangle$ direction, but nevertheless the characteristic sixfold pattern of the skyrmion lattice can be seen in the neutron scattering data. The applied magnetic field in panel (C) was $B = 0.164$ T at a temperature of $T = 26.77$ K.

Furthermore, the hexagonal magnetic scattering pattern and therefore the skyrmion lattice align perpendicular to the applied magnetic field. In reverse, this means that for precise measurements also small variations of the magnetic field direction across the sample volume like demagnetization fields should be avoided, which in the neutron scattering data presented in this Section were however present.

To check for consistency with previous works, also measurements in the usual setup for the conical phase (Fig. 3.6) were performed for different temperatures. Below T_c one observes only the spots of the conical phase, *i.e.* spot 9 and 10 in panel (F). When
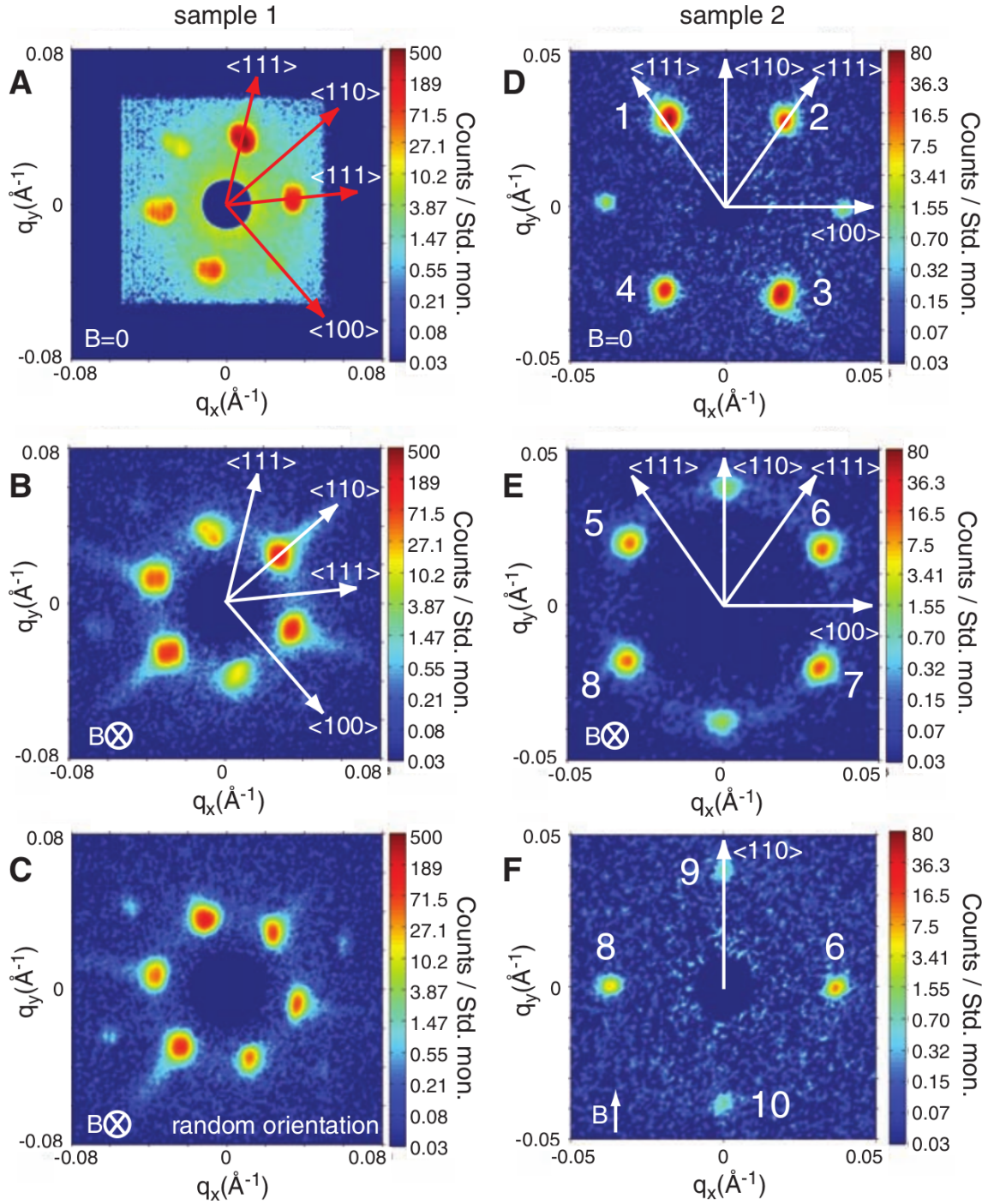
Figure 3.10: Typical small-angle neutron scattering (SANS) intensities. Panel (A) and (D) show measurements in the helical phase and all others in the skyrmion phase (see text for details). The intensity is given by the color scale that is logarithmic to enhance weak features. Red (blue) corresponds to high (low) intensity. From all panels except (A), where one observes the light blue square, a typical background measurement above T_c and $\boldsymbol{B} = 0$ is substracted. The picture is taken from Ref. [1].

increasing the temperature and entering the skyrmion phase, spots 9 and 10 become very weak, while spots 6 and 8 corresponding to those in panel (E) appear. The data of panel (F) shows such a measurement in the usual setup for the conical phase (Fig. 3.6) in the skyrmion phase at $T = 27.7$ K and $B = 0.190$ T. Within this measurement the spots of the conical phase are very weak, but don't disappear. For a weak first-order transition this may be interpreted as a phase coexistence of the conical and the skyrmion phase. Nevertheless, for this phenomenon also the mentioned demagnetizing fields may be the reason.

In conclusion, the key results of the neutron scattering study of Ref. [1] are the following. At a magnetic field strength of the order of $B_{c_2}/2$ the skyrmion lattice phase is the ground state instead of the competing conical phase. The wave-vectors $\boldsymbol{q}$ of the Fourier modes contributing to the skyrmion phase align perpendicular to the applied magnetic field, thus the neutron scattering spots are located in the plane perpendicular to the magnetic field $\boldsymbol{B}$. The main Bragg reflections form a regular hexagon independent of the orientation of the underlying atomic lattice. Moreover, within the skyrmion plane the magnetic lattice aligns very weakly with respect to the $\langle 110 \rangle$ orientation if possible. However, in total the skyrmion lattice unpins very efficiently from the atomic crystal lattice, and the skyrmion plane is perpendicular to the applied magnetic field.

Even more information on the magnetic structure, can be extracted from higher-order scattering peaks in neutron scattering. Nevertheless, in the first neutron scattering studies [1] discussed in this part, is was not possible to distinguish double or multiple scattering, *i.e.* neutrons that scattered more than one time from the magnetic structure, from real higher-order peaks, where neutrons scatter once with a higher moment. Moreover, within this study the spot sizes were quite large (due to the slightly inhomogeneous magnetic fields across the sample) and the intensity variation of the rocking scans was not as expected. To conclude, it was not possible to doubtlessly establish higher-order peaks. This was achieved later in Ref. [67] accompanied by a better resolution and is discussed in more detail in Chapter 5.

3.1.4   Susceptibility for the Skyrmion Phase

The magnetic susceptibility also shows characteristic features within the skyrmion phase and at its boundaries. Fig. 3.11 shows the AC susceptibility χ as a function of the applied magnetic field, measured at ambient pressure for a fixed temperature T just below the transition temperature T_c to the paramagnetic phase. When entering the skyrmion phase at H_{A1} (the subscript "A" was chosen according to the previous name "A-phase") the AC susceptibility first jumps to a lower value, and then rises again for higher magnetic field exceeding H_{A2} in the conical phase [52]. H_{c1} and H_{c2} denote the usual critical magnetic fields for the transition from the helical to the conical phase, and from the conical to the ferromagnetic phase, respectively.

Furthermore, also in the data of the Hall resistivity one notices the skyrmion lattice phase. This is explained in Chapter 7 in more detail.

To summarize, all data, in particular the neutron scattering data, indicate that the skyrmion lattice phase in chiral magnets, previously denoted as "A-phase", is a new form of magnetic order with a first-order transition to the conical phase. A theoretical Ginzburg-Landau analysis which confirms that the A-phase in MnSi is indeed a skyrmion lattice, *i.e.* a new form of magnetic order consisting of topologically stable knots in the spin structure, has also been published in Ref. [1]. We review and discuss the Ginzburg-Landau theory for helimagnets in the next Chapter. To demonstrate experimentally that the skyrmion lattice
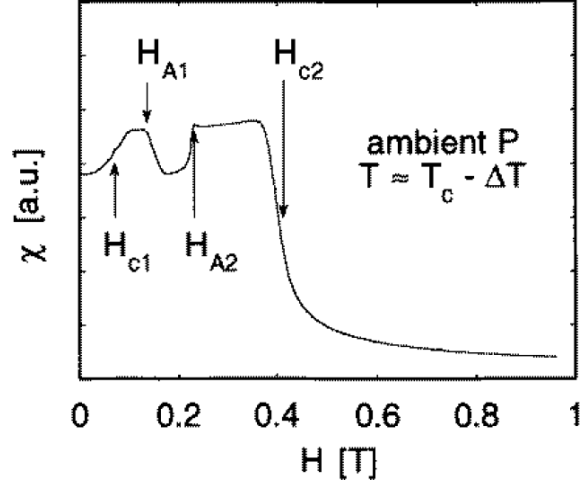
Figure 3.11: Plot of the AC susceptibility χ versus the applied magnetic field B, measured at ambient pressure and at a temperature slightly smaller than T_c. The picture is taken from Ref. [52].

indeed has a topologically non-trivial magnetic structure characterized by a finite winding number being quantized per unit cell cannot be extracted from these neutron scattering patterns. To this end, the so-called topological Hall effect was expoited [40], which is based on an emergent magnetic field that arises due to the finite winding number. This effect is discussed in more detail together with the emergent electric field in Chapter 7.

3.2 Further Evidence for the Skyrmion Lattice

Since 2009 the skyrmion lattice has been observed in other materials and with different experimental techniques, too. First, we would like to briefly review some of the materials, where the skyrmion phase has already been observed. The second material in which the skyrmion lattice phase was observed is the doped semiconductor material $Fe_{1-x}Co_xSi$ [39]. CoSi is a diamagnetic metal and FeSi a nonmagnetic insulator. When doping FeSi with Co, $Fe_{1-x}Co_xSi$ shows an insulator-to-metal transition at $x = 0.02$. For even larger doping, $0.05 \leq x \leq 0.7$, $Fe_{1-x}Co_xSi$ orders helimagnetically in a certain range of the temperature vs. magnetic field phase diagram. The pitch of the helix increases from about 200 to 2000 Å for increasing doping. In Ref. [39] it was shown using neutron scattering that for a doping of $x = 0.2$ also a skyrmion lattice phase exists in $Fe_{1-x}Co_xSi$ for temperatures of about roughly $25 - 27$ K and applied magnetic fields of about roughly $30 - 60$ mT (for details see Ref. [39]). Moreover, the skyrmion lattice phase was observed by small angle neutron scattering in iron and cobalt doped MnSi, i.e. in $Mn_{1-x}Fe_xSi$ and $Mn_{1-x}Co_xSi$ [41]. As suggested by the theoretical analysis [1], the skyrmion lattice is a general phenomenon and occurs in (at least) the B20 compounds that order helimagnetically at zero magnetic field. Note that the skyrmion lattice has not only been observed in metals like MnSi, but also in semiconductors and quite recently in an insulating, multiferroic material, Cu_2OSeO_3 [42, 43], too. In this Thesis, when mentioning experiments, we will often use MnSi as a reference material. We think that the results are similiar for the other appropriate compounds.

Now let us briefly focus on a different experimental technique to observe the skyrmion lattice phase. Since 2010 it has not only been observed by neutron scattering, but also
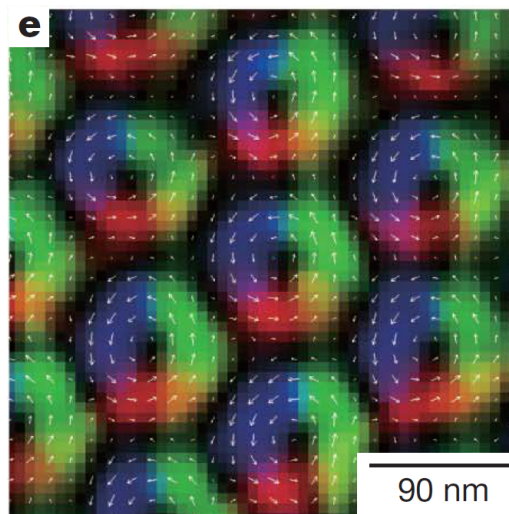
Figure 3.12: Real space image of the skyrmion lattice at a magnetic field of $B = 50$ mT obtained from Lorentz TEM. The figure is taken from Ref. [44].

using Lorentz transmission electron microscopy (TEM) on thin films [44, 45]. Lorentz TEM has the advantage, that one directly observes a real space picture of the magnetic structure. A disadvantage is, however, that the magnetic structure has to be electron-transparent, and therefore only thin samples can be studied. For the case of the skyrmion lattice, the magnetic field has to be applied into the direction normal to the thin sample. In this configuration, and provided that the sample is thinner than the pitch of the conical phase, the latter is energetically suppressed, and therefore the skyrmion lattice phase is stable in a much broader region of the phase diagram [44]. For thicker samples, the magnetic phase diagram approaches the one of the bulk samples, suggesting that in both thin films and bulk samples the same skyrmion lattice is realized [46]. Fig. 3.12 shows a typical result of a measurement by Yu *et al.* [44] for a thin film of $Fe_{1-x}Co_xSi$ with a doping of $x = 0.5$ and a magnetic field of $B = 50$ mT in the skyrmion lattice phase. The lattice spacing of the skyrmions is about 90 nm. With Lorentz TEM it is only possible to measure the in-plane component of the local magnetization. Therefore, in the center or at the boundaries of the skyrmions, where the magnetization is opposite or along the magnetic field and thus normal to the thin sample, the magnetization is not specified by this technique. However, in Fig. 3.12 one can clearly observe the winding of the magnetic structure.

In thin films of FeGe [45], the skyrmion lattice has been observed directly using this method, too. FeGe is also a B20 type material, yet with a much higher transition temperature of about 280 K between the helical and the paramagnetic phase. Here, Yu *et al.* [45] succeeded in observing the skyrmion crystal also at temperatures of about 260 K.

This brief section indicates that since the discovery of the first chiral magnetic skyrmion lattice in MnSi in 2009 [1], this has been a very active research field and skyrmions occur in bulk materials [1, 39, 41] as well as nano-scale systems [44, 45]. Spontaneous skyrmion lattices have also been observed in monatomic layers of Fe on an Ir substrate, *i.e.* also on atomic length scales [69]. We expect that even more materials exhibiting such winded magnetic structures will be observed in the future.

4 Ginzburg-Landau Theory

The Ginzburg-Landau theory is a phenomenological theory for a continuum description of phase transitions. It is named after V. L. Ginzburg and L. D. Landau and can be applied to various kinds of phase transitions. The central concept of this theory is based on the existence of an order parameter that is non-zero in the ordered phase below a critical temperature T_c, and which becomes zero when increasing the temperature above T_c. Close to the phase transition the order parameter is small, so that the appropriate energy functional can be expanded as a power series in the order parameter. Minimizing this functional with respect to the order parameter yields the equilibrium thermodynamics of the system.

In the case of ferromagnetism or smoothly varying magnetic textures the order parameter is the local magnetization $\boldsymbol{M}(\boldsymbol{r})$. In thermal equilibrium, the magnetic state of a system is the one that minimizes the free energy G. The dimensionless free energy G as a function of the applied magnetic field and temperature can be calculated from the partition function Z,

$$Z = e^{-G} = \int \mathcal{D}\boldsymbol{M} \, e^{-F[\boldsymbol{M}]}, \tag{4.1}$$

where the free energy functional F depending on the order parameter $\boldsymbol{M}$ respects the fundamental symmetries of the system. The crudest approximation to calculate the free energy G is to take its mean-field value that is obtained by minimizing the free energy functional with respect to the magnetization structure $\boldsymbol{M}(\boldsymbol{r})$:

$$G \approx \min_{\boldsymbol{M}(\boldsymbol{r})} F[\boldsymbol{M}] \equiv F[\boldsymbol{M}_0]. \tag{4.2}$$

Here, $\boldsymbol{M}_0$ is the minimum of the free energy functional F. The leading-order corrections to the mean-field result are thermal Gaussian fluctuations arround the mean-field minimum of the free energy functional. For a local minimum $\boldsymbol{M}_0(\boldsymbol{r})$ we find

$$G \approx F[\boldsymbol{M}_0] + \frac{1}{2} \ln \det \left(\frac{\delta^2 F}{\delta \boldsymbol{M} \delta \boldsymbol{M}} \right) \bigg|_{\boldsymbol{M}_0}. \tag{4.3}$$

In the Ginzburg regime very close to T_c, the contribution from order parameter fluctuations is of comparable size to its mean-field value, and this expansion becomes invalid.

In this Chapter, we will first motivate the Ginzburg-Landau functional $F[\boldsymbol{M}]$ for a usual ferromagnet. This part is followed by the extended model for helimagnets. The last Section of this Chapter is dedicated to the skyrmion lattice phase. First we discuss its stability, where we mainly review the results of Ref. [1] and then we consider the orientation, the distortion and the pinning of the skyrmion lattice with respect to the underlying atomic lattice. Parts of the latter we published in Refs. [10, 70, 71]
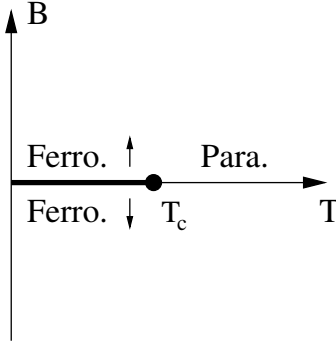
Figure 4.1: Magnetic phase diagram of a ferromagnet. Below the critical temperature T_c the system is ferromagnetically ordered. Above T_c it is paramagnetic.

4.1   Ginzburg-Landau Functional for a Usual Ferromagnet

The Ginzburg-Landau theory for a usual ferromagnet can be found in many textbooks, for example in Refs. [72–74]. Figure 4.1 shows the temperature versus magnetic field phase diagram. Below the critical temperature T_c, the system is ordered and can be characterized by the magnetization $\boldsymbol{M}$ which is the thermal average of the microscopic spins. $\boldsymbol{M}$ vanishes in the paramagnetic phase, *i.e.* above the critical temperature T_c. Since $\boldsymbol{M}$ changes continuously across T_c, the phase transition is of second order.

In the ordered phase close to the phase transition, the magnetization is small, so that according to the Landau theory one can expand the free energy functional F in powers of the slowly varying magnetization. Moreover, in the low-energy limit, fast fluctuations of the magnetic moments do not play an important role, and therefore one additionally expands F in derivatives of the local magnetization $\boldsymbol{M}(\boldsymbol{r})$. In the absence of a magnetic field and an underlying atomic structure, the system should be invariant under time reversal and under the rotation of all spins. Postulating this, the Ginzburg-Landau free energy functional for a conventional, inversion-symmetric ferromagnet is given by

$$F[\boldsymbol{M}(\boldsymbol{r})] = \int d^3r \left(r_0 \boldsymbol{M}^2 + J(\nabla \boldsymbol{M})^2 + U \boldsymbol{M}^4 - \boldsymbol{B}\boldsymbol{M} + \dots \right), \qquad (4.4)$$

where $(\nabla \boldsymbol{M})^2 \equiv \partial_i M_j \partial_i M_j$, $\boldsymbol{M}^4 = (\boldsymbol{M} \cdot \boldsymbol{M})^2$, and the dots indicate higher-order terms which are discussed below. Here, r_0, J, and U are phenomenological parameters which are determined by the microscopic theory of the particular system. For a ferromagnetic system J is positive and prevents a non-collinear magnetic structure. The quartic term accounting for mode-mode interactions to lowest order (as discussed below) has to have a positive prefactor U to ensure stability of the system. The free energy functional depends sensitively on the sign of r_0, as can be seen in Fig. 4.2, where the free energy functional is plotted as a function of a homogeneous magnetization.

When linearizing all temperature dependences around the critical temperature, and keeping only the linear temperature dependence of r_0, then a positive (negative) r_0 corresponds to a temperature T that is larger (smaller) than the mean-field critical temperature T_c^{MF}. Consequently, this implies that $r_0(T) \propto (T - T_c^{MF})$ with a positive prefactor. Due to fluctuations and further non-linear terms the actual critical temperature differs slightly from its mean-field value, so that in general $T_c \approx T_c^{MF}$.

For $\boldsymbol{B} = 0$ the Ginzburg-Landau free energy functional of Eq. (4.4) is minimized by a homogeneous ferromagnetic magnetization configuration with $\partial_i \boldsymbol{M} = 0$. The amplitude
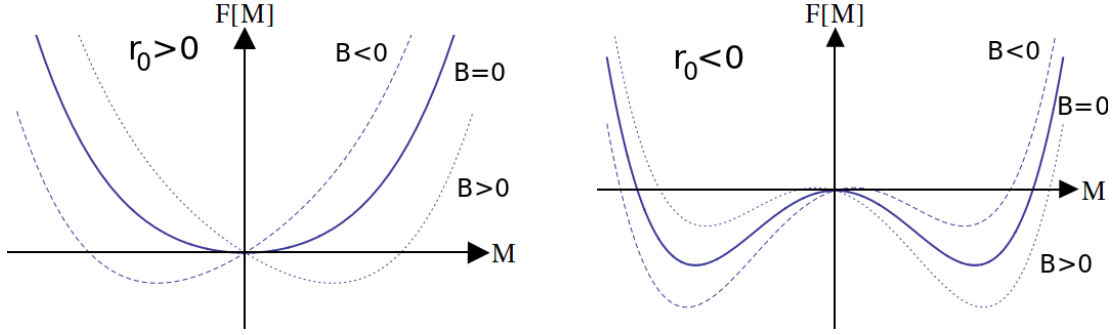
Figure 4.2: Sketch of the mean-field free energy functional for a homogeneous magnetization for a ferromagnet. Without an applied magnetic field the system is paramagnetic for $r_0 > 0$ (left panel) and ferromagnetic for $r_0 < 0$ (right panel).

of the magnetization is obtained by

$$\frac{\partial F}{\partial M} = 2MV(r_0 + 2UM^2) \quad \Rightarrow \quad M = 0 \vee M = \pm\sqrt{-\frac{r_0}{2U}}. \qquad (4.5)$$

It is zero for temperatures above the critical temperature ($r_0 > 0$), but assumes a finite value in the ordered phase, see Fig. 4.2. Without the magnetic field, the free energy functional is rotational invariant, and therefore the direction of $\boldsymbol{M}$ is not determined within Eq. (4.4). When applying a magnetic field, the magnetic moments align into the direction of the magnetic field.

The Ginzburg-Landau free energy functional as given in Eq. (4.4) obeys the following symmetries. It is symmetric under a translation or rotation in space and under spatial inversion. Moreover, it is invariant under the transformation $\boldsymbol{M} \to -\boldsymbol{M}$ and $\boldsymbol{B} \to -\boldsymbol{B}$ as well as under a combined rotation of space and spin-space around an arbitrary axis for $\boldsymbol{B} = 0$ or, for $\boldsymbol{B} \neq 0$, around the axis defined by $\boldsymbol{B}$. The rotation symmetry is broken by crystal anisotropies.

4.2   Ginzburg-Landau Theory for Helimagnets

In helimagnets, *i.e.* magnets without inversion symmetry, weak spin-orbit coupling leads to the formation of smooth twisted magnetic structures, *e.g.* helices [62], with a long period compared to the lattice constant. The lack of inversion symmetry allows for additional terms in the magnetic Ginzburg-Landau theory which have odd powers of spatial derivatives and thus are odd under spatial inversion. The most important additional contribution for helimagnets is the term linear in the spatial derivative. It is called Dzyaloshinskii-Moriya (DM) interaction [59, 60] and given by

$$\int d^3r \, 2 \, D \, \boldsymbol{M} \cdot (\nabla \times \boldsymbol{M}) \qquad (4.6)$$

A positive (negative) D selects left-handed (right-handed) twisted magnetic structures. We consider $D > 0$ which corresponds to left-handed spirals as being realized in the examined samples of MnSi. The pitch q, *i.e.* the wavelength or period of a helix, is determined by the competition between the strength D of the DM term, which favors a canted magnetization structure, and the ferromagnetic exchange interaction J, which energetically prefers a uniform magnetization, thus $q = D/J$.

The inverse wavevector corresponds to the length scale ξ_{so} on which the magnetic structures develop. As expected, ξ_{so} is characterized by the strength of spin-orbit coupling λ_{so} since $\xi_{\mathrm{so}} \sim 1/q \sim 1/D \sim 1/\lambda_{\mathrm{so}}$. Therefore, each derivative contributes with a power λ_{so} as $\nabla \sim \xi_{\mathrm{so}}^{-1} \sim \lambda_{\mathrm{so}}$. Because spin-orbit coupling is very weak, it is useful to order all terms in the Ginzburg-Landau free energy in powers of spin-orbit coupling strength λ_{so}. Hence, the Ginzburg-Landau free energy functional for a helimagnet up to order λ_{so}^2 is given by [55, 56]

$$F[\boldsymbol{M}(\boldsymbol{r})] = \int d^3 r \left(r_0 \boldsymbol{M}^2 + J(\nabla \boldsymbol{M})^2 + 2 D \, \boldsymbol{M} \cdot (\nabla \times \boldsymbol{M}) + U \boldsymbol{M}^4 - \boldsymbol{B} \boldsymbol{M} \right). \quad (4.7)$$

This functional also illustrates the three separated energy scales, controlled by the strength of spin-orbit coupling λ_{so}, as discussed in Section 3.1.2. The strongest one is ferromagnetic, followed by the weaker spin-orbit coupling energy scale. The weakest one which is not yet included in Eq. (4.7) originates from tiny crystalline field interactions, leading to, for example, the orientation of the magnetic structure with respect to the underlying atomic crystal lattice [55, 56]. Such terms are of even higher order in λ_{so} and break the rotational symmetry. They are discussed for the different chiral phases below. Note that in the presence of weak disorder r_0 (and, to be precise, also the prefactors of the other terms) fluctuates slightly as a function of the position, $\boldsymbol{r}$. By a rescaling of length $\tilde{\boldsymbol{r}} = D/J\boldsymbol{r}$, magnetization $\tilde{\boldsymbol{M}} = [UJ/(D^2)]^{1/2}\boldsymbol{M}$, and magnetic field $\tilde{\boldsymbol{B}} = [U(J/D)^3]^{1/2}\boldsymbol{B}$ one can reduce the number of parameters entering the free energy functional such that it reduces to [1]:

$$F[\tilde{\boldsymbol{M}}(\tilde{\boldsymbol{r}})] = \gamma \int d^3 \tilde{r} \left((1+t)\tilde{\boldsymbol{M}}^2 + (\tilde{\nabla}\tilde{\boldsymbol{M}})^2 + 2 \, \tilde{\boldsymbol{M}} \cdot (\tilde{\nabla} \times \tilde{\boldsymbol{M}}) + \tilde{\boldsymbol{M}}^4 - \tilde{\boldsymbol{B}} \cdot \tilde{\boldsymbol{M}} \right). \quad (4.8)$$

Here, γ is a positive, constant prefactor given by JD/U since we choose D to be positive. It determines the relative weight of the mean-field value and the fluctuation contribution to the approximated free energy in Eq. (4.3). In these rescaled units, the distance to the $B = 0$ mean-field critical temperature is determined by $t = r_0 J/D^2 - 1 \propto T - T_c^{MF}$. In the mean-field approximation with vanishing magnetic field, a negative t describes the helical phase, while a positive t represents the paramagnetic phase. In above units, the prefactor of the DM term is rescaled to one. Provided that the saddle point approximation is valid, the only remaining parameters determining the physics within the Ginzburg-Landau theory are then t and $\boldsymbol{B}$. In the following, to simplify the notation, we will omit all tildes, and consider

$$F[\boldsymbol{M}(\boldsymbol{r})] = \gamma \int d^3 r \left((1+t)\boldsymbol{M}^2 + (\nabla \boldsymbol{M})^2 + 2 \, \boldsymbol{M} \cdot (\nabla \times \boldsymbol{M}) + \boldsymbol{M}^4 - \boldsymbol{B} \cdot \boldsymbol{M} \right). \quad (4.9)$$

However, we have to keep in mind the particular chosen units. Since the free energy functional in Eq. (4.9) is still translational invariant, $\boldsymbol{M}(\boldsymbol{r})$ is a periodic function in space, and we can perform a Fourier transformation to momentum space:

$$\boldsymbol{M}(\boldsymbol{r}) = \sum_{\boldsymbol{q}} \boldsymbol{m}_{\boldsymbol{q}} \, e^{i \boldsymbol{q} \cdot \boldsymbol{r}}. \quad (4.10)$$

For a real magnetization, $\boldsymbol{M}(\boldsymbol{r}) \in \mathbb{R}$, it follows that $\boldsymbol{m}_{-\boldsymbol{q}} = \boldsymbol{m}_{\boldsymbol{q}}^*$, where $\boldsymbol{m}_{\boldsymbol{q}}^*$ denotes the complex conjugate of $\boldsymbol{m}_{\boldsymbol{q}}$, and we can rewrite Eq. (4.9) as a sum of quadratic terms plus a constant term [1]:

$$\frac{F[\boldsymbol{M}]}{\gamma} = -V \frac{t^2 - \boldsymbol{B}^2}{4} + V \sum_{\boldsymbol{q} \neq \boldsymbol{0}} \boldsymbol{m}_{-\boldsymbol{q}}^a [r^{ab}(\boldsymbol{q}) - t\delta^{ab}] \boldsymbol{m}_{\boldsymbol{q}}^b + \int \left(\boldsymbol{M}^2 + \frac{t}{2} \right)^2 d^3 r + V \left(\boldsymbol{M}_f - \frac{\boldsymbol{B}}{2} \right)^2$$

$$(4.11)$$

where $r^{ab}(\boldsymbol{q}) = (1+t+\boldsymbol{q}^2)\delta^{ab} - 2i\epsilon^{abc}q^c$, and V is the volume of the system. The eigenvalues of the matrix $(r^{ab}(\boldsymbol{q}) - t\delta^{ab})_{ab}$ are $\{(q-1)^2, 1+q^2, (q+1)^2\}$ with $q = |\boldsymbol{q}|$, meaning that this term is positive semi-definite as the last two terms on the right hand side. For $q = 1$ also the eigenvalue zero occurs. Since the last three terms on the right hand side are greater or equal to zero, F/γ is bounded from below by the constant $-V(t^2 - \boldsymbol{B}^2)/4$. This implies that the ansatz for the magnetization, which sets all three quadratic terms to zero, is proven to be the mean-field ground state. For $t < 0$ and $B < \sqrt{-2t}$ this is fulfilled by

$$\boldsymbol{M}(\boldsymbol{r}) = \begin{pmatrix} \sqrt{2}\Phi\cos(qz) \\ \sqrt{2}\Phi\sin(qz) \\ 0 \end{pmatrix} + \begin{pmatrix} 0 \\ 0 \\ M_f \end{pmatrix} \tag{4.12}$$

describing the conical phase [1, 75], where the wave vector $\boldsymbol{q}$ of the conical phase aligns with the direction of the magnetic field, $\boldsymbol{q} = (0,0,1)^T \parallel \boldsymbol{B}$, see Fig. 3.4. Due to the rotational invariance of Eq. (4.9) we considered in the ansatz above the magnetic field to point in z direction. Furthermore, the uniform ferromagnetic component $\boldsymbol{M}_f \equiv \int \boldsymbol{M}(\boldsymbol{r})d^3r/V = \boldsymbol{m}_{\boldsymbol{q}=0}$ is given by $\boldsymbol{M}_f = \boldsymbol{B}/2$ and $\sqrt{2}\Phi = \frac{1}{2}\sqrt{-2t - B^2}$. Since $M_f \sim B$, the conical phase changes smoothly into the helical phase for $B \to 0$. In this case, the direction of $\boldsymbol{q}$ relative to the crystallographic axes is not determined by the rotationally invariant free energy functional of Eq. (4.9). To determine this direction from a Ginzburg-Landau theory one has to include anisotropy terms [55, 56]. A term that pins the helical wave vector in the experimentally observed $\langle 111 \rangle$ direction is, to lowest order in spin-orbit coupling $\sim \lambda_{\text{so}}^4$, for example given by

$$\begin{aligned} F_p^{(1)}[\boldsymbol{M}(\boldsymbol{r})] &= c_1 \int_V d^3r\, \boldsymbol{M}(\boldsymbol{r}) \left(\partial_x^4 + \partial_y^4 + \partial_z^4\right) \boldsymbol{M}(\boldsymbol{r}) \\ &= c_1 V \sum_{\boldsymbol{q}} \left(q_x^4 + q_y^4 + q_z^4\right) |\boldsymbol{m}_{\boldsymbol{q}}|^2, \end{aligned} \tag{4.13}$$

with a positive prefactor c_1. This term is already written in our rescaled units, as introduced in Sec. 4.2. A systematic list of higher-order terms of the free energy that respect the B20 crystal structure is given in Appendix A.

For increasing magnetic field B, and neglecting such anisotropy terms, the amplitude a of the helical part shrinks until at $B = \sqrt{-2t}$ there is only the field-polarized phase left over. Above this threshold, $B > \sqrt{-2t}$, the field-polarized phase is the mean-field ground state. Taking the crystalline field interactions into account, the crossover from the helical to the conical phase at the critical magnetic field B_{c1} is, in general, characterized by a change of the direction of the helical wave vector from a $\langle 111 \rangle$ direction to the direction of the magnetic field $\boldsymbol{B}$.

In conclusion, the additional DM term causes canted magnetic structures of mainly conical type. The mean-field theory determines the chirality of the low-energy helical modes by the sign of the prefactor of the DM term and the wavelength $\lambda = 2\pi$ ($\lambda = 2\pi/Q = 2\pi J/|D|$) in rescaled units (see Eq. (4.7)), which is long compared to the crystallographic periods and, in general, incommensurate with them.

However, in Sec. 3.1.2 we have already discussed that in a small pocket of the phase diagram the conical phase is not the equilibrium ground state of the system, but the skyrmion phase is. As the skyrmion lattice phase occurs only close to the paramagnetic phase transition, one can also use a Ginzburg-Landau model to describe its equilibrium properties. Within the calculation of Eq. (4.11) and Eq. (4.12) we made basically two assumptions. First, we did not include higher-order terms to Eq. (4.9), and second we

only did a mean-field analysis. It has been shown in Ref. [1] that the skyrmion lattice has a lower free energy than the conical phase and thus becomes stable. To be precise, upon including Gaussian thermal fluctuations the free energy of the skyrmion phase becomes lower than the one of the conical phase, thereby favoring the skyrmion lattice phase. In the following, first we give intuitive arguments why the skyrmion lattice should be stabilized by Gaussian thermal fluctuations, and then briefly review the Ginzburg-Landau analysis of Ref. [1] for the skyrmion lattice including fluctuations.

4.3 Ginzburg-Landau Theory for the Skyrmion Lattice

In a small pocket of the phase diagram shown in Fig. 3.2, it becomes energetically favorable for helical magnets to establish a two-dimensional skyrmion lattice perpendicular to the external field $\boldsymbol{B}$. A skyrmion configuration takes advantage of the coupling to the external magnetic field by building up a finite ferromagnetic component parallel to the direction of the magnetic field on one hand, and on the other hand of the DM interaction by continuously twisting the magnetization on the length scale $\xi_{so} \sim 1/\lambda_{so}$ [1, 29, 30, 34, 35], as we will show below.

Already in 1989 A. N. Bogdanov and D. A. Yablonskii [29] and later in 1994 A. N. Bogdanov and A. Hubert [30] showed that skyrmion textures are a mean-field solution for anisotropic non-centrosymmetric magnetic materials subject to a magnetic field. Moreover, in these works it was stated that within a mean-field analysis a skyrmion lattice is only a thermodynamically metastable solution for cubic materials like MnSi. In contrast to these works, it has been shown in Ref. [1] that it suffices to include Gaussian thermal fluctuations to the mean-field results to stabilize the skyrmion solution also in cubic non-centrosymmetric bulk materials. Note that for thin films, where the magnetic field is applied in perpendicular direction, it has been shown that the skyrmion phase even becomes stable on the mean-field level [44]. In this Thesis, we focus, however, on bulk materials.

Since the skyrmion lattice is also a periodic stucture in real space, we consider the Fourier transformation of the magnetization,

$$\boldsymbol{M}(\boldsymbol{r}) = \sum_{\boldsymbol{q}} \boldsymbol{m}_{\boldsymbol{q}}\, e^{i\boldsymbol{q}\cdot\boldsymbol{r}} = \boldsymbol{M}_f + \sum_{\boldsymbol{q}_j \in L_R} \boldsymbol{m}_{\boldsymbol{q}_j}\, e^{i\boldsymbol{q}_j \cdot \boldsymbol{r}}, \tag{4.14}$$

where we explicitly introduced the uniform ferromagnetic component $\boldsymbol{M}_f$. The second sum extends over all elements $\boldsymbol{q}_j$ of L_R, where L_R denotes the reciprocal lattice except $\boldsymbol{q} = 0$.

Simple arguments for the skyrmion lattice solution: The main signal of a skyrmion lattice in the neutron experiments are six spots on a regular hexagon which is perpendicular to the applied magnetic field, implying that basically three different Fourier modes occur. To get an intuitive understanding why such a magnetic structure with three modes should be stabilized, one can exploit the analogies to the crystal formation. Crystal formation, *i.e.* the formation of a crystal out of a liquid state, is often driven by three-particle collisions [74]. In momentum space, the interaction of three density waves can be written as

$$\sum_{\boldsymbol{q}_1, \boldsymbol{q}_2, \boldsymbol{q}_3} \rho_{\boldsymbol{q}_1} \rho_{\boldsymbol{q}_2} \rho_{\boldsymbol{q}_3} \delta(\boldsymbol{q}_1 + \boldsymbol{q}_2 + \boldsymbol{q}_3) \tag{4.15}$$
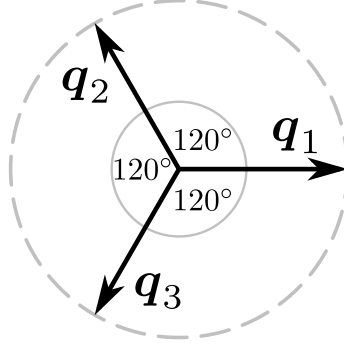
Figure 4.3: Main three momentum vectors $\boldsymbol{q}_1$, $\boldsymbol{q}_2$ and $\boldsymbol{q}_3$ of the skyrmion phase, lying in the same plane and enclosing relative angles of 120°.

It is only possible to gain energy from this term if the three momentum vectors $\boldsymbol{q}_1$, $\boldsymbol{q}_2$ and $\boldsymbol{q}_3$ add up to zero. This implies immediately that they all have to lie in the same plane.

In general, in a magnetic system three-mode interactions are forbidden by time-reversal symmetry. However, the skyrmion phase in MnSi occurs only in a finite external applied magnetic field which breaks time-reversal symmetry. Therefore, three-mode interactions are allowed, and one gets an analog scenario for parts of the quartic interaction term. The Fourier transform of the quartic term of the free energy functional in Eq. (4.9) is given by

$$\int d^3r \, \boldsymbol{M}^4 = V \sum_{\boldsymbol{q}_0, \boldsymbol{q}_1, \boldsymbol{q}_2, \boldsymbol{q}_3} (\boldsymbol{m}_{\boldsymbol{q}_0} \cdot \boldsymbol{m}_{\boldsymbol{q}_1})(\boldsymbol{m}_{\boldsymbol{q}_2} \cdot \boldsymbol{m}_{\boldsymbol{q}_3}) \delta(\boldsymbol{q}_0 + \boldsymbol{q}_1 + \boldsymbol{q}_2 + \boldsymbol{q}_3), \qquad (4.16)$$

using $\boldsymbol{M}(\boldsymbol{r}) = \sum_{\boldsymbol{q}} \boldsymbol{m}_{\boldsymbol{q}} \, e^{i\boldsymbol{q} \cdot \boldsymbol{r}}$. In the presence of a sufficiently large external magnetic field, a finite uniform magnetic component $\boldsymbol{M}_f$ arises. Within Eq. (4.16) there are effectively cubic terms in the Fourier modes with momentum vectors $\boldsymbol{q} \neq 0$,

$$\sum_{\boldsymbol{q}_1, \boldsymbol{q}_2, \boldsymbol{q}_3} (\boldsymbol{M}_f \cdot \boldsymbol{m}_{\boldsymbol{q}_1})(\boldsymbol{m}_{\boldsymbol{q}_2} \cdot \boldsymbol{m}_{\boldsymbol{q}_3}) \delta(\boldsymbol{q}_1 + \boldsymbol{q}_2 + \boldsymbol{q}_3). \qquad (4.17)$$

This term looks similar to the one for the crystal formation, and as above one can gain energy from this term if $\boldsymbol{q}_1 + \boldsymbol{q}_2 + \boldsymbol{q}_3 = 0$. In the case of the chiral magnets, the modulus of the $\boldsymbol{q}$ vectors is determined by the ratio of the DM interaction strength and the ferromagnetic exchange coupling, so that all three modes have the same modulus. In our rescaled units introduced above, the modulus of the momentum vectors is normalized to unity, $|\boldsymbol{q}| = 1$. This implies that these three momentum vectors have to be arranged in a plane, defined by a normal vector $\hat{\boldsymbol{n}}$ with their relative angles being 120°, see Fig. 4.3. Since the magnetization $\boldsymbol{M}(\boldsymbol{r})$ is real, for each $\boldsymbol{q} \neq 0$ also $-\boldsymbol{q}$ occurs in the sum of the Fourier transformation, and $\boldsymbol{m}_{-\boldsymbol{q}}$ coincides with the complex conjugate of $\boldsymbol{m}_{\boldsymbol{q}}$, i.e. $\boldsymbol{m}_{-\boldsymbol{q}} = \boldsymbol{m}_{\boldsymbol{q}}^*$. This consideration already displays the main six spots on a regular hexagon in the neutron scattering data for the skyrmion phase. To gain the most energy of the term in Eq. (4.17), the uniform magnetic component $\boldsymbol{M}_f$, which aligns in the direction of the external magnetic field, should have a large overlap with $\boldsymbol{m}_{\boldsymbol{q}_i}$, $i = 1, 2, 3$. Since the DM terms favors $\boldsymbol{m}_{\boldsymbol{q}_i} \perp \boldsymbol{q}_i$, the energy gain is largest for a uniform magnetic component $\boldsymbol{M}_f$ which is perpendicular to the three $\boldsymbol{q}$ vectors. Thus, the three $\boldsymbol{q}$ vectors must be perpendicular to the applied magnetic field, when neglecting small anisotropy effects. Upon including anisotropy effects the skyrmion plane is slightly tilted, as discussed below. This accounts for the second experimental fact that the Bragg spots are located in the plane

perpendicular to the applied magnetic field, independent of the orientation of the atomic lattice.

Therefore, to a very good approximation the skyrmion lattice can be described by a simple superposition of three helices and a uniform magnetic moment:

$$\boldsymbol{M}(\boldsymbol{r}) \approx \boldsymbol{M}_f + \sum_{j=1}^{3} \boldsymbol{M}_j^{\text{helix}}(\boldsymbol{r} + \Delta \boldsymbol{r}_j), \tag{4.18}$$

where

$$\boldsymbol{M}_j^{\text{helix}}(\boldsymbol{r}) = \sqrt{2}\,\Phi\big(\hat{\boldsymbol{n}}_j^I \cos(\boldsymbol{q}_j \cdot \boldsymbol{r}) - \hat{\boldsymbol{n}}_j^{II} \sin(\boldsymbol{q}^j \cdot \boldsymbol{r})\big), \tag{4.19}$$

is the magnetization of a single chiral helix with amplitude $\sqrt{2}\,\Phi$ and phase shift $\Delta \boldsymbol{r}_j$. Moreover, $\{\boldsymbol{q}_j, \hat{\boldsymbol{n}}_j^I, \hat{\boldsymbol{n}}_j^{II}\}$ forms an orthonormal basis. All three helices are left-handed since $\boldsymbol{q}_j = \hat{\boldsymbol{n}}_j^I \times \hat{\boldsymbol{n}}_j^{II}$ for $j = 1, 2, 3$, and their helical wave vectors $\boldsymbol{q}_j$ are perpendicular to the magnetic field, $\boldsymbol{q}_j \perp \boldsymbol{B}$ for $j = 1, 2, 3$. The relative angles between the $\boldsymbol{q}_j$ vectors are 120° as shown in Fig. 4.3. Moreover, within the minimization procedure it turns out that all three helices have the same weight.

Finally, $\Delta \boldsymbol{r}_j$ is the relative shift of the helices. For an infinite systems two of these three phases just correspond to translations of the magnetic structure within the plane and can therefore, without loss of generality, be set to zero. However, the third phase or in other words, the phase relationship between the helices is crucial for the magnetic structure [32, 33, 36] as will be discussed in more detail in Chapter 5. Since first-order neutron scattering data are only sensitive to $|\boldsymbol{m}_{\boldsymbol{q}_j}|^2$, no information about this relative phase can be inferred from the experiments of Refs. [1]. From higher-order scattering experiments it turns out that the phase relationship of the skyrmion lattice phase is indeed fixed in such a way that a lattice of anti-skyrmions occurs. We discuss this issue along with a mean-field theory in more detail in Chapter 5

Mean-field analysis: Eq. (4.14) for the skyrmion phase also includes higher-order Fourier modes, and for a proper minimization of the free energy functional they, of course, have to be taken into account for $t < 0$. To calculate the mean-field energy, we include all wavevectors $\boldsymbol{q}_j \in L_R$ up to a short-distance cutoff, $|\boldsymbol{q}_j| \leq \Lambda$, and minimize numerically with respect to amplitudes and phases of all modes. In Ref. [1] it has also been shown that the Fourier composition of Eq. (4.14) converges rapidly since the skyrmion lattice is a smooth and singularity-free magnetic structure. The inclusion of higher-order modes does not change the symmetry or the topology of the skyrmion crystal. Only the structure is slightly distorted from the simple form of Eq. (4.18), because the relative weight of the higher-order contributions is very small. This has been observed experimentally in Ref. [67], and we will further discuss this issue in comparison with our theory in Chapter 5. In the limit $t \to 0$, very close to the critical temperature, the skyrmion lattice is exacly described by Eq. (4.18).

Substituting Eq. (4.14) into Eq. (4.9), one finds that the skyrmion lattice phase is a local mean-field minimum of the Ginzburg-Landau free energy for a certain range of parameters for t and $\boldsymbol{B}$ [1, 29, 30]. Nevertheless, the conical phase is still the global minimum within the mean-field analysis. However, from the inset of Fig. 4.4, where the difference of the mean-field energy between the skyrmion phase and the conical phase is plotted as a function of the external magnetic field, it follows that this energy difference is quite small, especially for intermediate fields $B \approx 0.4\, B_{c2}$. To be more specific, the upper
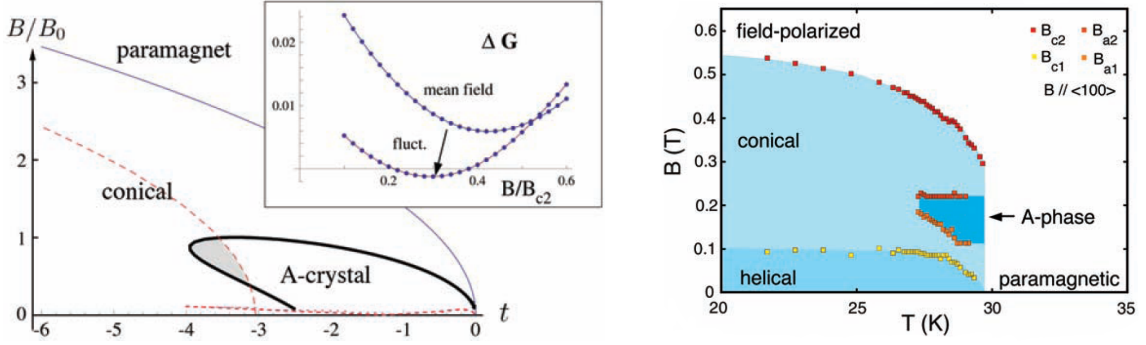
Figure 4.4: Theoretical phase diagram for the different magnetic phases as a function of temperature t and applied magnetic field B. For better comparison the experimental phase diagram of Fig. 3.2 is again shown on the right hand side. Inset: Energy difference of the skyrmion phase and the conical phase as a function of the applied magnetic field for $t = -3.5$. The mean-field curve is everywhere positive, indicating that the conical phase is the global mean-field minimum. However, including thermal fluctuation corrections reverses the picture in a small parameter range close to the critical temperature T_c. The energy difference is plotted in units of $\gamma\,t^2/4$, which is the energy difference between the ferromagnetic and the conical phase at $\boldsymbol{B} = 0$. Figures are taken from Ref. [1].

curve of the inset displays the mean-field calculation with

$$\frac{4}{\gamma\,t^2 V}\Delta G_{\mathrm{mf}} = \frac{4}{\gamma\,t^2 V}\left(G_{\mathrm{mf}}^{\mathrm{skyrm}} - G_{\mathrm{mf}}^{\mathrm{con}}\right), \tag{4.20}$$

where $G_{\mathrm{mf}}^{\mathrm{skyrm}}$ ($G_{\mathrm{mf}}^{\mathrm{con}}$) is the mean-field free energy of the skyrmion lattice phase (conical phase).

Corrections due to thermal fluctuations: The lower curve in the inset of Fig. 4.4 shows ΔG when considering also Gaussian thermal fluctuation corrections around the mean-field solution [1]. In that case, the free energy is given by Eq. (4.3). For a small range of magnetic fields, the skyrmion lattice has lower free energy than the conical phase, and thus it is the stabilized solution. Combining all information one can plot the theoretical magnetic phase diagram, as shown in Fig. 4.4. For a better comparison the experimental phase diagram of Fig. 3.2 is also shown next to the theoretical one. Qualitatively, they agree quite well. Nevertheless, very close to T_c, where fluctuations dominate over the mean-field part, the analysis of taking only Gaussian thermal fluctuations into account is no longer valid as already explained in the beginning of this Chapter. The dashed red line in Fig. 4.4 marks the region, where the fluctuation corrections are less than twenty percent of the mean-field value for the dominant Fourier modes, $|\delta\boldsymbol{m_q}| < 0.2\,|\boldsymbol{m_q}|$. Therefore, one has to be careful by interpreting this result very close to T_c. The transition between the skyrmion phase and the conical phase is expected to be fluctuation-driven first order [76, 77], which moves the phase transition line to the paramagnetic regime.

In Ref. [1], it has also been shown that the pocket, where the skyrmion lattice is stabilized, is related to the region in the phase diagram (close to $B \approx 0.4\,B_{c2}$), where the amplitude of the magnetization $|\boldsymbol{M}(\boldsymbol{r})|$ is almost constant. This is quite reasonable since modulations of the amplitude of the magnetization are energetically very expensive. In conclusion, this implies that the skyrmion lattice cannot be continuously deformed into

the competing conical phase, because locally suppressing $|\boldsymbol{M}|$ to zero costs a lot of energy. In other words, the two phases are topologically distinct. Having introduced this notion of topological different magnetic phases by the concept of continuously deforming the order parameter, one can assign to each magnetic stucture a topological invariant, the winding number W. For $\boldsymbol{B}\|\hat{\boldsymbol{z}}$ it is given by

$$W = \frac{1}{4\pi} \int\limits_{\text{UC}} dx\, dy\, \hat{\boldsymbol{\Omega}} \cdot (\partial_x \hat{\boldsymbol{\Omega}} \times \partial_y \hat{\boldsymbol{\Omega}}), \tag{4.21}$$

where $\hat{\boldsymbol{\Omega}} = \boldsymbol{M}/|\boldsymbol{M}|$ is the direction of the magnetization and "UC" denotes the integration over the magnetic unit cell.

As already explained in Chapter 2, the winding number measures how many times the order parameter wraps around the d-dimensional sphere. Here, the order parameter is the magnetization direction, and $d = 2$. For the skyrmion lattice, the winding number is quantized to -1 per magnetic unit cell, implying that one skyrmion fully winds around the sphere. The sign of W reflects that the magnetic whirls in the skyrmion lattice are anti-skyrmions. Again, comparing the stabilization of the skyrmion lattice to the example of crystal formation, where one has an integer number of atoms per unit cell, in the magnetic system the skyrmions correspond to the atoms in a usual crystal.

In the following, for simplicity, we neglect the effects of thermal fluctuations which lower the free energy of the skyrmion lattice and drive it to become a global minimum of the free energy, as long as we do not discuss the competition of various magnetic phases. This is possible since the skyrmion lattice phase is a local minimum of the Ginzburg-Landau free energy $F[\boldsymbol{M}(\boldsymbol{r})]$ in the presence of a magnetic field [1]. We expect that thermal fluctuation corrections are small for the obtained results discussed in the following.

Symmetries of the skyrmion lattice: A perfect undistorted skyrmion lattice that is coupled to the atomic lattice has a remaining sixfold rotational symmetry around the axis of the magnetic field $\boldsymbol{B}$. Furthermore, it is invariant under the combined transformation of $\boldsymbol{M} \to -\boldsymbol{M}$ and a rotation of $180°$ around an axis along one of the six main $\boldsymbol{q}$ vectors or around an axis along one of the $\boldsymbol{q} \times \boldsymbol{B}$ directions.

This symmetry implies that for a Fourier mode $\boldsymbol{m_q}$ contributing to the skyrmion lattice with a $\boldsymbol{q}$ vector parallel to one of the six main $\boldsymbol{q}$ vectors which split up into real and imaginary parts, $\boldsymbol{m_q} = \text{Re}(\boldsymbol{m_q}) + i\,\text{Im}(\boldsymbol{m_q}) \equiv \boldsymbol{m_q}^{(r)} + i\,\boldsymbol{m_q}^{(i)}$, its real (imaginary) part has to be aligned parallel (perpendicular) to the direction of the magnetic field, *i.e.* $\text{Re}(\boldsymbol{m_q}) \parallel \boldsymbol{B}$, $\text{Im}(\boldsymbol{m_q}) \parallel \boldsymbol{q} \times \boldsymbol{B}$. The reason for this is the following: Under the combined symmetry operation of $\boldsymbol{M} \to -\boldsymbol{M}$ (denoted by M_-) and a rotation of $180°$ around the axis along the $\boldsymbol{q}$ direction being along one of the six main $\boldsymbol{q}$ vector directions (denoted by $R_{\hat{\boldsymbol{q}}}(\pi)$), the component of $\boldsymbol{m_q}$ parallel to $\boldsymbol{q}$, *i.e.* $\boldsymbol{m_q} \cdot \boldsymbol{q}$ changes sign, wherefore $\boldsymbol{m_q}$ has to be perpendicular to $\boldsymbol{q}$:

$$\boldsymbol{m_q} \cdot \boldsymbol{q} \xrightarrow{M_- R_{\hat{\boldsymbol{q}}}(\pi)} -\boldsymbol{m_q} \cdot \boldsymbol{q} \overset{!}{=} \boldsymbol{m_q} \cdot \boldsymbol{q} \implies \boldsymbol{m_q} \perp \boldsymbol{q}. \tag{4.22}$$

Thus, $\boldsymbol{m_q}^{(r)}$ and $\boldsymbol{m_q}^{(i)}$ are restricted to a plane perpendicular to $\boldsymbol{q}$, *i.e.* they live in the plane spanned by $\boldsymbol{B}$ and $\boldsymbol{q} \times \boldsymbol{B}$.

Furthermore, when considering the combined symmetry operation of M_- and a rotation of $180°$ around the axis along the $\boldsymbol{q} \times \boldsymbol{B}$ direction (denoted by $R_{\widehat{\boldsymbol{q} \times \boldsymbol{B}}}(\pi)$), we obtain

$$\boldsymbol{m_q} \xrightarrow{M_- R_{\widehat{\boldsymbol{q} \times \boldsymbol{B}}}(\pi)} -\big(R_{\widehat{\boldsymbol{q} \times \boldsymbol{B}}}(\pi)\,\boldsymbol{m}\big)_{-\boldsymbol{q}} = -R_{\widehat{\boldsymbol{q} \times \boldsymbol{B}}}(\pi)\,\boldsymbol{m_q}^* \overset{!}{=} \boldsymbol{m_q}, \tag{4.23}$$

where the notation $\left(R_{\widehat{\boldsymbol{q}\times\boldsymbol{B}}}(\pi)\,\boldsymbol{m}\right)_{-\boldsymbol{q}}$ indicates that we have rotated already the $\boldsymbol{q}$ vector, but still have to rotate $\boldsymbol{m}$. From Eq. (4.23) follows that

$$-R_{\widehat{\boldsymbol{q}\times\boldsymbol{B}}}(\pi)\,\boldsymbol{m}_{\boldsymbol{q}}^{(r)} \overset{!}{=} \boldsymbol{m}_{\boldsymbol{q}}^{(r)} \quad \text{and} \quad R_{\widehat{\boldsymbol{q}\times\boldsymbol{B}}}(\pi)\,\boldsymbol{m}_{\boldsymbol{q}}^{(i)} \overset{!}{=} \boldsymbol{m}_{\boldsymbol{q}}^{(i)} \tag{4.24}$$

which implies

$$\boldsymbol{m}_{\boldsymbol{q}}^{(r)} \parallel \boldsymbol{B} \quad \text{and} \quad \boldsymbol{m}_{\boldsymbol{q}}^{(i)} \parallel \boldsymbol{q}\times\boldsymbol{B}. \tag{4.25}$$

Thus, $\boldsymbol{m}_{\boldsymbol{q}}^{(r)}$ has to be parallel to $\boldsymbol{B}$, and $\boldsymbol{m}_{\boldsymbol{q}}^{(i)}$ has to be oriented along the $\boldsymbol{q}\times\boldsymbol{B}$ direction.

The magnetic texture is, however, embedded in the atomic crystal breaking the rotational symmetry. This leads via tiny spin-orbit coupling effects to a preferred orientation and to a small distortion of the skyrmion lattice.

Orientation of the skyrmion lattice with respect to the atomic lattice: The free energy functional of Eq. (4.9) is fully isotropic for $\boldsymbol{B} = 0$. The external applied magnetic field breaks the full rotational symmetry and reduces it to a remaining rotational symmetry around the magnetic field axis. As discussed, the skyrmion lattice spanned by the Fourier modes $\boldsymbol{q}_j$ orients perpendicular to the magnetic field. Nonetheless, the free energy functional of Eq. (4.9) does not fix the orientation of the vectors $\boldsymbol{q}_j$ within this plane, described by an angle ϕ measured to some reference orientation. In a real sample, this orientation is determined by the anisotropy of the atomic crystal. In this part, we briefly discuss the orientation of the skyrmion lattice with respect to the atomic lattice within the Ginzburg-Landau theory as in Refs. [1, 70].

In the neutron scattering experiments discussed in Sec. 3.1.3 it is observed that the sixfold diffraction pattern of the skyrmion phase in MnSi orients weakly with respect to the atomic crystal, such that two of the six main scattering peaks align with a $\langle 110 \rangle$ crystal direction, as long as this is possible according to the chosen magnetic field direction. This breaking of the rotational symmetry can be incorporated into the Ginzburg-Landau theory by adding suitable terms of higher-order spin-orbit coupling to the free energy functional of Eq. (4.9). Since the undistorted skyrmion lattice has a sixfold symmetry around the axis of the magnetic field, one can fix the orientation within the skyrmion plane by terms that generate an effective potential of the form $-\cos(6n\phi)$ with $n \in \mathbb{N}$. Here, $\phi = 0$ is one of the preferred directions. Terms like $\sum_{\boldsymbol{q}}(q_x^4 + q_y^4 + q_z^4)|\boldsymbol{m}_{\boldsymbol{q}}|^2$ or $M_x^4 + M_y^4 + M_z^4$ which occur in lowest-order perturbation theory, *i.e.* of the order of λ_{so}^4, and that do orient the helical wave vector in the absence or in a weak magnetic field with respect to the atomic crystal, do not display such rapid oscillations to linear order. One example of a term that can lock the orientation described by ϕ in sixth-order spin-orbit coupling, $\sim \lambda_{\text{so}}^6$, is given by

$$F_L = \gamma_L \int d^3r \left((\partial_x^3\boldsymbol{M})^2 + (\partial_y^3\boldsymbol{M})^2 + (\partial_z^3\boldsymbol{M})^2\right) = \gamma_L V \sum_{\boldsymbol{q}}(q_x^6 + q_y^6 + q_z^6)|\boldsymbol{m}_{\boldsymbol{q}}|^2. \tag{4.26}$$

It is the lowest-order perturbation that manages to produce a potential of the form $-\cos(6n\phi)$.

This term is already written in our rescaled units introduced in Sec. 4.2. For the skyrmion phase a positive prefactor γ_L (where the index "L" stands for "lattice") describes the experimental observation that two of the six Bragg spots align along a $\langle 110 \rangle$ direction if the magnetic field is orthogonal to at least one of the $\langle 110 \rangle$ directions [1]. Since the ratio of γ_L and γ is proportional to fourth-order spin-orbit coupling, $\gamma_L/\gamma \sim \lambda_{\text{so}}^4$, the effect of

Figure 4.5: Orientation of the skyrmion lattice as a function of the direction of the magnetic field, $\boldsymbol{B} = \sqrt{-t/2}\,(\sin\theta/\sqrt{2},\, \sin\theta/\sqrt{2},\, \cos\theta)$ with $t = -0.8$, which is rotated from the [001] direction for $\theta = 0$ to the [110] direction for $\theta = \pi/2 = 90°$. φ denotes the angle between the [1$\bar{1}$0] direction and the $\boldsymbol{q}$ vector of the skyrmion plane that is aligned along the [1$\bar{1}$0] direction for $\theta = \pi/2 = 90°$. Left panel: $\gamma_L = 0.001$ and different distortion strengths γ_D. Right panel: $\gamma_D = 0.012$ and different strengths of γ_L.

this term is very small, and the generated effective potential is very weak compared to the other contributions to the free energy functional.

However, if the magnetic field is applied in a $\langle 100 \rangle$ direction, F_L does not lead to an orientation of the skyrmion lattice within the plane to linear order in γ_L. The reason for this is the following. On one hand, F_L is symmetric under a rotation by $\pi/2$ around a $\langle 100 \rangle$ direction, but on the other hand F_L induces a potential of the form $-\cos(6\phi)$ to linear order in γ_L. It has a periodicity of 60° and is, in particular, minimal for $\phi = 0°$, but maximal for $\phi = 90°$. Thus, $-\cos(6\phi)$ is not invariant by $\pi/2$ rotations around the axis of the magnetic field. Therefore, the directions of the $\boldsymbol{q}$ vectors within the plane of the skyrmion lattice are determined by effects of higher-order in λ_{so}, for a magnetic field in a $\langle 100 \rangle$ direction. Theoretically we expect for a magnetic field along a $\langle 100 \rangle$ axis that one of the $\boldsymbol{q}$ vectors should orient along a different perpendicular $\langle 100 \rangle$ axis: The orientation of the skyrmion lattice as a function of the direction of the magnetic field is shown in Fig. 4.5. Here, the magnetic field is rotated from the [001] direction to the [110] direction. To be precise, $\boldsymbol{B} = \sqrt{-t/2}\,(\sin\theta/\sqrt{2},\, \sin\theta/\sqrt{2},\, \cos\theta)$, and θ increases from 0 to $\pi/2 = 90°$. The angle φ is defined as the angle between the [1$\bar{1}$0] direction and the $\boldsymbol{q}$ vector of the skyrmion plane that is aligned along the [1$\bar{1}$0] direction for $\theta = \pi/2 = 90°$, i.e. $\varphi = |\arccos(\hat{\boldsymbol{q}} \cdot (1, -1, 0)^T/\sqrt{2})|$. For $\theta = 0$ the orientation angle φ assumes a value of 15°, and one of the $\boldsymbol{q}$ vectors aligns along the [100] direction. In the left panel we varied the distortion strength γ_D (discussed below), and in the right panel the strength of γ_L. As expected from our symmetry analysis, for smaller distortions strength γ_D and larger γ_L, the function $\varphi(\theta)$ becomes sharper and falls off more quickly.

Such a $\langle 100 \rangle$ $\boldsymbol{q}$ vector orientation for a magnetic field aligned along a different $\langle 100 \rangle$ direction of the skyrmion lattice has been observed in iron-doped MnSi and in $Fe_x Co_{1-x} Si$ [39, 78]. Recent unpublished measurements confirm this behaviour also for the skyrmion lattice phase in MnSi [79] and agree very well with the curves shown in Fig. 4.5.

Distortion of the skyrmion lattice: Terms of higher order in spin-orbit coupling also distort the skyrmion lattice, so that it deviates from the perfect hexagonal structure
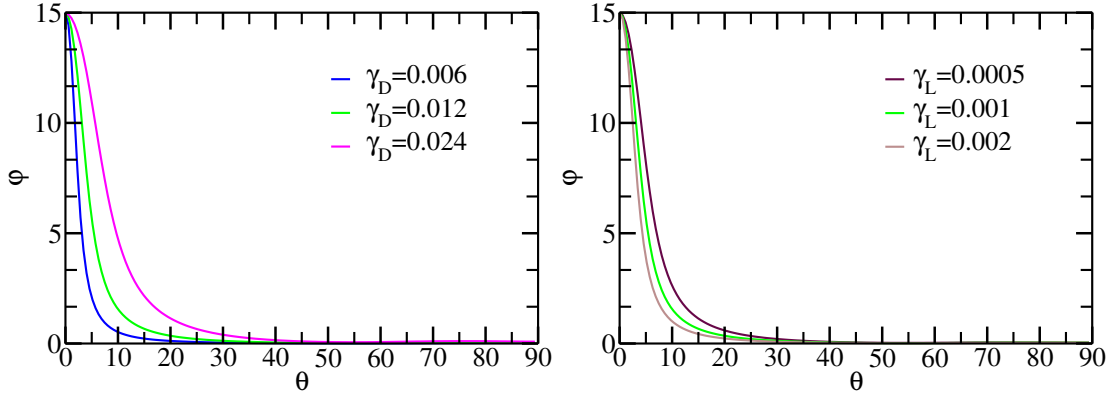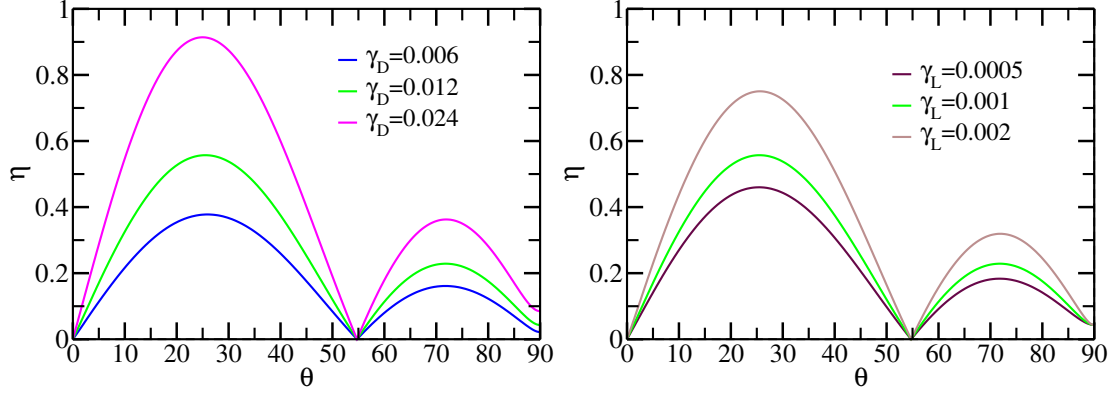
Figure 4.6: Tilt of the skyrmion lattice plane as a function of the direction of the magnetic field, $\boldsymbol{B} = \sqrt{-t/2}\,(\sin\theta/\sqrt{2},\,\sin\theta/\sqrt{2},\,\cos\theta)$ with $t = -0.8$, which is rotated from the [001] direction for $\theta = 0$ to the [110] direction for $\theta = \pi/2 = 90°$. η denotes the angle (in degree) between the magnetic field direction and the normal vector $\hat{\boldsymbol{n}}$ to the skyrmion lattice plane spanned by the three $\boldsymbol{q}$ vectors. Left panel: $\gamma_L = 0.001$ and different distortion strengths γ_D. Right panel: $\gamma_D = 0.012$ and different strengths of γ_L.

predicted by Eq. (4.9). For example, a term written also in the rescaled variables that distorts the skyrmion lattice to lowest order in spin-orbit coupling strength λ_{so}, but is still consistent with the B20 crystal symmetries of MnSi is given by

$$
\begin{aligned}
F_D &= \gamma_D \int d^3r \left[(\partial_x M^y)^2 + (\partial_y M^z)^2 + (\partial_z M^x)^2 \right] \\
&= \gamma_D V \sum_{\boldsymbol{q}} \left[q_x^2 |m_{\boldsymbol{q}}^y|^2 + q_y^2 |m_{\boldsymbol{q}}^z|^2 + q_z^2 |m_{\boldsymbol{q}}^x|^2 \right].
\end{aligned}
\tag{4.27}
$$

Compared to the prefactor γ_L of Eq. (4.26), γ_D (where the index "D" stands for "distortion") is expected to be much larger since $\gamma_L/\gamma_D \sim \lambda_{\text{so}}^2$. However, F_D does not lock the orientation of the skyrmion lattice to the atomic lattice to linear, but only to quadratic order, where $\gamma_D^2 \ll \gamma_L$. Compared to γ of Eq. (4.9), the prefactor of the distortion term is small, $\gamma_D/\gamma \sim \lambda_{\text{so}}^2$. In the distorted hexagonal skyrmion lattice, i.e. the solution in the presence of the term (4.27), the reciprocal lattice vectors $\boldsymbol{q}_j$ are tilted. They are still confined to a two-dimensional plane, but they are in general no longer perpendicular to the applied magnetic field $\boldsymbol{B}$, but to a slightly changed vector $\hat{\boldsymbol{n}}$ that is normal to the plane, $\hat{\boldsymbol{n}} \cdot \boldsymbol{q}_j = 0$. Moreover, we define $\hat{\boldsymbol{n}}$ to be a unit vector, $\hat{\boldsymbol{n}}^2 = 1$, that has a positive overlap with the magnetic field $\boldsymbol{B} \cdot \hat{\boldsymbol{n}} > 0$. To summarize, $\hat{\boldsymbol{n}}$ is defined by

$$
\hat{\boldsymbol{n}}^2 = 1, \qquad \hat{\boldsymbol{n}} \cdot \boldsymbol{q}_j = 0, \qquad \text{and} \qquad \boldsymbol{B} \cdot \hat{\boldsymbol{n}} > 0.
\tag{4.28}
$$

In Fig. 4.6, we plot the tilt of the skyrmion lattice as a function of the direction of the magnetic field. Here, the magnetic field is rotated from the [001] direction to the [110] direction. To be precise, $\boldsymbol{B} = \sqrt{-t/2}\,(\sin\theta/\sqrt{2},\,\sin\theta/\sqrt{2},\,\cos\theta)$, and θ increases from 0 to $\pi = 90°$. η is defined as the angle between the magnetic field direction and the normal vector $\hat{\boldsymbol{n}}$, i.e. $\eta = |\arccos(\hat{\boldsymbol{B}} \cdot \hat{\boldsymbol{n}})|$. It vanishes due to symmetry if the magnetic field is applied along one of the high symmetry directions $\langle 100 \rangle$ or $\langle 111 \rangle$ (note that $\arccos(1/\sqrt{3}) \approx 54.7°$), because these are twofold and threefold rotation axes of the crystal, respectively and the magnetic structure should be invariant under these rotations, which would not be the case if the magnetic lattice is tilted. For the considered anisotropy terms, η does

not vanish for a magnetic field along a $\langle 110 \rangle$ direction, but, note that $\langle 110 \rangle$ is not a high symmetry direction for B20 structures. In the left panel of Fig. 4.6 we varied the distortion strength γ_D, and in the right panel the strength of γ_L. For a generic direction η increases with increasing distortion strength γ_D and increasing γ_L. Also, the tilt of the skyrmion lattice has been recently measured, and the unpublished data [79] agree qualitatively quite well with the curves of Fig. 4.6.

The effect of distortions will in particular become important in Section 10.2, where we discuss the spin-transfer torque effects due to a distorted skyrmion lattice. Nonetheless, without such distortions $\hat{\boldsymbol{n}} = \hat{\boldsymbol{B}}$. Therefore, when we are not explicitly considering distortions of the skyrmion lattice, we will write $\hat{\boldsymbol{B}}$ instead of $\hat{\boldsymbol{n}}$ in the following.

Pinning of the skyrmion lattice due to disorder: Inhomogeneities arising from crystalline imperfections distort the perfect skyrmion lattice and pin the magnetic structure. We expect pinning due to disorder in the skyrmion lattice phase to be weak. This is based on a few considerations. First of all, this is suggested by the experimental observation of a very low threshold current density $j_c \sim 10^6$ A/m^2 [10, 80], as is discussed in the next chapters. Second, the samples used in Refs. [10, 80] are very clean and exhibit a low defect concentration expressed by the large charge carrier mean free paths of around 1000 Å. Moreover, the pinning strengths of different defects cannot just be added, *i.e.* one cannot calculate the total pinning force per volume by multiplying the pinning force of a single defect by the defect density. The reason for this is that for a sufficiently rigid and crystalline skyrmion lattice [67] pinning forces from several defects within a domain partially average out [81, 82]. Furthermore, also very strong single defects, which locally destroy completely the magnetization in a fraction of the unit cell, for example by replacing a Mn atom by a nonmagnetic impurity, lead only to very small pinning forces. For the skyrmion lattice, however, the magnetization is smooth and does not vanish anywhere [1]. The variations of the amplitude of the magnetization are small, less than twenty percent within the magnetic unit cell [1]. Therefore, pinning forces arising from the coupling to the magnitude of the magnetization are small. Also, contributions to the pinning force from the coupling of disorder to the direction of the magnetization are small, since this effect originates from spin-orbit interactions. For example, from the pinning theory of type-II superconductors [81–83] it is known that the pinning force F of an impurity can be estimated by $F \sim \Delta E / r_c$, where ΔE is the energy difference between a defect in the core center and a defect outside of the superconducting vortex core, divided by the typical radius r_c of the core. To estimate the pinning force arising from a single localized defect in the case of the skyrmion lattice we assume that the free energy difference between a defect in the center of a skyrmion and a defect in-between two skyrmions is only a fraction of the free energy density of the skyrmion lattice $\Delta F / V$. This assumption is based on the small variations of the amplitude of the magnetization in the skyrmion lattice phase. From specific heat data [84] $\Delta F / V$ can be estimated to $\Delta F / V \sim 10^{-2} k_B T_c / a^3$ which is tiny. To summarize, we estimate the pinning force from a single strong defect to be less than a few $10^{-5} k_B T_c / a$ per impurity. In the last step, we also used the important fact that the distance between the skyrmions is large, about a factor 40 larger than the lattice constant a. Therefore, the energy changes per length, *i.e.* the forces, are small. These are, however, rough estimates. A full quantitative theory of pinning is much more complicated and requires further input like the rigidity of the skyrmion lattice, the defect concentration, and the nature of single pinning centers. In particular, the latter is presently not clear.

In conclusion, we expect the pinning forces in the skyrmion lattice phase to be weak due to its smoothness. Also strong pinning defects with a rather low density might occur, but they do not have such a strong effect on the skyrmion lattice since pinning forces of random orientation partially average out. It is also possible that the skyrmion lattice is in the collective pinning regime, where the cancelation of pinning forces happens to a large extent due to the rigidity of the skyrmion lattice.

In the following chapter, we will consider the higher-order modes of the skyrmion lattice in more detail.

5 Crystalline Nature and Long-Range Order of the Skyrmion Lattice in MnSi

To show that the skyrmion phase really is a skyrmion *lattice* phase, *i.e.* of long-range crystalline nature, one has to analyze the precise spatial variation of the magnetization on long length scales. In particular, a long-range crystalline order implies the existence of higher-order modes with a $\boldsymbol{q}$ vector of $n\boldsymbol{q}_1 + m\boldsymbol{q}_2$, where n and m are integers. The vectors $\boldsymbol{q}_1$ and $\boldsymbol{q}_2$ are the lowest modes contributing to the skyrmion lattice as introduced in Sec. 4.3. Note that $\boldsymbol{q}_3 = -\boldsymbol{q}_1 - \boldsymbol{q}_2$ is included in the previous expression. From an experimental observation of these higher-order modes ($|n| + |m| > 1$) one can get, in principle, by reconstruction quantitative information on the magnetic structure. In conclusion, the experimental observation of higher-order neutron scattering spots is a direct microscopic evidence for the skyrmion phase being a magnetic *lattice* with long-range order.

In this Chapter, we will briefly discuss the experimental observation of these higher-order peaks. The neutron scattering studies were performed on one hand on the cold diffractometer MIRA at the FRM II in Munich[1], and on the other hand at the small-angle neutron scattering (SANS) instrument V4 at the Berlin neutron scattering center (BENSC). At the MIRA diffractometer, neutrons with a wavelength of $\lambda = 9.7$ Å $\pm 5\%$ are irradiated onto the sample with an instrumental resolution of $\Delta\beta_{az} = 4°$ in azimuthal direction, $\Delta\beta_{\boldsymbol{q}} = 0.004$ Å^{-1} in radial $|\boldsymbol{q}|$ direction, and $\Delta\beta_{\boldsymbol{k}_f} = 0.35°$ perpendicular to $|\boldsymbol{q}|$ in the direction of $\boldsymbol{k}_f$. At the SANS instrument V4, neutrons with a wavelength of $\lambda = 4.5$ Å $\pm 10\%$ were used, and the resolution was $\Delta\beta_{az} = 4.9°$, $\Delta\beta_{\boldsymbol{q}} = 0.003$ Å^{-1}, and $\Delta\beta_{\boldsymbol{k}_f} = 0.21°$.

After reviewing the experimental observations we compare the results to our mean-field theory. To obtain a fully quantitative theory for the skyrmion lattice phase one would, of course, have to take fluctuations into account. However, already the mean-field analysis is able to explain semi-quantitatively the experimental observations. We have published most of the work presented in this Chapter in Ref. [67], where also further experimental details can be found.

5.1 Observation of Higher-Order Neutron Scattering Peaks

The main experimental problem to observe higher-order scattering peaks is to distinguish them from multiple scattering events, *i.e.*, neutrons that scattered multiple times from the magnetic structure. For example, a neutron that scattered once with a momentum $\boldsymbol{q}_1 + \boldsymbol{q}_2$ and neutron that scattered twice (one time with momentum $\boldsymbol{q}_1$ and the other time with $\boldsymbol{q}_2$)

---

[1]Forschungsreaktor München
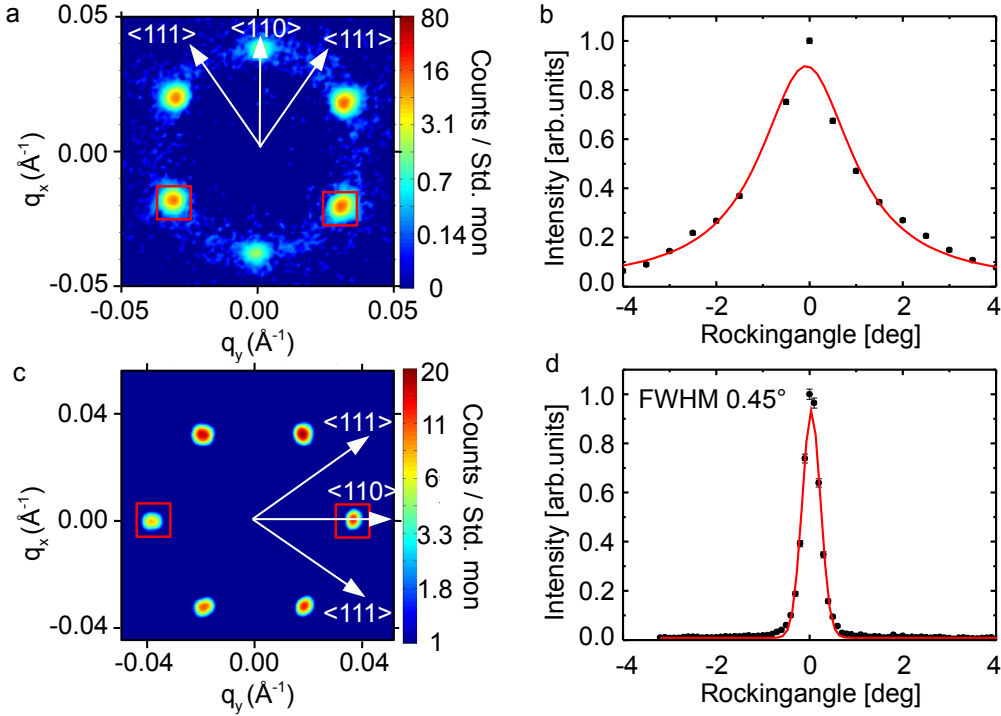
Figure 5.1: Comparison between previous SANS data (panel (a) and (b)) as discussed in Ref. [1] and data of the improved setup minimizing double-order scattering (panel (c) and (d)) for the skyrmion phase of MnSi. Panel (a) displays the neutrons scattering intensity pattern at $\mu_0 H = 0.16$ T for a thick cylindrical sample and (c) for a thin platelet (sample A) at $\mu_0 H = 0.2$ T. Panel (b) and (d) show the corresponding rocking scans. In panel (d), which has been measured in the improved setup, the rocking scan is Gaussian with a very narrow width. The Figure is taken from our publication, Ref. [67].

will finally impinge on the same spot on the detector. Furthermore, in the experimental setup the magnetic field has to be very homogeneous, since the skyrmion lattice is almost perpendicular to the magnetic field and only weakly coupled to the atomic lattice. To observe experimentally the higher-order neutron scattering spots, an improved small angle neutron scattering setup with a high-resolution had to be implemented which minimizes double scattering and demagnetizing fields. To avoid double and multiple scattering, thin samples (with a thickness of about 1 mm) were illuminated only in a small central section. In our publication Ref. [67], two samples of MnSi were studied. One sample, in the following denoted as sample A, was of the size $14 \times 9 \times 1.4$ mm^3, while the second sample, denoted as B, had the geometry $12 \times 7 \times 1$ mm^3. Both were cut from the same ingot used previously [1, 10, 85–87] and had a crystalline $\langle 110 \rangle$ direction normal to the platelet.

Fig. 5.1 shows a direct comparison of the previous SANS data obtained in the study of Ref. [1], shown in Fig. 5.1 (a), and the improved SANS data, in particular using the thin samples in Fig. 5.1 (c). Panel (a) reproduces the data shown in Fig. 3.10 (E), that corresponds to Fig. 2 (E) in the original paper, Ref. [1]. The corresponding rocking dependences are shown in panels (b) and (d) respectively. The previous data, which were subject to multiple scattering, had a very unusual line shape and a broad rocking width as shown in panel (b) of Fig. 5.1. It is comparable in size to the rocking width of the helical phase. In contrast, the new data for thin samples display the expected Gaussian rocking
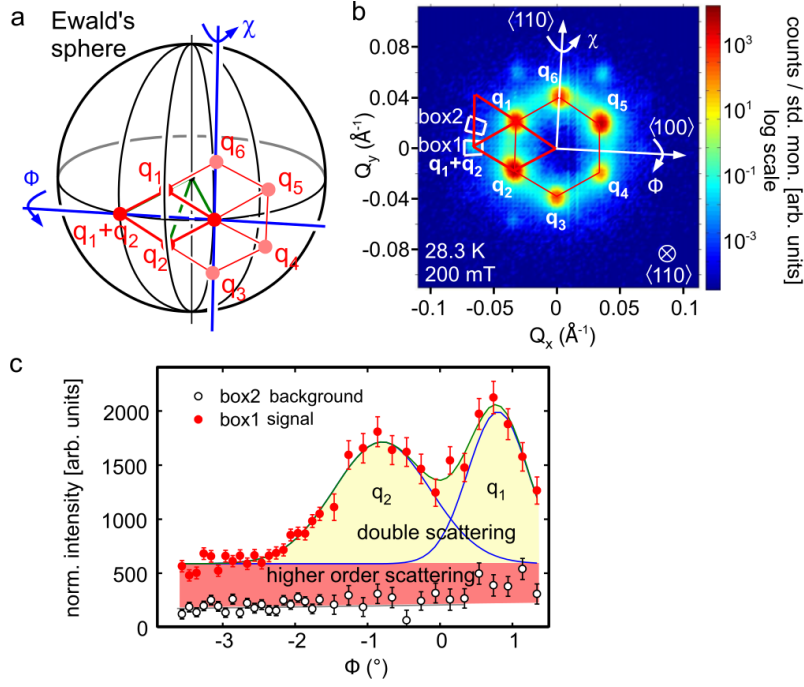
Figure 5.2: This Figure illustrates the operating principle of a Renniger scan (see main text for further information). Panel (a) shows a schematic plot of the Ewald sphere, the relevant Fourier modes of the skyrmion lattice, and the rocking angles of the Renninger scans. Panel (b) displays a characteristic scattering pattern obtained by summing over the rocking scans around ϕ. The background was subtracted as in most previous neutron scattering measurements of Sec. 3.1.3. The red (white) data points in panel (c) show the intensity of a Renninger scan, integrated over box 1 (box 2) of panel (b), as a function of the rocking angle ϕ. The intensity at $\boldsymbol{q}_1 + \boldsymbol{q}_2$ contains two contributions: Two Gaussian peaks due to double scattering when either $\boldsymbol{q}_1$ or $\boldsymbol{q}_2$ intersect the Ewald sphere, and a constant intensity arising due to true higher-order reflections, displayed by the red background color. The Figure is taken from our publication, Ref. [67].

dependence. The width of the Gaussian distribution is very narrow with $\eta_A = 0.45°$. The resolution limit $\Delta\beta_{\mathbf{k}f} = 0.35°$ is just slightly smaller. From the narrow rocking width, it follows that in the skyrmion lattice the intrinsic magnetic correlation length is larger than $100\ \mu$m. Compared to the correlation length of a zero-field helical state of about 10^4 Å, the correlation length in the skyrmion phase is at least a factor 100 larger than for the helical state.

To perform observations of higher-order neutron scattering peaks, a special neutron scattering technique was used which is displayed in panel (a) of Fig. 5.2. One first rotates the sample together with the magnetic field by an angle χ around the axis perpendicular to both $(\boldsymbol{q}_1 + \boldsymbol{q}_2)$ and the original magnetic field direction, until the desired higher-order mode $\boldsymbol{q}_1 + \boldsymbol{q}_2$ matches the scattering condition, i.e. is located on the Ewald sphere. This is followed by a so-called Renninger scan [88] which allows to differentiate between higher-order scattering and double scattering. A Renninger scan is a rocking scan around the axis $\boldsymbol{q}_1 + \boldsymbol{q}_2$, while measuring the intensity of interest, i.e. the intensity at $\boldsymbol{q}_1 + \boldsymbol{q}_2$. The rocking angle in panel (a) of Fig. 5.2 is denoted by ϕ. For the true higher-order contribution to the neutron scattering peak, the scattering condition is fullfilled for all rocking angles ϕ. This

is, however, not true for the double-order scattering processes. It can only contribute to the intensity when q_1 (or q_2 respectively) are also located on the Ewald sphere. Consequently, by changing the rocking angle one can "rock double scattering out".

The neutron scattering result of a typical Renniger scan measurement, a sum over a rocking scan around ϕ, is shown in panel (b) of Fig. 5.2, where one clearly observes a finite scattering intensity in box 1 at $q_1 + q_2$, whereas the intensity in a box of equal size slightly next to $q_1 + q_2$, denoted by box 2, is almost zero. In the measurement, the sample B was oriented with a $\langle 110 \rangle$ crystalline direction parallel to the neutron beam. The Renniger rocking was performed approximately around the $\langle 100 \rangle$ direction. The temperature T was 28.3 K, and the applied magnetic field $\mu_0 H = 200$ mT. As in almost all previous measurements shown in Sec. 3.1.3, the background neutron scattering signal, determined for T well above T_c, was carefully subtracted. Panel (c) of Fig. 5.2 displays the intensities, integrated over the corresponding boxes as a function of the rocking angle ϕ for $\mu_0 H = 200$ mK and $T = T_c - 0.5$ K, where T_c is the helimagnetic transition temperature determined by SANS. The red data points correspond to the intensities observed in box 1, which comprises the higher-order mode $q_1 + q_2$. They present maxima at the positions, where q_1 or q_2 intersect the Ewald sphere and double scattering occurs. Besides the Gaussian contributions to the scattering intensity at $q_1 + q_2$ due to double scattering, a further contribution accounts for higher-order scattering. The latter is illustrated by the red background color in Fig. 5.2 (c) and remains constant also for large rocking angles.

To study the magnetic field and temperature dependence of higher-order scattering intensities, Renniger scans at different fields and temperatures were examined. A few Renniger scans as a function of the applied rocking angle ϕ are shown in Fig. 5.3. Panel (a), (b) and (c) are measured at a temperature of $T = T_c - 1.5$ K, and (d), (e) and (f) at $T = T_c - 0.5$ K. The applied magnetic field in panel (a) and (d) is $\mu_0 H = 220$ mT. It decreases to $\mu_0 H = 200$ mT in panel (b) and (e), and furthermore to $\mu_0 H = 180$ mT in panel (c) and (f). As shown in Fig. 5.3, the amount of higher-order scattering (plotted in a red background color) increases with increasing temperature, meaning that deep in the ordered phase higher-order contributions are less pronounced. Furthermore, the higher-order scattering intensities also increase with increasing magnetic field.

The quantity of interest is, however, not the absolute value of the neutron scattering intensity of the higher-order modes, but rather the ratio of the second-order peaks with respect to the first-order peaks. The latter determines how important higher-order corrections to the magnetic structure really are. To study the magnetic field and temperature dependence of this ratio, one also has to take the thermal and magnetic field variation of the first-order peaks into account. An example of the magnetic field dependence of the intensity of the first-order peak at q_1 (see Fig. 5.2, where $B \parallel \langle 110 \rangle$) measured at a temperature of $T = T_c - 0.5$ K is shown in panel (a) of Fig. 5.4. The Figure is taken from our publication, Ref. [67], where we used a slightly different notation. M_q in Fig. 5.4 corresponds in this Thesis to m_q, and M_0 to $|M_f| = M_f$.

Panel (b) of Fig. 5.4 comprises the temperature and the magnetic field dependence of the ratio between the higher-order peak intensity at $q_1 + q_2$ and the first-order intensity at q_1. First of all, one can observe that the relative weight of the higher-order peaks is of the order of 10^{-3} and thus tiny. This quantity is displayed for three different temperatures, $T = T_c - 1.5$ K, $T_c - 1.0$ K, and $T_c - 0.5$ K and it increases with increasing temperature. Within the mean-field theory we will also obtain this behaviour which is not very intuitive, because at first glance one would expect that the non-linear effects leading to higher-order peaks should become less pronounced when all amplitudes decrease with increasing T.
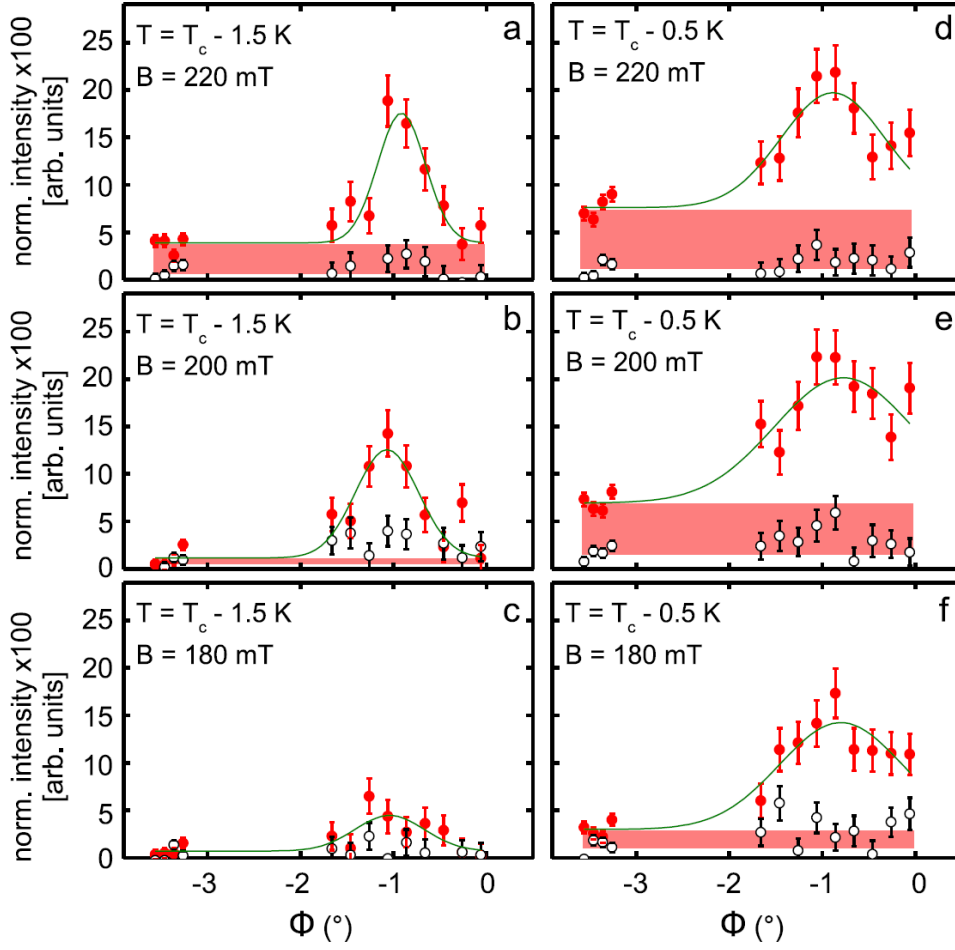
Figure 5.3: Renninger scans in the skyrmion lattice phase as a function of the rocking angle ϕ for different temperatures and different magnetic fields. The plots in the left (right) column are measured at a temperature of $T = T_c - 1.5$ K ($T = T_c - 0.5$ K). From the first to the third row, the applied magnetic field is $\mu_0 H = 220$ mT, 200 mT and 180 mT, respectively. The contribution to the neutron scattering intensity originating from higher-order scattering is marked by a red background color. It remains constant for large rocking angles ϕ. The Figure is taken from our publication, Ref. [67].

We will discuss the reason for this unexpected behaviour within the mean-field analysis below. Furthermore, this ratio also increases for increasing magnetic fields above $\mu_0 H \approx$ 180 mT. Below $\mu_0 H = 180$ mT, the first-order intensity was too weak, so that there are unfortunately no data points available. However, the plot indicates that the second-order intensity vanishes for a certain magnetic field $B \approx B_{\text{int}}$ inside the skyrmion phase.

The main experimental results of the higher-order scattering study in the skyrmion lattice phase are basically three findings. First, the relative weight of the higher-order peaks is tiny, being of the order of 10^{-3}. Second, the second-order intensity increases with increasing T. Third, it is strongly magnetic field dependent and seems to vanish for a certain magnetic field. In the following, we will give a semi-quantitative explanation for the experimental observations in the framework of a mean-field theory.
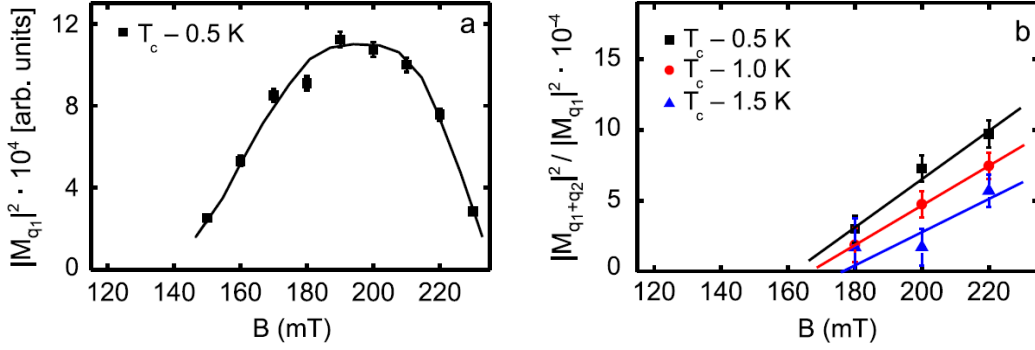
Figure 5.4: Intensities and intensity ratios in the skyrmion lattice phase obtained by neutron scattering, where the applied magnetic field was in the $\langle 110 \rangle$ direction, as in the measurements before in this Chapter. Panel (a) shows the measured neutron scattering intensity, $|\boldsymbol{m}_{\boldsymbol{q}_1}|^2$, (in arbitrary units) of the first order peak $\boldsymbol{q}_1$ at a temperature of $T = T_c - 0.5$ K as a function of the applied magnetic field strength. Panel (b) basically displays the ratio between the intensity at $\boldsymbol{q}_1 + \boldsymbol{q}_2$ and the one at $\boldsymbol{q}_1$ as a function of the applied magnetic field for three different temperatures. The Figure is taken from our publication, Ref. [67], where the notation was slightly different. $\boldsymbol{M_q}$ corresponds in this Thesis to $\boldsymbol{m_q}$, and M_0 to $|\boldsymbol{M}_f| = M_f$.

5.2   Theory for Higher-Order Neutron Scattering

As already explained in Sec. 4.3, a pure rotationally invariant mean-field theory does not stabilize the skyrmion lattice phase. Nonetheless, it is a local minimum of the free energy functional of Eq. (4.9). Therefore, a fully quantitative theory has to include thermal fluctuations [1]. However, on the basis of a mean-field description it is possible to understand the main experimental observations on a semi-quantitative level. To this end we minimize the free energy functional F of Eq. (4.9) with the following ansatz:

$$\boldsymbol{M}(\boldsymbol{r}) = \sum_{n,m \in \mathbb{Z}} e^{i(n\boldsymbol{q}_1 + m\boldsymbol{q}_2)\boldsymbol{r}} \; \boldsymbol{m}_{n\boldsymbol{q}_1 + m\boldsymbol{q}_2} \tag{5.1}$$

For the numerical calculation of the mean-field free energy, we include all wavevectors $n\boldsymbol{q}_1 + m\boldsymbol{q}_2$ for n and m integer up to a short-distance cutoff, $|n\boldsymbol{q}_1 + m\boldsymbol{q}_2| \leq \Lambda$, and perform a numerical minimization with respect to the amplitudes and the complex phases of all modes. The corresponding solution provides the relative weight of higher-order peaks as, e.g., the relative weight of the second-order peak $|\boldsymbol{m}_{\boldsymbol{q}_1 + \boldsymbol{q}_2}|^2/|\boldsymbol{m}_{\boldsymbol{q}_1}|^2$ which is plotted in panel (d) of Fig. 5.5 as a function of the magnetic field for three different temperatures, $t = -0.9, -1.0, -1.1$. Since panel (d) is the theory version of Fig. 5.4 (b), we plotted the experimental data again next to the theory plot for a better comparison. The dashed and the dot-dashed lines in panel (d) of Fig. 5.5 repesent the relative weight of even higher-order scattering contributions. To be specific, $|\boldsymbol{m}_{2\boldsymbol{q}_1}|^2/|\boldsymbol{m}_{\boldsymbol{q}_1}|^2$ is plotted with a dashed line and $|\boldsymbol{m}_{2\boldsymbol{q}_1 + \boldsymbol{q}_2}|^2/|\boldsymbol{m}_{\boldsymbol{q}_1}|^2$ with a dotted line. Both are illustrated in red, since they are evaluated for $t = -1.0$.

By comparing the mean-field theory with the experimental data we can conclude that the mean-field theory includes all of the main experimental observations. The predicted relative weight of the second-order peak is also tiny and of the same order of magnitude within the mean-field theory. In the theory plot, one clearly observes that for each temperature there exists a certain magnetic field $B \approx B_{\text{int}}$, where the relative weight of the
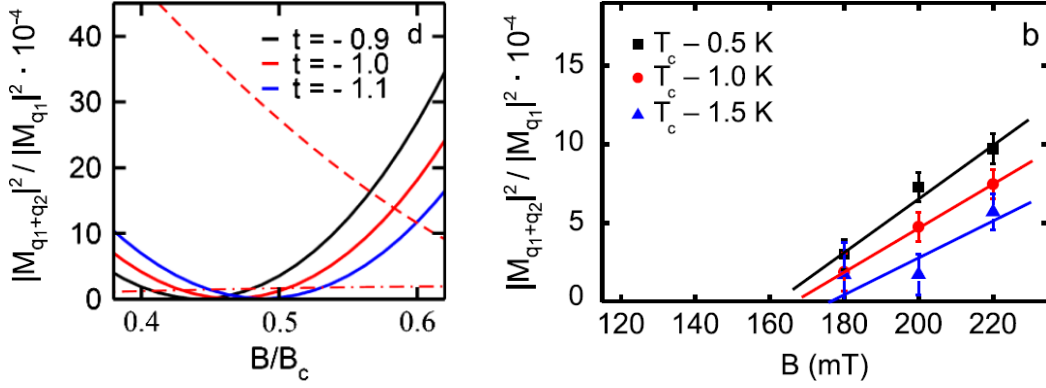
Figure 5.5: Panel (d) shows the theory version of panel (b) (see also panel (b) of Fig. 5.4), *i.e.* the intensity ratio of the higher-order diffraction at $\boldsymbol{q}_1 + \boldsymbol{q}_2$ and the first-order diffraction, $|\boldsymbol{m}_{\boldsymbol{q}_1+\boldsymbol{q}_2}|^2/|\boldsymbol{m}_{\boldsymbol{q}_1}|^2$. It is plotted as a function of the magnetic field in mean-field theory for three different temperatures, $t = -0.9$, $t = -1.0$, and $t = -1.1$ in the rescaled units of Eq. (4.9). The dashed (dot-dashed) line repesents a ratio of an even higher-order scattering contribution to the first-order one, $|\boldsymbol{m}_{2\boldsymbol{q}_1}|^2/|\boldsymbol{m}_{\boldsymbol{q}_1}|^2$ ($|\boldsymbol{m}_{2\boldsymbol{q}_1+\boldsymbol{q}_2}|^2/|\boldsymbol{m}_{\boldsymbol{q}_1}|^2$) for $t = -1$. For a better comparison the corresponding experimental plot is shown again one the right hand side. We published these Figures in Ref. [67], where we used a slightly different notation. $\boldsymbol{M}_{\boldsymbol{q}}$ corresponds in this Thesis to $\boldsymbol{m}_{\boldsymbol{q}}$, and M_0 to $|\boldsymbol{M}_f| = M_f$.

second-order peak approximately vanishes. Moreover, the theory reproduces the increase of the signal for increasing temperatures (described by increasing t). This can be understood since one can infer from Fig. 5.5 (d) that for larger temperatures the decrease of all higher-order scattering amplitudes is overcompensated by a shift of the field B_int towards smaller values. Unfortunately, a precise quantitative prediction how, for example, the temperature exactly depends on the parameter t is not possible. This is due to the neglected fluctuation corrections and due to the experimental uncertainty to properly determine the absolute value of the scattering intensities. An issue that cannot be really explained so far is the gradual variation of the amplitude $|\boldsymbol{m}_{\boldsymbol{q}_1}|$ for small magnetic fields, as is shown in panel (a) of Fig. 5.4. Here, theory predicts a sharp first-order transition [1]. It might allude to a phase coexistence in this regime.

The obvious question that arises after this analysis is: Why does $|\boldsymbol{m}_{\boldsymbol{q}_1+\boldsymbol{q}_2}|^2$ almost vanish for a certain magnetic field B_int? The answer to that question is that $|\boldsymbol{m}_{\boldsymbol{q}_1+\boldsymbol{q}_2}|^2$ is strongly suppressed around B_int by an interference effect. This turns out to be a key property of the skyrmion lattice, as we will explain in the following. Since the higher-order scattering contributions are tiny and almost all of the scattering intensity arises from the six resolution-limited first-order scattering peaks, to a good approximation one can describe the magnetic structure by a superposition of three helices with phase shifts $\Delta\boldsymbol{r}_j$ and uniform magnetization, as already described in Eq. (4.18). It was also already mentioned in Sec. 4.3 that for infinite systems two of these three phases $\Delta\boldsymbol{r}_j$ just correspond to translations of the magnetic structure within the plane and can therefore, without loss of generality, be set to zero. To be more concrete, let us consider $\boldsymbol{B} = B\hat{\boldsymbol{z}}$. In this case, only interactions with the atomic lattice fix the orientation of the three main $\boldsymbol{q}$ vectors. At this point we are, however, not interested in the particular orientation of the three $\boldsymbol{q}$ vectors with respect to the atomic lattice, but rather in the relative phase shift. Therefore,

45

we set

$$\boldsymbol{M}_1^{\mathrm{helix}}(\boldsymbol{r}) = \sqrt{2}\,\Phi \begin{pmatrix} 0 \\ \sin(qx + \alpha_1) \\ -\cos(qx + \alpha_1) \end{pmatrix} = \boldsymbol{m}_{\boldsymbol{q}_1} e^{i\boldsymbol{q}_1 \boldsymbol{r}} + \boldsymbol{m}_{-\boldsymbol{q}_1} e^{-i\boldsymbol{q}_1 \boldsymbol{r}}, \qquad (5.2)$$

with $\boldsymbol{q}_1 = (1, 0, 0)^T$, $\boldsymbol{m}_{\boldsymbol{q}_1} = \boldsymbol{m}_{-\boldsymbol{q}_1}^* = e^{i\alpha_1}(\Phi/\sqrt{2})\,(0, -i, -1)^T$, Φ^2 being the weight of the scattering peak, and α_1 the phase shift of the helix. The other two helices are given by rotations of the first helix around the magnetic field axis by an angle of $120°$ and $240°$, respectively. Since for an infinite system only one relative phase is needed, we set the phases of the two rotated helices to zero, *i.e.* $\alpha_2 = \alpha_3 = 0$, which corresponds to translations, and we denote the relative phase α_1 just by α. This remaining phase strongly affects the magnetic structure, as can be seen in Fig. 5.6.

The left panel of Fig. 5.6 displays the superposition of three helices in the following way. Each helix is represented by parallel lines that are equally separated and perpendicular to its $\boldsymbol{q}$ vector and to the applied magnetic field. They show the regions of constant and equal phases of helix. For example, let us assume that on all lines the magnetization points into the direction of the magnetic field vector. A phase shift of a helix corresponds then to a shift of these lines along the direction of the $\boldsymbol{q}$ vector. Since the $\boldsymbol{q}$ vectors of the skyrmion lattice have relative angles of $120°$, these lines of constant phases also have relative angles of $120°$. If we neglect, for a moment, the helix which is, for clarity, drawn in red, then one can immediately see that a shift of the phase of the other two helices just leads to a translation of the whole pattern. Thus, the diamond-shaped pattern is independent of these two phases. By adding the third helix it is clear from the Figure that only certain relative phases of α lead to crossing points, where all three lines intersect. This is a topologically different pattern compared to those, where only crossing points with two lines exist. In our convention, $\alpha = 0$ describes the case, where three lines intersect. Exactly this configuration describes a lattice of anti-skyrmions, where in the center of skyrmion lattice all three helices point opposite to the external magnetic field $\boldsymbol{B}$, see Fig. 3.5.

In particular, upon changing α the local amplitude of the magnetization is affected. In the right panel of Fig. 5.6, we plot the minimum and the maximum of the magnetization amplitude of the superposition of the helices and a uniform magnetic moment. For $\alpha \neq 0$, the amplitude variations in the magnetic structure are much larger compared to the $\alpha = 0$ case, where the amplitude is almost constant. Furthermore, the minimal amplitude as a function of α is maximal for $\alpha = 0$. However, only for particular phase differences the amplitude vanishes, *i.e.* the order parameter vanishes. For a generic phase shift, the amplitude is everywhere finite, and the winding number is given by -1 or 1, respectively. In Fig. 5.7, we plot the normalized magnetization direction for the different phase shifts 0, $\pi/4$, $\pi/2$, and π. In these plots one also observes that the relative phase relationship α has an affect on the magnetic texture. Note, in particular, the shift of the center of the skyrmions as well as the "color inversion" comparing the first three panels with the last one, where the winding number has the opposite sign.

An experimental verification of α is therefore important to underline the nature of the skyrmion lattice phase. As mentioned earlier in Sec. 4.3, one cannot infer information about α only from first-order scattering measurements, since this signal is only sensitive to $|\boldsymbol{m}_{\boldsymbol{q}_j}|^2$. In contrast, the higher-order terms are very sensitive to such relative phases, because they are subject to interference effects. If we consider, for example, the Fourier transformation of the $\boldsymbol{M}^4$ term, which previously was crucial to obtain the particular
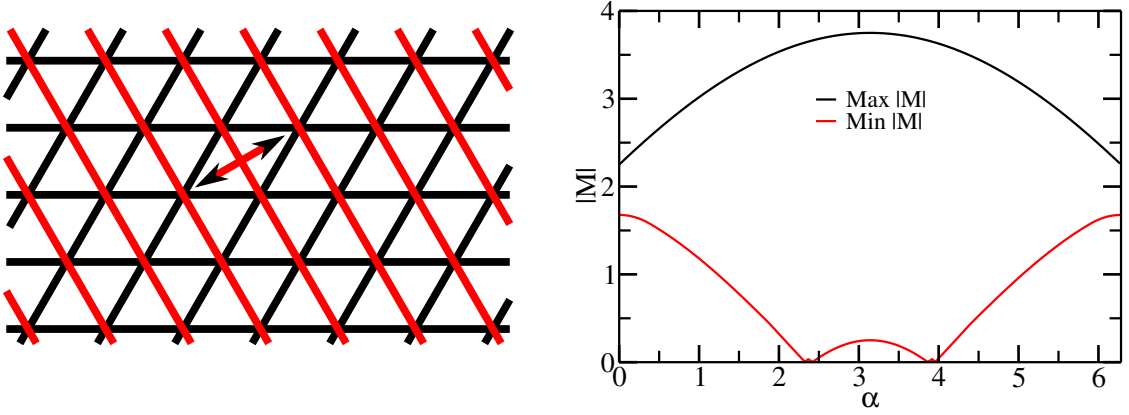
Figure 5.6: The left panel shows a superposition of three helices, illustrated by lines of constant phases. One relative phase shift corresponding to a parallel translation of, *e.g.*, the red lines and indicated by the arrows determines whether the magnetic order is a lattice of anti-skyrmions with small amplitude variations or not. A detailed explanation of this Figure is given in the main text. The panel on the right hand side shows the minimum and maximum of the magnetization amplitude of the superposition of three helices and a uniform magnetic component as a function of the phase shift α for $M_f = -0.75$ and $\sqrt{2}\Phi = 1$. In this example, the amplitude of the minimum of $|\boldsymbol{M}|$ vanishes only for $\alpha \approx 2.33$, $\alpha \approx 2.42$, $\alpha \approx \pi - 2.42$, and $\alpha \approx \pi - 2.33$.
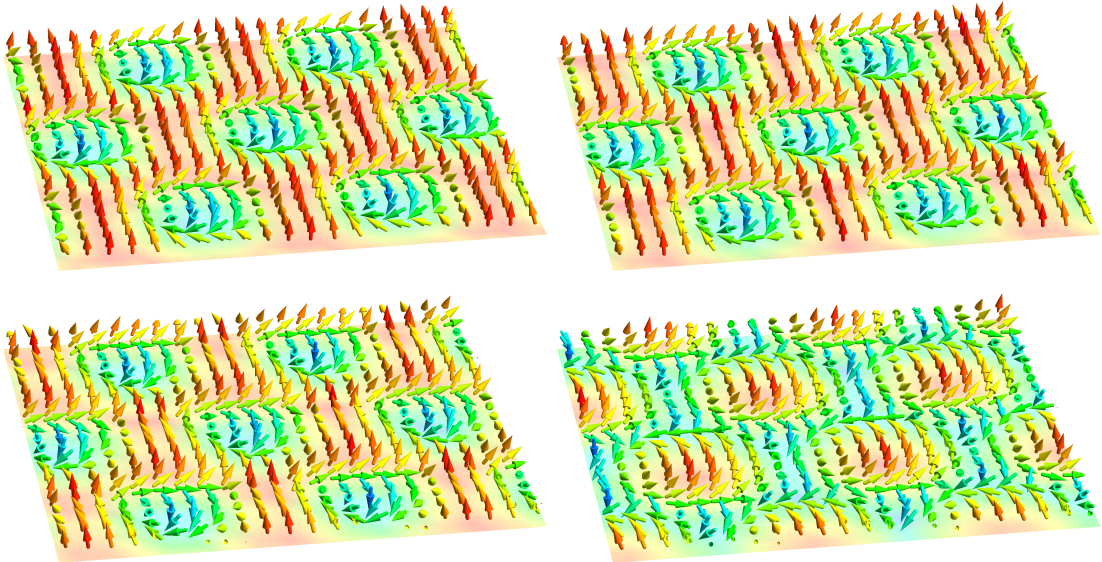
Figure 5.7: Normalized magnetization direction for different phase shifts α. Upper left panel: $\alpha = 0$; upper right panel: $\alpha = \pi/4$; lower left panel: $\alpha = \pi/2$; lower right panel: $\alpha = \pi$.
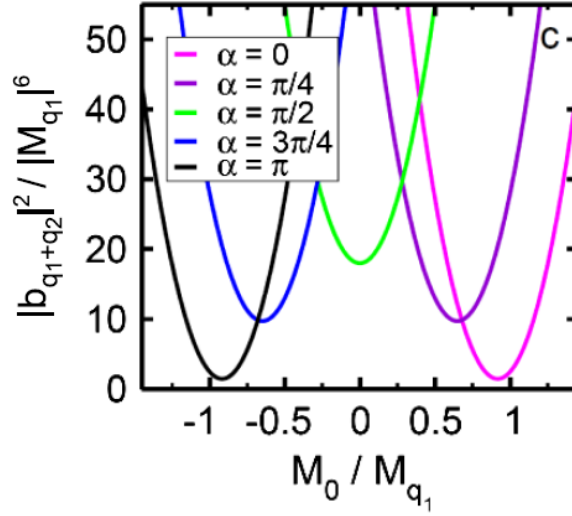
Figure 5.8: Square of the absolute value of the oscillating effective field, $|\boldsymbol{b}_{q_1+q_2}|^2$ in units of $|\boldsymbol{m}_{q_1}|^6$ as a function of $M_f/|\boldsymbol{m}_{q_1}|$ for different values of the relative phase α, introduced in the text. An analytic formula for this expression, obtained from a mean-field theory, is given in Eq. (5.4), where $\Phi = |\boldsymbol{m}_{q_1}|$. This is the term that is resposible for inducing scattering at $\boldsymbol{q}_1 + \boldsymbol{q}_2$. We published this Figure in Ref. [67], where we used a slightly different notation. $\boldsymbol{M}_q$ corresponds in this Thesis to $\boldsymbol{m}_q$ and M_0 to $|\boldsymbol{M}_f| = M_f$.

arrangement of the $\boldsymbol{q}$ vectors of the skyrmion lattice phase, we get

$$
\frac{1}{V}\int d^3 r \boldsymbol{M}^4 = \sum_{\boldsymbol{q}_I,\boldsymbol{q}_{II},\boldsymbol{q}_{III},\boldsymbol{q}_{IV}} \boldsymbol{m}_{q_I}\boldsymbol{m}_{q_{II}}\boldsymbol{m}_{q_{III}}\boldsymbol{m}_{q_{IV}}\delta_{q_I+q_{II}+q_{III}+q_{IV}} \tag{5.3}
$$
$$
= \boldsymbol{m}_{q_1+q_2}\boldsymbol{b}_{q_1+q_2} + ...,
$$

where in the last equation we have collected all terms linear in $\boldsymbol{m}_{q_1+q_2}$. The term $\boldsymbol{b}_{q_1+q_2}$ behaves as an effective magnetic field to which all terms consisting of factors of $\boldsymbol{m}_{q_{1...6}}$ and of the uniform magnetization $\boldsymbol{m}_0 \equiv \boldsymbol{M}_f$ with total momentum $-(\boldsymbol{q}_1+\boldsymbol{q}_2)$ contribute. Since $\boldsymbol{q}_1 + \boldsymbol{q}_2 = 2\boldsymbol{q}_1 + \boldsymbol{q}_3 = 2\boldsymbol{q}_2 + \boldsymbol{q}_6$ (see Fig. 5.2b), several terms contribute to $\boldsymbol{b}_{q_1+q_2}$, e.g., $\boldsymbol{m}_{-q_1}(\boldsymbol{m}_{-q_1}\boldsymbol{m}_{q_3})$ or $\boldsymbol{M}_f(\boldsymbol{m}_{-q_1}\boldsymbol{m}_{-q_2})$. The strength of the oscillating effective field $\boldsymbol{b}_{q_1+q_2}$ is therefore determined by several processes given by

$$
\frac{|\boldsymbol{b}_{q_1+q_2}|^2}{2\Phi^6} = 9 + 74\frac{M_f^2}{\Phi^2} - 96\sqrt{2}\frac{M_f}{\Phi}\cos\alpha + 54\cos^2\alpha, \tag{5.4}
$$

where $\sqrt{2}\Phi$ was defined to be the amplitude of the helix, and consequently $|\boldsymbol{m}_{q_1}| = \Phi$. Fig. 5.8 shows a plot of this function for different values of the relative phase shift α. As a negative absolute value of the uniform magnetization $\boldsymbol{M}_f$ is physically not reasonable, the left part of this picture has no relevance. For α close to zero the strength of the oscillating effective magnetic field $\boldsymbol{b}_{q_1+q_2}$ becomes very small for a certain magnetic field, where $M_f/\Phi = \sqrt{2}\,24/37 \approx 0.92$. This value has to be compared to 0.94 and 0.96, which we obtained from the mean-field theory for $t = -1$ and $t = -5$, respectively. The experimentally observed strong suppression of $|\boldsymbol{m}_{q_1+q_2}|^2$ is due to an interference effect. It has been observed at a magnetic field of B_{int} that was also confirmed by our mean-field theory. This fact is a characteristic feature of the special $\alpha = 0$ phase relationship which

is experimentally established by the results of higher-order scattering measurements and which is characteristic for the skyrmion lattice phase.

To summarize, higher-order scattering was observed, and the quantitative explanation of its dependence on the magnetic field $\boldsymbol{B}$ and the temperature T was given. In conclusion, this demonstrates microscopically the existence of a skyrmion lattice in bulk samples of MnSi within a certain temperature and magnetic field range, which can be characterized as a chiral spin crystal with a quantized winding number $W = -1$ per unit cell and small amplitude variations of the magnetization. Furthermore, we expect that similar results will occur in other magnetic materials with skyrmion phases.

Part II

Current-Induced Magnetization Dynamics

6 Interplay of Magnetic Structures and Currents

In the previous Chapters, we have discussed magnetic structures in equilibrium, in particular the skyrmion crystal. In the following, we consider the mutual influence of magnetic structures and an electric current. Notably, we again focus on the (bulk) skyrmion lattice and the interplay with a current, where due to the non-trivial topology of the magnetic whirl-lines new phenomena emerge. Before that, we would like to motivate why the interplay of magnetic structures and electric currents, which belongs to the field of spintronics, provides interesting phenomena.

6.1 Spintronics and Spin-Transfer Torques

Spintronics, previously also called magnetoelectronics, makes use of the fact that electrons have not only a charge, but also a spin. A central part of this field is to control the spin degree of freedom electrically and to exploit the electric and magnetic properties of the electrons for information processing and data storage. As one of the long-term goals of this field one might see the fusion of semiconductor technology with the advantages of spintronics to improve solid-state devices.

The highlight in the field of spintronics, concerning applications, was the discovery of the giant magnetoresistance (GMR) effect in 1988. It was independently found by Peter Grünberg *et al.* [3] and by Albert Fert *et al.* [4]. This effect allows for a very efficient control of electric currents by altering the magnetic structures. Because of its great applicability for hard disk drives in the computer industry the Nobel prize was awarded to them in 2007. Another fundamental work was the theoretical proposal of a spin field-effect-transistor by Supriyo Datta and Biswajit Das in 1990 [89]. It provides an important gateway to merge semiconductor technology with spintronics. Nevertheless, it has not been realized experimentally so far.

In 1996, J. Slonczewski and L. Berger theoretically proposed the so-called spin-transfer torque effect [5, 6]. It describes the transfer of angular momentum from an electric current flowing through an inhomogeneous magnetization configuration to the local magnetization. Since it allows to manipulate the magnetization of a material using an electric current, it might be considered as a kind of an inverted GMR effect. Since altering a magnetic structure with a current can, in principle, be done much more locally than via magnetic fields, spin-transfer torques also have become interesting for applications. For example, S. Parkin *et al.* [7] implemented a non-volatile memory device, called racetrack memory, which exploits the phenomenon of current-induced domain wall motion in a magnetic nanowire [90–93].

Amongst other interesting phenomena, where the magnetic structure is spatially non-

uniform [94], a spin-polarized current is able, for example, to switch magnetic domains in multilayer devices [95, 96], to induce microwave oscillations in nanomagnets [97, 98], and also to induce vortex oscillations in magnetic nano-pillars [99].

However, the current densities needed to induce observable spin-transfer torque effects in traditional spin-torque experiments, like current-driven magnetization dynamics in ferromagnetic metals and semiconductors, are still very high. Presently, they are of the order of $\sim 10^{11}$ A/m^2 which leads to a large Ohmic heating of the device. Therefore, spin-transfer torque effects at such high current densities can only be studied in nano structures.

6.2 Spintronics with Skyrmions

Concerning the interplay of currents and skyrmions, the first experimental results, obtained in the group of C. Pfleiderer, were published in 2010 [10]. In neutron scattering experiments, they observed a rotation of the diffraction pattern upon subjecting the skyrmion lattice to an electric current. Together we figured out that this observed rotation only occured, because an additional temperature gradient was present [10]. Up to now, further interesting spin-torque effects in the skyrmion lattice were observed, for which no temperature or other gradients are required. The experimental findings revealed an ultra-low electrical threshold current density above which spin-transfer torque effects do occur. For MnSi, the threshold current density $\sim 10^6$ A/m^2 [10, 80] is about five orders of magnitude smaller compared to traditional setups with spin-transfer torque effects. The very low value of the threshold current density stems from different effects [10, 80]. First of all, as discussed in Section 4.3, the skyrmion lattice couples only very weakly to the atomic crystal structure [1]. Second, as we also considered in Section 4.3, pinning due to disorder is expected to be weak. In addition, the skyrmion lattice itself couples very efficiently to the spin-polarized electric current due to the peculiar twist of the local magnetization which extends over macroscopic magnetic domains. In contrast, in traditional spin structures the spin-polarized electric current couples only to a nanoscopic volume, where the magnetic structure is inhomogeneous. The very low threshold current density makes skyrmion systems very interesting to study spin-transfer torques effects, and it allows for spin-torque experiments in bulk materials, avoiding the surface effects that dominate in nanoscopic samples. Furthermore, effects like heating and Oersted magnetic fields created by a current are much smaller for these current densities.

In this Thesis, we do not follow the historical sequence of the experimental and theoretical findings, but rather order them as follows. In Chapter 7, we first consider the effects on the current-carrying electrons when traversing an inhomogeneous magnetic texture like the skyrmion lattice. We briefly discuss their Berry phase physics and their emergent electrodynamics. In the subsequent Chapters, we switch the perspective and consider the influence of the current on the magnetic structure. To describe the current-induced magnetization dynamics we use the Landau-Lifshitz-Gilbert equation which is an effective equation of motion for the magnetization direction. The latter is introduced and discussed in Chapter 8. In Chapter 9, with the help of the so-called Thiele method [100] we discuss the current-induced forces on the skyrmion lattice and the induced drift motion of the skyrmion crystal, provided the applied current density is strong enough. In Chapter 10, we discuss the current-induced rotation of the skyrmion lattice which historically is the first experimentally observed spin-transfer torque effect in the skyrmion lattice phase. Although the main reason for the observed rotation was the temperature gradient present in

the experimental setup, we also discuss further rotation mechanisms in this Chapter. To describe the different current-induced rotation mechanisms, we extend the Thiele method for the rotational mode.

7 Emergent Electrodynamics of Skyrmions

In the previous Chapter we discussed why it is interesting to study the interplay of electric currents and magnetic structures. In this Chapter, we focus on what happens to the conduction electrons while moving through a magnetic texture, and in particular through the skyrmion lattice. Most of the results shown in this Chapter have been published in Refs. [40, 80]

Since the skyrmion structures are very smooth, we assume that the conduction electrons pass the topologically stable knots adiabatically, implying that their spins adjust to the orientation $\hat{\boldsymbol{\Omega}}(\boldsymbol{r}, t) = \boldsymbol{M}(\boldsymbol{r}, t)/|\boldsymbol{M}(\boldsymbol{r}, t)|$ of the local magnetization $\boldsymbol{M}(\boldsymbol{r}, t)$, as shown in Fig. 7.1. Non-adiabatic corrections are, for example, discussed in Refs. [80, 101]. While following adiabatically the magnetic structure of the skyrmion lattice, the spins of the conduction electrons change their orientation and pick up a Berry phase [33, 102–108]. Note that, since the sign of the Berry phase depends on the direction of the local magnetization, it reflects the chirality and the winding number of the skyrmions.

During this process several forces act on both the electrons and the magnetic structure. This adiabatic Berry phase physics as well as the acting forces can be mapped onto a problem, where the electrons move in a simple uniform magnetic field, but instead "feel" additional emergent electric $\boldsymbol{E}^e$ and magnetic fields $\boldsymbol{B}^e$. The way to understand this is to view the Berry phase as an Aharonov-Bohm phase due to these emergent fields [8, 9, 33, 104–106, 110–113]. The emergent fields then lead to the aforementioned effective forces on the conduction electrons which are, in particular, Lorentz forces.

In the adiabatic case, where a free electron moves across a magnetic structure, the emergent magnetic and electric fields are given by

$$\boldsymbol{B}_i^e = \frac{\hbar}{2}\epsilon_{ijk}\hat{\boldsymbol{\Omega}} \cdot (\partial_j\hat{\boldsymbol{\Omega}} \times \partial_k\hat{\boldsymbol{\Omega}}), \tag{7.1}$$

$$\boldsymbol{E}_i^e = \hbar\hat{\boldsymbol{\Omega}} \cdot (\partial_i\hat{\boldsymbol{\Omega}} \times \partial_t\hat{\boldsymbol{\Omega}}), \tag{7.2}$$

where ∂_i is the short notation for $\partial/\partial r_i$. We review the derivation of $\boldsymbol{B}^e$ and $\boldsymbol{E}^e$ in Sec. 7.1. The emergent magnetic (electric) field measures the solid angle for an infinitesimal loop in space (space-time). A spin-polarized electron with majority spin, *i.e.* with magnetic moment parallel to $\hat{\boldsymbol{\Omega}}$, collects the opposite Berry phase than an electron with minority spin. This sign can be accounted for by assigning emergent charges with different signs to the two configurations. In our convention, a majority spin carries the emergent charge $q_\downarrow^e = -1/2$, while a minority spin carries the emergent charge $q_\uparrow^e = +1/2$ [80].

For the skyrmion lattice the emergent fields are of particular interest. Since $\boldsymbol{B}^e$ is proportional to the skyrmion density, and since skyrmions have a quantized winding number of $W = -1$, the "emergent flux" per skyrmion given by $\int \boldsymbol{B}^e d\boldsymbol{\sigma} = -4\pi\hbar$ is also topologically quantized [1, 40, 44] to one flux quantum $-2\pi\hbar/|q^e|$ per unit cell. Since in MnSi the
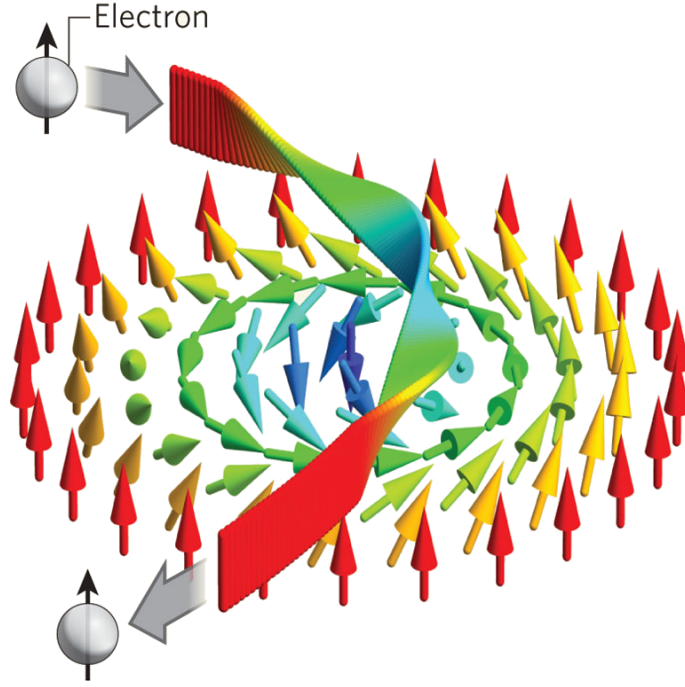
Figure 7.1: The magnetic moment of the electron adjusts adiabatically to the direction of the local magnetization of the skyrmion. This picture is taken from Ref. [109].

magnetic lattice is a lattice of anti-skyrmions, not only the winding number has a negative sign but also the emergent flux, implying that the emergent magnetic field $\boldsymbol{B}^e$ is oriented opposite to the external applied magnetic field $\boldsymbol{B}$. Furthermore, in Sec. 7.3 we show that for a moving skyrmion lattice with a drift velocity $\boldsymbol{v}_d$ the emergent magnetic and electric fields are connected according to Faraday's law of induction, wherefore this quantization of B^e also is transferred to E^e/v_d [9].

In the following, we first review the derivation of the emergent electric and magnetic fields given in Eqs. (7.1) and (7.2), and then we discuss their experimental observation. Note that the emergent electric field $\boldsymbol{E}^e$ can only be non-zero for a time-dependent magnetic structure, $i.e.$ for a moving skyrmion lattice. As we will see in the next Sections and Chapters, a sufficiently strong current leads to a motion of the skyrmion lattice.

7.1 Derivation of the Emergent Magnetic and Electric Fields

The emergent magnetic and electric fields given in Eqs. (7.1) and (7.2) can be basically derived within two equivalent approaches. On one hand, they can be derived by making a product ansatz for the wavefunction which consists of a spatial and time-dependent amplitude and a spinor that locally ($i.e.$ space- and time-dependent) adjusts to the direction of the magnetic field. By writing down the Schrödinger equation for the amplitude one obtains the artificial gauge potentials leading to emergent electrodynamics. On the other hand, the emergent electric and magnetic fields can be obtained by perfoming a local unitary transformation of the system, so that in the new basis the quantization axis is parallel to the local magnetization direction. Here, we review the latter version as presented in Ref. [8].

Let us consider a simple model Hamiltonian for a free electron with a spin moving

across a smoothly varying magnetic structure $\boldsymbol{M}(r,t)$ with a constant amplitude M:

$$H = \frac{\boldsymbol{p}^2}{2m}\mathbb{1} - J\boldsymbol{\sigma} \cdot \hat{\boldsymbol{\Omega}}(\boldsymbol{r},t). \tag{7.3}$$

Here, $\mathbb{1}$ is the 2×2 unit matrix, and $\hat{\boldsymbol{\Omega}}(\boldsymbol{r},t) = \boldsymbol{M}(r,t)/M$ is the direction of the magnetization that varies in space and time. $\boldsymbol{\sigma} = (\sigma_x, \sigma_y, \sigma_z)^T$ denotes the usual vector of Pauli matrices with

$$\sigma_x = \begin{pmatrix} 0 & 1 \\ 1 & 0 \end{pmatrix}, \qquad \sigma_y = \begin{pmatrix} 0 & -i \\ i & 0 \end{pmatrix}, \qquad \sigma_z = \begin{pmatrix} 1 & 0 \\ 0 & -1 \end{pmatrix}. \tag{7.4}$$

$J > 0$ is the strength of the exchange coupling which comprises the amplitude of the magnetization. In the Schrödinger picture, the dynamics is given by

$$i\hbar\partial_t\psi = \left[\frac{\boldsymbol{p}^2}{2m}\mathbb{1} - J\boldsymbol{\sigma} \cdot \hat{\boldsymbol{\Omega}}(\boldsymbol{r},t) \right]\psi. \tag{7.5}$$

The main idea is to perform a local transformation of the system, so that the second part of the Hamiltonian becomes trivial in the sense that $J\boldsymbol{\sigma} \cdot \hat{\boldsymbol{\Omega}}(\boldsymbol{r},t)$ goes over to $J\sigma_z$. This means to rotate the quantization axis from the $\hat{\boldsymbol{z}}$ axis to the axis parallel to the local magnetization direction $\hat{\boldsymbol{\Omega}}$ for a given point $\boldsymbol{r}$ in space and time t. This corresponds to a unitary transformation $U(\boldsymbol{r},t)$ of the two-component wave function $\psi = (\psi_\uparrow, \psi_\downarrow)^T$ that is given by $\psi = U(\boldsymbol{r},t)\zeta$, where $U = \exp(-i\frac{\theta}{2}\boldsymbol{\sigma} \cdot \boldsymbol{n})$. Here, $\theta = \theta(\boldsymbol{r},t)$ denotes the angle of the rotation, and $\boldsymbol{n} = \boldsymbol{n}(\boldsymbol{r},t) = \hat{\boldsymbol{z}} \times \hat{\boldsymbol{\Omega}}(\boldsymbol{r},t)/|\hat{\boldsymbol{z}} \times \hat{\boldsymbol{\Omega}}(\boldsymbol{r},t)|$ is the axis of the rotation. When inserting $\psi = U(\boldsymbol{r},t)\zeta$ into Eq. (7.5) and multiplying it by $U(r,t)^\dagger$ from the left, one obtains the following Schrödinger equation for ζ:

$$i\hbar\partial_t\zeta = \left[q^e V^e + \frac{(\boldsymbol{p}\mathbb{1} - q^e\boldsymbol{A}^e)^2}{2m} - J\sigma_z \right]\zeta, \tag{7.6}$$

with q^e being the emergent charge. The emergent "scalar" and "vector" potentials V^e and $\boldsymbol{A}^e$ are given by

$$V^e = -(i\hbar/q^e)U^\dagger\partial_t U, \tag{7.7}$$
$$\boldsymbol{A}^e = -(i\hbar/q^e)U^\dagger\nabla U. \tag{7.8}$$

Note that so far q^e drops out of equation Eq. (7.6). Since we started with the assumption that the magnetization $\boldsymbol{M}(\boldsymbol{r},t)$ and thus $\hat{\boldsymbol{\Omega}}(\boldsymbol{r},t)$ varies smoothly in space and time, one can treat the scalar and vector potentials as a perturbation to the unperturbed Hamiltonian

$$H_0 = \frac{\boldsymbol{p}^2}{2m}\mathbb{1} - J\sigma_z. \tag{7.9}$$

H_0 describes two bands, one for electrons with majority spins, *i.e.* with magnetization parallel to to the local magnetization direction $\hat{\boldsymbol{\Omega}}$, and one for minority spins. In the adiabatic approximation, the scalar and vector potentials V^e and $\boldsymbol{A}^e$ act on each band separately and modify them slightly. Technically, one has to project V^e and $\boldsymbol{A}^e$ on the two bands, and then one can introduce for each band an emergent electric and an emergent magnetic field that is "felt" by the conduction electrons as

$$B_i^e \equiv \epsilon_{ijk}\partial_j A_k^e = \mp \frac{\hbar}{2q^e} \frac{\epsilon_{ijk}}{2} \hat{\boldsymbol{\Omega}} \cdot \left(\partial_j\hat{\boldsymbol{\Omega}} \times \partial_k\hat{\boldsymbol{\Omega}} \right), \tag{7.10}$$

and

$$E_i^e \equiv -\partial_i V^e - \partial_t A_i^e = \mp \frac{\hbar}{2q^e} \hat{\boldsymbol{\Omega}} \cdot \left(\partial_i \hat{\boldsymbol{\Omega}} \times \partial_t \hat{\boldsymbol{\Omega}} \right), \tag{7.11}$$

where the upper (lower) sign corresponds to the band for electrons with majority (minority) spin. Motivated by the insight that an electron with majority spin collects the opposite Berry phase than an electron with minority spin, let us now introduce different emergent charges for the two bands by defining $q_\downarrow^e = -1/2$ for a majority spin and $q_\uparrow^e = +1/2$ for minority spin [80]. This leads to the emergent magnetic and electric fields given in Eqs. (7.1) and (7.2).

Note that the emergent magnetic and electric fields have been derived under the assumption that the electron follows the magnetic texture adiabatically. Corrections due to non-adiabatic processes are discussed in Refs. [80, 101]. Furthermore, they do not contain fluctuations of the amplitude of the magnetization, and they do not take into account modifications due to the band structure of the system. Moreover, also dissipative drag forces acting on the electrons are not covered by Eqs. (7.1) and (7.2).

For the case of the skyrmion lattice, only in a tiny region close to the depinning transition, dissipative drag forces on the electrons arising from the motion of the skyrmion lattice might be relevant. Otherwise, they are much smaller than the force from the emergent electric field and may therefore be neglected. The reason for this is the following [80]: The skyrmion lattice induces a weak effective periodic potential on the electrons which has at least three origins: spin-orbit coupling in the band structure, small modulations in the amplitude of the magnetization, and small variations of the emergent magnetic field around its average value. To estimate the strength of these dissipative forces for small drift velocities $\boldsymbol{v}_d$ of the skyrmion lattice, let us consider a weak, time-dependent, periodic electric potential $\Phi(\boldsymbol{r} - \boldsymbol{v}_d t)$ moving in a diffusive system described by charge density n, diffusion constant $D(n)$ and conductivity $\sigma(n)$. The dissipative drag force is then given by $F_d = ej/\sigma = env_d/\sigma$ with the current $j = v_d n$. To obtain the density n we have to solve the diffusion equation

$$\partial_t n = \nabla(D(n)\nabla n) + \nabla(\sigma(n)\nabla\Phi(\boldsymbol{r} - \boldsymbol{v}_d t)). \tag{7.12}$$

To this end let us switch to the comoving reference frame, *i.e.* we perform the transformation $\boldsymbol{r} \to \boldsymbol{r} + \boldsymbol{v}_d t$ and $n \to n(\boldsymbol{r} - \boldsymbol{v}_d t)$ such that Eq. (7.12) transforms to

$$-\boldsymbol{v}_d \nabla n = \nabla(D(n)\nabla n) + \nabla(\sigma(n)\nabla\Phi(\boldsymbol{r})) \tag{7.13}$$

which can now be integrated. Multiplying the result by $\boldsymbol{v}_d$ we obtain

$$-v_d^2(n - n_0) = D(n)\boldsymbol{v}_d \nabla n + \sigma(n)\boldsymbol{v}_d \nabla\Phi(\boldsymbol{r}). \tag{7.14}$$

with the integration constant $-\boldsymbol{v}_d n_0$. To solve Eq. (7.14) further, let us first consider it to linear order and use the approximations $D(n) \equiv D$ and $\sigma(n) \equiv \sigma$. Performing a Fourier transformation using the convention $n(\boldsymbol{r}) = \sum_{\boldsymbol{q}} n_{\boldsymbol{q}} e^{i\boldsymbol{qr}}$ we obtain the following relation for the Fourier components $n_{\boldsymbol{Q}_i}$ of the density operator:

$$n_{\boldsymbol{Q}_i} \approx \frac{-i(\boldsymbol{v}_d \cdot \boldsymbol{Q}_i)\,\sigma\,\Phi_{\boldsymbol{Q}_i}}{v_d^2 + i(\boldsymbol{Q}_i \cdot \boldsymbol{v}_d)D}, \tag{7.15}$$

where $\boldsymbol{Q}_i \neq 0$ are the reciprocal lattice vectors of the periodic potential. Hence, considering Eq. (7.14) only to linear order and within the assumptions that $D(n) \equiv D$ and $\sigma(n) \equiv$

σ, the weak, time-dependent, periodic electric potential induces only a small periodic variation of the density, but it does not lead to a dc current and therefore not to dissipative forces.

To obtain dissipative forces from this ansatz, *i.e.* to obtain a uniform electric current, one has to expand one order higher in the potential. Taking the variations of $D(n)$ and $\sigma(n)$ to linear order in the changes of n into account, one obtains the following average current density in the direction of the drift velocity $\boldsymbol{v}_d$ for small v_d:

$$
\begin{aligned}
j &= -\frac{1}{v_d V} \int d^3 r \left(D(n) \boldsymbol{v}_d \nabla n + \sigma(n) \boldsymbol{v}_d \nabla \Phi(\boldsymbol{r}) \right) \\
&\approx v_d \,\sigma \frac{\partial \sigma}{\partial n} \sum_i \frac{(\boldsymbol{v}_d \cdot \boldsymbol{Q}_i)^2 |\Phi_{\boldsymbol{Q}_i}|^2}{v_d^4 + ((\boldsymbol{Q}_i \cdot \boldsymbol{v}_d) D)^2} \\
&\approx v_d \,\sigma \frac{\partial \sigma}{\partial n} \sum_{\boldsymbol{v}_d \cdot \boldsymbol{Q}_i \neq 0} \frac{|\Phi_{\boldsymbol{Q}_i}|^2}{D^2}
\end{aligned}
\tag{7.16}
$$

with V being the integration volume. For the dissipative forces we obtain

$$
F_d = \frac{ej}{\sigma} \approx e\, v_d \frac{\partial \sigma}{\partial n} \sum_{\boldsymbol{v}_d \cdot \boldsymbol{Q}_i \neq 0} \frac{|\Phi_{\boldsymbol{Q}_i}|^2}{D^2}.
\tag{7.17}
$$

Using $D \sim v_F^2 \tau$ and $\sigma \sim ne\tau/m$, *i.e.* $\partial \sigma / \partial n \sim e\tau/m$, where v_F is the Fermi velocity, $1/\tau$ denotes the scattering rate, and m is the quasiparticle mass, and using that the variations of the potential are of the order of $\Delta V \sim |e\Phi_{\vec{Q}_i}|$, we can estimate the size of the dissipative forces to

$$
F_d \sim \frac{m v_d}{\tau} \left(\frac{\Delta V}{\epsilon_F} \right)^2,
\tag{7.18}
$$

where ϵ_F is the Fermi energy. Within this approximation the dissipative force is proportional to the scattering rate, while the current density is independent of τ.

For the case of the skyrmion lattice, different mechanisms contribute to ΔV, as discussed above. However to obtain a crude estimate for ΔV, note that the change of the electronic energy due to ΔV, which is of the order of $(\Delta V)^2/\epsilon_F$ (or much larger), is at most of the same order as the energy difference ΔE_s of the ferromagnetic and the skyrmion state. The latter can be estimated to $\Delta E_s \sim E_M/(k_F R)^2$, where E_M is a magnetic energy scale and R is the radius of the skyrmions which in the case of MnSi is also characteristic for the distance of the skyrmions [40]. Thus, we can estimate the dissipative forces from below by

$$
F_d \lesssim v_d \frac{\hbar}{R^2} \frac{1}{k_F l} \frac{E_M}{\epsilon_F},
\tag{7.19}
$$

where l is the mean free path and k_F the Fermi momentum. When further using that the emergent magnetic field B^e in the skyrmion lattice phase is of the order of $\hbar/R^2$, because it is quantized to one flux quantum per magnetic unit cell, we see that

$$
F_d \lesssim v_d B^e \frac{1}{k_F l} \frac{E_M}{\epsilon_F}
\tag{7.20}
$$

is strongly suppressed by the two small factors $1/(k_F l)$ and E_M/ϵ_F compared to the force from the emergent electric field $\boldsymbol{E}^e = -\boldsymbol{v}_d \times \boldsymbol{B}^e$. Hence, we expect that dissipative forces are completely negligible compared to the forces arising from the emergent electric field.
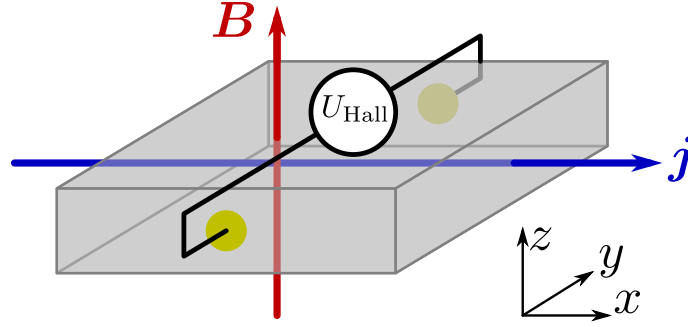
Figure 7.2: Setup of a Hall measurement.

Only very close to the depinning transition, where the Hall forces due to the emergent electric field are suppressed due to the drift velocity being approximately perpendicular to the current (see Chapter 9), dissipative forces might have a chance of becoming relevant. This is, however, well below the experimental resolution of the experiments of Ref. [80] and will therefore be neglected in the following.

Furthermore, corrections due to a violation of adiabaticity or band structure effects are probably small due to the smoothness of the skyrmion structure and the large distance in-between the skyrmions, ~ 200 Å. This suggests that the most important corrections to the emergent fields may arise from spin-flip scattering processes which scatter electrons, *e.g.*, from the majority to the minority band. Spin-flip scattering processes can be interaction- or disorder-induced and arise only due to weak spin-orbit scattering. A quantitative analysis of corrections to adiabatic transport can, for example, be found in Ref. [101]. Concerning MnSi, the spin-flip scattering length is probably much larger than the distance between the skyrmions ~ 200 Å, because the much smaller non-spin-flip scattering length is estimated to be between 10 Å and 100 Å. Therefore, in the following, we use the emergent electric and magnetic fields of Eqs. (7.1) and (7.2).

7.2   Emergent Magnetic Field

In the previous Section, we have derived the emergent magnetic field an electron "feels" while moving adiabatically through a non-collinear magnetic structure. For the skyrmion lattice, each skyrmion induces due to its non-trivial topology, *i.e.* its winding number, exactly one quantum of emergent magnetix flux. For the surrounding phases, the skyrmion density vanishes [33], and therefore no emergent magnetic field is expected. This observation allows to detect the topological winding number via the emergent magnetic field using Hall measurements [32, 33, 36, 40, 114, 115], which we discuss in the following.

When an electric current flows through a conductor which is subject to a perpendicular magnetic field, a Lorentz force acts on the electrons. Typically, as shown in Fig.7.2, the current is applied in the x direction and the magnetic field in the z direction. Since the Lorentz force is perpendicular to both the direction of the current flow and the magnetic field, a potential difference builds up in the y direction. It can be measured as a transverse voltage by applying contacts. This effect is called Hall effect, and the transverse voltage is usually denoted as Hall voltage. In most experiments, one does not plot the Hall voltage depending on the strength of the applied current, but rather the Hall resisitivity ρ_{xy} which is defined as the ratio between the Hall voltage and the applied current. In non-magnetic materials and for small fields, the Hall resisitivity increases linearly with

the applied magnetic field. In many ferromagnetic materials, an additional signal occurs due to the finite ferromagnetic magnetization M. This is known as the anomalous Hall effect, and it is proportional to the magnetization M [116–119], so that the Hall resistivity for ferromagnetic materials is usually given by

$$\rho_{xy} = R_0 B + \mu_0 R_s M, \tag{7.21}$$

where R_0 (R_S) is the normal (anomalous) Hall coefficient, and μ_0 is the vacuum permeability. The prefactor of the normal Hall effect, R_0, depends on details of the band structure – note that MnSi is a multi-band system – and on the relative sizes of the scattering rates.

Since only in the skyrmion lattice phase (and not in the conical or helical phases) the emergent magnetic field derived in Sec. 7.1 occurs, the statement is, that only in this phase a further contribution to the Hall signal exists. As the emergent magnetic field arises due to the non-trivial topology of the skyrmion lattice, this effect is denoted as the topological Hall effect. Its size is proportional to the emergent magnetic field, thus to the skyrmion winding number and to the skyrmion density [115]. The topological Hall effect occurs besides the normal and the anomalous Hall effect, and allows for a direct measurement of the topological properties (chirality and winding number) of the spin structure in the skyrmion lattice phase. For MnSi the topological Hall effect in the skyrmion phase as well as the absence of a topological Hall signal in the helical or conical phase have already been verified, and the results are published in Ref. [40]. These Hall measurements were the first evidence of the non-trivial topological nature of the skyrmion lattice phase, and we review the results of Ref. [40] in this Section.

In the adiabatic limit, where the spin of the charge carriers (with infinite lifetime) adjusts constantly to the smoothly varying magnetic structure, the size of the topological Hall signal may be estimated as [105, 106]

$$\Delta\rho_{xy}^B \approx P \, R_0 \, \left| \frac{q^e}{e} \right| B_z^e, \tag{7.22}$$

where e is the electron charge, and $|q^e| = 1/2$ is the emergent charge as introduced in Sec. 7.1. Here, the external magnetic field is applied in z direction, so that the skyrmion lattice lies in the xy plane and induces an emergent magnetic field in z direction, too. To avoid confusion with the next Section, where we consider the change of the resisitivity as a function of the emergent electric field instead of the emergent magnetic field, we use the label "B" in this Section and the label "E" in the next Section. In the plots, which are taken from Ref. [40] and our publication Ref. [80] respectively, the resisitivity changes are, however, just denoted by $\Delta\rho_{xy}$, because in the corresponding publication the focus was on only one of these effects. As the size of the topological Hall effect also depends on many details similar to the prefactor of the normal Hall effect, R_0, one can use its experimental value for a semi-quantitative prediction of $\Delta\rho_{xy}^B$. Moreover, the topological Hall signal is proportional to the local spin-polarization P of the conduction electrons and vanishes for $P \to 0$. The reason for this is that, as shown previously, charge carriers with a majority or minority spin collect Berry phases of opposite signs. The polarization P can be calculated from the ratio $P = \mu_{\mathrm{spo}}/\mu_{\mathrm{sat}}$ of the ordered magnetic moment in the skyrmion phase and the saturated magnetic moment. For MnSi, in the temperature and field region of the skyrmion phase, these quantities are given by $\mu_{\mathrm{spo}} \approx (0.2 \pm 0.05)\, \mu_{\mathrm{B}}$ and $\mu_{\mathrm{sat}} \approx (2.2 \pm 0.2)\, \mu_{\mathrm{B}}$, respectively [40]. Hence, for MnSi the polarization P is given by $P \approx 0.1 \pm 0.02$.
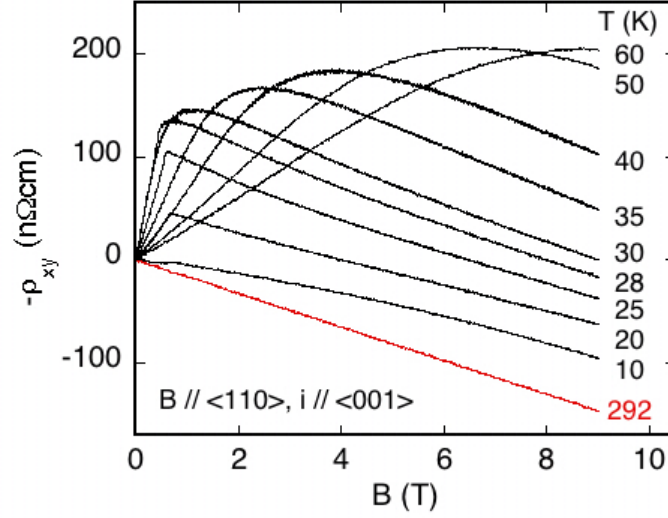
Figure 7.3: Hall resistivity for MnSi measured for a magnetic field $\boldsymbol{B}$ in [110] and the applied current in [001] direction. This Figure is taken from Ref. [40]. Note that the sign of the Hall effect reported in Ref. [40] is not correct and we have therefore added a minus sign to ρ_{xy} compared to the original Figure.

Using an emergent magnetic field of $B^e \approx 2.5$ T$|e/q^e|$ for MnSi [40] which is oriented opposite to the applied magnetic field $\boldsymbol{B}$, a polarization of $P \approx 0.1 \pm 0.02$ and the experimental value for R_0 discussed below in the experimental part, a theoretical estimate for the size of the topological Hall contribution is given by $\Delta\rho_{xy}^B \approx 4$ nΩ cm.

Experiments: For the Hall experiments of Ref. [40] mainly two single-crystal samples of MnSi were used. They were cut from an ingot that had been used also in the measurements of Refs. [1, 50]. Sample 1 was about $1 \times 1.5 \times 0.13$ mm^3 in size and oriented such that the external magnetic field $\boldsymbol{B}$ was applied in the [110] and the electric current in the [001] direction in the measurements. Sample 2 with a size of about $1.6 \times 3.1 \times 0.15$ mm^3 was oriented such that $\boldsymbol{B}$ was aligned in [111] direction and the current in [1$\bar{1}$0] direction. In this work, the Hall effect and the resistivity where measured, and the obtained data agreed with the previous studies of Ref. [120]. However, the authors used an experimental setup with a much better resolution to make the small topological contributions of the Hall signal visible. Further experimental details can be found in Refs. [40, 121].

In Fig. 7.3, a typical measurement for the Hall resistivity ρ_{xy} of MnSi for sample 1 is shown. Here, the magnetic field was aligned along the [110] direction, and the current was applied along the [001] direction. At high temperatures, the Hall signal is dominated by the normal Hall effect, whereas for lower temperatures the behaviour of ρ_{xy} is more complicated. From the Hall resistivity ρ_{xy}, one can infer basically the normal Hall coefficient, R_0, and the nominal charge carrier concentration, $n = (R_0 e)^{-1}$. Neubauer *et al.* [40] obtained a value of $n = 3.78 \cdot 10^{22}$ cm^{-3}. Lee *et al.* [120] obtained the same order of magnitude, but their value differs by a factor of two, while analysing the data in a slightly different way. Nevertheless, the precise value of n is not important for the conclusions.

To observe the additional topological Hall contribution in the skyrmion phase, detailed measurements of the Hall resistivity as a function of the magnetic field for different temperatures were performed. The results are shown in the left panel of Fig. 7.4. Basically,
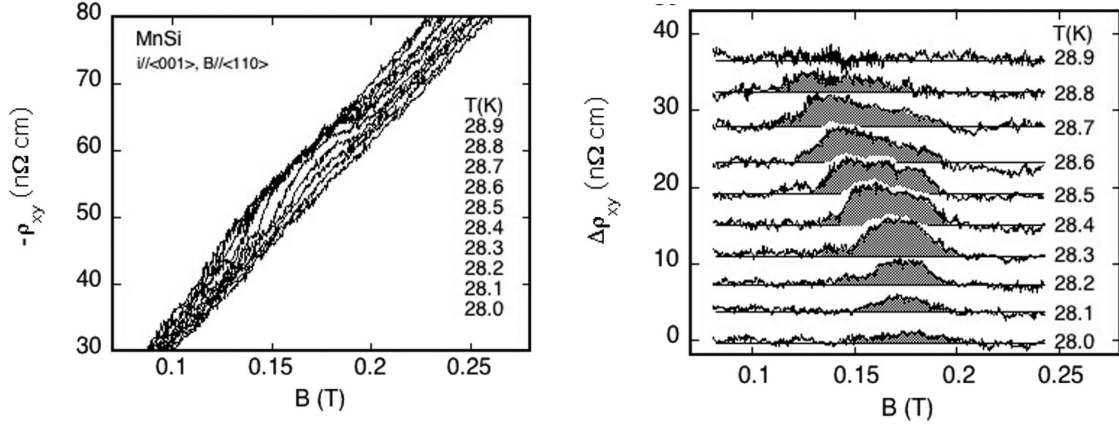
Figure 7.4: The left panel shows the total Hall resistivity ρ_{xy} of MnSi in the skyrmion phase. The right panel shows only the additional Hall contribution in the skyrmion phase. For a better visibility, curves for different temperatures are shifted vertically. The Figures are taken from Ref. [40]. Note that the sign of the Hall effect reported in Ref. [40] is not correct and we have therefore added a minus sign to ρ_{xy} compared to the original Figure.

the Hall signal rises linearly with increasing magnetic field, but for magnetic fields in the range of the skyrmion phase, a small additional contribution can be observed. To make this additional contribution better visible, the authors approximated the Hall signal by a straight line for temperatures slightly above and below the skyrmion phase and substracted this linear part from the whole curves. The result of this data analysis is plotted in the right panel of Fig. 7.4. For better visibility, the curves for different temperatures have been shifted vertically.

To exclude the fact that the observed additional signal is not just due to an enhanced anomalous Hall effect, which could in principle explain such a feature, Neubauer *et al.* [40] considered the behaviour of $M(B)$. Inside the skyrmion phase, the slope of the magnetization as a function of magnetic field is reduced, while it is enlarged at both boundaries of the skyrmion phase. Therefore, the additional contribution to the Hall signal does not track the evolution of the magnetization. Consequently, it has to be mainly attributed to the topological winding of the magnetic structure. However, due to the variations of the slope of $M(B)$ the additional contribution to the Hall signal, which is plotted in the right panel of Fig. 7.4, does not have the shape of a simple step function, *i.e.* constant inside the skyrmion lattice phase and zero outside, as does $\Delta\rho_{xy}^{B}$.

One can roughly estimate the size of the experimentally observed topological Hall contribution by $\Delta\rho_{xy}^{B} \approx (4.5 \pm 1)$ nΩ cm which fits very well with the theoretically predicted value of $\Delta\rho_{xy}^{B} \approx 4$ nΩ cm discussed above. Another main result of the experiments of Ref. [40] is that the sign of the topological signal is opposite to that of the normal Hall contribution. Furthermore, the Hall signal was observed to be basically the same for the two different orientations of the magnetic fields that were studied, implying that also the topological contribution is mainly independent of the direction of the magnetic field.

To conclude, the study of the Hall effect allows to observe experimentally the emergent magnetic field felt by the charge carriers while constantly adapting their spin-orientation with respect to the smoothly varying magnetic texture. The sign and quantitative size

of the observed topological resistivity contribution $\Delta\rho_{xy}^B$ agreed for MnSi perfectly with the theoretically expected value, emphasizing the topological character of the skyrmion lattice.

7.3   Emergent Electric Field

In Section 7.1, we have derived an expression for the emergent electric field an electron feels while moving adiabatically through a magnetic structure, given by

$$\boldsymbol{E}_i^e = \hbar\,\hat{\boldsymbol{\Omega}}\cdot(\partial_i\hat{\boldsymbol{\Omega}}\times\partial_t\hat{\boldsymbol{\Omega}}). \tag{7.23}$$

From this expression one can immediately infer that the emergent electric field is only finite for a non-collinear and *time-dependent* magnetic structure. In Chapter 9, we discuss the current-induced forces on the skyrmion lattice, and we show that above a critical threshold current density the skyrmion lattice starts to drift with a drift velocity $\boldsymbol{v}_d$. For a moving skyrmion lattice one would then expect to observe also the emergent electric field [9] or, conversely, the observation of an emergent electric field allows inferences on the motion of the skyrmion lattice.

In this Section, we discuss the relation between the emergent magnetic field, the emergent electric field, and the connection to the Hall signal for a moving skyrmion structure. The latter allows for an experimental detection of the emergent electric field as well as a direct evidence of a moving skyrmion lattice. We published most of the work presented in this Section in Ref. [80].

For a drifting skyrmion lattice, the direction of the magnetization $\hat{\boldsymbol{\Omega}}(\boldsymbol{r},t)$ depends only on the difference $\boldsymbol{r}-\boldsymbol{v}_d t$, *i.e.* $\hat{\boldsymbol{\Omega}}(\boldsymbol{r},t)=\hat{\boldsymbol{\Omega}}(\boldsymbol{r}-\boldsymbol{v}_d t)$. Substituting this ansatz into the expression for the emergent electric field of Eq. (7.2) and using $\partial_t\hat{\boldsymbol{\Omega}}=-(\boldsymbol{v}_d\cdot\nabla)\,\hat{\boldsymbol{\Omega}}$ this leads to

$$\boldsymbol{E}_i^e = \hbar\,\hat{\boldsymbol{\Omega}}\cdot(\partial_i\hat{\boldsymbol{\Omega}}\times(\boldsymbol{v}_d\cdot\nabla)\,\hat{\boldsymbol{\Omega}}) = -(\boldsymbol{v}_d\times\boldsymbol{B}^e)_i\,, \tag{7.24}$$

which provides a general connection between the emergent magnetic and the emergent electric field for a drifting magnetic structure. Equation (7.24) is but the Faraday law of induction, indicating that a change of the magnetic flux causes an electric field. Since the emergent magnetic field $\boldsymbol{B}^e$ is non-zero only in the skyrmion phase and furthermore quantized, this also carries over to the emergent electric field due to Eq. (7.24) for fixed $\boldsymbol{v}_d$. Note that $\boldsymbol{E}^e$ is perpendicular to the applied magnetic field and the drift velocity, and induces extra forces on the charge carriers. Since $\boldsymbol{v}_d$ is, for current densities well above the threshold current density ($j > j_c$), mainly oriented parallel to the applied current, as is discussed in Chapter 9, the drift of the skyrmion lattice reduces the relative speed between the spin currents and the magnetic structure. Furthermore, the force exerted by the emergent Faraday field $\boldsymbol{E}^e$ on the charge carriers is in perpendicular direction to the applied current, for current densities well above the threshold current density. In total, the forces that act on the electrons with momentum $\boldsymbol{k}$ and spin orientation σ are given by [9, 80]:

$$\begin{aligned}
\boldsymbol{F}_{\sigma\boldsymbol{k}} &= e\boldsymbol{E} + \boldsymbol{F}_H + q^e\boldsymbol{E}^e + q_\sigma^e\boldsymbol{v}_{\sigma\boldsymbol{k}n}\times\boldsymbol{B}^e + \boldsymbol{F}_{\text{diss}} \\
&= e\boldsymbol{E} + \boldsymbol{F}_H + q_\sigma^e(\boldsymbol{v}_{\sigma\boldsymbol{k}n}-\boldsymbol{v}_d)\times\boldsymbol{B}^e + \boldsymbol{F}_{\text{diss}}.
\end{aligned} \tag{7.25}$$

Here, $\boldsymbol{E}$ is the external applied electric field, $\boldsymbol{F}_H$ denotes the Hall force from the normal and anomalous Hall effect. With $\boldsymbol{v}_{\sigma\boldsymbol{k}n}$ being the velocity of quasi-particles in band n, $\boldsymbol{v}_{\sigma\boldsymbol{k}n}-\boldsymbol{v}_d$ denotes the relative velocity of the quasi-particles and the magnetic structure.

Furthermore, dissipative drag forces $\boldsymbol{F}_{\text{diss}}$ arising for $\boldsymbol{v}_d \neq 0$ act on the electrons. These are suppressed by two small factors, $1/(k_F l)$, where k_F is the Fermi momentum and l is the mean free path, and by $\frac{E_M}{\epsilon_F}$, being the magnetic energy scale divided by the Fermi energy [80]. Thus, the dissipative forces are negligible compared to the forces from the emergent electric field. Nonetheless, in a very small regime close to the depinning transition (but well below the resolution of the experiments in Ref. [80]), the drift velocity is almost perpendicular (instead of parallel) to the current, and therefore does not give a strong contribution to the Hall signal. In this tiny region, the dissipative forces may be important.

As can be seen from Eq. (7.25), the emergent electric field originating from the motion of the skyrmion lattice leads to a reduction of the Hall signal, compared to the Hall field of the non-moving skyrmion lattice. To be more precise, in a Galilean invariant one-band system, the extra electric current induced by $-q_\sigma^e \boldsymbol{v}_{d\parallel} \times \boldsymbol{B}^e$ has to be exactly canceled by the change of the electric Hall field, *i.e.* $\Delta \boldsymbol{E}_\perp \equiv -q_\sigma^e \boldsymbol{v}_{d\parallel} \times \boldsymbol{B}^e$, where $\boldsymbol{v}_{d\parallel}$ is the part of the drift velocity parallel to the applied current that differs only slightly from $\boldsymbol{v}_d$ for current densities well above j_c. The reason for this is that a Galilean transformation of a coordinate system, where skyrmions and electrons are at rest (*i.e.* no current is applied and no current induced forces are present), to a coordinate system with a uniform motion corresponds to a state with a finite electric current and a moving skyrmion lattice. In this moving reference frame, the drift velocities of the electrons and the skyrmions are the same, and the force from the emergent magnetic field cancels the force from the emergent electric field. Hence, in a Galilean invariant one-band system, the relative sizes of the emergent Hall- and the Faraday effect are equal.

In general, *i.e.* in a system without Galilean invariance, the contributions from both emergent fields to the Hall signal do not cancel each other. For example, in Section 9.2 we show that the drift velocity $\boldsymbol{v}_d$ is only in the Galilean invariant equal to the spin velocity $\boldsymbol{v}_s$, describing the drift of the emergent current $\boldsymbol{j}^e$. This originates from different damping mechanims which are introduced in the next Chapter. We expect that the correction due to damping is a small effect and that for larger applied currents it is $\boldsymbol{v}_s \approx \boldsymbol{v}_d$, when pinning can be neglected. Consequently, the average force given by $\langle q_\sigma^e (\boldsymbol{v}_{\sigma kn} - \boldsymbol{v}_s) \times \boldsymbol{B}^e \rangle$ still vanishes. However, in a more complex system with multiple bands, where the quasiparticle velocity $v_{\sigma kn}$ and thus the average force depend on the orientation of the spin relative to the local magnetization σ, the momentum vector $\boldsymbol{k}$, and the band index n, one nevertheless expects a finite contribution to the Hall effect.

This insight paves the way for the experimental detection of the emergent electric field by measuring the change of the Hall field. Using basically the same geometries as in Sec. 7.2, where the magnetic field was applied in z direction and the electric current in x direction, and defining the difference in the resitivity due to the applied current $\Delta \rho_{xy}^E$ by

$$\Delta \rho_{xy}^E \equiv \rho_{xy}(j) - \rho_{xy}(0) = -\Delta \rho_{yx}^E, \tag{7.26}$$

we obtain

$$\Delta E_\perp = j \, \Delta \rho_{yx}^E \approx -\frac{\Delta \sigma_{yx}^E \, E}{\sigma_{xx}} = -\frac{\Delta j_\perp^E}{\sigma_{xx}} = -\tilde{P} \left| \frac{q^e}{e} \right| E_y^e = \tilde{P} \left| \frac{q^e}{e} \right| (\boldsymbol{v}_{d\parallel} \times \boldsymbol{B}^e)_y, \tag{7.27}$$

where $\boldsymbol{\sigma}$ denotes the conductivity tensor and $\Delta \sigma_{yx}^E$ the corresponding conductivity difference. As mentioned previously, to avoid confusion we label the resisitivity change due to the emergent magnetic (electric) field by $\Delta \rho_{xy}^B$ ($\Delta \rho_{xy}^E$). As the plots are taken from Ref. [40] and our publication Ref. [80], respectively, where in each figure just one of the

two effects was studied, the resisitivity changes in the plots are just denoted by $\Delta\rho_{xy}$. The difference in the transverse current $\Delta j_\perp^E$ is accordingly given by $\Delta j_\perp^E = \Delta\sigma_{yx}^E E$, and $\tilde{P}$ is the dimensionless spin polarization which can be obtained by calculating the cross correlation of the charge current j and the emergent current j^e

$$\tilde{P} = \left|\frac{e}{q^e}\right| \frac{\langle\langle j, j^e\rangle\rangle}{\langle\langle j, j\rangle\rangle}. \tag{7.28}$$

It is the ratio of the electric currents obtained from E^e and E. Within a relaxation time approximation for a multiband system $\tilde{P}$ can be approximated by

$$\tilde{P} \approx -\frac{\sum_{n,\vec{k},\sigma=\pm 1} \sigma\,\tau_{\sigma n}(v_{\sigma\vec{k}n}^y)^2\,\partial_\epsilon f_{n\sigma}^0}{\sum_{n,\vec{k},\sigma=\pm 1} \tau_{\sigma n}(v_{\sigma\vec{k}n}^x)^2\,\partial_\epsilon f_{n\sigma}^0} \tag{7.29}$$

where $f_{n\sigma}^0$ is the Fermi distribution for the band n with the scattering rate $1/\tau_{\sigma n}$ and spin-orientation σ relative to the local magnetization. The relation between the difference in the Hall field $\Delta E_\perp$ and the emergent electric field E^e, given by $\Delta E_\perp = -\tilde{P}|q^e/e|E_y^e$ from Eq. (7.27), confirms that up to the factor of the spin polarization $\tilde{P}$ it is possible to measure the emergent electric field E^e via a Hall measurement. Because the emergent magnetic field B^e is quantized, this also corresponds to a direct measurement of the parallel component of the drift velocity:

$$v_{d\parallel} = \frac{E^e}{B^e} \approx \left|\frac{e}{q^e}\right| \frac{\Delta E_\perp}{B^e\tilde{P}} \approx -\left|\frac{e}{q^e}\right| \frac{j\Delta\rho_{xy}^E}{B^e\tilde{P}} = v_{\text{pin}} \frac{j\Delta\rho_{xy}^E}{j_c\Delta\rho_{xy}^\infty}, \tag{7.30}$$

where in the last step we introduced $\Delta\rho_{xy}^\infty = \Delta\rho_{xy}^E(j \gg j_c) - \Delta\rho_{xy}^E(j \ll j_c)$, and the pinning velocity v_{pin} is given by

$$v_{\text{pin}} \approx -j_c\left|\frac{e}{q^e}\right| \frac{\Delta\rho_{xy}^\infty}{B^e\tilde{P}}. \tag{7.31}$$

We used that $\Delta\rho_{xy}^\infty|e|/(B^e\tilde{P}|q^e|) \approx -v_s/j = -|q^e/(eM)|\tilde{P}$ is approximately independent of the local magnetization and therefore of the temperature. Here, $\boldsymbol{v_s} = \langle\boldsymbol{j^e}\rangle/M$ is the velocity of the current associated to the charges q_σ^e. With this expression for the pinning velocity (Eq. (7.31)), the term $4\pi\hbar M v_{\text{pin}}$ can be interpreted as the force per skyrmion and per length needed to depin the skyrmion lattice.

The main goal of the Hall measurements that were performed in Ref. [80] was to confirm the current-induced motion of the skyrmions. In principle, the depinning and motion of the skyrmions might also be detected using microscopic experimental techniques such as Lorentz force microscopy or neutron scattering techniques, but those methods are not able to observe the emergent electrodynamics. In that sense, Hall measurements are a perfect tool (and much cheaper than neutron scattering) to observe both the motion of the skyrmion lattice and the emergent electrodynamics since the emergent electric field is directly proportional to the velocity of the skyrmions. Below we review the experimental results obtained by the Hall measurements, published in Ref. [80].

Experiments: The Hall measurements were perfomed using very clean single crystal MnSi samples. Since the goal is to study the skyrmion lattice under a current flow using the Hall effect, a modified experimental technique was used. It allowed for measurements with a large DC current on which a small AC excitation (with an amplitude not larger than a few
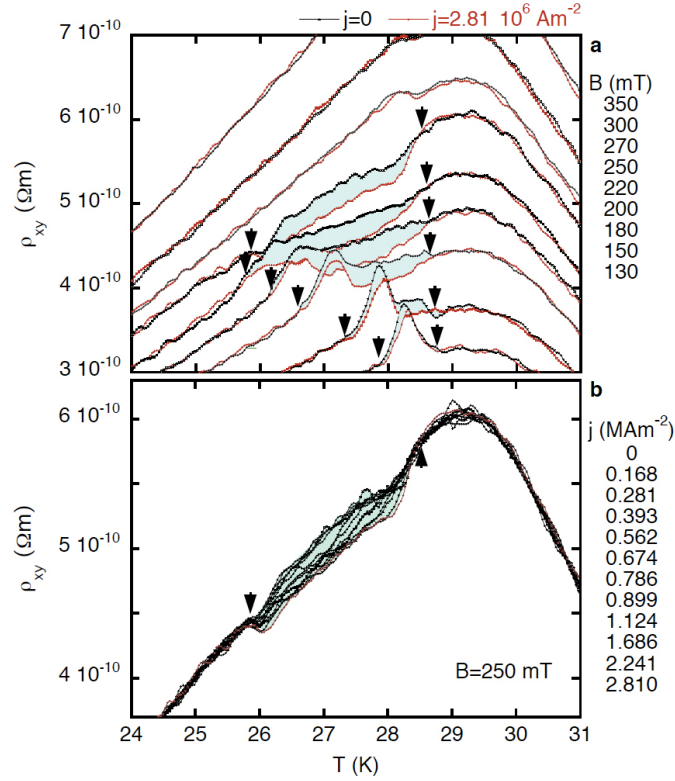
Figure 7.5: Hall resistivity as function of temperature T in the skyrmion phase of MnSi. In the upper panel, the black curves represent the Hall resistivity for various magnetic fields without an applied electric DC current, and the red curves are the corresponding ones with an applied DC current of $j = 2.81 \cdot 10^6$ A/m^2. With the applied current the Hall signal is suppressed in the skyrmion phase (colored blue). In the lower panel, the magnetic field is fixed, $B = 250$ mT, and the different curves represent different current densities. The Figure is taken from our publication, Ref. [80].

percent compared to the applied DC currents) could be superimposed. The AC excitation frequency was about 22.5 Hz, and the Hall resisitivity ρ_{xy} as well as the longitudinal resistivity ρ_{xx} were measured at the same time. Ohmic heating and temperature gradients were minimized by a good coupling to the cryogenic system. For further experimental details see Ref. [80].

Fig. 7.5 shows the Hall resistivity ρ_{xy} as a function of temperature in the skyrmion lattice phase of MnSi. The curves plotted in black represent Hall resistivities in the absence of an electric DC current. Different curves correspond to different applied magnetic fields. As described in Sec. 7.2, the electrons in MnSi are subject to the normal, the anomalous and – in the skyrmion phase – also to the topological Hall effect. In Fig. 7.5, the pronounced features are due to the temperature dependence of the anomalous Hall effect. Close to the lower boundary of the skyrmion phase, one can observe a small maximum in the Hall resisitivity. This is due to a characteristic change in the magnetization, while going from the conical phase to the skyrmion phase and in-between passing a small regime of phase coexistence [84]. The red curves of the upper panel are measured with an applied electric DC current of $j = 2.81 \cdot 10^6$ A/m^2, and each curve belongs to a different magnetic field strength. With the applied current the Hall signal is suppressed in the skyrmion

lattice phase compared to the zero-current Hall signal. The difference between two corresponding (black and red) curves is colored in blue. The boundaries of the skyrmion phase are indicated by black arrows marking the suppression region of the Hall signal. Note that they agree very well with the boundaries of the skyrmion phase obtained from other results like susceptibility measurements. In the lower panel, the magnetic field is fixed, $B = 250$ mT, and the different curves represent different applied DC current densities.

By considering the data of Fig. 7.5 at several fixed temperatures and tracing for each temperature the resisitivity by varying the current densities, one obtains the plot shown in Fig. 7.6. The left-hand-side axis labels the absolute data, and the right-hand-side axis labels the relative size with respect to the zero-current case. The temperature decreases from top to bottom. In the first (last) panel, the temperature is above (below) the temperatures for the skyrmion phase, and therefore the signal does not change while increasing the strength of the current density. For the three panels in the middle the temperatures are in the skyrmion lattice phase. For small current densities, $j < j_c$, the Hall signal remains the same (within experimental precision). Above the critical current threshold, $j > j_c$, however, the Hall resisitivity ρ_{xy} decreases until at large currents the signal remains constant at the reduced value. For better visibility, the difference between the signal without a DC current and with the corresponding applied current is colored in blue.

As discussed in Eq. (7.30), the drift velocity component parallel to the current is approximately proportional to the product of the current density and the change of Hall resistivity, *i.e.* $v_{d\parallel} \sim j\Delta\rho_{xy}^E$. Therefore, $j\Delta\rho_{xy}^E$ as a function of the applied current j is shown in Fig. 7.7. The data presented was measured in an external magnetic field of 250 mT for various temperatures, used to determine the critical current densities above which $j\Delta\rho_{xy}$ is no longer zero and the skyrmion lattice starts to move.

To determine the drift velocities from the experimental data, one can estimate $\Delta\rho_{xy}^\infty$ (defined just below Eq. (7.30)) in the center of the skyrmion phase to $\Delta\rho_{xy}^\infty \approx 3 \cdot 10^{-11}$ Ωm from Fig. 7.6. Using the estimated polarization [40] of $\tilde{P} \approx 0.1$ and the strength of emergent magnetic field for MnSi 2.5 T, *i.e.* $B^e \approx 2.5$ T$|e/q^e|$ we obtained for the pinning velocity

$$v_{\text{pin}} \approx j_c \left|\frac{e}{q^e}\right| \frac{\Delta\rho_{xy}^\infty}{B^e\tilde{P}} \approx \frac{j_c}{10^6 \text{ A/m}^2}0.12 \frac{\text{mm}}{\text{s}}, \tag{7.32}$$

and accordingly for the drift velocity

$$v_{d\parallel} \approx v_{\text{pin}} \frac{j\Delta\rho_{xy}^E}{j_c\Delta\rho_{xy}^\infty} \approx \frac{j}{10^6 \text{ A/m}^2} \frac{\Delta\rho_{xy}^E}{\Delta\rho_{xy}^\infty} 0.12 \frac{\text{mm}}{\text{s}}. \tag{7.33}$$

The drift velocities, inferred from these experimental data, are displayed on the right axis of Fig. 7.7. For current densities smaller than the critical current density, the drift velocity of the skyrmion lattice is zero (within the experimental precision and up to a very small creep, *i.e.* a tiny motion due to thermal (or quantum) fluctuations [83]). In this case, the current-induced forces on the skyrmion lattice are not strong enough to overcome the pinning forces due to disorder and the atomic lattice. A detailed discussion of the current-induced forces on the skyrmion lattice including pinning forces can be found in Chapter 9. Above j_c the skyrmion lattice gets depinned by the current and starts to move. In this case, the cystal inhomogeneities locally still distort the skyrmion lattice in a time-dependent way which effectively can be characterized by a velocity-dependent friction force acting on the skyrmion lattice. For $j \gg j_c$, the drift velocity of the skyrmion lattice increases linearly with the applied current density (see Fig. 7.7), because in this regime the pinning forces are much smaller than the current-induced forces and can therefore be ignored. The size of
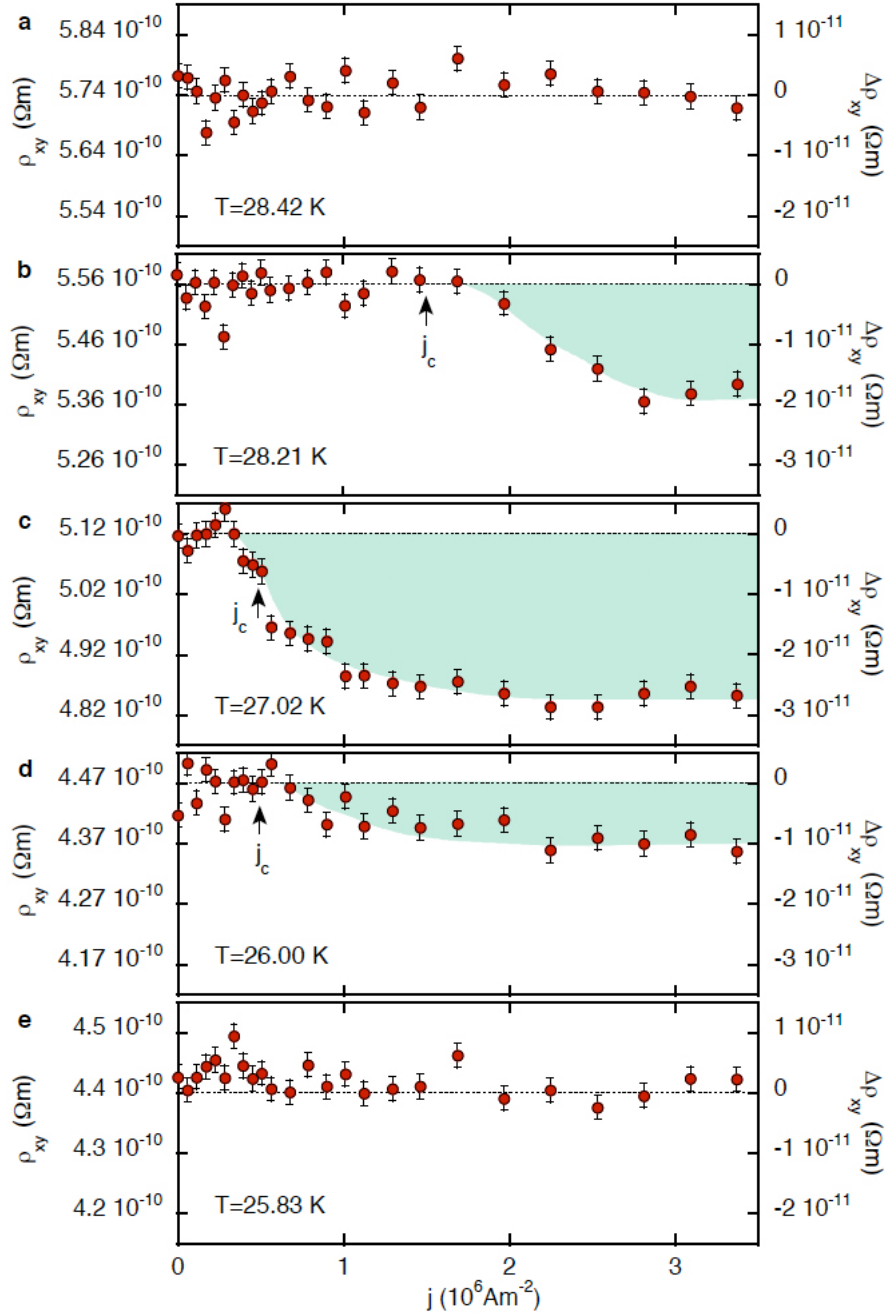
Figure 7.6: Hall resisitivity of MnSi as a function of the applied electric DC current for different temperatures. The axis on the left hand side shows the absolute value, and the axis on the right hand side labels the relative size with respect to the zero-current case. The applied magnetic field is $B = 250$ mT. The temperature decreases from the first to the last panel. In the first and the last panels, the temperature is outside the temperature range of the skyrmion lattice phase. As expected, no reduction of the Hall signal due to an applied current can be observed. For the three plots in the center, above the critical current density j_c the signal is suppressed and saturates for even larger current densities to a lower value. The Figure is taken from our publication, Ref. [80].
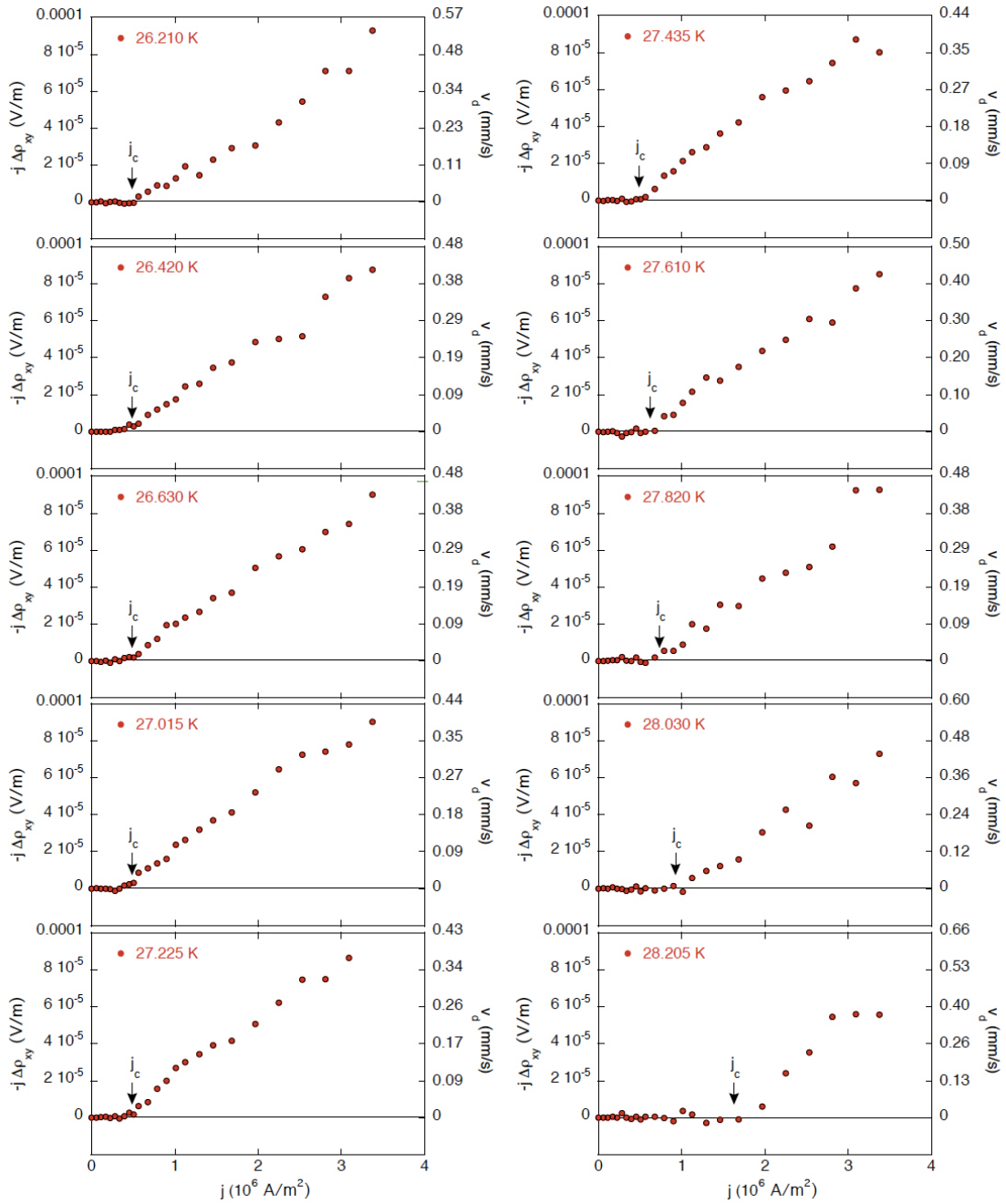
Figure 7.7: Product of the change of the Hall resistivity $\Delta\rho^E_{xy}$ due to the emergent electric field and of the current density (left-hand-side axis) and drift velocity (right-hand-side axis) as a function of the applied current density at a magnetic field of 250 mT. Each plot corresponds to a different temperature. The arrows mark the critical current density above which the skyrmion lattice starts to move. The Figure is taken from our publication, Ref. [80].
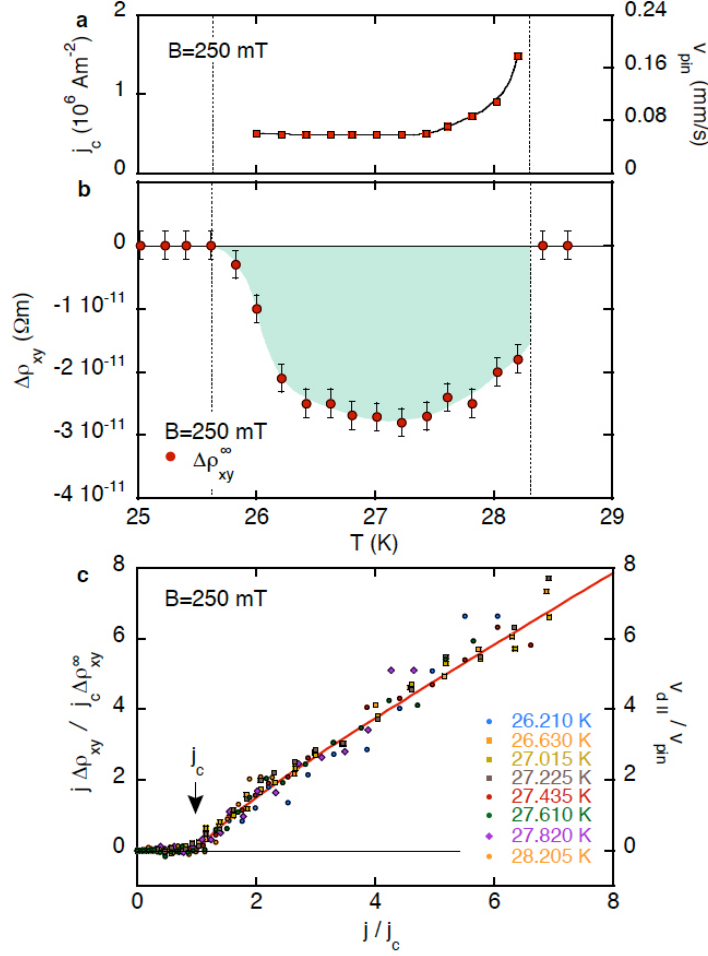
Figure 7.8: Summary of features of the skyrmion lattice phase in MnSi subject to an electric current. Panel (a) displays the temperature dependence of the critical current density and the pinning velocity (see Eq. (7.31)) given in absolute units on the left-hand-side and right-hand-side axes, respectively. Panel (b) illustrates the change of Hall resistivity due to the emergent electric field for large currents, $i.e.$ plotted is $\Delta\rho_{xy}^{\infty} = \Delta\rho_{xy}^{E}(j \gg j_c) - \Delta\rho_{xy}^{E}(j \ll j_c)$ as a function of temperature. The scaling plot shown in panel (c) is produced by plotting the transverse electric field, $\Delta E_{\perp} = -j\Delta\rho_{xy}^{E}$, in units of $-j_c\Delta\rho_{xy}^{\infty}$ as a function of j/j_c using the data from Fig. 7.7. This is equivalent to plotting the drift velocity $v_{d\parallel}$ in units of v_{pin} as indicated by the right-hand-side axis. The Figure is taken from Ref. [80]

the critical current density needed to depin the skyrmion lattice is about $j_c \sim 10^6$ A/m^2. It is by a factor of about 10^5 smaller than the current densities needed to depin, $e.g.$ ferromagnetic domain walls in present-day spin-torque experiments [90, 91, 122].

Figure 7.8 summarizes the main features of the skyrmion lattice phase in MnSi subject to an electric current. In panel (a) the critical curent density is plotted as a function of temperature. The corresponding pinning velocities are illustrated on the right-hand-side axis of the Figure. They are, as expected, of the same order of magnitude as the electronic

73

drift velocities, since

$$v_{\text{drift}} \sim \frac{j}{en} \approx 0.16 \, \frac{\text{mm}}{\text{s}}, \tag{7.34}$$

with a current density of $j \sim j_c \sim 10^6$ A/m^2 and a nominal charge carrier concentration of $n \approx 3.8 \cdot 10^{22}$ cm^{-3} [40] as used in the previous Section.

The critical current density j_c increases when raising the temperature to the boundary of the skyrmion lattice phase. Close to the weakly first-order transition to the paramagnetic phase, j_c and thus also v_{pin} characterizing the pinning forces are about a factor of two larger compared to the center of the skyrmion phase. Note that this cannot be explained by the fact that the local magnetization amplitude M decreases as the temperature increases. Instead, the explanation for the increase in j_c is most likely that close to the phase transition the stiffness of the skyrmion lattice is reduced, so that the local magnetic structure can adjust much better to the disorder potential. In total, this leads to much higher pinning forces [82, 83, 123] that have to be overcome by the current. At the lower temperature boundary of the skyrmion lattice, where the phase transition is strongly first order, the critical current density is within experimental precision independent of the temperature, in agreement with the theoretical considerations above.

In panel (b) of Fig. 7.8, the change of the Hall resisitivity due to the emergent magnetic field for large current densities $\Delta\rho_{xy}^{\infty}$ is plotted as a function of the temperature. It has an extremum in the center of the skyrmion lattice phase. The size of the reduction of the Hall resisitivity is about $\Delta\rho_{xy} \approx 4$ nΩ cm. This is similar to the value obtained from the emergent magnetic field [40]. However, these two contributions to the Hall resisitivity cancel each other only in a Galilean invariant system and not in general. At the higher temperature boundary of the skyrmion lattice, $\Delta\rho_{xy}^{\infty}$, jumps to zero when crossing the first-order phase transition. At the lower temperature boundary, $\Delta\rho_{xy}^{\infty}$ decreases continuously to zero with decreasing temperature. The latter may be explained by a region of phase coexistence of the skyrmion and the conical phase [84].

Panel (c) of Fig. 7.8 is a scaling plot showing the transverse electric field, $\Delta E_{\perp} = -j\Delta\rho_{xy}^{E}$, in units of $-j_c\Delta\rho_{xy}^{\infty}$ as a function of j/j_c, using the data from Fig. 7.7. Since $\Delta E_{\perp} \sim E^e$ and $E^e \sim v_{d\parallel}$, this corresponds also to measurements of the emergent electric field E^e and the parallel drift velocity $v_{d\parallel}$ in units of $v_{\text{pin}}B^e$ and v_{pin} respectively.

To conclude, the experimental data clearly establish the quantitatively predicted emergent electrodynamics, implying the evidence of the motion of the skyrmion lattice. From the experimental data the critical current densities at which the depinning of the skyrmions from the impurities occurs were quantitatively determined. They are of the order of $j_c \sim 10^6$ A/m^2, being ultra-low compared to the critical current densities needed to depin, for example, ferromagnetic domain walls in magnetic wires [90, 91, 122] that are five orders of magnitude larger. Furthermore, the drift velocities were determined, and the motion of the skyrmion lattice was studied.

In this Chapter, we discussed the forces on the electrons and the corresponding emergent electric and magnetic fields an electron feels while moving through a non-collinear magnetic structure. In the next Chapters, we focus on the forces the electric current exerts on the magnetic structure. Thereby, we also discuss in more detail the pinning forces that pin the skyrmion lattice to the disorder potential. We also show that a measurement of the drift velocity in principle allows to gain information on the functional form of the pinning force.

8 Landau-Lifshitz-Gilbert Equation

The standard Landau-Lifshitz-Gilbert (LLG) equation [5, 6, 124–126] in the presence of an electric current is given by

$$(\partial_t + \boldsymbol{v}_s \cdot \nabla)\,\hat{\boldsymbol{\Omega}} = -\hat{\boldsymbol{\Omega}} \times \boldsymbol{H}_{\text{eff}} + \alpha\,\hat{\boldsymbol{\Omega}} \times \left(\partial_t + \frac{\beta}{\alpha}\boldsymbol{v}_s \cdot \nabla\right)\hat{\boldsymbol{\Omega}}. \tag{8.1}$$

It is an equation of motion for the slow, *i.e.* up to first order in time derivatives, and smooth, *i.e.* up to first order in space derivatives, varying magnetization direction

$$\hat{\boldsymbol{\Omega}}(\boldsymbol{r}, t) = \boldsymbol{M}(\boldsymbol{r}, t)/M, \tag{8.2}$$

with a constant amplitude of the magnetization $|\boldsymbol{M}| \equiv M$. Note that Eq. (8.1) does not include the dynamics of the amplitude of M.

The electric current enters via $\boldsymbol{v}_s$ which denotes an effective spin velocity parallel to $\boldsymbol{j}_s$, the spin current density.[1] The effective spin velocity $\boldsymbol{v}_s$ can be calculated from the ratio of the spin current (projected onto the local direction of the magnetization) and the amplitude of the local magnetization, provided the magnetic structure is smooth and has a constant amplitude M, *i.e.*, $\boldsymbol{v}_s \approx \boldsymbol{j}_s/M$. In good metals like, for example, MnSi, $\boldsymbol{v}_s$ is expected to be parallel to the applied electric current, $\boldsymbol{v}_s \sim \boldsymbol{j}P/(Me)$, where P is the local spin polarization and e the electron charge. Furthermore, it is expected to depend only weakly on the applied magnetic field and on temperature. Note that in the following we will consider only effects that are linear in $\boldsymbol{v}_s$, as we assume that $\boldsymbol{v}_s$ is small compared to all characteristic velocity scales of the skyrmion lattice (*e.g.*, $T_c - T$ multiplied by the skyrmion distance).

The first term on the left hand side of Eq. (8.1) describes the Berry phase physics (see Appendix B), and the part proportional to $\boldsymbol{v}_s$ is called reactive or adiabatic spin-transfer torque.

The first term on the right hand side describes the precession of the magnetization in the effective magnetic field $\boldsymbol{H}_{\text{eff}} \equiv -\frac{\delta F}{\delta \boldsymbol{M}} \approx -\frac{1}{M}\frac{\delta F}{\delta \hat{\boldsymbol{\Omega}}}$. As mentioned, Eq. (8.1) is an equation for a magnetization structure with a constant amplitude. Here, we make use of the fact that in the skyrmion lattice phase the amplitude of the magnetization varies only slightly [1]. In such a case, one still has to define how $\boldsymbol{H}_{\text{eff}}$ is obtained from the Ginzburg-Landau free energy functional $F[\boldsymbol{M}]$ depending on $\boldsymbol{M}$. Within our numerical calculations we use the approximation $\boldsymbol{H}_{\text{eff}} \approx -\frac{1}{M}\frac{\delta F}{\delta \boldsymbol{M}}\frac{\partial \boldsymbol{M}}{\partial \hat{\boldsymbol{\Omega}}}$, with the average local equilibrium magnetization $M^2 = \langle \boldsymbol{M}^2 \rangle$. Other implementations of $\boldsymbol{H}_{\text{eff}}$ will influence our results only slightly. The effective magnetic field accounts for the applied external magnetic field as well as additional contributions due to magnetostatic interactions and anisotropies.

---

[1]Note that the spin current is a tensor, where j_s^{ji} describes the current of the spin component j flowing in the direction i. Here, to describe spin torques, we have to consider the projection of j_s^{ji} onto the local direction of the magnetization, $j_s^i = \hat{\boldsymbol{\Omega}}_j j_s^{ji}$.
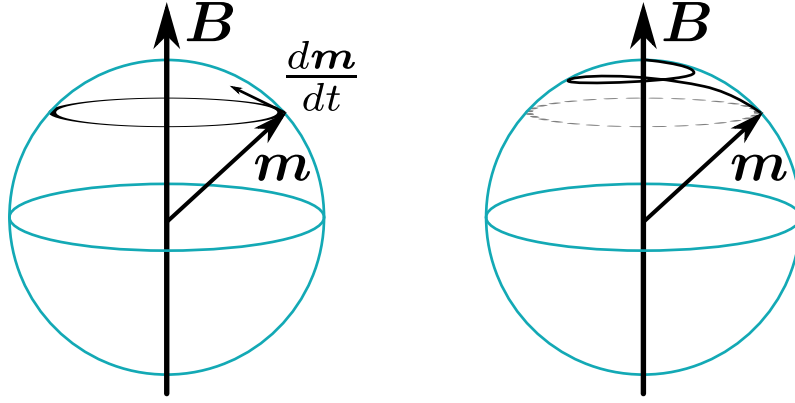
Figure 8.1: Left (right) panel: Sketch of the behavior of a single magnetic moment in a magnetic field B without (with) damping.

The last term in Eq. (8.1) describes dissipation [124]. The term proportional to $\alpha > 0$ is called Gilbert damping, and the one proportional to $\beta > 0$ parametrizes the dissipative spin-transfer torque. To show that the last term is really a damping term for $\alpha > 0$, let us consider the change of the free energy for $\boldsymbol{v}_s = 0$:

$$\partial_t F = \frac{\delta F}{\delta \hat{\boldsymbol{\Omega}}}\, \partial_t \hat{\boldsymbol{\Omega}} = -\alpha M (\partial_t \hat{\boldsymbol{\Omega}})^2 < 0. \tag{8.3}$$

Here, for the last equality we solved Eq. (8.1) for $\delta F/\delta \hat{\boldsymbol{\Omega}}$ and inserted the result. The Gilbert damping term controls the rate at which the magnetization structure equilibrates. Both phenomenological parameters α and β are dimensionless. In general, they are not equal as indicated by experiments and microscopic theories [127], but of the same order. Furthermore, α and β depend on the concrete material, and also vary in temperature. Their typical magnitude [128] ranges from 10^{-3} to 10^{-1}.

8.1   Motivation of the Landau-Lifshitz-Gilbert Equation

The LLG equation is often derived phenomenologically. The parameters $\boldsymbol{H}_{\text{eff}}$, α, β, and $\boldsymbol{v}_s$ have to be either measured or determined from a microscopic theory. Here, we only motivate the different terms in the LLG equation phenomenologically, while derivations are considered in Appendix B.

The LLG equation models the evolution of the orientation $\hat{\boldsymbol{\Omega}}(\boldsymbol{r}, t)$ of a magnetic texture in the presence of spin-transfer torques due to electric currents. To motivate it, let us consider the basic ingredient, namely a single normalized magnetic moment $\boldsymbol{m}$ ($|\boldsymbol{m}| = 1$) in a magnetic field $\boldsymbol{B}$ (as in Ref. [129]). Ignoring damping effects, the magnetic moment precesses around the axis defined by the direction of the magnetic field, as shown in the left panel of Fig. 8.1. For this scenario, the equation of motion is given by

$$\frac{d\boldsymbol{m}}{dt} = -\boldsymbol{m} \times \boldsymbol{B}. \tag{8.4}$$

This pure precession does not describe the equilibrium situation with the lowest energy, which corresponds to an alignment of the magnetic moment $\boldsymbol{m}$ to the external magnetic field. Therefore, a damping term is needed which represents the rate at which the magnetization relaxes to equilibrium, as shown in the right panel of Fig. 8.1. This damping

torque should be orthogonal to $\boldsymbol{m}$, because the length of the magnetic moment is constant, and it shall also be orthogonal to $\frac{d\boldsymbol{m}}{dt}$. Since $\boldsymbol{m} \perp \frac{d\boldsymbol{m}}{dt}$, the damping term is well-defined by a constant, the Gilbert damping parameter $\alpha > 0$, times the cross product between these two vectors, such that the equation of motion taking damping into account is given by

$$\frac{d\boldsymbol{m}}{dt} = -\boldsymbol{m} \times \boldsymbol{B} + \alpha\,\boldsymbol{m} \times \frac{d\boldsymbol{m}}{dt}. \tag{8.5}$$

This covers basically all terms for $\boldsymbol{v}_s = 0$ of Eq. (8.1), where the single magnetic moment $\boldsymbol{m}$ has to be replaced by the magnetization direction $\hat{\boldsymbol{\Omega}}$ and the magnetic field $\boldsymbol{B}$ by the effective magnetic field $\boldsymbol{H}_{\text{eff}}$ including not only the external applied magnetic field, but also additional contributions due to magnetostatic interactions and anisotropies.

To motivate the term on the left hand side of Eq. (8.1) including $\boldsymbol{v}_s$, let us consider the following intuitive picture [126]. When traversing the smoothly varying magnetic texture, the spin of the conduction electrons adjusts adiabatically to the local magnetization direction. This means that when the magnetization direction changes from $\hat{\boldsymbol{\Omega}}(\boldsymbol{r}, t)$ to $\hat{\boldsymbol{\Omega}}(\boldsymbol{r} + d\boldsymbol{r}, t)$, the magnetic moment of the conduction electron rotates, experiencing a torque from the magnetization. As spin is almost conserved, there is an opposite torque on the local magnetization, the reactive or adiabatic spin-transfer torque, which leads to a net displacement or motion of the magnetic structure in the same direction as the current [5, 6, 95, 130, 131]. Hence, the change of the magnetic texture in time is directly related to the motion of the spin-polarized electrons via

$$\left.\frac{\partial\hat{\boldsymbol{\Omega}}(\boldsymbol{r}, t)}{\partial t}\right|_{\text{current}} \propto \boldsymbol{v}_s \cdot \left(\hat{\boldsymbol{\Omega}}(\boldsymbol{r} + d\boldsymbol{r}, t) - \hat{\boldsymbol{\Omega}}(\boldsymbol{r}, t)\right) \propto (\boldsymbol{v}_s \cdot \nabla)\hat{\boldsymbol{\Omega}}(\boldsymbol{r}, t). \tag{8.6}$$

Thus, the current-induced drift of the magnetic structure can be described by substituting $\frac{\partial}{\partial t}$ by $\frac{\partial}{\partial t} + (\boldsymbol{v}_s \cdot \nabla)$ [132]. To explain some discrepancies with experiments, the dissipative or non-adiabatic spin-transfer torque was added to the Landau-Lifshitz-Gilbert equation [124, 127, 133, 134]:

$$\beta\,\hat{\boldsymbol{\Omega}}(\boldsymbol{r}, t) \times (\boldsymbol{v}_s \cdot \nabla)\,\hat{\boldsymbol{\Omega}}(\boldsymbol{r}, t). \tag{8.7}$$

It describes to which degree the spin conserservation is violated in the spin-transfer process. Physically, it is based on electron-spin relaxation and spin-flip scattering events [132]. Note that the above substitution also produces the same term if $\beta = \alpha$ which is the Galilean invariant case.

8.2 Modifications of the Standard Landau-Lifshitz-Gilbert Equation

The LLG equation is widely and successfully used in the spintronics community to model magnetization dynamics, despite the fact that it covers the coupling to the conduction electrons only indirectly via $\boldsymbol{v}_s$. We also use it to describe the dynamics of the magnetization direction of the skyrmion lattice subjected to an electric current, as the magnetic structure is very smooth in the skyrmion lattice phase and its amplitude varies only slightly, as discussed in Chapter 5. Furthermore, the applied current densities of $j \sim 10^6$ A/m^2 and the associated spin current density $j_s \approx jP/e$ are tiny compared to $j_0 = k_B T_c/(\hbar a^2)$. Since $j_s/j_0 \sim 10^{-8}$, it is too small to affect the amplitude of the magnetization, so that we can use the LLG equation as a good approximation to describe the dynamics of the skyrmion lattice. Actually, for most systems it is also too small to overcome spin-orbit coupling

effects which orient the direction of the magnetization. However, as mentioned in Chapter 6, skyrmion structures couple much more efficiently to electric currents. Therefore also such ultra-low currents are able to induce observable spin-transfer torque effects.

Moreover, Eq. (8.1) neglects the effect of thermal fluctuations. Taking them into account can, for example, be achieved by adding stochastic contributions $\boldsymbol{h}$ to the effective magnetic field [126], *i.e.* $\boldsymbol{H}_{\text{eff}} \to \boldsymbol{H}_{\text{eff}} + \boldsymbol{h}$, where $\boldsymbol{h}$ has, *e.g.*, white-noise correlations, *i.e.* $\langle h_i(\boldsymbol{r}, t) h_j(\boldsymbol{r}', t') \rangle \sim \delta_{ij}\,\delta(\boldsymbol{r} - \boldsymbol{r}')\delta(t - t')$ and $\langle h_i(\boldsymbol{r}, t) \rangle = 0$. Since in the following we do not discuss the competition of the conical and the skyrmion phase, we neglect the rather subtle effects of thermal fluctuations as well the corrections to Eq. (8.1) arising from fluctuations. We expect that fluctuation corrections are small and will only slightly influence our results. They might, however, be important for a full account of the depinning transition of the skyrmion lattice which is not fully described by our theory presented in the next Chapters. Furthermore, Eq. (8.1) does also not include the effects of disorder which, for example, lead to pinning effects. One way to account for disorder is to include a disorder potential $V_{\text{dis}}(\boldsymbol{r})$ in the free energy functional. In the following Chapters, we account in our theory for the effects of pinning by including phenomenological pinning terms.

Quite recently, a novel damping term relevant for non-collinear spin textures has been introduced [8, 9]:

$$-\alpha' \Big[\hat{\boldsymbol{\Omega}} \cdot \big(\partial_i \hat{\boldsymbol{\Omega}} \times \partial_t \hat{\boldsymbol{\Omega}} \big) \Big] \partial_i \hat{\boldsymbol{\Omega}}. \tag{8.8}$$

As all other terms of Eq. (8.1), it is perpendicular to $\hat{\boldsymbol{\Omega}}$ since $\hat{\boldsymbol{\Omega}} \cdot \partial_i \hat{\boldsymbol{\Omega}} = 0$. It contains two more derivatives compared to the Gilbert damping term, where each derivative contributes a factor of λ_{so} with λ_{so} being the strength of spin-orbit coupling. Naively, one would expect that for smooth magnetic textures this term is much smaller compared to the Gilbert term proportional to α due to the two more derivatives, and therefore negligible.

Nonetheless, assuming that the α term arises only from spin-orbit coupling, $\alpha \propto \lambda_{\text{so}}^2$, this new damping term is of the same order in spin-orbit coupling, λ_{so} due to the following reason. The α' term originates from Ohmic damping of electrons coupled by Berry phases to the magnetic structure, as can be seen by rewriting it in the form $-\alpha'(\boldsymbol{E}^e \cdot \nabla)\hat{\boldsymbol{\Omega}}$, where $\boldsymbol{E}_i^e = \hat{\boldsymbol{\Omega}} \cdot (\partial_i \hat{\boldsymbol{\Omega}} \times \partial_t \hat{\boldsymbol{\Omega}})$ is the emergent electric field as introduced in Chapter 7. Hence $\alpha' \propto \lambda_{\text{so}}^0$ since Ohmic damping does not require spin-orbit effects. Therefore, the two more derivatives of the novel damping term compared to the Gilbert damping term are compensated by the spin-orbit coupling strength of the corresponding prefactors. Note that due to the two more derivatives, the prefactor α' is, in contrast to the Gilbert damping constant α, not dimensionless. Furthermore, α' is proportional to a conductivity (see below) and therefore to the scattering time [8, 9], whereas α is proportional to the scattering rate. Thus, the novel damping term might actually be the dominating one in good metals, and therefore we take it into account in the following.

According to the intuitive argument that all forces have to cancel in a Galilean invariant system, where the magnetic structure is co-moving with the conduction electrons, we also add the corresponding drift term with a prefactor β',

$$-\beta' \Big[\hat{\boldsymbol{\Omega}} \cdot \big(\partial_i \hat{\boldsymbol{\Omega}} \times (\boldsymbol{v}_s \cdot \nabla)\hat{\boldsymbol{\Omega}} \big) \Big] \partial_i \hat{\boldsymbol{\Omega}}. \tag{8.9}$$

For Galilean invariant systems one has $\beta' = \alpha'$. Since, however, solids are usually not Galilean invariant, we therefore expect that β' is, in general, not identical to α', but of the same order. Finally, note the β' term can also be expressed in terms of the emergent fields, see Eq. (8.12) below.

To summarize, we obtain the following extended Landau-Lifshitz-Gilbert equation:

$$(\partial_t + \boldsymbol{v}_s \cdot \nabla)\,\hat{\boldsymbol{\Omega}} = -\hat{\boldsymbol{\Omega}} \times \boldsymbol{H}_{\text{eff}} + \alpha\,\hat{\boldsymbol{\Omega}} \times \left(\partial_t + \frac{\beta}{\alpha}\boldsymbol{v}_s \cdot \nabla\right)\hat{\boldsymbol{\Omega}}$$
$$- \alpha'\Big[\hat{\boldsymbol{\Omega}} \cdot \big(\partial_i\hat{\boldsymbol{\Omega}} \times (\partial_t + \frac{\beta'}{\alpha'}\boldsymbol{v}_s \cdot \nabla)\hat{\boldsymbol{\Omega}}\big)\Big]\partial_i\hat{\boldsymbol{\Omega}}. \quad (8.10)$$

By taking the cross product with $\hat{\boldsymbol{\Omega}}$, Eq. (8.10) can be equivalently written as

$$-\frac{1}{M}\frac{\delta F}{\delta\hat{\boldsymbol{\Omega}}} = \hat{\boldsymbol{\Omega}} \times (\partial_t + \boldsymbol{v}_s \cdot \nabla)\,\hat{\boldsymbol{\Omega}} + \alpha\Big(\partial_t + \frac{\beta}{\alpha}\boldsymbol{v}_s \cdot \nabla\Big)\hat{\boldsymbol{\Omega}}$$
$$+ \hat{\boldsymbol{\Omega}} \times \alpha'\Big[\hat{\boldsymbol{\Omega}} \cdot \big(\partial_i\hat{\boldsymbol{\Omega}} \times (\partial_t + \frac{\beta'}{\alpha'}\boldsymbol{v}_s \cdot \nabla)\hat{\boldsymbol{\Omega}}\big)\Big]\partial_i\hat{\boldsymbol{\Omega}} \quad (8.11)$$

We further multiply Eq. (8.11) by M to obtain

$$-\frac{\delta F}{\delta\hat{\boldsymbol{\Omega}}} = M\hat{\boldsymbol{\Omega}} \times (\partial_t + \boldsymbol{v}_s \cdot \nabla)\,\hat{\boldsymbol{\Omega}} + \alpha M\Big(\partial_t + \frac{\beta}{\alpha}\boldsymbol{v}_s \cdot \nabla\Big)\hat{\boldsymbol{\Omega}} + M\hat{\boldsymbol{\Omega}} \times \alpha'\Big[\boldsymbol{E}_i^e + \frac{\beta'}{\alpha'}(\boldsymbol{v}_s \times \boldsymbol{B}^e)_i\Big]\partial_i\hat{\boldsymbol{\Omega}}$$
$$(8.12)$$

where $\boldsymbol{E}_i^e = \hat{\boldsymbol{\Omega}} \cdot (\partial_i\hat{\boldsymbol{\Omega}} \times \partial_t\hat{\boldsymbol{\Omega}})$ is the emergent electric field and $\boldsymbol{B}_i^e = \frac{1}{2}\epsilon_{ijk}\hat{\boldsymbol{\Omega}} \cdot (\partial_j\hat{\boldsymbol{\Omega}} \times \partial_k\hat{\boldsymbol{\Omega}})$ the emergent magnetic field as introduced in Chapter 7. When considering the change of the free energy in time for $\boldsymbol{v}_s = 0$ we obtain

$$\partial_t F = \frac{\delta F}{\delta\hat{\boldsymbol{\Omega}}}\,\partial_t\hat{\boldsymbol{\Omega}} = -\alpha M(\partial_t\hat{\boldsymbol{\Omega}})^2 - \alpha'M(\boldsymbol{E}^e)^2 < 0. \quad (8.13)$$

This shows that the novel term is really a damping term, and that it leads to a dissipated power of $\propto (\boldsymbol{E}^e)^2$ arising from the emergent electric field $\boldsymbol{E}^e$. Interpreting this result, $\alpha'M$ approximately corresponds to the spin-conductivity σ_s.

Eq. (8.12) is our starting point for the next Chapters to describe the dynamics of the magnetic structure in the skyrmion lattice phase.

9 Current-Induced Forces Acting on the Skyrmion Lattice and Calculation of the Drift Velocity

In Chapter 7 we have seen that forces act on conduction electrons when traversing the skyrmion structures. According to Newton's third law, if the magnetic structure exerts forces on the electrons the electrons react by exerting forces on the magnetic structure. We have also seen in Section 7.3 that above a critical threshold current density the skyrmion lattice starts to drift. We have predicted this motion of the skyrmion lattice [10, 70, 129] before its experimental verification via the measurements of the emergent electric field [80]. In this Chapter, we derive an equation for the different forces acting on the skyrmion lattice, and study the drift velocity by using the Thiele method. Before that we will consider qualitatively the types of current-induced forces acting on the skyrmion lattice. We have published several parts of this Chapter in Refs. [10, 70, 71, 80].

9.1   Qualitative Discussion of Current-Induced Forces on Skyrmions

Basically, two types of current-induced forces act on the skyrmion lattice. On one side, there are dissipative forces [124] that try to drag the (non-moving) skyrmion lattice parallel to the spin-current, similar to the case of the current-induced domain wall motion. We refer to the other type of forces as Magnus forces. They are the counter forces of the effective Lorentz forces acting on the electrons originating from the accumulated Berry phases due to traversing the skyrmions. They act (for a non-moving skyrmion lattice) in the direction perpendicular to the applied current and perpendicular to the magnetic field. The reason, why these forces are called Magnus forces, can be very well understood by a direct comparison to the physics of a spinning ball in viscous air which, for example, leads to the curved motion of the match-ball in sports like "banana kicks" in soccer.

Both the drag and the Magnus forces together with the analogy to the physics of the spinning ball are illustrated in Fig. 9.1. Let us consider first the left panel. In a banana kick, the soccer ball does not just fly straight through the air, but it also rotates around its own axis. The Magnus effect has been studied intensively, and a lot of explanations more or less profound can be found. Since we are using it here just for the analogy of the Magnus force acting on the skyrmions, we will reduce our description of this effect to a basic level which is appropriate for the analogy. In the rest frame of the ball, it rotates around its own axis, and the air flow has to pass around the ball. For a non-rotating ball, the air would pass the ball on both sides equally fast, and the forces acting on the ball in perpendicular direction cancel exactly. However, for the spinning ball the air gets accelerated on one side (the left side of the ball in Fig. 9.1) and decelerated on the other
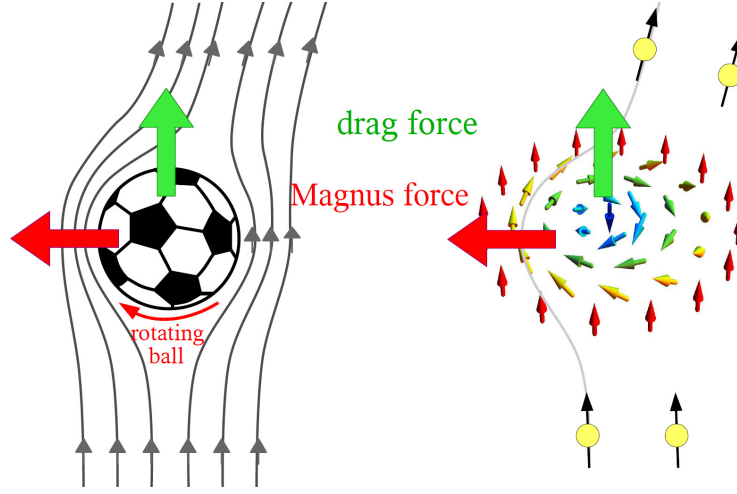
Figure 9.1: Illustration of the current-induced forces acting on a skyrmion (right panel) in comparison with the forces acting on a spinning ball in viscous air (left panel).

(the right side of the ball) due to the rotation of the ball. In total, the air does not pass the ball straight, but gets deflected (to the right in the figure), implying that a force acts on the air. According to Newton's third law, the ball experiences a force in the opposite direction (to the left in Fig. 9.1) which is the so-called Magnus force.

In the analogy, the air corresponds to the external spin current and the spinning ball to the skyrmion, as can be seen explicitly by comparing the left and right panel of Fig. 9.1. Moreover, we may consider the skyrmion lattice from an alternative point of view, namely as an array of circulating dissipationless spin currents, since skyrmions are characterized by gradients in their spin-orientation [10]. When an external spin current (by applying an electric current through a magnetic metal) passes a skyrmion, its velocity is enhanced on one side of the skyrmion and reduced on the other side. This leads to a deflection of the spin current (to the right in Fig. 9.1) in analogy to the physics of the spinning ball. As a reaction a force in perpendicular direction acts on the skyrmions. In analogy, we refer to this force also as Magnus force. This intuitive picture is, however, not complete in the sense that the spin is not a conserved quantity, and as mentioned already above, there are further dissipative forces acting on the skyrmions [124] which drag the skyrmions parallel to the current.

Furthermore the magnetic structure is pinned by impurities and the underlying atomic lattice, leading to forces counteracting the current-induced ones. Nevertheless, when the current-induced forces overcome a critical strength set by the strength of pinning, they induce a translational motion of the skyrmion lattice. Note that also below the critical current there might be small creep (which is not included in our theory), *i.e.* a tiny motion due to thermal (or quantum) fluctuations, which occurs even in the pinning regime [83].

9.2   Theory for the Translational Motion

To describe the dynamics of the orientation $\hat{\boldsymbol{\Omega}}(\boldsymbol{r}, t) = \boldsymbol{M}(\boldsymbol{r}, t)/|\boldsymbol{M}(\boldsymbol{r}, t)|$ of the magnetization $\boldsymbol{M}(\boldsymbol{r}, t)$ in presence of spin-transfer torques due to electric currents we start with

Eq. (8.12), introduced in Chapter 8:

$$-\frac{\delta F}{\delta \hat{\boldsymbol{\Omega}}} = M\hat{\boldsymbol{\Omega}} \times (\partial_t + \boldsymbol{v}_s \cdot \nabla) \hat{\boldsymbol{\Omega}} + \alpha M \left(\partial_t + \frac{\beta}{\alpha} \boldsymbol{v}_s \cdot \nabla\right) \hat{\boldsymbol{\Omega}} + M\hat{\boldsymbol{\Omega}} \times \alpha' \left[\boldsymbol{E}_i^e + \frac{\beta'}{\alpha'} (\boldsymbol{v}_s \times \boldsymbol{B}^e)_i\right] \partial_i \hat{\boldsymbol{\Omega}}$$
$$(9.1)$$

with the emergent electric field $\boldsymbol{E}_i^e = \hat{\boldsymbol{\Omega}} \cdot (\partial_i \hat{\boldsymbol{\Omega}} \times \partial_t \hat{\boldsymbol{\Omega}})$ and the emergent magnetic field $\boldsymbol{B}_i^e = \frac{1}{2}\epsilon_{ijk}\hat{\boldsymbol{\Omega}} \cdot (\partial_j \hat{\boldsymbol{\Omega}} \times \partial_k \hat{\boldsymbol{\Omega}})$. The main effect of the applied current is that the skyrmion lattice starts to drift above a certain threshold current density determined by the strength of pinning of the magnetic structure by disorder. Therefore, we use the ansatz

$$\hat{\boldsymbol{\Omega}}(\boldsymbol{r}, t) = \hat{\boldsymbol{\Omega}}(\boldsymbol{r} - \boldsymbol{v}_d t), \tag{9.2}$$

which represents a magnetic structure that drifts with a constant velocity $\boldsymbol{v}_d$. We expect that below the threshold current density the drift velocity $\boldsymbol{v}_d$ remains zero, whereas above it is finite. In this case, a time derivative of $\hat{\boldsymbol{\Omega}}(\boldsymbol{r}, t)$ can be translated into a derivative in space by $\partial_t \hat{\boldsymbol{\Omega}} = -(\boldsymbol{v}_d \cdot \nabla)\hat{\boldsymbol{\Omega}}$.

9.2.1 Thiele Method for the Translational Mode

Assuming an ideal system without anisotropies, the perfect skyrmion lattice spontaneously breaks the translational invariance in the plane that is perpendicular to the applied magnetic field. In the case, where a magnetic structure spontaneously breaks translational invariance, A. A. Thiele [100] suggested in 1972 to project the LLG equation onto the corresponding translational modes. In the following, we apply this method to the skyrmion lattice. Technically, we multiply Eq. (9.1) by $\hat{\boldsymbol{G}}_{\text{trans}} \hat{\boldsymbol{\Omega}}$, where $\hat{\boldsymbol{G}}_{\text{trans}}$ is the generator of the translation mode, and integrate the system over a two-dimensional unit cell (UC) of the skyrmion crystal to obtain an effective equation of motion. From the obtained equation one may in principle determine the drift velocity [131] $\boldsymbol{v}_d$ of the skyrmion lattice induced by the spin-current. The i-th component of the generator $\hat{\boldsymbol{G}}_{\text{trans}}$ for the translational mode is given by

$$\hat{\boldsymbol{G}}_{\text{trans}}^i \hat{\boldsymbol{\Omega}} = \partial_i \hat{\boldsymbol{\Omega}}. \tag{9.3}$$

Applying the Thiele method in the stationary limit, where the magnetic structure drifts with the constant velocity $\boldsymbol{v}_d$, the right hand side of Eq. (9.1) reduces to the expression [70, 71, 100, 131]

$$\boldsymbol{G} \times (\boldsymbol{v}_s - \boldsymbol{v}_d) + \boldsymbol{\mathcal{D}}(\beta \boldsymbol{v}_s - \alpha \boldsymbol{v}_d) + \boldsymbol{\mathcal{D}}'(\beta' \boldsymbol{v}_s - \alpha' \boldsymbol{v}_d), \tag{9.4}$$

where $\boldsymbol{G}$, $\boldsymbol{\mathcal{D}}$ and $\boldsymbol{\mathcal{D}}'$ are given by[1]

$$\boldsymbol{G}_i = \epsilon_{ijk} \int_{UC} d^2r \, \frac{M}{2} \hat{\boldsymbol{\Omega}} \cdot (\partial_j \hat{\boldsymbol{\Omega}} \times \partial_k \hat{\boldsymbol{\Omega}}), \tag{9.5a}$$

$$\boldsymbol{\mathcal{D}}_{ij} = \int_{UC} d^2r \, M \partial_i \hat{\boldsymbol{\Omega}} \, \partial_j \hat{\boldsymbol{\Omega}}, \tag{9.5b}$$

$$\boldsymbol{\mathcal{D}}'_{ij} = \int_{UC} d^2r \, M \left[\hat{\boldsymbol{\Omega}} \cdot (\partial_l \hat{\boldsymbol{\Omega}} \times \partial_i \hat{\boldsymbol{\Omega}})\right] \left[\hat{\boldsymbol{\Omega}} \cdot (\partial_l \hat{\boldsymbol{\Omega}} \times \partial_j \hat{\boldsymbol{\Omega}})\right]. \tag{9.5c}$$

The first term of Eq. (9.4) describes the current-induced Magnus force acting on the skyrmions. Using the expression for the emergent magnetic field of Eq. (7.1), $\boldsymbol{G}$ can be rewritten as

$$\boldsymbol{G}_i = \int_{UC} d^2r \, M \boldsymbol{B}_i^e = \mathcal{G}\hat{\boldsymbol{B}}_i \quad \text{with} \quad \mathcal{G} = 4\pi MW \tag{9.6}$$

---

[1] Note that $\boldsymbol{G}$, $\boldsymbol{\mathcal{D}}$, and $\boldsymbol{\mathcal{D}}'$ are defined as in Ref. [71]. In our previous publication [70], we have defined $\boldsymbol{G}$ and $\boldsymbol{D}$ without the factor of M which is needed in Chapter 10 for the discussion of gradients.

In the last step of Eq. (9.6) we used that for an (almost) constant amplitude of the magnetization the emergent magnetic field integrated over a magnetic unit cell is given by 4π times the winding number W per magnetic unit cell, being $W = -1$ for the skyrmion lattice. Besides being topologically quantized, $\boldsymbol{G}$ points in the direction orthogonal to the two-dimensional skyrmion lattice which is, without distortions, given by $\hat{\boldsymbol{B}}$, as explained in Section 4.3. According to Thiele [100], $\boldsymbol{G}$ is denoted as the gyrocoupling vector, because it translates a spin current to a Magnus force in perpendicular direction. In contrast to traditional spintronic devices, where the gyrocoupling is very small as it is only finite in a nano-size volume, the gyrocoupling extends over macroscopic domains in the skyrmion crystal phase. As demonstrated by Eq. (9.6), the gyrocoupling vector is directly proportional to the integration volume.

The other two terms of Eq. (9.4) are dissipative forces. $\boldsymbol{D}$ is a dimensionless 3×3 matrix which Thiele [100] denoted as the "dissipative tensor", because it describes the effects of dissipative forces on the skyrmion lattice. It possesses a zero eigenvalue corresponding to the direction normal to the skyrmion lattice which is, without distortions of the skyrmion lattice, given by the direction of the magnetic field. The reason for this is that the magnetization direction $\hat{\boldsymbol{\Omega}}$ is translationally invariant in this orthogonal direction. Due to the sixfold symmetry of the skyrmion lattice the matrix $\boldsymbol{D}$ is diagonal within the plane of the skyrmion lattice to lowest order in spin-orbit coupling λ_{so}. It is approximately given by

$$\boldsymbol{D}_{ij} \approx \mathcal{D}\boldsymbol{P}_{ij}, \tag{9.7}$$

where $\boldsymbol{P}$ is the projector into the plane of the skyrmion lattice, $\boldsymbol{P}_{ij} = (\mathbb{1} - \hat{\boldsymbol{B}} \cdot \hat{\boldsymbol{B}}^T)_{ij}$, and

$$\mathcal{D} = \frac{1}{2} \int_{UC} d^2r\, M (\nabla\hat{\boldsymbol{\Omega}})^2. \tag{9.8}$$

The 3×3 tensor $\boldsymbol{D}'$ has the same symmetry properties as the dissipative tensor $\boldsymbol{D}$, *i.e.* it is (to lowest order in λ_{so}) diagonal within the plane of the skyrmion lattice, and it has a zero eigenvalue corresponding to the direction normal to the skyrmion lattice:

$$\boldsymbol{D}'_{ij} = \mathcal{D}'\boldsymbol{P}_{ij}, \tag{9.9}$$

where $\mathcal{D}'$ is proportional to the square of the skyrmion density:

$$\mathcal{D}' = \int_{UC} d^2r\, M (\boldsymbol{B}^e)^2. \tag{9.10}$$

However, in general, $\mathcal{D}'$ is not quantized unlike the gyrocoupling strength $\mathcal{G}$. To lowest order in the current $\boldsymbol{v}_s$, the quantities $\mathcal{G}$, $\mathcal{D}$ and $\mathcal{D}'$ can be evaluated using the equilibrium magnetization. By introducing the renormalized dimensionless damping parameters $\tilde{\alpha}$ and $\tilde{\beta}$ as

$$\tilde{\alpha} = \alpha + \alpha'\frac{\mathcal{D}'}{\mathcal{D}}, \tag{9.11}$$

$$\tilde{\beta} = \beta + \beta'\frac{\mathcal{D}'}{\mathcal{D}}, \tag{9.12}$$

we can rewrite the expression given in Eq. (9.4) as

$$\boldsymbol{G} \times (\boldsymbol{v}_s - \boldsymbol{v}_d) + \boldsymbol{D}(\tilde{\beta}\boldsymbol{v}_s - \tilde{\alpha}\boldsymbol{v}_d). \tag{9.13}$$
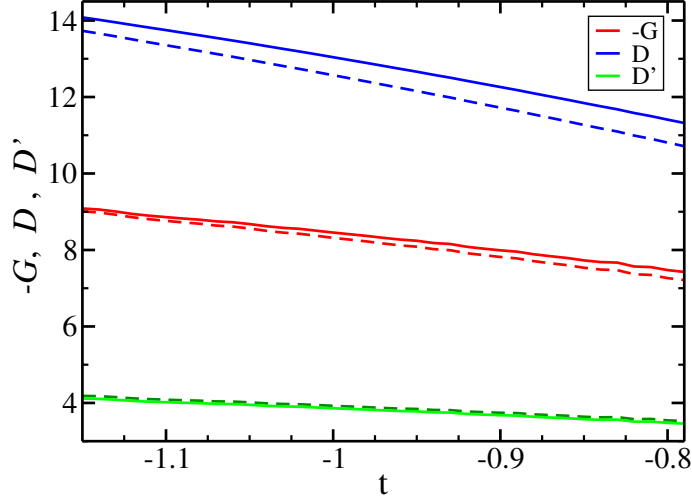
Figure 9.2: Change of the parameters $\mathcal{G}, \mathcal{D}$ and $\mathcal{D}'$ with temperature t in the skyrmion phase. The applied magnetic field is $h/\sqrt{2}\,(0,0,1)^T$. Dashed lines are for $h = 0.9$ and continuous lines for $h = 1.1$. We published this Figure in Ref. [71].

In Fig. 9.2 we show typical values for the parameters $\mathcal{G}, \mathcal{D}$ and $\mathcal{D}'$ in the skyrmion phase as a function of temperature t for two different strength of the applied magnetic field. Note, that $\mathcal{D}/|\mathcal{G}|$ is of the order of 1.

Applying the Thiele method for the translational mode to the left hand side of Eq. (9.1) leads to the expression

$$ -\int d^2r\,\left(\partial_i\hat{\boldsymbol{\Omega}}\right)\cdot\frac{\delta F}{\delta\hat{\boldsymbol{\Omega}}}, \tag{9.14} $$

which vanishes (to lowest order in spin-orbit coupling λ_{so}) for a perfect skyrmion lattice due to translational invariance. In the case of an underlying atomic structure with impurities, we also have to take into account pinning forces prohibiting the motion of the skyrmion lattice for small currents. Technically, they arise from spatial fluctuations of $\delta F/\delta\hat{\boldsymbol{\Omega}}$, and formally they are included in the expression of Eq. (9.14). While using the Thiele approach and explicitly assuming a rigid skyrmion lattice by using the ansatz of Eq. (9.2), it is not possible to deduce the pinning physics directly. The reason for this is, that random pinning forces cancel each other for a perfectly rigid magnetic structure such that no net pinning force remains for large domains. In principle, to properly describe the pinning physics, one has to allow the magnetic structure to adjust locally (and in a time-dependent way) to the pinning forces [81–83]. As this is a very complicated issue, we instead describe the pinning effects within the Thiele approach by extending the equation for the forces by a phenomenological pinning force $\boldsymbol{F}_{\mathrm{pin}}$, which for a finite drift velocity is given by

$$ \boldsymbol{F}_{\mathrm{pin}} = -4\pi M v_{\mathrm{pin}} f(v_d/v_{\mathrm{pin}})\,\hat{\boldsymbol{v}}_d. \tag{9.15} $$

It accounts for the fact that, for $j \gtrsim j_c$, inhomogeneities induce an effective velocity-dependent friction force on the moving skyrmion lattice. Note that due to the non-linear dependence of the pinning force on the drift velocity it cannot be described just by one of the usual damping terms that are used to characterize the dissipative dynamics of magnetic structures. $\boldsymbol{F}_{\mathrm{pin}}$ is oriented in the opposite direction of the drift velocity $\boldsymbol{v}_d$. Not very much is known about the dimensionless function $f(x)$ that describes the non-linear dependence of the pinning force on the drift velocity. Since the so-called pinning

velocity v_{pin} characterizes the strength of the pinning force, and by defining $4\pi M v_{\text{pin}}$ as the force per skyrmion and per length needed to depin the skyrmion lattice, one obtains $f(x \to 0) = 1$. For large drift velocities, pinning becomes less important [83, 135, 136]. Therefore, we expect that f scales as $f(x \gg 1) \sim x^{\nu}$ with an unknown exponent $\nu < 1$. In general, we expect an analog behavior of the pinning forces for the skyrmion lattice compared to those of the superconducting vortices [81, 82, 136]. Nevertheless, due to their different dynamics (as discussed in Chapter 11) they are not identical. Furthermore, f will most probably depend on, *e.g.*, various elastic constants of the skyrmion lattice, and therefore it will not be fully universal. Nevertheless, panel (c) of Fig. 7.8 showing $v_{d\|}/v_{\text{pin}}$ as a function of $j/j_c \approx v_s/v_{\text{pin}}$ indicates that the dimensionless function f does not depend very much on the distance to the transition temperature, in contrast to the pinning velocity v_{pin}.

As a result, by applying the Thiele method to Eq. (9.1) we obtain the equation for the forces (per skyrmion, per length, and per $\hbar$) acting on the skyrmion lattice:[2]

$$\boldsymbol{G} \times (\boldsymbol{v}_s - \boldsymbol{v}_d) + \boldsymbol{\mathcal{D}}(\tilde{\beta}\boldsymbol{v}_s - \tilde{\alpha}\boldsymbol{v}_d) + \boldsymbol{F}_{\text{pin}} = 0. \qquad (9.16)$$

In the case of small applied current densities, where the Magnus and disspative forces are still smaller than $4\pi M v_{\text{pin}}$, the skyrmion lattice stays pinned, *i.e.* the pinning forces cancel exactly the other forces, and the drift velocity $\boldsymbol{v}_d$ remains zero. For stronger forces the skyrmion lattice moves with a finite drift velocity $\boldsymbol{v}_d$.

9.2.2   Discussion of the Drift Velocity

In principle, Eq. (9.16) allows us to evaluate the drift velocity. However, as $\boldsymbol{F}_{\text{pin}}$ is not really known, this is not completely possible. Therefore, we mainly consider two limits below. First, we analyze the limit of large applied current densities, where the pinning forces can be neglected. In this limit, it is possible to analytically solve Eq. (9.16) for the drift velocity. In the second limit, we neglect the damping term, and try to identify the behavior of the pinning forces on the drift velocity exploiting the measurements of the drift velocity.

However, for a given behaviour of f we can solve Eq. (9.16) numerically for $\boldsymbol{v}_d$. In Fig. 9.3, we plot the parallel and the perpendicular components of the drift velocity for different damping strengths and different pinning strengths in the case of a constant dimensionless force f, $4\pi v_{\text{pin}} f = 1$ and $4\pi v_{\text{pin}} f = 2$, respectively. One clearly observes the onset of the drift velocity at a threshold current which is mainly determined by the strength of the pinning forces. Furthermore, one observes that close to the threshold non-linear effects in the damping constants play a crucial role. In the limit of small damping (discussed below), the drift velocity is mainly given by $\boldsymbol{v}_s$, as expected.

Neglecting pinning forces: In the limit of large current densities, *i.e.* $v_s \gg v_{\text{pin}}$, the pinning force $\boldsymbol{F}_{\text{pin}}$ is much smaller than the driving forces and therefore can be neglected. In this case, Eq. (9.16) reduces to

$$\boldsymbol{G} \times (\boldsymbol{v}_s - \boldsymbol{v}_d) + \boldsymbol{\mathcal{D}}(\tilde{\beta}\boldsymbol{v}_s - \tilde{\alpha}\boldsymbol{v}_d) = 0. \qquad (9.17)$$

In the Galilean invariant case, $\alpha = \beta$ and $\alpha' = \beta'$ or more generally $\tilde{\alpha} = \tilde{\beta}$, the magnetic structure would just drift with the current and $\boldsymbol{v}_d = \boldsymbol{v}_s$. However, generically the dissipa-

---

[2]Note that the relative sign of the pinning force is defined as in Ref. [71]. In our previous publication [80], the sign of $v_{\text{pin}} f(v_d/v_{\text{pin}})$ was different.
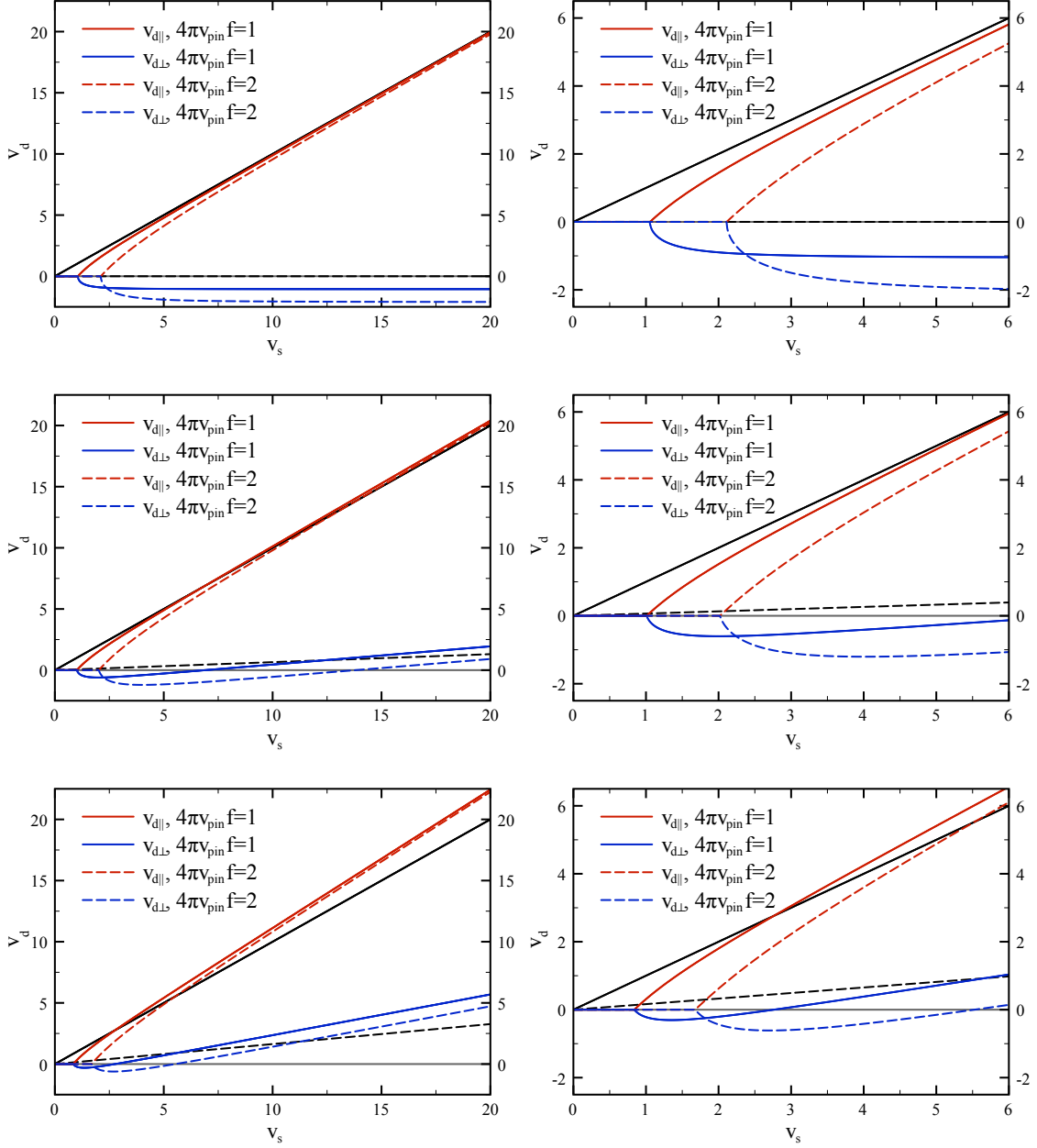
Figure 9.3: Drift velocity $\boldsymbol{v}_d$ as a function of v_s for $\boldsymbol{v}_s = v_s\,(1,0,0)^T$, $t = -1$, and $\boldsymbol{B} = \sqrt{-t/2}\,(0,0,1)^T$. Right panels show the detailed version of the corresponding left panels. The red (blue) curves show the parallel (perpendicular) component $v_{d\parallel}$ ($v_{d\perp}$) of the drift velocity $\boldsymbol{v}_d$ with respect to $\boldsymbol{v}_s$. The solid (dashed) lines are for $4\pi v_{\text{pin}}\,f = 1$ ($4\pi v_{\text{pin}}\,f = 2$). Furthermore, the black solid (dashed) curves show v_s ($\frac{\mathcal{D}}{\mathcal{G}}(\tilde{\alpha} - \tilde{\beta})\,v_s$) for comparison. From top to bottom the damping strength increases: top panel: $\tilde{\alpha}$, $\tilde{\beta} \to 0$; center panel: $\tilde{\alpha} = 0.1$, $\tilde{\beta} = 0.2$; bottom panel: $\tilde{\alpha} = 0.25$, $\tilde{\beta} = 0.5$.

tive forces break the Galilean invariance, *i.e.*, $\tilde{\alpha} \neq \tilde{\beta}$, and thus the drift velocity $\boldsymbol{v}_d$ is not equal to $\boldsymbol{v}_s$.

For most of the magnetic bulk structures the gyrocoupling vector $\boldsymbol{G}$ vanishes, and therefore the drift velocity is usually given by $\boldsymbol{v}_d = (\tilde{\beta}/\tilde{\alpha})\,\boldsymbol{v}_s$. For the skyrmion lattice as described above, the gyrocoupling vector is quantized due to the quantized winding number $W = -1$. We obtained $\boldsymbol{G} = \mathcal{G}\hat{\boldsymbol{B}}$ and $\boldsymbol{\mathcal{D}} = \mathcal{D}\boldsymbol{P}$ with a zero eigenvalue of $\boldsymbol{\mathcal{D}}$ associated to the direction of the magnetic field. To be concrete, we assume that the magnetic field is aligned along the z direction, *i.e.* $\hat{\boldsymbol{B}} = \hat{\boldsymbol{z}}$, so that we obtain

$$
\begin{aligned}
0 &= \mathcal{G}\hat{\boldsymbol{B}} \times (\boldsymbol{v}_s - \boldsymbol{v}_d) + \mathcal{D}\boldsymbol{P}(\tilde{\beta}\boldsymbol{v}_s - \tilde{\alpha}\boldsymbol{v}_d) \\
&= \mathcal{G}\begin{pmatrix} 0 & -1 & 0 \\ 1 & 0 & 0 \\ 0 & 0 & 0 \end{pmatrix}(\boldsymbol{v}_s - \boldsymbol{v}_d) + \mathcal{D}\begin{pmatrix} 1 & 0 & 0 \\ 0 & 1 & 0 \\ 0 & 0 & 0 \end{pmatrix}(\tilde{\beta}\boldsymbol{v}_s - \tilde{\alpha}\boldsymbol{v}_d).
\end{aligned}
\tag{9.18}
$$

The previous equation can be rewritten in the form of a 2×2 matrix equation, where only the in-plane drift velocity $\boldsymbol{v}_d^{\boldsymbol{P}} = \boldsymbol{P}\boldsymbol{v}_d$ and the in-plane spin-velocity $\boldsymbol{v}_s^{\boldsymbol{P}} = \boldsymbol{P}\boldsymbol{v}_s$ enter:

$$
\begin{pmatrix} \tilde{\alpha}\mathcal{D} & -\mathcal{G} \\ \mathcal{G} & \tilde{\alpha}\mathcal{D} \end{pmatrix}\boldsymbol{v}_d^{\boldsymbol{P}} = \begin{pmatrix} \tilde{\beta}\mathcal{D} & -\mathcal{G} \\ \mathcal{G} & \tilde{\beta}\mathcal{D} \end{pmatrix}\boldsymbol{v}_s^{\boldsymbol{P}}.
\tag{9.19}
$$

Note that in the 2×2 matrix equation $\boldsymbol{v}_d^{\boldsymbol{P}}$ and $\boldsymbol{v}_s^{\boldsymbol{P}}$ denote the reduced two-component vectors which include only the x and y components. In the performed experiments [1, 10], the electric current was applied in the direction perpendicular to the magnetic field. In the case of $\boldsymbol{v}_s \perp \boldsymbol{B}$ the in-plane spin-velocity $\boldsymbol{v}_s^{\boldsymbol{P}}$ is equal to $\boldsymbol{v}_s$. Since

$$
\det\begin{pmatrix} \tilde{\alpha}\mathcal{D} & -\mathcal{G} \\ \mathcal{G} & \tilde{\alpha}\mathcal{D} \end{pmatrix} = \alpha^2\mathcal{D}^2 + \mathcal{G}^2 \neq 0,
\tag{9.20}
$$

it is always possible to invert the matrix on the left hand side of Eq. (9.19) and to find a solution for $\boldsymbol{v}_d^{\boldsymbol{P}}$. Solving Eq. (9.19) for the in-plane component of the drift velocity leads to

$$
\boldsymbol{v}_d^{\boldsymbol{P}} = \frac{\tilde{\beta}}{\tilde{\alpha}}\boldsymbol{v}_s^{\boldsymbol{P}} + \frac{\tilde{\alpha} - \tilde{\beta}}{\tilde{\alpha}^3(\mathcal{D}/\mathcal{G})^2 + \tilde{\alpha}}\left(\boldsymbol{v}_s^{\boldsymbol{P}} + \tilde{\alpha}\frac{\mathcal{D}}{\mathcal{G}}\hat{\boldsymbol{B}} \times \boldsymbol{v}_s^{\boldsymbol{P}}\right).
\tag{9.21}
$$

In the following we assume, that $\boldsymbol{v}_s$ is applied in one of the inplane directions of the skyrmion lattice and therefore we omit the index $\boldsymbol{P}$

$$
\boldsymbol{v}_d = \frac{\tilde{\beta}}{\tilde{\alpha}}\boldsymbol{v}_s + \frac{\tilde{\alpha} - \tilde{\beta}}{\tilde{\alpha}^3(\mathcal{D}/\mathcal{G})^2 + \tilde{\alpha}}\left(\boldsymbol{v}_s + \tilde{\alpha}\frac{\mathcal{D}}{\mathcal{G}}\hat{\boldsymbol{B}} \times \boldsymbol{v}_s\right).
\tag{9.22}
$$

Note that when considering distortions of the skyrmion lattice, which lead to a tilt of the skyrmion plane with respect to the applied magnetic field, one has to replace $\hat{\boldsymbol{B}}$ by the normal vector $\hat{\boldsymbol{n}}$ of the skyrmion plane in the equation for the drift velocity $\boldsymbol{v}_d^{\boldsymbol{P}}$, Eq. (9.22).

In the limit of small damping parameters $\tilde{\alpha}, \tilde{\beta} \ll 1$, Eq. (9.22) simplifies to

$$
\boldsymbol{v}_d \approx \boldsymbol{v}_s + (\tilde{\alpha} - \tilde{\beta})\frac{\mathcal{D}}{\mathcal{G}}\hat{\boldsymbol{B}} \times \boldsymbol{v}_s.
\tag{9.23}
$$

From the obtained result we can infer that, as expected, the drift velocity $\boldsymbol{v}_d$ is approximately given by $\boldsymbol{v}_s$, *i.e.*, the skyrmions move *parallel* to the current in such a way that the Magnus force is canceled. The corrections to the drift velocity are of the order of $(\tilde{\beta} - \tilde{\alpha})D/|G|$.

Neglecting damping: For typical parameters in the skyrmion lattice in MnSi, $\mathcal{D}/|G|$ is of the order of 1, and the dissipative forces are probably suppressed by small damping parameters. Therefore, we consider the limit of vanishing dissipative forces in this paragraph. In this case, Eq. (9.16) reduces to

$$\boldsymbol{G} \times (\boldsymbol{v}_s - \boldsymbol{v}_d) + \boldsymbol{F}_{\mathrm{pin}} = 0. \tag{9.24}$$

For known pinning forces, *i.e.* known f, one can calculate from Eq. (9.24) the drift velocity in units of v_{pin}, $\boldsymbol{v}_d/v_{\mathrm{pin}}$. Conversely, it is in principle possible to obtain the dimensionless function f from a measurement of the drift velocity of the skyrmion lattice as a function of the applied current (like the one presented in Section 7.3). To see this, we project Eq. (9.24) on the directions perpendicular and parallel to the drift velocity $\boldsymbol{v}_d$. Moreover we make use of the theorem of Pythagoras, $v_d^2 = v_{d\parallel}^2 + v_{d\perp}^2$ and exploit Eq. (7.30). To summarize, we can calculate the strength v_d and the components of $\boldsymbol{v}_d$ parallel and perpendicular to $\boldsymbol{v}_s$, *i.e.* $v_{d\parallel}$ and $v_{d\perp}$. Thus, it is also possible to calculate the angle θ between $\boldsymbol{v}_d$ and $\boldsymbol{v}_s$. As a result, we obtain the following equations:

$$\frac{v_{d\parallel}}{v_{\mathrm{pin}}} \approx \frac{j}{j_c} \frac{\Delta\rho_{xy}}{\Delta\rho_{xy}^\infty}, \tag{9.25a}$$

$$\frac{v_d}{v_{\mathrm{pin}}} \approx \sqrt{\frac{v_{d\parallel} v_s}{v_{\mathrm{pin}}^2}} \approx \frac{j}{j_c} \sqrt{\frac{\Delta\rho_{xy}}{\Delta\rho_{xy}^\infty}}, \tag{9.25b}$$

$$\frac{v_{d\perp}}{v_{\mathrm{pin}}} \approx \frac{1}{v_{\mathrm{pin}}} \sqrt{v_{d\parallel}(v_s - v_{d\parallel})} \approx \frac{j}{j_c} \sqrt{\frac{\Delta\rho_{xy}}{\Delta\rho_{xy}^\infty}\left(1 - \frac{\Delta\rho_{xy}}{\Delta\rho_{xy}^\infty}\right)}, \tag{9.25c}$$

$$\theta = \arccos\frac{v_{d\parallel}}{v_d} \approx \arccos\sqrt{\frac{\Delta\rho_{xy}}{\Delta\rho_{xy}^\infty}}. \tag{9.25d}$$

The first equation, Eq. (9.25a), just repeats Eq. (7.30). It provides the means to detect the parallel component of the drift velocity (in units of v_{pin}) by a measurement of the Hall effect as a function of j/j_c. The other three equations are only valid when damping is negligible. In this case, one can also determine these quantities experimentally.

Moreover, we can calculate f under these assumptions. By multiplying Eq. (9.24) with $\hat{\boldsymbol{v}}_d/(4\pi M v_{\mathrm{pin}})$ we obtain

$$f \approx \frac{1}{v_{\mathrm{pin}}} \hat{\boldsymbol{v}}_d \cdot (\boldsymbol{v}_s \times \hat{\boldsymbol{B}}) = \frac{v_s}{v_d v_{\mathrm{pin}}} \boldsymbol{v}_d \cdot (\hat{\boldsymbol{v}}_s \times \hat{\boldsymbol{B}}) = \frac{v_s v_{d\perp}}{v_d v_{\mathrm{pin}}} \tag{9.26}$$

Using the results of Eqs. (9.25a) – (9.25d), we obtain

$$f \approx \frac{v_s v_{d\perp}}{v_d v_{\mathrm{pin}}} \approx \frac{v_s \sqrt{v_{d\parallel}(v_s - v_{d\parallel})}}{v_{\mathrm{pin}} \sqrt{v_{d\parallel} v_s}} \approx \frac{j}{j_c} \sqrt{1 - \frac{\Delta\rho_{xy}}{\Delta\rho_{xy}^\infty}}, \tag{9.27}$$

implying that also the dimensionless pinning force can, in principle, be obtained from a measurement of the Hall effect as a function of j/j_c. The corresponding plot is shown in Fig. 9.4. Unfortunately, the data is too noisy to get reasonable information about f or about the perpendicular component of the drift velocity $v_{d\perp}$. (For the latter the corresponding data are not shown.) However, what can be observed from Fig. 9.4 is that for current densities j below the threshold current density f increases with increasing j. In this case, the drift velocity is still zero within our experimental precision as the skyrmion
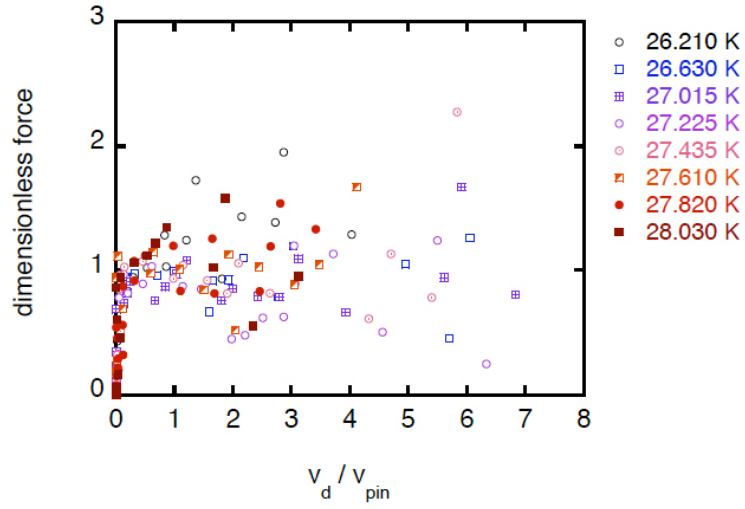
Figure 9.4: Dimensionless function f as a function of v_d/v_{pin} obtained by exploiting the experimental data from Ref. [80] and using the Eqs. (9.25b) and (9.27). This Figure is taken from our publication Ref. [80].

lattice is pinned by disorder. This leads to the vertical line on the left side of the plot, defined by $v_d = 0$ and $f < 1$. For $j > j_c$, the pinning forces are weaker than the driving forces, and the skyrmions start to move. However, for $v_d > 0$ it is not possible to obtain the behavior of f as a function of v_d/v_{pin} from the data.

10 Rotation of the Skyrmion Lattice

The first experiment that hinted at the very low threshold current density of $j_c \sim 10^6$ A/m^2 was a neutron scattering experiment, where a rotation of the scattering pattern by a finite angle was observed in the skyrmion lattice phase [10]. This motivated us to develop a theory for the rotation of the skyrmion lattice. Our first theory for the rotation angle almost agreed with the experimental observations, *except for an important sign* for certain experimental configurations. However, within our first theoretical approach the experimental result was forbidden by symmetry, and therefore this sign problem between theory and experiment led to the conclusion that there should be an additional effect present in the experiment. This turned out to be a temperature gradient which we then included in our theory.

In this Chapter, we describe different rotation mechanisms, and introduce the main method to describe rotations which is an extension of the Thiele method. Afterwards, in Section 10.2, we explain how it is possible to obtain a finite rotational torque using lattice distortions of the skyrmion lattice (even in the absence of thermal gradients). Most of this work we published in Ref. [70]. In Section 10.3, we review the experiment, and discuss a symmetry argument why there must be an additional ingredient, namely a temperature gradient, present in the experiment. We published the experimental part together with a theoretical explanation in Ref. [10]. Finally, in Section 10.4, we write down the theory for the skyrmion lattice to lowest order in spin-orbit coupling in the presence of a force gradient which can, for instance, experimentally be achieved by a temperature gradient or a magnetic field gradient. Most of this work can be found in Ref. [71].

10.1 Theory for the Rotational Mode and Discussion of Different Rotation Mechanisms

For a perfect skyrmion lattice with a sixfold rotation symmetry, a small uniform spin current cannot induce any rotational torques due to symmetry. Correspondingly, there are basically two possibilities for a rotation. Either the skyrmion lattice is not fully rotational symmetric, or the applied spin current is not uniform.

The first case occurs if, for example, the skyrmion lattice is distorted. This occurs, *e.g.*, due to the underlying atomic lattice, and distortions of the skyrmion lattice can be described within a Ginzburg-Landau theory by higher-order spin-orbit coupling terms, as discussed in Section 4.3. Also, disorder might cause distortions of the skyrmion lattice which can lead to a re-orientation of a sliding lattice based on the non-linear response of the moving skyrmion lattice. For sliding vortex lattices in superconductors, these mechanims have already been investigated [81, 137]. Moreover, in principle, also the current itself can distort the skyrmion lattice. By symmetry this effect does not occur to linear order in the current density, but only to third order. Finally, also the shape of the domain might lead

to rotational torques which, however, have a "random" sign and strength depending on the shape of the particular domain. Therefore, they can be easily distinguished from the other torques. In MnSi, they appear to be relatively small [1]. In the following, we will not consider torques due to different domain shapes, and we will restrict the discussion mainly to rotationally invariant domains. Furthermore, we will not study the interface dynamics of different domains, or what happens when a domain comes close to the surface of the sample. Compared to torques arising from the bulk, surface forces are usually suppressed by a factor of $1/\sqrt{A}$ with the domain size A, but the relevant prefactors are not easy to estimate. However, all of these effects have not yet been observed and are small compared to the second possible scenario, *i.e.* a non-uniform spin current. The latter leads to a gradient in the current-induced forces acting on the skyrmion lattice and therefore to torques. It can be achieved by various means. Experimentally, it is probably quite difficult to create a controlled non-uniform electric current across a sample, but as the strength of the spin current is related to the amplitude of the local magnetization, it suffices to create a gradient in the magnetization amplitude across the sample. This can, for instance, be achieved by applying a magnetic field gradient or, as has already been done experimentally, by a small temperature gradient across the sample [10].

To describe the rotation of the skyrmion lattice our starting point is again the Landau-Lifshitz-Gilbert equation (8.12) introduced in Chapter 8:

$$-\frac{\delta F}{\delta \hat{\boldsymbol{\Omega}}} = M\hat{\boldsymbol{\Omega}} \times (\partial_t + \boldsymbol{v}_s \cdot \nabla)\,\hat{\boldsymbol{\Omega}} + \alpha M\Big(\partial_t + \frac{\beta}{\alpha}\boldsymbol{v}_s \cdot \nabla\Big)\hat{\boldsymbol{\Omega}} + M\hat{\boldsymbol{\Omega}} \times \alpha'\Big[\boldsymbol{E}_i^e + \frac{\beta'}{\alpha'}\,(\boldsymbol{v}_s \times \boldsymbol{B}^e)_i\Big]\partial_i\hat{\boldsymbol{\Omega}}$$
(10.1)

with the emergent electric field $\boldsymbol{E}_i^e = \hat{\boldsymbol{\Omega}} \cdot (\partial_i\hat{\boldsymbol{\Omega}} \times \partial_t\hat{\boldsymbol{\Omega}})$ and the emergent magnetic field $\boldsymbol{B}_i^e = \frac{1}{2}\epsilon_{ijk}\hat{\boldsymbol{\Omega}} \cdot (\partial_j\hat{\boldsymbol{\Omega}} \times \partial_k\hat{\boldsymbol{\Omega}})$. As we would like to consider rotations, we make the following ansatz for the magnetization direction $\hat{\boldsymbol{\Omega}}(\boldsymbol{r}, t)$:

$$\hat{\boldsymbol{\Omega}}(\boldsymbol{r}, t) = \boldsymbol{R}_{\phi(t)} \cdot \hat{\boldsymbol{\Omega}}_0\Big(\boldsymbol{R}_{\phi(t)}^{-1} \cdot (\boldsymbol{r} - \boldsymbol{v}_d t)\Big),$$
(10.2)

where $\hat{\boldsymbol{\Omega}}_0(\boldsymbol{r})$ describes the static skyrmion lattice.[1] $\boldsymbol{R}_\phi$ denotes a rotation matrix which causes a rotation by the angle ϕ around the direction of the skyrmion lines, *i.e.* around the magnetic field direction when distortions are neglected. In this case, the time derivative $\partial_t\hat{\boldsymbol{\Omega}}$ can be related to $\partial_t\hat{\boldsymbol{\Omega}} = \partial_t\phi\,\partial_\phi\hat{\boldsymbol{\Omega}} - (\boldsymbol{v}_d \cdot \nabla)\hat{\boldsymbol{\Omega}}$. Eq. (10.2) describes a magnetic structure that rotates around its center, while the center located at $\boldsymbol{v}_d t$ is drifting with a constant velocity $\boldsymbol{v}_d$. Note that when the affecting torques are sufficiently large, we expect that not a rotation by a finite angle sets in, *i.e.* $\partial_t\phi = 0$ as experimentally observed so far [10], but instead a continuous rotation.

10.1.1   Extended Thiele Method for the Rotational Mode

Assuming an ideal system without anisotropies, the perfect skyrmion lattice with a sixfold rotation symmetry spontaneously breaks the rotational invariance within the plane of the skyrmion lattice. Therefore, to describe the rotational torques we project the LLG equation, Eq. (10.1), not onto the translational, but on the rotational mode, in analogy to the Thiele method [100], discussed in Section 9.2. Technically, we multiply Eq. (10.1) by $\hat{\boldsymbol{G}}_{\text{rot}}\,\hat{\boldsymbol{\Omega}}$, where $\hat{\boldsymbol{G}}_{\text{rot}}$ is the generator of the rotational mode, and integrate the system over a two-dimensional volume to obtain an effective equation of motion for the magnetization texture from which we can infer the torques acting on the skyrmion crystal. In the absence

---

[1]Note that within this ansatz one obtains the same solution for the drift velocity as in Chapter 9.

of gradients, we integrate over a two-dimensional unit cell (UC) of the skyrmion crystal as before in Section 9.2. In Section 10.4, where we consider gradients, we integrate over a whole domain with size A. From the resulting equation one may, in principle, determine the rotation angle or, in the case of a continuous rotation, the angular velocity of the skyrmion lattice.

The generator $\hat{\boldsymbol{G}}_{\text{rot}}$ for rotations of the magnetization around the axis defined by the normal vector $\hat{\boldsymbol{n}}$ is given by

$$\hat{\boldsymbol{G}}_{\text{rot}}\hat{\boldsymbol{\Omega}} = \partial_\phi\hat{\boldsymbol{\Omega}} = \hat{\boldsymbol{n}} \times \hat{\boldsymbol{\Omega}} - (\hat{\boldsymbol{n}}(\Delta\boldsymbol{r} \times \nabla))\hat{\boldsymbol{\Omega}} \tag{10.3}$$

with $\Delta\boldsymbol{r} = \boldsymbol{r} - \boldsymbol{v}_d t$, and $\hat{\boldsymbol{n}}$ is the normal vector of the skyrmion lattice plane defined by Eq. (4.28) of Section 4.3. When neglecting distortions $\hat{\boldsymbol{n}} = \hat{\boldsymbol{B}}$. Note that the second term is linear in $\Delta\boldsymbol{r}$. When multiplying it by a term of Eq. (10.1) that is also linear in $\Delta\boldsymbol{r}$, it becomes much larger than the first one. The generator of the rotation can be derived by calculating the derivative of $\hat{\boldsymbol{\Omega}}$ with respect to ϕ, given by Eq. (10.2). A similar way to calculate $\hat{\boldsymbol{G}}_{\text{rot}}$ is to expand the rotation matrix for small rotation angles $(\boldsymbol{R}_{\phi(t)})_{ij} = \delta_{ij} + \phi\epsilon_{ikj}\hat{\boldsymbol{n}}_k + \mathcal{O}(\phi^2)$ with the totally antisymmetric epsilon tensor ϵ_{ikj}, and then reading off the generator from the equation $\boldsymbol{R}_{\phi(t)} \cdot \hat{\boldsymbol{\Omega}}_0\big(\boldsymbol{R}_{\phi(t)}^{-1} \cdot (\Delta\boldsymbol{r})\big) - \hat{\boldsymbol{\Omega}}(\Delta\boldsymbol{r}) = \phi\,\hat{\boldsymbol{G}}_{\text{rot}}\hat{\boldsymbol{\Omega}} + \mathcal{O}(\phi^2)$.

Despite the technical analogy to the discussion of the translational mode, the rotational mode is different in several aspects. A very important point to mention is that in a real system like MnSi there is no full rotational symmetry around the axis defined by $\hat{\boldsymbol{n}}$. In particular, the presence of weak spin-orbit interactions breaks this rotational invariance, and therefore a rotational torque due to the current can be balanced by a counter-torque of the underlying atomic crystal lattice. Furthermore, when rotating a magnetic structure by a small angle, parts close to the rotation center just have to adopt slightly, whereas the parts of the magnetic structure further apart from the center have to change over much larger distances, being proportional the corresponding radius. This implies that for an infinitely large domain the time the skyrmion lattice needs to reorient is formally also infinitely long. In practice, domains have a finite size, and therefore it is possible for a small current to re-orient the skyrmion lattice.

The generalization of the Thiele method as a tool to describe the rotational motion is probably also useful for other problems, where rotations play a role like, for example, vortex oscillations in nanopillars [138, 139].

10.2   Rotational Torques due to Distortions of the Skyrmion Lattice

In this Section, we would like to investigate the mechanism how spin-transfer torques can lead to a spatial rotation of a slightly distorted magnetic skyrmion texture by a finite angle, *i.e.* $\partial_t\phi = 0$. In particular, we analyze the current-induced torques on the magnetic structure due to small distortions of the skyrmion lattice caused by the underlying atomic lattice. Such rotations without thermal gradients are not observed experimentally so far, but might be relevant for future experiments, where also different materials with a skyrmion phase will be studied.

Here, we explicitly take care of the distortion and orientation terms of the skyrmion lattice introduced in Section 4.3. Therefore, the normal vector of the skyrmion lattice $\hat{\boldsymbol{n}}$ does, in general, not coincide with the direction of the external magnetic field. When applying the extended Thiele method to Eq. (10.1), we obtain the effective equation for the rotational degree of freedom (neglecting torques due to pinning by disorder as, for

example, discussed in Ref. [81] for the case of a superconducting vortex lattice):[2]

$$\boldsymbol{P}_R\left(\boldsymbol{v}_s - \boldsymbol{v}_d\right) + \boldsymbol{P}_D\left(\beta\boldsymbol{v}_s - \alpha\boldsymbol{v}_d\right) + \boldsymbol{P}_{D'}\left(\beta'\boldsymbol{v}_s - \alpha'\boldsymbol{v}_d\right) + \mathcal{T}_L = 0 \qquad (10.4)$$

In the following, we define and discuss the first three terms and the last term of Eq. (10.4) separately. We start with a discussion of the first three terms of Eq. (10.4), which describe the rotational torques around the axis defined by the normal $\hat{\boldsymbol{n}}$ exerted by the current. Since we are considering only rotations around one axis, the reactive and dissipative rotational coupling terms, $\boldsymbol{P}_R$, $\boldsymbol{P}_D$, and $\boldsymbol{P}'_D$, respectively, reduce to vectors instead of matrices. They are given by[3]

$$\boldsymbol{P}^i_R = \int_{\mathrm{UC}} d^2r\, M\left(\hat{\boldsymbol{\Omega}} \times \partial_i\hat{\boldsymbol{\Omega}}\right) \cdot (\hat{\boldsymbol{G}}_{\mathrm{rot}}\hat{\boldsymbol{\Omega}}), \qquad (10.5\mathrm{a})$$

$$\boldsymbol{P}^i_D = \int_{\mathrm{UC}} d^2r\, M\partial_i\hat{\boldsymbol{\Omega}} \cdot (\hat{\boldsymbol{G}}_{\mathrm{rot}}\hat{\boldsymbol{\Omega}}), \qquad (10.5\mathrm{b})$$

$$\boldsymbol{P}^i_{D'} = \int_{\mathrm{UC}} d^2r\, M\left(\hat{\boldsymbol{\Omega}} \times \left[\hat{\boldsymbol{\Omega}} \cdot (\partial_j\hat{\boldsymbol{\Omega}} \times \partial_i\hat{\boldsymbol{\Omega}})\right]\partial_j\hat{\boldsymbol{\Omega}}\right) \cdot (\hat{\boldsymbol{G}}_{\mathrm{rot}}\hat{\boldsymbol{\Omega}}), \qquad (10.5\mathrm{c})$$

and can be traced back to the terms of the LLG equation describing the Berry phase physics and damping, respectively. The three rotational coupling vectors live in the plane of the skyrmion lattice, *i.e.* $\hat{\boldsymbol{n}} \cdot \boldsymbol{P}_R = \hat{\boldsymbol{n}} \cdot \boldsymbol{P}_D = \hat{\boldsymbol{n}} \cdot \boldsymbol{P}_{D'} = 0$, because the magnetization of the skyrmion lattice varies only within this plane. Therefore, only the components of the velocities $\boldsymbol{v}_d$ and $\boldsymbol{v}_s$, which are in the plane of the skyrmion lattice, enter Eq. (10.4).

Inserting the generator of the rotation mode, Eq. (10.3), into Eq. (10.4) leads to two terms for each rotational coupling vector which, for instance, for $\boldsymbol{P}_R$ are given by

$$\boldsymbol{P}^i_R = \int_{\mathrm{UC}} d^2r\, M\left(\hat{\boldsymbol{\Omega}} \times \partial_i\hat{\boldsymbol{\Omega}}\right) \cdot \left(\hat{\boldsymbol{n}} \times \hat{\boldsymbol{\Omega}}\right) - \int_{\mathrm{UC}} d^2r\, M\left(\hat{\boldsymbol{\Omega}} \times \partial_i\hat{\boldsymbol{\Omega}}\right) \cdot \left((\hat{\boldsymbol{n}} \cdot (\Delta\boldsymbol{r} \times \nabla))\hat{\boldsymbol{\Omega}}\right). \quad (10.6)$$

The second term is linear in $\Delta\boldsymbol{r}$. For a symmetrically shaped macroscopic domain we checked that terms linear in $\Delta\boldsymbol{r}$ vanish. However, as already mentioned above, further torques arise for non-symmetric domains. As discussed, they have a shape-dependent sign and strength, and thus we assume in the following that these contributions will average to zero. Therefore, we neglect all terms linear in $\Delta\boldsymbol{r}$ in the following, and the expressions for the rotational coupling vectors given in Eqs. (10.5a), (10.5b) and (10.5c) reduce to

$$\boldsymbol{P}^i_R \approx \int_{\mathrm{UC}} d^2r\, M\left(\hat{\boldsymbol{\Omega}} \times \partial_i\hat{\boldsymbol{\Omega}}\right) \cdot \left(\hat{\boldsymbol{n}} \times \hat{\boldsymbol{\Omega}}\right), \qquad (10.7\mathrm{a})$$

$$\boldsymbol{P}^i_D \approx \int_{\mathrm{UC}} d^2r\, M\partial_i\hat{\boldsymbol{\Omega}} \cdot \left(\hat{\boldsymbol{n}} \times \hat{\boldsymbol{\Omega}}\right), \qquad (10.7\mathrm{b})$$

$$\boldsymbol{P}^i_{D'} = \int_{\mathrm{UC}} d^2r\, M\left(\hat{\boldsymbol{\Omega}} \times \left[\hat{\boldsymbol{\Omega}} \cdot (\partial_j\hat{\boldsymbol{\Omega}} \times \partial_i\hat{\boldsymbol{\Omega}})\right]\partial_j\hat{\boldsymbol{\Omega}}\right) \cdot \left(\hat{\boldsymbol{n}} \times \hat{\boldsymbol{\Omega}}\right). \qquad (10.7\mathrm{c})$$

Note that the three rotational coupling vectors of Eqs. (10.7a), (10.7b), and (10.7c) are only finite (in linear order in $\boldsymbol{v}_s$) due to the small distortion of the skyrmion lattice by the weak

---

[2]Note that in our previous publication [70] the relative sign of the torque due to the lattice is defined differently which means that the rotation angle in Ref. [70] is defined with the opposite sign.

[3]Note that in our previous publication [70] we have defined the rotational coupling vectors without the factor of M which is needed in this Chapter for the discussion of gradients. In Ref. [70], the factor of M was included in the counter-torque $\mathcal{T}_L$. For a constant amplitude of the magnetization the factor of M drops out in the formulas for the rotatation angle. A small amplitude variation of the magnetization in the skyrmion lattice phase influences the numerical results only slightly.

coupling to the underlying atomic crystal lattice. For the undistorted skyrmion lattice, *i.e.* for the rotationally symmetric Ginzburg-Landau free energy functional of Eq. (4.9), they vanish in linear order in $\boldsymbol{v}_s$ due the sixfold rotational symmetry of the hexagonal magnetic lattice. Since the orientation of a hexagon is described by a third-rank tensor, a rotational torque arises only in the order of $\boldsymbol{v}_s^3$ which is too small to yield observable effects for relatively small current densities as used in bulk materials. We evaluate the three rotational coupling vectors of Eqs. (10.7a), (10.7b), and (10.7c) numerically, and details concerning the numerics can be found in Appendix C.

After having considered the rotational torques exerted by the current, let us now consider the last term of Eq. (10.4) describing the counter-torques from the atomic lattice. Those are independent of the applied current $\boldsymbol{v}_s$ and given by

$$\mathcal{T}_L = -\int_{\text{UC}} d^2r \, \frac{\delta F}{\delta \hat{\boldsymbol{\Omega}}} \cdot (\hat{\boldsymbol{G}}_{\text{rot}} \hat{\boldsymbol{\Omega}}) = -\int_{\text{UC}} d^2r \, \frac{\delta F}{\delta \hat{\boldsymbol{\Omega}}} \frac{\partial \hat{\boldsymbol{\Omega}}}{\partial \phi} = -\frac{\partial f}{\partial \phi}, \tag{10.8}$$

which describes the change of the free energy per magnetic unit cell upon a rotation of the magnetic structure by the angle ϕ, *i.e.* $f = F/(MN_{\text{UC}})$, where N_{UC} is the number of unit cells. As discussed in Section 4.3, the orientation of the skyrmion lattice within the plane perpendicular to the skyrmion lines has a sixfold symmetry in the absence of a current. Hence, the orientation of the skyrmion lattice is fixed by anisotropy terms that produce a potential being at least proportional to $-\cos(6\phi)$, where ϕ is the rotation angle, and $\phi = 0$ describes an equilibrium situation. Note that such anisotropy terms are a least of sixth order in spin-orbit coupling, λ_{so}^6. The torque per volume resulting from a potential proportional to $-\cos(6\phi)$ is given by

$$\mathcal{T}_L \approx \frac{\chi}{6} \, \partial_\phi \cos(6\phi) = -\chi \sin(6\phi). \tag{10.9}$$

The counter-torque from the atomic lattice $\mathcal{T}_L$ expresses that angular momentum can be transferred directly from the skyrmion lattice to the underlying atomic structure mediated by spin-orbit coupling and small anisotropy terms. For small rotation angles, the torque $\mathcal{T}_L$ can be further expanded as

$$\mathcal{T}_L \approx -\chi \sin(6\phi) \approx -\chi \, \delta\phi. \tag{10.10}$$

In the last approximation of Eq. (10.10), $\delta\phi$ describes small deviations from the preferred equilibrium orientation of the skyrmion lattice, where the restoring forces from the atomic lattice are finite. It is only valid in the linear response regime, where one can expand $\mathcal{T}_L$ in $\delta\phi$. Furthermore, we used that $\partial f/\partial \phi$ vanishes in the equilibrium situation, *i.e.* for $\boldsymbol{v}_s = 0$. We denote the susceptibility χ as the "spring constant":

$$\chi = \frac{\partial^2 f}{\partial \phi^2}. \tag{10.11}$$

Similar to the three rotational coupling vectors of Eqs. (10.7a), (10.7b), and (10.7c), these restoring forces characterized by χ arise from higher-order spin-orbit coupling terms.

Combining Eq. (10.4) with the linear response approximation of Eq. (10.10) we get:[4]

$$0 = \boldsymbol{P}_R \left(\boldsymbol{v}_s - \boldsymbol{v}_d\right) + \boldsymbol{P}_D \left(\beta\boldsymbol{v}_s - \alpha\boldsymbol{v}_d\right) + \boldsymbol{P}_{D'} \left(\beta'\boldsymbol{v}_s - \alpha'\boldsymbol{v}_d\right) - \chi\delta\phi. \tag{10.12}$$

---

[4]Note that in our previous publication [70] we have defined the rotation angle with the opposite sign.

Note that in this equation also only the in-plane components of the velocities $\boldsymbol{v}_s$ and $\boldsymbol{v}_d$ enter, *i.e.* $\boldsymbol{v}_s^P$ and $\boldsymbol{v}_d^P$, because the three rotational coupling vectors are orthogonal to the normal vector $\hat{\boldsymbol{n}}$. Interpreting Eq. (10.12) we see that the induced spatial rotation of the magnetic structure corresponds to a double-transfer of angular momentum. In a first process, the spins of the conduction electrons transfer angular momentum on the magnetic texture when traversing the magnetic structure. In the following process, the magnetization transforms via spin-orbit coupling the transferred angular momentum to its orbital motion, leading to a rotation of the magnetic texture. Since the magnetic texture is embedded in the atomic crystal, which breaks the rotational symmetry, there is a preferred orientation of the skyrmion lattice in equilibrium, as mentioned above. Thus, the flow of angular momentum to the orbital sector originating from spin-transfer torques is partially absorbed by the atomic crystal lattice until all rotational torques are balanced. In the linear response regime, where the applied current does not fully overcome the counter-torque from the atomic lattice, the balance of these two torques determines the finite rotation angle. Eq. (10.12) can be easily solved for the rotation angle $\delta\phi$, provided that the spring constant $|\chi|$ does not vanish:

$$\delta\phi = \frac{1}{\chi}\left[\boldsymbol{P}_R\left(\boldsymbol{v}_s - \boldsymbol{v}_d\right) + \boldsymbol{P}_D\left(\beta\boldsymbol{v}_s - \alpha\boldsymbol{v}_d\right) + \boldsymbol{P}_{D'}\left(\beta'\boldsymbol{v}_s - \alpha'\boldsymbol{v}_d\right)\right]. \tag{10.13}$$

Since we consider only terms up to linear order in $\boldsymbol{v}_s$, and since the three rotational coupling vectors are already multiplied by terms that are of linear order in $\boldsymbol{v}_s$, we evaluate $\boldsymbol{P}_R$, $\boldsymbol{P}_D$, and $\boldsymbol{P}_{D'}$ using the equilibrium magnetization structure. An alternative derivation of the rotation angle leading to the same results can be found in Appendix C. Neglecting pinning and using the explicit solution for the drift velocity $\boldsymbol{v}_d$, Eq. (9.22), in the limit of small damping the equation for $\delta\phi$ simplifies to

$$\delta\phi \approx \frac{1}{\chi}\left((\tilde{\beta} - \tilde{\alpha})\frac{\mathcal{D}}{\mathcal{G}}\boldsymbol{P}_R(\hat{\boldsymbol{n}} \times \boldsymbol{v}_s) + (\beta - \alpha)\boldsymbol{P}_D\boldsymbol{v}_s + (\beta' - \alpha')\boldsymbol{P}_{D'}\boldsymbol{v}_s\right). \tag{10.14}$$

As many other spin-torque effects [140], the rotation also vanishes in the case of Galilean invariance.

10.2.1   Numerical Solution for the Skyrmion Lattice

As we have seen above, the rotation angle is only finite when taking account a distorted skyrmion lattice. In Section 4.3, we have considered symmetry-allowed terms in the Ginzburg-Landau theory which provide the preferred orientation of the skyrmion lattice and distort it to leading order in λ_{so}. In the following, we use the term F_L of Eq. (4.26), characterized by the coupling constant γ_L, for the preferred in-plane alignment of the skyrmion lattice. It leads to a finite susceptibility χ which is of the order of $\sim \mathcal{O}(\gamma_L)$. To obtain a distorted skyrmion lattice we use the term F_D of Eq. (4.27). It is characterized by the coupling constant γ_D and leads to small, but finite rotational coupling vectors $\boldsymbol{P}_R$, $\boldsymbol{P}_D$ and $\boldsymbol{P}_{D'}$ of the order of $\sim \mathcal{O}(\gamma_D)$. To be precise, we use in this Section the free energy functional

$$F = F[\boldsymbol{M}(\boldsymbol{r})] = \gamma \int d^3r \left[(1+t)\boldsymbol{M}^2 + (\nabla\boldsymbol{M})^2 + 2\,\boldsymbol{M}\cdot(\nabla\times\boldsymbol{M}) + \boldsymbol{M}^4 - \boldsymbol{B}\cdot\boldsymbol{M}\right.$$
$$\left. + \gamma_L\left((\partial_x^3\boldsymbol{M})^2 + (\partial_y^3\boldsymbol{M})^2 + (\partial_z^3\boldsymbol{M})^2\right) + \gamma_D\left((\partial_x M^y)^2 + (\partial_y M^z)^2 + (\partial_z M^x)^2\right)\right] \tag{10.15}$$

The rotation angle $\delta\phi$ is proportional to the ratio of the two coupling strengths, $\delta\phi \propto \gamma_D/\gamma_L$. This is a ratio of two tiny quantities, but γ_L is even smaller than γ_D as $\gamma_L/\gamma_D \sim \lambda_{\text{so}}^2$, meaning that one can expect a sizable effect $\delta\phi \propto \gamma_D/\gamma_L$.

To obtain the numerical results presented in the following, we first calculated the approximate magnetization texture $\boldsymbol{M}(\boldsymbol{r})$ of the skyrmion lattice within the following mean-field approximation. We minimized the free energy functional of Eq. (10.15) with the ansatz for the magnetization given by Eq. (4.14), including only the three smallest reciprocal lattice vectors $\boldsymbol{q}_j$ to the sum. As we have already seen, this is quite a good approximation for the skyrmion lattice since higher-order terms contribute (experimentally [67] and also theoretically [1, 67]) only a few percent to the total magnetization. As we are not discussing the stability competition of the skyrmion crystal with another phase, we will not take into account the effects of thermal fluctuations. Using the results of Ref. [1] we expect that the incorporation of thermal fluctuations into our theory just leads to a small renormalization of prefactors at least not too close to the phase transition. Similarly, we ignore for simplicity corrections arising from fluctuations to the Landau-Lifshitz-Gilbert equation, Eq. (10.1), that are probably important for a complete description of the depinning transition which is beyond our analysis. Using our obtained equilibrium magnetization structure $\boldsymbol{M}(\boldsymbol{r})$ we calculated the expressions of Eq. (10.13), *i.e.* the three rotational coupling vectors, the drift velocity, the susceptibility χ, and finally the rotation angle $\delta\phi$. Further details about the numerical evalutation can be found in Appendix C.

Note that the numerical results presented in the following are obtained in the absence of pinning forces and for $\alpha' = \beta' = 0$. Finite α' and β' will modify prefactors in our results for the rotation angle, but we do not expect qualitative changes, because the symmetry arguments explained in the following still hold for finite α' and β', and one can rewrite the expression $\boldsymbol{P}_D\left(\beta\boldsymbol{v}_s - \alpha\boldsymbol{v}_d\right) + \boldsymbol{P}_{D'}\left(\beta'\boldsymbol{v}_s - \alpha'\boldsymbol{v}_d\right)$ as $\boldsymbol{P}_D\left(\beta_{\text{eff}}\boldsymbol{v}_s - \alpha_{\text{eff}}\boldsymbol{v}_d\right)$ with $\beta_{\text{eff}} = \beta + \frac{|\boldsymbol{P}_D|}{|\boldsymbol{P}_{D'}|}\beta'$ and $\alpha_{\text{eff}} = \alpha + \frac{|\boldsymbol{P}_D|}{|\boldsymbol{P}_{D'}|}\alpha'$.

In the limit of small $\alpha, \beta \ll 1$, Eq. (10.13) reduces to

$$\delta\phi \approx \frac{\beta - \alpha}{\chi}\left(\frac{\mathcal{D}}{\mathcal{G}}\boldsymbol{P}_R(\hat{\boldsymbol{n}} \times \boldsymbol{v}_s) + \boldsymbol{P}_D\boldsymbol{v}_s\right), \tag{10.16}$$

where the rotation angle depends on the chosen parameters as follows:

$$\delta\phi = \phi_0\,\delta\varphi(t, \boldsymbol{B}, \hat{\boldsymbol{j}}) \quad \text{for} \quad \alpha, \beta, \gamma_L, \gamma_D \ll 1, \tag{10.17}$$

and ϕ_0 depends on the original parameters as[5]

$$\phi_0 = v_s\frac{\hbar(\beta - \alpha)\sqrt{UJ}}{D^2}\frac{\gamma_D}{\gamma_L}. \tag{10.18}$$

Note that by construction we get a term that is linear in the strength of the current v_s. Furthermore, the rotation angle should be proprotional to γ_D, because the distortion anisotropy term provides an overlap with the rotation mode. Since the counter-torque $\sim \gamma_L$ occurs on the right hand side of Eq. (10.15), the rotation angle is inversely proportional to γ_L. Moreover, we expect that in the Galilean invariant case, $\beta = \alpha$, no rotation of the skyrmion lattice occurs, as is apparent from Eq. (10.18). The remaining factors $\hbar\sqrt{UJ}/D^2$ arise from the transformation back to the original units of Eq. (4.7). $\delta\varphi(t, \boldsymbol{B}, \hat{\boldsymbol{j}})$

---

[5]Note that in our previous publication [70] we have defined ϕ_0 and the rotation angle with opposite signs. Since we consider $\delta\phi/\phi_0$ in the following plots, the two signs cancel.
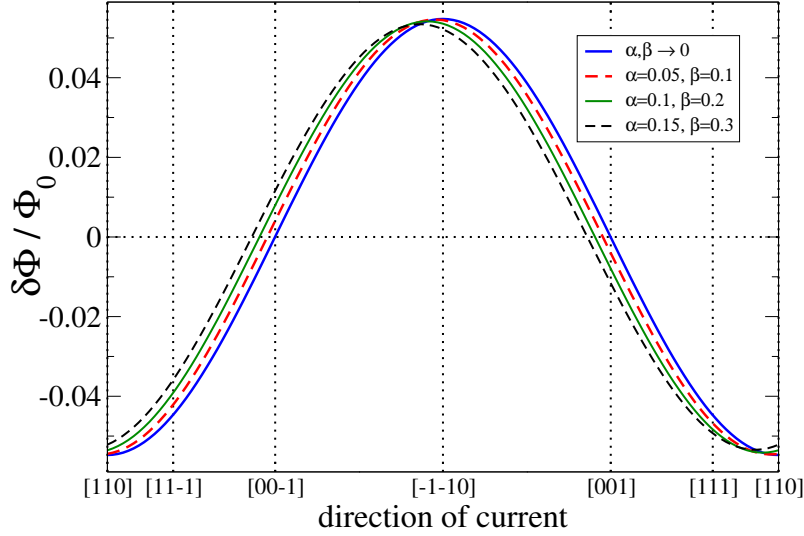
Figure 10.1: Effective rotation angle $\delta\phi$ in units of ϕ_0 defined by Eq. (10.18) for various values of the damping constants as a function of the direction of the applied current. The magnetic field $\boldsymbol{B}$ is applied in the $[1\bar{1}0]$ direction, and the direction of the current is always perpendicular to $\boldsymbol{B}$. Furthermore, we choose $t = -0.8$, $|\boldsymbol{B}| = 0.5\sqrt{-2t}$, $\gamma_D = 0.01$, and $\gamma_L = 0.001$. We published this Figure in Ref. [70].

of Eq. (10.17) is a dimensionless function which depends only on the external parameters, namely the distance t to the critical temperature, the orientation of the applied current $\hat{\boldsymbol{j}}$, and the dimensionless rescaled magnetic field $\boldsymbol{B}$ (note that we have chosen particular units in Eq. (4.8)). In the following, we further analyze $\delta\varphi(t, \boldsymbol{B}, \hat{\boldsymbol{j}})$. First, we discuss the dependence of the rotation angle on different directions of the applied magnetic field $\boldsymbol{B}$ and the applied current $\boldsymbol{v}_s$. Second, we consider the behavior of $\delta\phi$ on the distance to the phase transition. We close with an order-of-magnitude estimate for the rotation angle.

Orientational dependence of $\delta\phi$: For a fixed magnetic field, the orientational dependence of the rotation angle on $\boldsymbol{v}_s$ is rather simple. Within our theory $\delta\phi$ is proportional to the product of $\boldsymbol{v}_s$ and another vector in the skyrmion lattice plane denoted by $\boldsymbol{w}$ for the moment. $\boldsymbol{w}$ depends on the external parameters t, $\boldsymbol{B}$, and is almost perpendicular to the magnetic field with corrections of order γ_D. When rotating $\boldsymbol{v}_s$ around the direction of the magnetic field for fixed external parameters (*i.e.* fixed $\boldsymbol{w}$), there exist directions, where $\boldsymbol{v}_s$ becomes almost parallel (perpendicular) to $\boldsymbol{w}$ and the signal becomes maximal (almost zero). Therefore, for this setup the rotation angle exhibits a simple cosine dependence as is confirmed by the numerical results for $\delta\phi$ in units of ϕ_0, shown in Fig. 10.1 for various values of the damping constants α and β. The limit of small α, β, where $\delta\phi$ reduces to Eq. (10.17), is indicated by the blue line in Fig. 10.1. As, by construction, our theory is limited to effects linear in the applied current, a reversal of the current direction always leads to a sign change of the rotation angle, $\delta\phi \to -\delta\phi$.

For a fixed direction of the applied current, the dependence of the rotation angle $\delta\phi$ on the direction of the applied magnetic field $\hat{\boldsymbol{B}}$ is not so simple, because the relevant distortions of the skyrmion lattice depend sensitively on the direction of the magnetic field. In the following, we consider three directions of the current $\boldsymbol{v}_s$ around which we then rotate the direction of the applied magnetic field (being always perpendicular to $\boldsymbol{v}_s$).
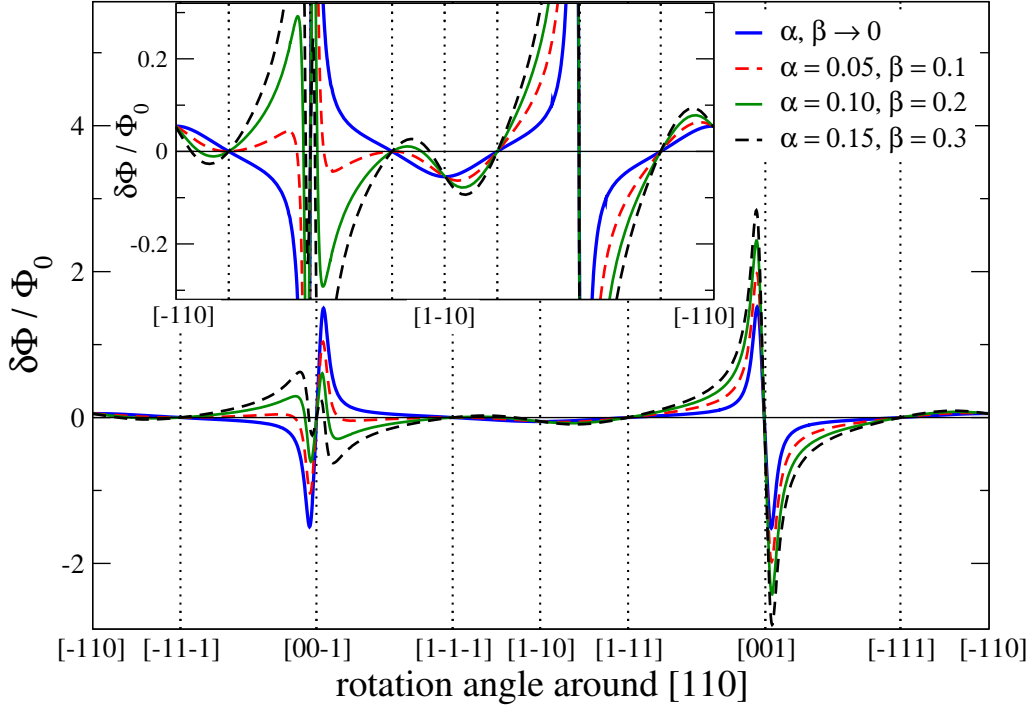
Figure 10.2: Effective rotation angle $\delta\phi$ in units of ϕ_0 as defined by Eq. (10.18) with the current $\boldsymbol{v}_s$ applied in the [110] direction. $\delta\phi$ is plotted as a function of the direction of the magnetic field $\boldsymbol{B}$ which is perpendicular to $\boldsymbol{v}_s$. The other parameters are chosen as in Fig. 10.1. The rotation angle vanishes for a magnetic field applied into one of the high symmetry directions, *i.e.* if $\boldsymbol{B}$ is oriented along $\langle 111 \rangle$ or $\langle 100 \rangle$. Close to the $\langle 100 \rangle$ direction, the rotation angle is maximal, as explained in the main text. For certain directions the size of the rotation angle depends sensitively on values of the damping constants. We published this Figure in Ref. [70].

The numerical results for the rotation angle for $\boldsymbol{v}_s$ in [110] direction are shown in Fig. 10.2, for $\boldsymbol{v}_s$ in [111] direction in Fig. 10.3, and for $\boldsymbol{v}_s$ in [100] direction in Fig. 10.4. They give an overview how $\delta\phi$ depends on the orientation of the magnetic field. We discuss their main features, which can be mostly understood from symmetry considerations, in the following. For this, in particular those cases are important, where the magnetic field is applied in one of the main symmetry directions, *i.e.* the twofold $\langle 100 \rangle$ axes and the threefold $\langle 111 \rangle$ axes. Moreover, the system possesses another symmetry if the magnetic field is applied in a direction perpendicular to a $\langle 100 \rangle$ axis. In that case, the combined symmetry operation of time-reversal and a rotation by 180° around the corresponding $\langle 100 \rangle$ axis maps the magnetic field and the skyrmion lattice onto itself.

For the setup and the parameters of Fig. 10.2, one of the reciprocal lattice vectors is always oriented in the [1$\bar{1}$0] direction when no current is applied. With an applied current $\boldsymbol{v}_s$ along the [110] axis, the rotation angle in units of ϕ_0 is shown in Fig. 10.2 as a function of the direction of the applied magnetic field for various values of the damping constants. When the magnetic field is rotated around the direction of the current, which is along the [110] axis, it passes a few high-symmetry directions like [1$\bar{1}$1] or [001], as can be seen from Fig. 10.2. For most directions of the magnetic field, the rotation angle depends within our theory on the specific chosen anisotropy terms, their sign and size, as well as on the

damping constants. Thus, the behavior of the rotation angle is not universal for most directions of the magnetic field. However, for high-symmetry directions, the situation is different. If the magnetic field is oriented along one of the twofold screw axes $\langle 100 \rangle$ or along one of the threefold symmetry axes $\langle 111 \rangle$, the rotation angle $\delta\phi$ vanishes to linear order in $\boldsymbol{v}_s$. The reason for this is that for these high-symmetry directions the normal vector to the skyrmion lattice $\hat{\boldsymbol{n}}$ becomes parallel to $\boldsymbol{B}$, and therefore the rotational coupling vectors vanish. Thus, for these directions of the magnetic field the contributing torques and hence the rotation angle $\delta\phi$ vanish for a velocity $\boldsymbol{v}_s$ perpendicular to the applied magnetic field.

Away from these two different types of high-symmetry directions (note that $\langle 110 \rangle$ is not a symmetry axis of the B20 structure of MnSi) the rotational coupling vectors are finite. These finite coupling vectors give rise to a transfer of angular momentum from the magnetic texture to the crystal lattice, leading to a rotation of the magnetic texture by the finite angle $\delta\phi$, as can be seen in Fig. 10.2. The $\langle 100 \rangle$ directions for the magnetic field are special as can be seen immediately in Fig. 10.2. In these geometries, the susceptibility χ of Eq. (10.11) vanishes to linear order in γ_L, since F_L of Eq. (4.26) does not lead to an orientation of the skyrmion lattice within the plane to linear order in γ_L, as discussed below Eq. (4.26) in Section 4.3. When denoting for a moment by δ the angle between $\hat{\boldsymbol{B}}$ and the [001] direction, then the relevant potential is quadratic in δ. It is proportional to $\gamma_L \delta^2 \cos 6\phi$ (for the geometry of Fig. 10.2). The rotational coupling vectors vanish only linearly in δ, leading to a rotation angle which is inversely proportional to δ, *i.e.* $\delta\phi \sim 1/\delta$. For very small δ, effects of order γ_L^2 lead to a rounding of the divergence. Within this analysis we did not consider even further anisotropy terms which are necessary for these special directions, and therefore our theory is limited in predicting the behavior of the rotation angle along such special symmetry directions.

The blue line in Fig. 10.2 corresponds again to the limit of small α, β, where $\delta\phi$ can be simplified to Eq. (10.17) by expanding Eq. (10.13) (for $\alpha' = \beta' = 0$) to linear order in the damping coefficients α and β. In this case, also a reversal of the magnetic field direction, $\boldsymbol{B} \to -\boldsymbol{B}$ leads to a sign reversal $\delta\phi \to -\delta\phi$, as can be seen from the blue solid line in Fig. 10.2). However, for larger damping coefficients, *i.e.* when one has to take higher-order contributions in α and β into account, this is in general not the case. This can be easily seen in Fig. 10.2 by considering a magnetic field close to the [001] or [00$\bar{1}$] direction, respectively. Even for values of $\alpha \sim 0.1$ [141], the absolute value of the rotation angle shows a strong difference for some directions of the magnetic field compared to the opposite field direction. Also, sign changes of $\delta\phi$ for certain crystallographic directions are possible in the sense that for $\boldsymbol{B}$ and $-\boldsymbol{B}$ both rotation angles have the same sign, as can be seen for example in the inset of Fig. 10.2 for magnetic fields in directions close to [1$\bar{1}$1] and [$\bar{1}$1$\bar{1}$], respectively. The absence of this symmetry stems from the fact that time-reversal symmetry is not only broken by the magnetic field, but also by $\boldsymbol{v}_s$, and by the dissipative and the reactive forces which have opposite signatures under time-reversal. An exception is a configuration, where, for example, the magnetic field is oriented along the [110] direction and the current along the [1$\bar{1}$0] direction. In this geometry, both $\boldsymbol{v}_s$ and $\boldsymbol{B}$ are orthogonal to the [001] direction. Since a $\langle 100 \rangle$ axis is a twofold rotation axis of MnSi, which in this particular geometry allows to map $\boldsymbol{B} \to -\boldsymbol{B}$ and $\boldsymbol{j} \to -\boldsymbol{j}$, the rotation angle remains the same when reversing the magnetic field and the current. Note that within our conventions $\delta\phi$ is defined relative to the field orientation.

Summarizing the symmetry considerations above of the magnetic field and the current we obtain

$$\delta\phi(\boldsymbol{B}, \boldsymbol{j}) = -\delta\phi(\boldsymbol{B}, -\boldsymbol{j}), \tag{10.19}$$
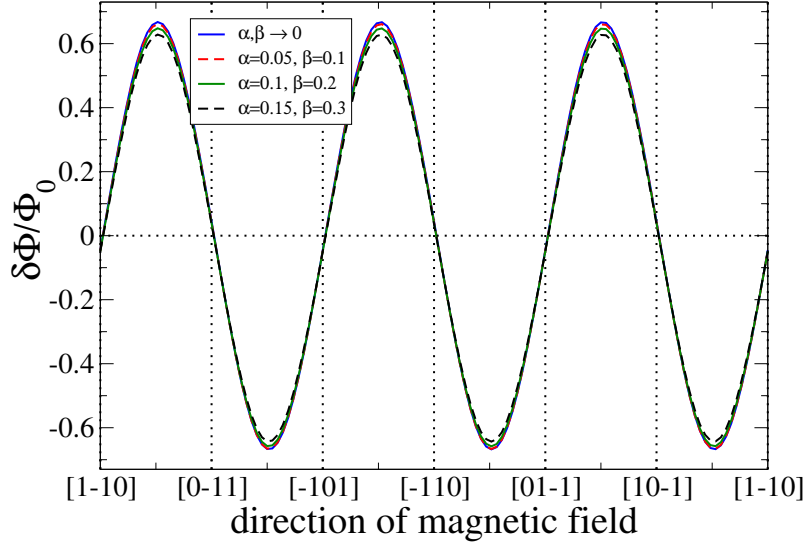
Figure 10.3: Effective rotation angle $\delta\phi$ in units of ϕ_0 as defined in Eq. (10.18) as a function of the direction of the magnetic field $\boldsymbol{B}$. Here, the current $\boldsymbol{v}_s$ is oriented along the [111] direction, and the magnetic field is rotated around $\boldsymbol{v}_s$. The other parameters are chosen as in Fig. 10.1. We published this Figure in Ref. [70].

but in general

$$\delta\phi(\boldsymbol{B}, \boldsymbol{j}) \neq -\delta\phi(-\boldsymbol{B}, \boldsymbol{j}). \tag{10.20}$$

Hence, in general, there is no specific symmetry with respect to the reversal of the current and the magnetic field, $\delta\phi(\boldsymbol{B}, \boldsymbol{j}) \neq \delta\phi(-\boldsymbol{B}, -\boldsymbol{j})$. Only for geometries, where $\boldsymbol{v}_s \perp \boldsymbol{B}$ and where both are orthogonal to a twofold screw $\langle 100 \rangle$ axis, we have $\delta\phi(\boldsymbol{B}, \boldsymbol{j}) = \delta\phi(-\boldsymbol{B}, -\boldsymbol{j})$.

Fig. 10.3 and Fig. 10.4 show similar plots as Fig. 10.2. The difference between them is that the current, around which the magnetic field is rotated, is applied in different directions. While the current in Fig. 10.2 is applied in the [110] direction, it is oriented along the [111] axis in Fig. 10.3, and along [100] in Fig. 10.4. In Fig. 10.3, the pattern repeats itself every 120° due to symmetry. For magnetic fields in the $\langle 110 \rangle$ directions, the rotation angle $\delta\phi$ becomes small, but does not vanish, as can be seen more clearly in Fig. 10.1. Note that there is no $\langle 100 \rangle$ direction which is perpendicular to the [111] direction, so that in this case there is no direction of the magnetic field, where the susceptibility χ vanishes.

In Fig. 10.4, the current is applied in the [100] direction, and therefore there are four possible directions for the magnetic field along a $\langle 001 \rangle$ axis perpendicular to [100]. Along these directions the rotation angle takes again large values, as in Fig. 10.2. This configuration is special considering the limit $\alpha, \beta \to 0$. In this scenario, the rotation angle $\delta\phi/\phi_0$ vanishes exactly. This can also be understood by symmetry arguments. When the current is applied along the [100] direction, a rotation around this axis does not alter the direction of the current. Since [100] is a twofold screw axis, rotations around 180° (followed by a translation of half a lattice vector) map the atomic system onto itself. Just performing this rotation would map $\boldsymbol{B}$ onto $-\boldsymbol{B}$. Thus, performing a rotation by 180° followed by time-reversal would map $\boldsymbol{B}$ upon itself, and in the equilibrium situation one would obtain the same skyrmion lattice solution. This implies that under the product of this rotation and time-reversal the rotational coupling vectors have to be invariant. Since $\boldsymbol{P}_R$ is even under time-reversal, it remains only invariant under this transformation when pointing
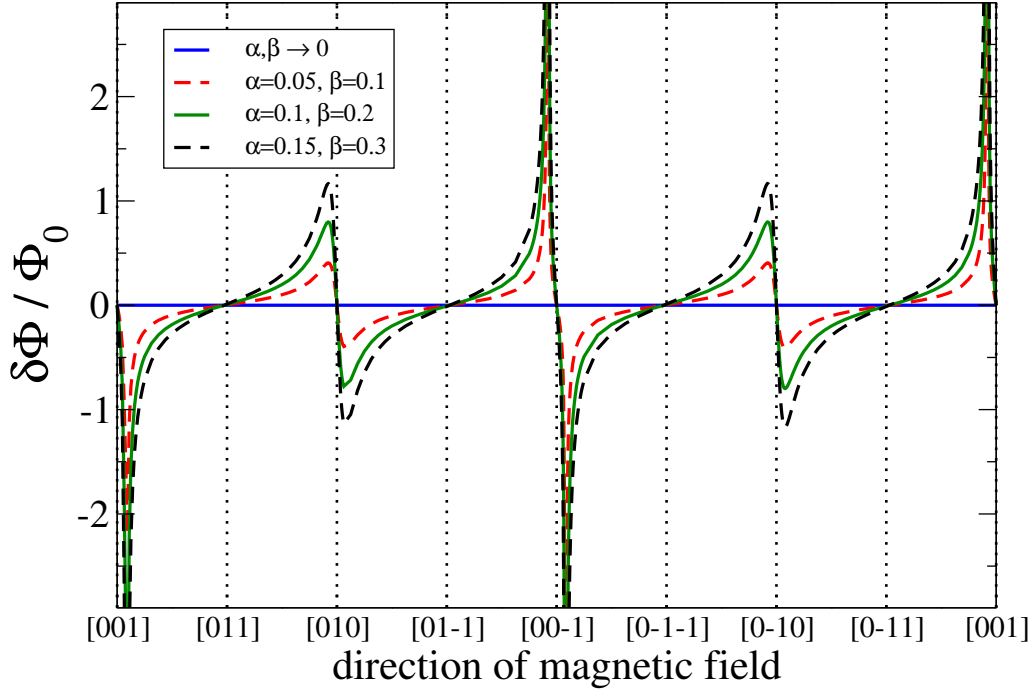
Figure 10.4: Effective rotation angle $\delta\phi$ in units of ϕ_0 as defined in Eq. (10.18) for a current $\boldsymbol{v}_s$ along the [100] axis as a function of the direction of the magnetic field $\boldsymbol{B}$ which is perpendicular to the [100] direction. The other parameters are chosen as in Fig. 10.1. For this orientation the rotation angle vanishes quadratically in the limit $\alpha, \beta \to 0$ due to a combined symmetry operation being a product of a rotation by 180° around the [100] axis and time-reversal. An explicit explanation is given in the main text. We published this Figure in Ref. [70].

in the [100] direction, *i.e.* in the direction of the current. In contrast, the dissipative rotational coupling vectors $\boldsymbol{P}_D$ and $\boldsymbol{P}_{D'}$ are odd under time-reversal, and thus they have to be perpendicular to the [100] direction. Moreover, from Eq. (9.23) it follows that $\boldsymbol{v}_s$ and $\boldsymbol{v}_d$ behave in this limit such that $\boldsymbol{v}_s - \boldsymbol{v}_d$ becomes perpendicular to $\boldsymbol{v}_s$, while $\tilde{\beta}\boldsymbol{v}_s - \tilde{\alpha}\boldsymbol{v}_d$ becomes parallel to $\boldsymbol{v}_s$ to leading order in $\tilde{\beta}$ and $\tilde{\alpha}$. Hence, the contributing terms to the rotation angle Eq. (10.13) vanish since the corresponding scalar products of the coupling vectors with the velocities are zero (for $\alpha' = \beta' = 0$). Thus, all current-induced torques vanish for $\alpha, \beta \to 0$ according to Eq. (10.13) for a current in [100] direction.

Dependence of $\delta\phi$ on the distance t to the phase transition: At a first-order phase transition the rotation angle $\delta\phi$ is formally non-singular. In practice, however, a complex interplay of phase transition dynamics, pinning effects, the external drive by currents, heating effects, and even surface properties can be expected in the regime, where both phases are locally stable. This complex interplay is not described by our theory, and we restrict our analysis to the overall dependence of the rotation angle on the parameter t that can be controlled by temperature in an experiment. Fig. 10.5 shows the dependence of the rotation angle $\delta\phi$ in units of ϕ_0 on the distance t from the mean-field phase transition for a fixed magnetic field strength and $\boldsymbol{v}_s$ oriented along the [110] direction in the limit of small α and β when Eq. (10.17) is valid. The various curves correspond to different orientations of the magnetic field $\boldsymbol{B}$. For the set of parameters used in Fig. 10.5, the magnitude
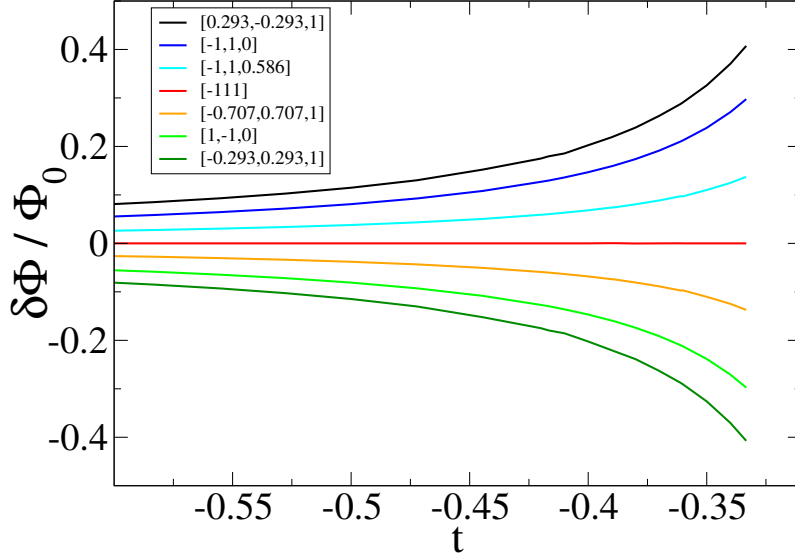
Figure 10.5: Effective rotation angle $\delta\phi$ in units of ϕ_0, see Eqs. (10.17) and (10.18), in the limit of small α, β as a function of the dimensionless distance t from the critical point. The current $\boldsymbol{v}_s$ is applied along the [110] direction. The different curves correspond to different directions of the magnetic field $\boldsymbol{B}$ which is perpendicular to the current direction, see legend. The other parameters are $|\tilde{\boldsymbol{B}}| = 0.5\sqrt{1.6}$, $\gamma_D = 0.01$, and $\gamma_L = 0.001$. We published this Figure in Ref. [70].

of the rotation angle increases for increasing t, *i.e.* for higher temperatures. However, a mean-field theory is not able to describe the first-order transition quantitatively, and therefore the magnitude of the effect might be overestimated. Furthermore, one obtains qualitatively different results for the t dependence when including anisotropy terms which dominate and are not quadratic in the order parameter as assumed by us, but are of higher order. In this case, the system behaves more sensitively to the distance to the phase transition.

Order-of-magnitude estimate: To determine the quantitative value of the rotation angle, in principle all quantities of ϕ_0 have to be known from the experiments. So far, not all of them are determined, in particular γ_L and γ_D as well as the damping constants are unknown. Therefore, by counting powers of spin-orbit coupling λ_{so} we would like to give a crude estimate of the order of magnitude of the rotation, which is caused by torques arising from lattice distortions.

For $|t| \sim 1$, the rotation angle $\delta\phi$ can be estimated to be of the order of ϕ_0, *i.e.* $\delta\phi \sim \phi_0$, where ϕ_0 is defined in Eq. (10.18):

$$\phi_0 = v_s \frac{\hbar(\alpha - \beta)\sqrt{UJ}}{D^2} \frac{\gamma_D}{\gamma_L} = v_s \hbar(\alpha - \beta) \left(\frac{J}{D}\right)^2 \frac{\sqrt{U}}{J^{3/2}} \frac{\gamma_D}{\gamma_L}. \tag{10.21}$$

Approximating $v_s \sim a^3 j/e$, $D/J = \lambda_{\mathrm{so}}/a$, $a^3\sqrt{U}/J^{3/2} \sim 1/k_B T_c$, and $\gamma_L/\gamma_D \sim \lambda_{\mathrm{so}}^2$ we obtain for the rotation angle

$$\delta\phi \sim \delta\phi_0 \sim \frac{\hbar j a^2}{e k_B T_c} \frac{\alpha - \beta}{\lambda_{\mathrm{so}}^4}. \tag{10.22}$$

For MnSi, the lattice constant a and the critical temperature T_c are given by $a \approx 4.56$ Å and $T_c \approx 29$ K, respectively. Spin-torque effects for MnSi were observed above current densities of the order of 10^6 A/m^2 [10, 80] which, rewritten in the appropriate dimensionless units, corresponds to $j_s/j_0 \approx \frac{\hbar j P a^2}{e k_B T_c} \sim 10^{-8}$ (cf. Section 8.2). This expresses again the smallness of the applied current densities in comparison to most spin-torque experiments, where the critical current densities are five to six orders of magnitude larger. Using $\alpha \sim 0.1$ as obtained from the rather broad peaks in electron-spin-resonance experiments for MnSi [141], and a spin-orbit coupling strength $\lambda_{so} \sim 0.01$, one could in principle obtain sizable rotation angles $\delta\phi \sim \mathcal{O}(1)$. As mentioned already, such kind of rotations have not yet been observed. This is, however, not suprising taking into account the crudeness of our estimate. Moreover, according to our theory, in the current experimental setup (*i.e.* for a magnetic field along [110] and a current along [1$\bar{1}$0]) the effect is even more suppressed by another factor of 0.05, see Fig. 10.1.

To summarize, in this Section we have investigated the influence of spin-transfer torques on the magnetic skyrmion texture originating from small distortions of the skyrmion lattice due to the underlying atomic lattice. We have also seen that due to anisotropy terms the skyrmion lattice plane tilts slightly which agrees qualitatively quite well with the recently measured unpublished data [79], as discussed in Section 4.3. Furthermore, due to a double-transfer of angular momentum a spatial rotation by a finite angle may occur. First, angular momentum is transferred from the spins of the conduction electrons to the magnetization inducing torques on the magnetic structure. This momentum transfer and the corresponding torques are balanced by the flow of angular momentum from the magnetic texture (via spin-orbit coupling effects) to the underlying atomic lattice, leading to a rotation of the skyrmion lattice.

10.3 Spin-Transfer Torques in Neutron Scattering Experiments

In this Section, we review the first experiment in which the ultra-low threshold current density of $j_c \sim 10^6$ A/m^2 was observed, above which spin-transfer torques are measurable in bulk MnSi. These experiments were performed using small angle resolved neutron scattering (SANS). We have published the results together with a theoretical explanation in Ref. [10]. In Chapter 7 and Chapter 9 we have already seen that for an applied current strong enough to overcome the counter-forces induced by the atomic lattice and disorder, the current-induced forces may lead to a translational motion of the skyrmion lattice. It is very difficult to detect this effect in a scattering experiment, because for the small applied current densities the induced motion of the order of 10^{-4} m/s is not really fast.

In contrast to a translational motion, a rotation is much easier to measure with this technique, because a rotation of the skyrmion lattice corresponds to a rotation of the diffraction pattern. However, this rotation occured only in the presence of a small temperature gradient (~ 1 K/cm) as can be understood from the schematic illustration of the spin-transfer torque effects on the skyrmion lattice shown in Fig. 10.6. As explained in Chapter 9, there are mainly two current-induced forces acting on the skyrmion lattice. The Magnus force, which acts perpendicularly to the direction of the current for a non-moving skyrmion lattice, and the dissipative force, which in the pinned case acts along the direction of the current. Both act perpendicularly to the normal direction of the skyrmion lattice which is, neglecting distortion terms, equivalent to the direction of the magnetic field. In Fig. 10.6, the red and green arrows represent the Magnus force and the dissipative force for a non-moving skyrmion lattice, respectively. For a moving skyrmion lattice,
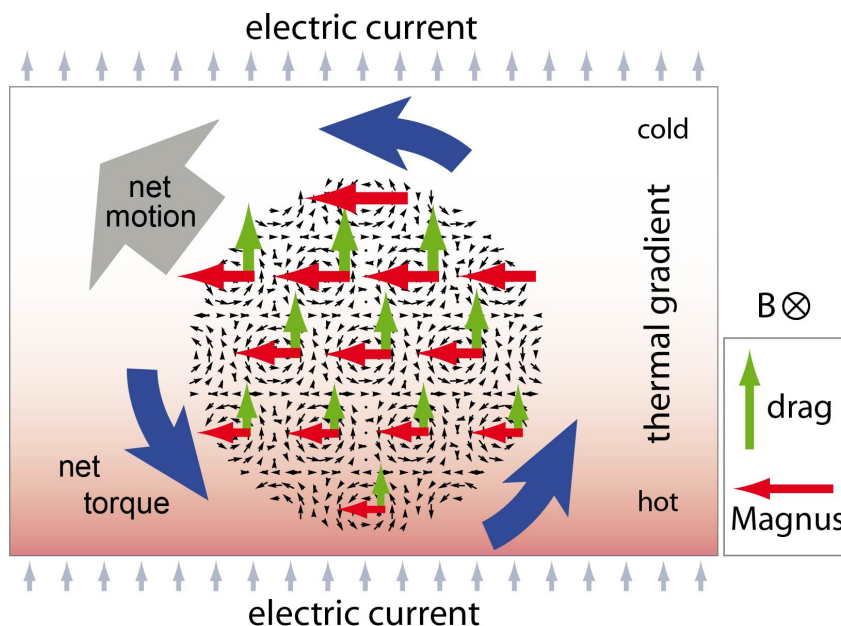
Figure 10.6: Illustration showing that gradients in the forces originating from a temperature gradient lead to a rotation of the skyrmion lattice. The skyrmion lattice is illustrated by the black arrows, and the current-induced forces by the red and green arrows. For a non-moving skyrmion lattice, these correspond to the Magnus and dissipative forces, respectively. The temperature gradient is indicated by the red-white gradient in the background. In the hotter regime of the sample, the forces are weaker, and in total the gradient in the forces leads to rotational torques indicated by the blue arrows. This Figure is taken from our publication, Ref. [10].

the situation is more complex. Nonetheless, there are still forces acting parallel and perpendicular to the applied current. A temperature gradient across the sample (indicated by the color gradient in the background of Fig. 10.6) causes the local magnetization to vary in magnitude across a domain, and therefore induces inhomogeneous spin currents. In turn, a gradient in the strength of the acting forces arises, leading to current-induced net torques. The balance between these torques and the counter-torques coming from the atomic lattice and pinning finally determines the rotation angle (or angular velocity) of the skyrmion lattice. Necessary for the rotation is, in principle, only a gradient in the forces which, aside from a temperature gradient, can for example also be obtained by a magnetic field gradient. The latter will probably soon be realized experimentally.

Neutron scattering experiments with a small temperature gradient parallel to the current have, however, already been done. Also these neutron scattering experiments were performed at the diffractometer MIRA [68] at FRM II at the Technische Universität München, where an incident neutron wavelength of $\lambda = 9.6$ Å with a 5% FWHM wavelength spread was used. The position resolution of the detector was of the order of 2×2 mm^2 with a total dimension of 200×200 mm^2. For details to the used experimental techniques see Ref. [10].

Typical neutron scattering results, where an electric current was applied along high-quality bar-shaped single crystals, are shown in Fig. 10.8, Fig. 10.9, and Fig. 10.10. These measurements were performed in the neutron scattering setup of Fig. 10.7 which corresponds to the setup of Fig. 3.9 for zero current, as introduced in Section 3.1.3. In this
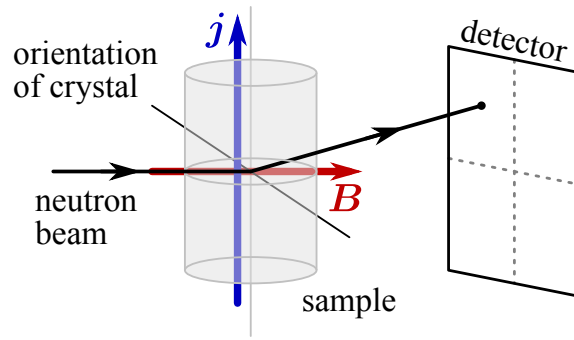
Figure 10.7: Neutron scattering setup, where the applied magnetic field $\boldsymbol{B}$ is parallel and the electric current $\boldsymbol{j}$ perpendicular to the incident neutron beam.
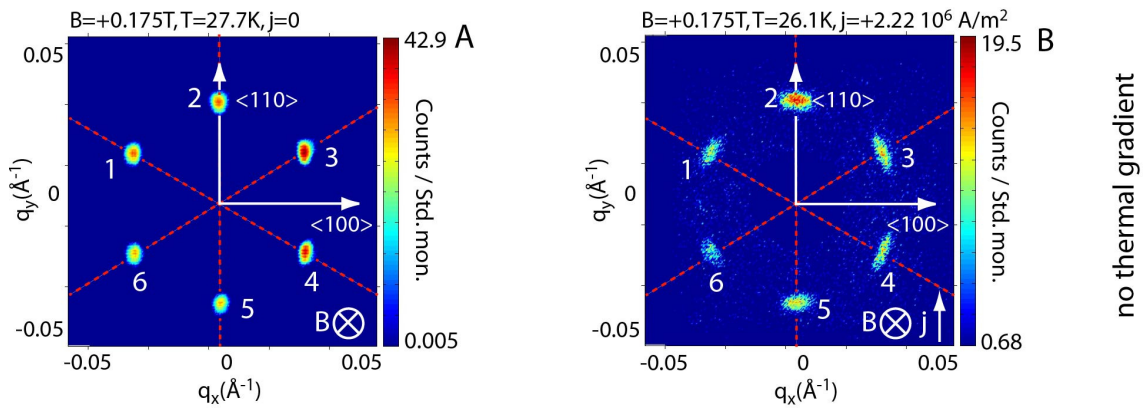
Figure 10.8: Typical neutron scattering intensity patterns in the skyrmion phase of MnSi. The measurements were performed in the setup of Fig. 10.7 with a magnetic field oriented along the [110] direction. The dashed red lines are a guide to the eye. The left panel shows just the characteristic main six spots on a regular hexagon of the skyrmion lattice without an applied current, which is in agreement with the neutron scattering data of Ref. [1] as discussed in Chapter 3. The right panel shows the neutron scattering pattern of the skyrmion lattice when a current is applied along the $[1\bar{1}0]$ direction, indicated by the white arrow. In these measurements no gradient was applied. This Figure is taken from our publication, Ref. [10].

setup, the magnetic field determining the direction of the skyrmion lines is collinear with the direction of the neutron beam. The profile of the magnetic field was found to be uniform (better than one percent) over the sample volume. The direction of the current is perpendicular to the magnetic field and therefore also to the skyrmion lines.

In Fig. 10.8, the magnetic field and the neutron beam were oriented along the [110] axis. The horizontal (vertical) direction in the plot is along [001] ($[1\bar{1}0]$). The left panel of Fig. 10.8 shows the six main neutron scattering peaks of the skyrmion lattice in the absence of an electric current, $j = 0$, as discussed in Chapter 3. In the right panel of Fig. 10.8, a current $j = 2.22 \cdot 10^6$ A/m^2 was applied along the vertical $[1\bar{1}0]$ direction (indicated by the white arrow in the lower right corner of the plot). Note that the arrows denote the technical current direction, and the line of sight is opposite to the direction of the neutron beam. In the experimental setup of the right panel of Fig. 10.8, any thermal gradients along the current direction were minimized, and thus no rotation occurs. The

Figure 10.9: Typical neutron scattering intensity patterns in the skyrmion phase of MnSi. The measurements were performed in the setup of Fig. 10.7 with a magnetic field oriented along the [110], and a current was applied along the vertical direction. The dashed red lines are a guide to the eye. Panel C shows the counter-clockwise rotation of the scattering pattern in the presence of a small temperature gradient which is applied antiparallel to the direction of the current. In Panel D, the direction of the current was reversed compared to panel C. In this case, the rotation of the skyrmion lattice is clockwise. Panel E displays the difference between panel C and D. Panel F illustrates that the difference between the scattering intensities from panel C and a measurement, where both current and magnetic field were reversed, vanishes approximately. This Figure is taken from our publication, Ref. [10].

diffraction spots remain at the same positions, but the peaks are broadened azimuthally due to the current.

However, upon generating a small temperature gradient ($\nabla T \sim 1$ K/cm) along the direction of the current, one can clearly observe a rotation of the diffraction pattern (for a discussion of the experimental realization of the temperature gradient see below). This rotation is, for example, shown in panel C of Fig. 10.9 which was measured, aside from an additional small temperature gradient, in the same setup as the measurement of the right panel of Fig. 10.8. Here, compared to the measurements without the gradient, the diffraction pattern is rotated counter-clockwise by a finite angle. Note that the entire scattering pattern rotates with respect to its center, *i.e.*, all spots move by the same angle even though the electric current has a distinct direction. In Fig. 10.9 D, the direction of the current was reversed compared to Fig. 10.9 C. In this case, the rotation angle changes sign, and the neutron scattering pattern is rotated by a finite angle in clockwise direction.

The difference of Fig. 10.9 C and Fig. 10.9 D is plotted in Fig. 10.9 E. Panel F of Fig. 10.9 shows the difference between panel C of Fig. 10.9 and a measurement, where the magnetic field and the current direction are both reversed (the latter is not shown). In this case, the intensity approximately vanishes, implying that reversing the electric current and the magnetic field direction leads to the same scattering pattern. Thus, in these experiments, the rotation changes sign, when reversing either the direction of the magnetic field or the direction of the current.

In Sec. 10.2 we have discussed that for a perfect skyrmion lattice the rotation angle should be invariant when reverting both current and magnetic field direction, *i.e.* $\delta\phi(\boldsymbol{B}, \boldsymbol{j}) = \delta\phi(-\boldsymbol{B}, -\boldsymbol{j})$, under the conditions that $\boldsymbol{B}$ is applied along [110], the current along [1$\bar{1}$0], and the rotation angle is defined with respect to the orientation of the magnetic field. Remember that this particular symmetry holds only for these special configurations of directions of the magnetic field and current and is in general not true. In the experiments, the angle is measured with respect to the neutron beam which is just the reverse direction when applying the magnetic field opposite to the beam direction. Hence, for a perfect skyrmion lattice, a magnetic field along [110], and a current along [1$\bar{1}$0] we would expect that the scattering patterns should not be the same upon reversing both current and magnetic field, and the experiments should show rotations with opposite directions. However, Fig. 10.9 F shows that this is not the case in the experiments. The reason for this apparent contradiction is that in the experimental setup this symmetry is broken due to the presence of an additional temperature gradient. This also shows that the theory presented in Section 10.2 cannot describe the experiment, because it does not include thermal gradients. They are, however, explicitly taken into account in Sec. 10.4.

The direction of the temperature gradient is given in the lower left corner of figures Fig. 10.9 C–J. In Fig. 10.9 G and H, basically the same measurements as in Fig. 10.9 C and D are shown, however the direction of the temperature gradient was reversed. By comparison of the data it can be clearly seen that upon reversing the direction of the temperature gradient also the sign of the rotation changes, as expected. This can also be observed when comparing the difference pictures. As Fig. 10.9 E, Fig. 10.9 I shows the difference between two measurements when reversing the direction of the current. Comparing Fig. 10.10 I with Fig. 10.9 E one observes that the intensity differences are reversed (red and blue spots are swapped). When reversing both the magnetic field and the current direction, the difference of the scattering patterns vanishes as before, compare Figs. 10.10 F and 10.10 J.

Furthermore, for a current applied along a ⟨111⟩ axis, *i.e.* a different crystallographic direction, the same features of the diffraction pattern were observed when reversing the current, the magnetic field, or the direction of the temperature gradient. Thus, the results do not depend on the specific crystallographic orientation of the sample. Typical data for a current along the ⟨111⟩ axis are shown in Fig. 10.11. Panel A was measured without a current and a gradient, and therefore no rotation occurs. In panels B and C, a current and a small temperature gradient were present. From panel B to C the direction of the current was reversed, changing the rotation from counter-clockwise to clockwise.

Also, measurements, where the current was parallel to the skyrmion lines, were performed. To study this case the setup shown in Fig. 10.12 was used which corresponds to the setup of Fig. 3.6, introduced in Section 3.1.3 for zero current. In this setup, the magnetic field determining mainly the direction of the skyrmion lines is perpendicular to the direction of the neutron beam. Typical data for this setup are shown in Fig. 10.13. Panel A shows the scattering pattern for $j = 0$. The horizontal spots labelled by "3" and
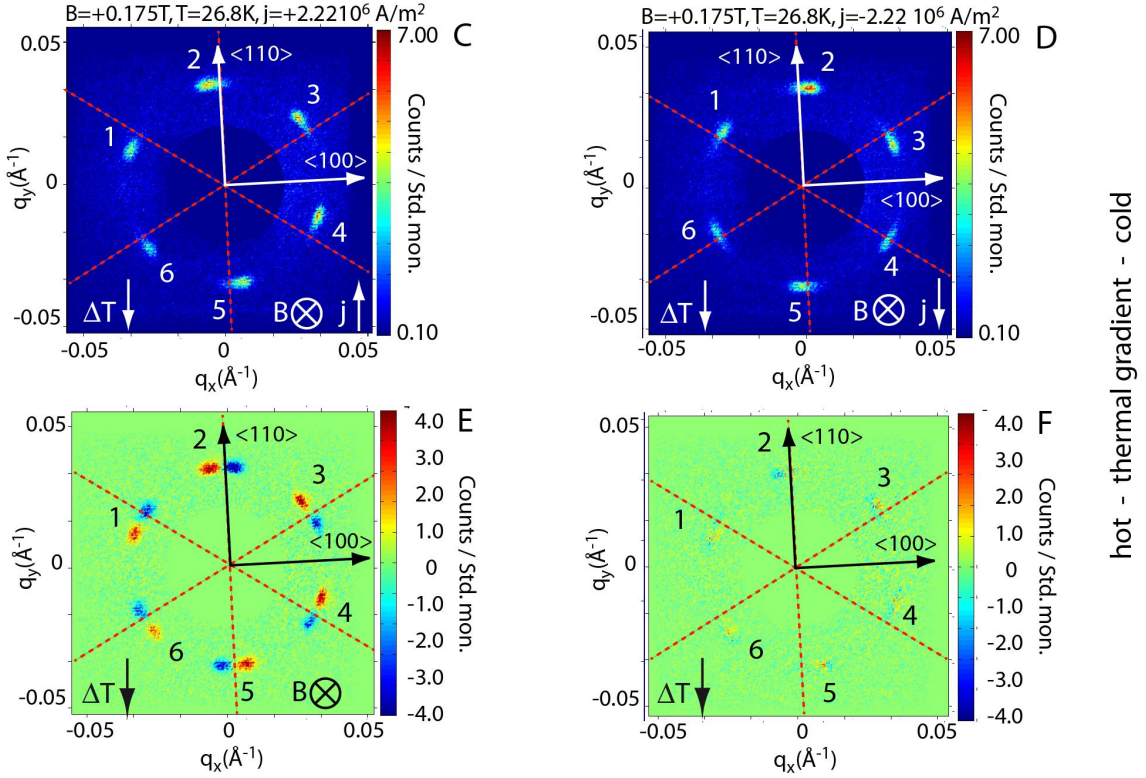
Figure 10.10: Typical neutron scattering intensity patterns in the skyrmion phase of MnSi. The measurements were performed in the setup of Fig. 10.7 with a magnetic field oriented along the [110], and a current was applied along the vertical direction. The dashed red lines are a guide to the eye. In the panels G–J basically the same data as in Fig. 10.9 panel C–F is shown, but with a reversed direction of the temperature gradient, leading to a sign change in the rotation of scattering pattern. This Figure is taken from our publication, Ref. [10].

"6" correspond to spots "3" and "6" of the sixfold patterns shown in Fig. 10.8. The two vertical spots are weak diffraction spots of the conical phase which occur, because in this particular setup a small temperature gradient was present even in the absence of a current (also a different sample holder was used). Panel B shows the scattering pattern for an applied electric current density $j = 1.24 \cdot 10^6$ A/m^2. For such a current parallel to the skyrmion lines no spin-transfer torque effect like a rotation or a broadening of the neutron scattering spots were observed in neutron scattering. Nevertheless, the same sample (studied on the same sample holder) shows the same features in the neutron scattering patterns as shown in Fig. 10.9 and Fig. 10.10, when instead the setup of Fig. 10.7 is used. Furthermore, experimentally it has also been verified that the obtained data do not depend on the order of cooling and applying the magnetic field. The data for the skyrmion phase were identical after zero-field cooling and field cooling.

To ensure that the results do not depend on sample shapes or other specific conditions, in total six different samples with different sizes and shapes of high quality (with mean free paths up to 1000 Å [142]) and two different sample holders were used. For example, in the measurements shown in Fig 10.8, a sample with a length of about 10 mm along the [1\overline{1}0] direction, a thickness of 1.5 mm along [001], and a width of 1.8 mm along the [110]
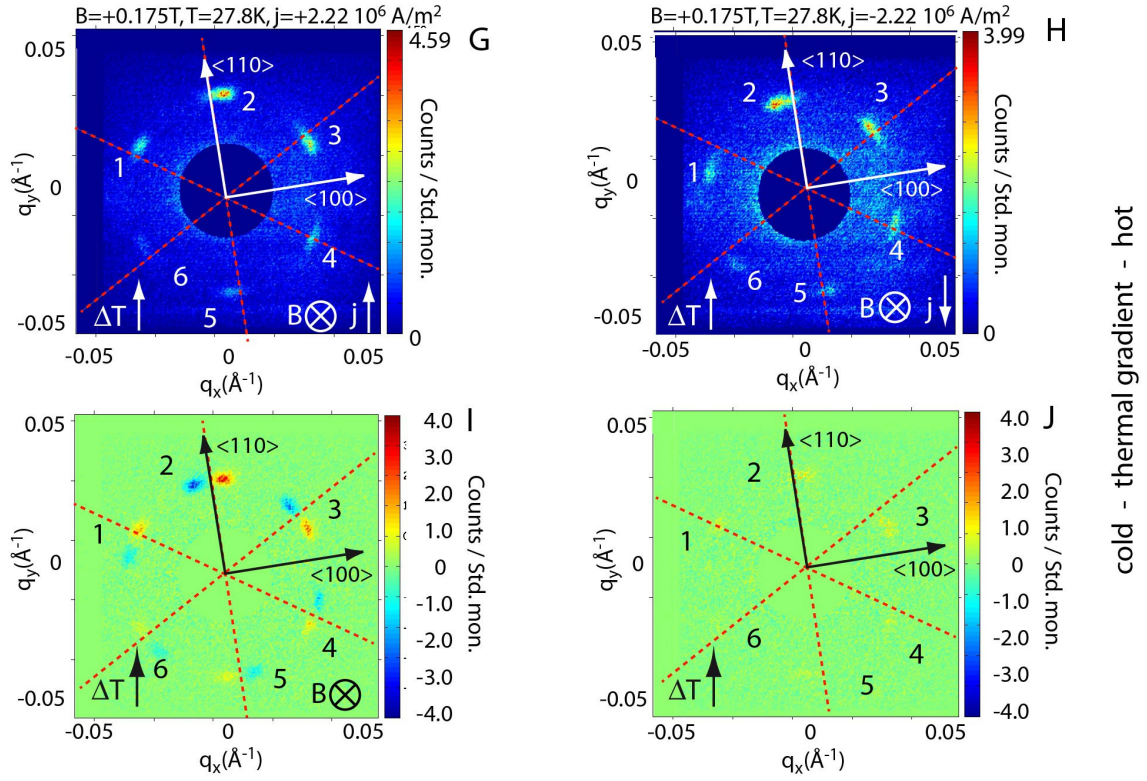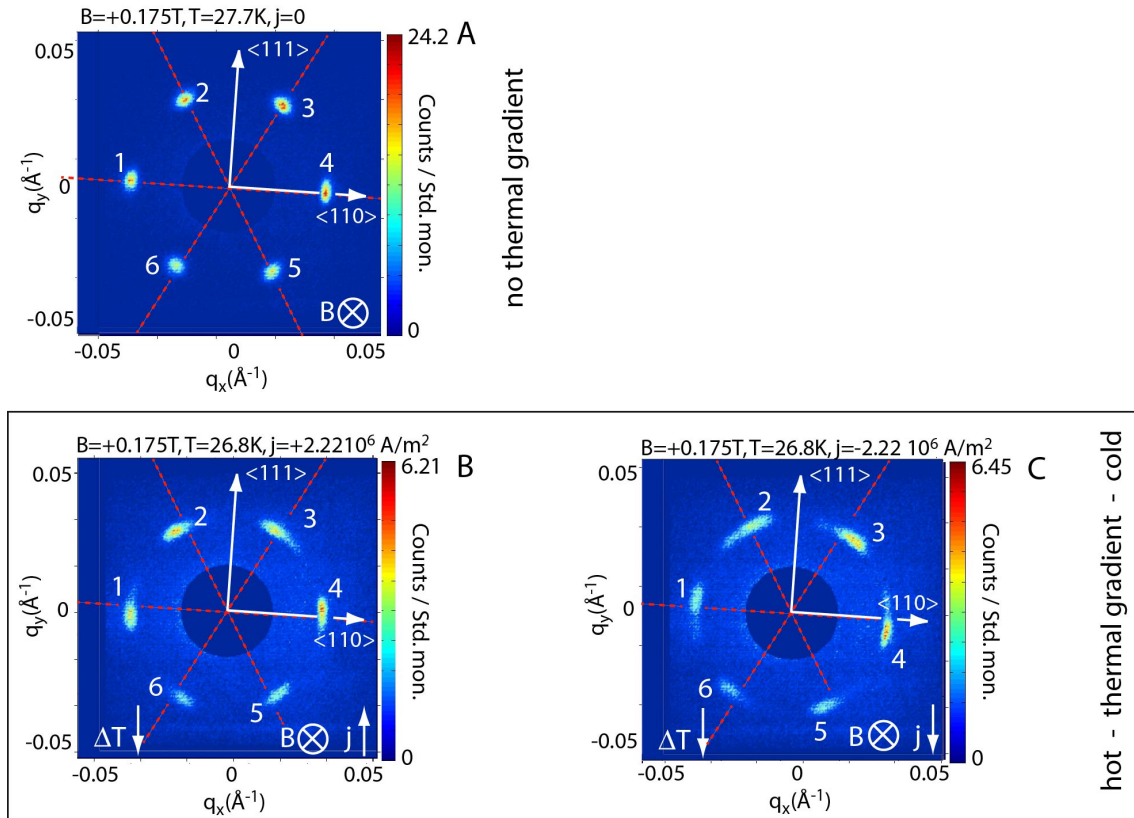
Figure 10.11: Typical neutron scattering intensity patterns in the skyrmion phase of MnSi. The measurements were performed in the setup of Fig. 10.7, where the current was applied along a $\langle 111 \rangle$ direction. The dashed red lines are a guide to the eye. In panel A, neither a current nor a temperature gradient were applied. Panel B shows the scattering pattern when a current and a small temperature gradient are present. Panel C shows the same as panel B, however, with a reversed current direction which changes the rotation from counter-clockwise to clockwise. This Figure is taken from our publication, Ref. [10].

direction was used. In Fig. 10.11, however, where the current was along the $\langle 111 \rangle$ axis, a different sample of dimensions 12 mm $\times$ 1.4 mm $\times$ 1.95 mm and arbitrarily cut was used. For further experimental details see Ref. [10].

Experimentally, the temperature gradient along the direction of the current flow was achieved by a gradient in the thermal coupling of the sample to the sample holder, realized by a small wedge of GE varnish between the sample and the sample holder. The tiny tilt of the sample due to the GE varnish was tested to be negligible. The sample holder used to measure the above data is shown in Fig. 10.14 together with the three settings: minimizing all gradients, a gradient along or a gradient opposite to the direction of the current. Fig. 10.14 A shows a configuration, where the sample was firmly attached to the heat sink, and which was used in the measurements of Fig. 10.8. Fig. 10.14 B and C show the configurations, where the sample was attached to the heat sink with the small wedge of GE varnish. Note that from panel B to C the direction of the wedge of GE varnish is reversed. A well-defined tilting angle was obtained by putting a small support underneath the sample. The data of Fig. 10.9 (Fig. 10.10) were measured in the setup shown in panel B (C). In Fig. 10.14 B (C) the cold spot is at the right (left) hand side of the sample. The
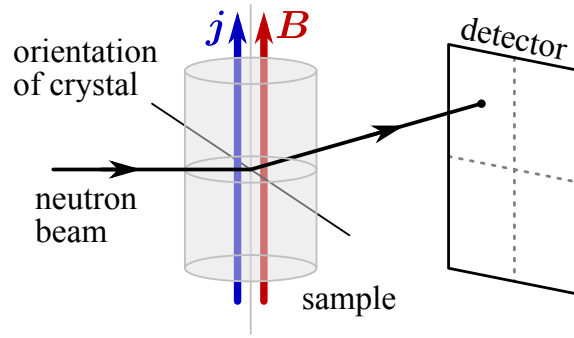
Figure 10.12: Neutron scattering setup, where the applied magnetic field $\boldsymbol{B}$ is parallel to the electric current $\boldsymbol{j}$. Both are perpendicular to the incident neutron beam. In this setup, the current is flowing parallel to the skyrmion lines.

cold side corresponds to the top (bottom) side of Fig. 10.9 (Fig. 10.10), where the arrows illustrating the thermal gradient point down (up).

The average rotation angle (defined as the maximum of the azimuthal distribution of the scattering intensity) as a function of the applied current density was also systematically studied for different samples and different temperatures. For this purpose, the temperature measured at the surface of the sample (see Fig. 10.14) was kept at a constant value, and the induced temperature gradients pointed always in the same direction. Typical results of these measurements are shown for three different temperatures in panel A of Fig. 10.15, where the azimuthal rotation angle $\Delta\phi$ as a function of the applied current density is plotted. Note that $\Delta\Phi$ remains zero, until j exceeds the critical current density j_c. From Fig. 10.15 A one can read off the critical current density $j_c \approx 10^6$ A/m^2. The observed critical current density agrees (within a factor of about two) with the observed critical current density in the Hall measurements [80], above which the skyrmion lattice starts to move, as discussed in Sec. 7.3. Above j_c, the entire scattering pattern rotates. As a function of j the rotation angle increases abruptly at $j \approx j_c$, followed by a slower increase for larger current densities. Note that the maximal average rotation angle observed was about 10°. Here, the azimuthal position and width of the scattering peaks were determined by a simple Gaussian fit.

Panel B of Fig. 10.15 shows the typical temperature differences between the surface of the sample and the heat sink as a function of the applied current density for three different temperatures. For these measurements the temperature of the sample was kept constant at a specific spot on the surface, and the temperature of the heat sink was adjusted. For increasing current density, the temperature difference between the surface of the sample and the heat sink increases smoothly (quadratic in the current density) and does not depend on the direction of the applied current, as expected. Compared to panel A, where a rotation sets in abruptly at j_c, there is no particular feature at j_c in the temperature difference, as shown in panel B of Fig. 10.15.

Interpretation of neutron scattering results and estimate of the rotation angle:
To confirm that the observed rotation in the neutron scattering results arises from the interplay of spin-torque effects and thermal gradients as sketched in Fig. 10.6, one has to exclude potential parasitic effects. The first observation is that without an electric current the skyrmion lattice as a function of temperature does not rotate [39, 41, 44]. Moreover, compared to the applied magnetic field of 175 mT the current-induced Oersted fields, which
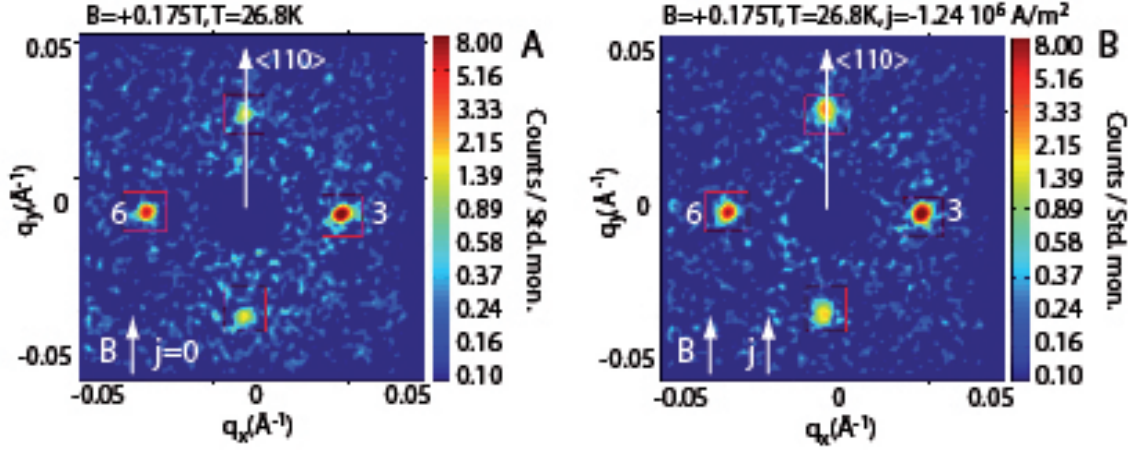
Figure 10.13: Typical diffraction patterns of the skyrmion phase in MnSi measured in the setup shown in Fig. 10.12, where the magnetic field was applied perpendicular to the incident neutron beam. Panel A shows the diffraction pattern in the skyrmion lattice for $j = 0$. The spots labelled as "3" and "6" correspond to the same spots shown in Fig. 10.8. Panel B shows the diffraction pattern for a current $j = 1.24 \cdot 10^6$ A/m^2 parallel to the skyrmion lines. In this case, the current neither leads to a rotation nor a broadening of the spots, whereas for the same current density applied perpendicular to the skyrmion lines strong rotations are seen. This Figure is taken from our publication, Ref. [10].

increase from zero at the center of the sample to about 1 mT at the surface of the sample, are negligible. Furthermore, in panel B of Fig. 10.15 we have seen that the temperature difference between the sample and the heat sink varies smoothly and is an even function of the current density j, in contrast to the rotation angle. Finally, we have seen that for a current parallel to the skyrmion lines no rotation or broadening was observed, which was also found for the helical state for the range of current densities studied. To conclude, we expect that the observation of the rotation of the skyrmion lattice can be qualitatively understood by the mechanism described at the beginning of this Chapter and sketched in Fig. 10.6, but not by heating effects. We would like to strengthen this by an estimate of the acting torques on the skyrmion lattice, and show that they can lead to a sizeable rotation angle which can be measured by neutron scattering.

The strength of the dissipative forces is not known, especially due to unknown damping parameters. However, we expect the dissipative forces not to be larger than the Magnus force, and thus for an order-of-magnitude estimate we will just consider the Magnus force quantitatively. The size of the Magnus force f_G is given by the product of the spin current and the fictitious magnetic field, $|q^e/e|\, B^e \approx 2.5$ T, corresponding to the emergent magnetic field B^e, i.e. $f_G \approx e j_s |q^e/e|\, B^e$. For moving domains, j_s has to be substituted by the spin currents in a frame of reference that is co-moving with the domain. By introducing a local temperature-dependent polarization $P(T)$ as the ratio of the spin and charge current densities times the charge e, i.e. $P(T) = e j_s / j$, the Magnus force can be estimated to

$$f_G \approx P(T) \cdot \frac{j}{10^6 \text{ A/m}^2} \frac{2.5 \cdot 10^6 \text{ N}}{\text{m}^3} \approx P(T) \cdot \frac{j}{10^6 \text{ A/m}^2} \frac{2.7 \cdot 10^{-10} k_B T_c}{a^4}, \qquad (10.23)$$

where a is the atomic lattice constant of MnSi, T_c is the ordering temperature, and k_B denotes the Boltzmann constant. As in the previous Section, we use $P(T) \approx 0.1$ for the
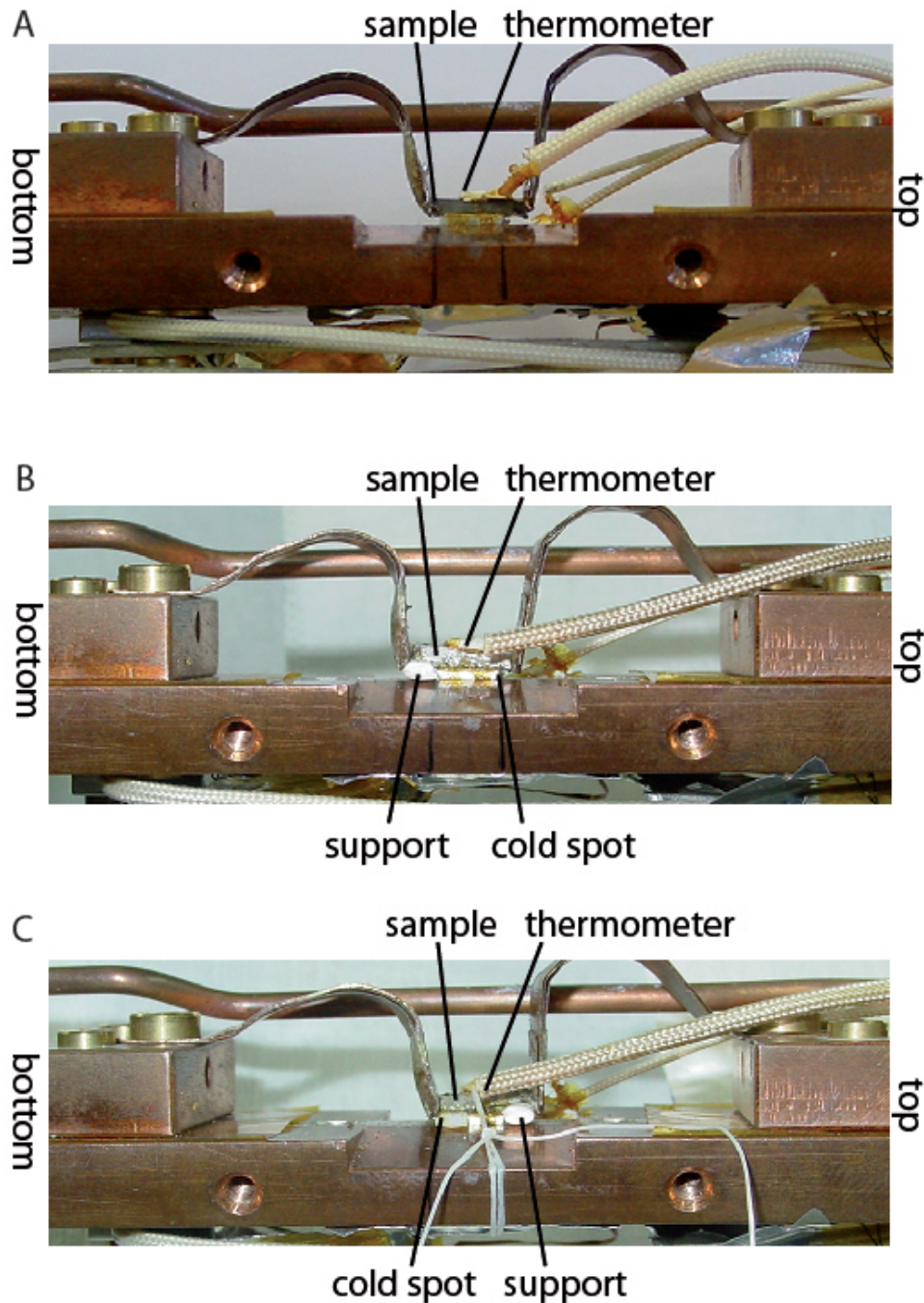
Figure 10.14: Photo of a part of the sample holder which was used for the neutron scattering data of Figs. 10.8, 10.9, and 10.10. The data of Fig. 10.8 were measured in the setup shown in panel A, where the sample was firmly attached to the copper heat sink. In panels B and C, there is a small wedge of GE varnish to induce a gradient in the heat coupling, and a small support below the sample to obtain a well defined tilting angle. The data of Fig. 10.9 (Fig. 10.10) were obtained in the setup shown in panel B (C). The cold spot which corresponds to the top of Fig. 10.9 (bottom of Fig. 10.10) is in panel B (C) at the right (left) hand side. This Figure is taken from our publication, Ref. [10].
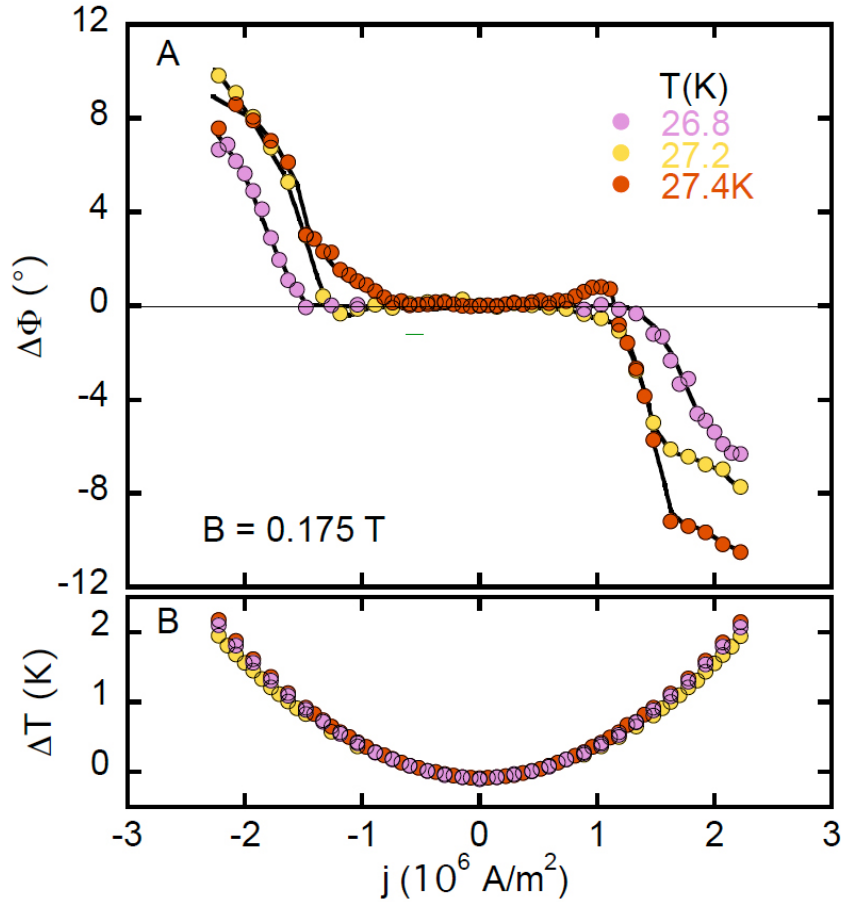
Figure 10.15: Panel A: Average rotation angle $\Delta\phi$ (in units of $1°$) of the skyrmion lattice in MnSi as a function of the applied current density for three different temperatures. The data are measured by neutron scattering in the presence of an electric current and a temperature gradient parallel to the current. The applied magnetic field strength was 0.175 T. Below the critical current density of about $j_c \approx 10^6$ A/m^2 no rotation is observed. Above j_c, the amplitude of the rotation angle depends on the current strength, and its sign depends on the direction of the applied current. Panel B shows the temperature difference between the sample holder and the surface of the sample as a function of the applied current density. The temperature of the sample surface was kept constant for each of the three temperature values given by the color code in panel A, and the temperature of the heat sink was adjusted accordingly. As expected, the temperature difference does not depend on the direction of the applied current. This Figure is taken from our publication, Ref. [10].

skyrmion lattice phase [40]. The absolute value of the Magnus force at current densities of 10^6 A/m^2 is larger compared to, *e.g.*, gravitational forces on the sample. In the microscopic units $k_B T_c/a^4$, however, it is tiny, see Eq. (10.23).

A small gradient in temperature leads to sizable variations in the amplitude of the magnetization. These lead to a gradient in the polarization $P(T)$ of the electric currents which, in total yield a gradient in the Magnus force. As indicated in Fig. 10.6, the current-induced forces will be stronger (weaker) on the cold (hot) side of the sample, leading to a net torque per volume in the direction of the skyrmion lines:

$$\boldsymbol{\mathcal{T}}_G \sim \frac{1}{V} \int d^3 r \left(\boldsymbol{r} \times \boldsymbol{f}_G(\boldsymbol{r}) \right). \tag{10.24}$$

With $|\nabla P| \approx |\frac{\partial P}{\partial T} \nabla T| \approx 0.1/10$ mm, $j \approx j_c$, and ignoring dissipative forces we obtain

$$\mathcal{T}_G \sim 10^{-10} \frac{\boldsymbol{j} \cdot \nabla P}{10^6 \, \text{Am}^{-2}} \frac{R^2}{a} \frac{k_B T_c}{a^3} \sim 10^{-5} \frac{k_B T_c}{a^3} \left(\frac{R}{1 \, \text{mm}} \right)^2, \tag{10.25}$$

where R is the radius of a skyrmion domain. From the width of the resolution-limited rocking scans in the skyrmion phase [10] one can estimate the radius from below by $R > 1 \, \mu$m. The torque induced by the interplay of the temperature gradient and the Magnus force is proportional to the applied current and to the temperature gradient, as $\nabla P \approx \frac{\partial P}{\partial T} \nabla T$. Therefore, the rotational torque due to the Magnus force changes sign when one of those directions is reversed.

The current-induced forces are balanced by pinning forces and forces of the underlying atomic lattice which orient the skyrmion lattice relative to the atomic lattice. For $j < j_c$, the skyrmion lattice is pinned. In that case, the pinning forces balance the current-induced forces exactly, and thus there are no net torques. As discussed in Section 4.3, skyrmions are only very weakly pinned by disorder. Because of the smooth magnetization structure [1] and due to the large distance between the skyrmions, even a strong defect, which locally destroys the magnetization completely, will result only in a very small pinning force, less than a few $10^{-5} \, k_B T_c/a$ per impurity. Moreover, the samples were of a very good quality and exhibited a low defect concentration with large charge carrier mean free paths of around 1000 Å. We would like to stress again that the total pinning force per volume cannot be obtained by adding up all the pinning forces of the single defects, because the pinning forces from several defects within a domain may partially average out for a sufficiently rigid skyrmion lattice.

Therefore, the observed ultra-low threshold current density $j_c \sim 10^{-6}$ A/m^2 together with the estimate for the current-induced torques, Eq. (10.23), is consistent even with a small density of strong pinning defects. Either the defect density is expected to be below 1 ppm or, if it is in reality higher, then we expect the system to be in a "collective pinning" regime, where the pinning forces of random orientation average out to a large extent due to the rigidity of the skyrmion lattice.

For $j > j_c$, the size of the rotation angle can be estimated mainly by balancing the torques from the inhomogeneous Magnus force $\mathcal{T}_G$ and the torqes due to the coupling of the skyrmion lattice to the atomic lattice $\mathcal{T}_L$.

As discussed above, due to the sixfold symmetry of the skyrmion lattice the torque $\mathcal{T}_L$ is of the form $\mathcal{T}_L \approx -\chi \sin(6\phi)$. It arises from anisotropy terms which are of at least sixth order in spin-orbit coupling, λ_{so}^6. Hence, the torque per volume resulting from the coupling to the atomic lattice can be estimated as $\mathcal{T}_L \sim -\lambda_{\text{so}}^6 \sin(6\phi)$. This factor of λ_{so}^6 has to be compared to the factor of λ_{so}^2 determining the energy density of the skyrmion

lattice [1]. Expressing the orientational torque from the lattice in units of the energy density of the skyrmion lattice yields $\mathcal{T}_L \sim -\lambda_{so}^4 \sin(6\phi) \Delta F/V$. According to specific heat measurements, $\Delta F/V$ is of the order of $\Delta F/V \sim 10^{-2} k_B T_c/a^3$ [84], so that we estimate the balancing torque per volume $\mathcal{T}_L$, which orients the skyrmion lattice relative to the atomic lattice, to

$$\mathcal{T}_L \sim -10^{-2} \lambda_{so}^4 \frac{k_B T_c}{a^3} \sin(6\phi). \tag{10.26}$$

For small rotation angles, the torque $\mathcal{T}_L$ arising from the lattice increases linearly in the rotation angle ϕ.

Note that $\mathcal{T}_L$ is independent of the size R of the domains, in contrast to the torques arising from, for example, the inhomogeneous Magnus force. Therefore, the observed broadening of the neutron scattering spots in the presence of a current may arise from a distribution of rotation angles for domains with different sizes, as will be discussed further in Section 10.4. As noted previously, also irregularly shaped domains might result in extra rotational torques of random sign. These shape-dependent torques may also contribute to the observed broadening of the neutron scattering signal. Finally, also experimental issues like demagnetization fields may lead to a broadening of the signals. Demagnetization fields may tilt the local magnetic fields inside some parts of the sample, and also potentially lead to a finite rotation angle. The average rotation angle arising from demagnetization fields is, however, zero, but the neutron scattering peaks are broadened even for $j = 0$ [1].

The rotation angle is finally determined by the balance of $\mathcal{T}_G$ and $\mathcal{T}_L$. Since the balancing torque from the lattice $\mathcal{T}_L$ is so tiny (due to the prefactor $10^{-2}\lambda_{so}^4$ in Eq. (10.26)), even a small torque from the inhomogeneous Magnus force $\mathcal{T}_G$ may lead to the rotation angles observed in the experiments even for moderately large domains. When taking into account that charge carriers are experimentally determined to be hole-like in MnSi [40, 115], we would like to note that the signs of the torques and forces considered above are consistent with the experimental results.

In this Section, we have considered the neutron scattering experiments which observe a current-induced rotation of the skyrmion lattice in the presence of a temperature gradient. We have explained the experiment as an interplay of three tiny forces acting on the skyrmion lattice: current-induced forces that act via spin-transfer torques, pinning forces, and forces due to anisotropy terms originating from the coupling of the magnetic structure to the atomic lattice. We have shown that in the presence of a temperature gradient these three forces are able to explain the origin of the rotation and the existence of a threshold current density. Furthermore, by balancing all torques it is possible to determine the rotation angle. As we discuss in more detail in the next Section, we expect that for even higher current densities or larger temperature gradients not only a rotation by a finite angle, but a continuous rotation sets in. We also show that the maximal rotation angle is given by $15°$, and therefore the experiments performed so far were probably not too far away from (or may have already observed indirectly) a continuous rotation.

10.4   Rotational Torques due to Field or Temperature Gradients

In this Section, we present a theory for the rotational torques due to small gradients in the applied magnetic field or in the temperature. We describe the current-induced rotation by a finite angle up to $15°$ or – for larger gradients – a continuous rotation with a finite angular velocity within the framework of the LLG equation, Eq. (8.12), and as before we treat pinning forces phenomenologically.
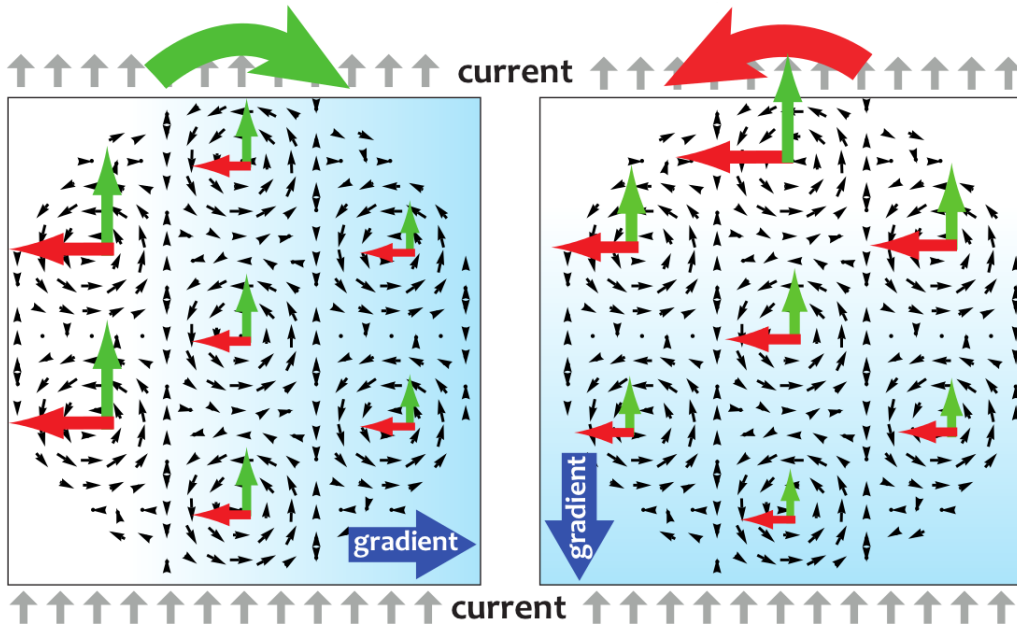
Figure 10.16: Schematic illustration of the forces acting on the skyrmion lattice in parallel and perpendicular to the direction of the current. The small black arrows illustrate the local orientation of the magnetization projected into the plane perpendicular to the magnetic field, and the red horizontal and the green vertical arrows denote the acting forces. For a static, non-moving skyrmion lattice the red arrows correspond to the Magnus force and the green arrows to the dissipative forces. These forces change smoothly across a domain when a temperature or field gradient is present. The smooth gradient in these forces then leads to rotational torques. Note that the rotational torques do depend very sensitively on the relative orientation of the current and the gradient on one hand and on the other also on the direction in which the skyrmion lattice drifts. For example, for the static skyrmion lattice, in the left (right) panel where the current and the gradient are perpendicular (parallel) to each other, the dissipative (Magnus) forces induce the rotation. We published this Figure in Ref. [71].

The basic idea underlying the theoretical analysis was shown already in Fig. 10.6 for the case of a temperature gradient and an electric current parallel to the direction of the temperature gradient. Fig. 10.16 shows a slightly generalized schematic plot of the rotational torques. The right panel corresponds to Fig. 10.6, where the current and the gradient are parallel to each other, but in the left panel of Fig. 10.16 they are perpendicular to each other. As before, the red horizontal and the green vertical arrows illustrate the forces perpendicular and parallel to the applied current, respectively, and the small black arrows sketch the projection of the skyrmion lattice onto the direction perpendicular to the applied magnetic field. Note that in the static case the red horizontal (green vertical) arrows correspond to the Magnus (dissipative) forces, but for a moving skyrmion lattice the situation is more complicated. The background color denotes the gradient, where the different background color (blue instead of red as in Fig. 10.6) should indicate that we are not necessarily considering a temperature gradient, but also, for example, magnetic field gradients in this Section. As can be seen from the Figure, in the left panel the green vertical arrows are responsible for the torques, whereas in the right panel the rotation is induced by the red horizontal arrows, indicated by the colored curved arrow above

each plot. This shows that the rotational torques depend very sensitively on the relative orientation of the current and the gradient. Whether the torque stems from the Magnus forces or the dissipative forces depends therefore on the relative orientation of current and gradient, and on the direction of the drift velocity of the skyrmion lattice.

In this Section, we assume that $\boldsymbol{v}_s$ is small compared to all characteristic velocity scales of the skyrmion lattice (*e.g.* $T_c - T$ multiplied with the skyrmion distance), as before. Hence, we derive our theory only to linear order in $\boldsymbol{v}_s$. Furthermore, we consider only tiny gradients, *i.e.* their effects on the length scale set by the skyrmion distance is negligible, as it is the case in the experiments described in the previous Section. Nevertheless, when multiplying the tiny gradient with the size of a domain of radius r_d of the skyrmion lattice, which is much larger than the size of the skyrmion distance, this leads to a sizable variation of the forces across the domain and thus to measureable rotational torques. Note that in MnSi the distance between skyrmions is of the order of 20 nm, but the size of a domain can be several hundred µm [67]. In the following, we denote by λ the quantity with the gradient, *e.g.* λ is B or $T_c - T$. We also assume that the total change of λ across a domain remains small compared to λ, *i.e.* $r_d|\nabla\lambda| \ll \lambda$. In this limit, the drift velocity $v_d \lesssim v_s$ as well as the angular velocity $\partial_t\phi \propto \boldsymbol{v}_s \cdot \nabla\lambda$ characterizing the rotational motion remain small. Below we show that in this limit even the velocity at the boundary of the domain, $\partial_t\phi\, r_d$, remains small. Moreover, in the following we neglect the effects of torques due to distortions as well as macroscopic deformations of the skyrmion lattice, and focus only on torques due gradients in the acting forces. We again consider the ansatz given in Eq. (10.2):

$$\hat{\boldsymbol{\Omega}}(\boldsymbol{r},t) = \boldsymbol{R}_{\phi(t)} \cdot \hat{\boldsymbol{\Omega}}_0\left(\boldsymbol{R}_{\phi(t)}^{-1} \cdot (\boldsymbol{r} - \boldsymbol{v}_d t)\right), \tag{10.27}$$

where $\hat{\boldsymbol{\Omega}}_0(\boldsymbol{r})$ describes the static skyrmion lattice.[6] To obtain the equation for the rotational torques which determine the rotations around the $\boldsymbol{B}$ axis, by multiplying the LLG equation, Eq. (8.12), by the generator of the rotational mode:

$$\hat{\boldsymbol{G}}_{\rm rot}\,\hat{\boldsymbol{\Omega}} = \partial_\phi\hat{\boldsymbol{\Omega}} = \hat{\boldsymbol{B}} \times \hat{\boldsymbol{\Omega}} - (\hat{\boldsymbol{B}} \cdot (\Delta\boldsymbol{r} \times \nabla))\hat{\boldsymbol{\Omega}} \tag{10.28}$$

and integrate over $\boldsymbol{r}$. Note that the second part of the generator is linear in $\Delta\boldsymbol{r}$ and for large domains much larger than the first term.

In the case of a gradient, this procedure leads to several types of contributions. The first type arising from $\hat{\boldsymbol{B}}\times\hat{\boldsymbol{\Omega}}$ can, however, be neglected whenever the second (much larger) term of the generator contributes. The second part of the generator induces torques of the form $\boldsymbol{r} \times \boldsymbol{f}$, where the force f_i is obtained by multiplying $\nabla_i\hat{\boldsymbol{\Omega}}$ with the terms of the Landau-Lifshitz-Gilbert equation, Eq. (8.12). In the presence of a small gradient of the parameter λ, we obtain $\boldsymbol{f}(\lambda(r)) \approx \boldsymbol{f}(\lambda) + (\boldsymbol{r}\cdot\nabla\lambda)\partial_\lambda\boldsymbol{f}$, and therefore

$$\begin{aligned}
\int d^2r\,\hat{\boldsymbol{B}} \cdot [\boldsymbol{r} \times \boldsymbol{f}(\lambda(\boldsymbol{r}))] &\approx \int d^2r\,\left(\hat{\boldsymbol{B}} \cdot [\boldsymbol{r} \times \partial_\lambda\boldsymbol{f}]\right)(\boldsymbol{r}\cdot\nabla\lambda) \\
&= \int d^2r\,\epsilon_{ijk}\,B_i r_j(\partial_\lambda f_k)\,r_l\,(\partial_l\lambda) \\
&\approx \left(\frac{1}{2}\int d^2r\,\boldsymbol{r}^2\right)\frac{1}{A}\int d^2r\,\epsilon_{ilk}\,B_i(\partial_\lambda f_k)\,(\partial_l\lambda) \\
&= \frac{A}{4\pi}\hat{\boldsymbol{B}} \cdot \left[\nabla\lambda \times \partial_\lambda\int d^2r\,\boldsymbol{f}\right],
\end{aligned} \tag{10.29}$$

---

[6]Note that within this ansatz one obtains the same solution for the drift velocity as in Chapter 9 to leading order in the gradient, *i.e.* to order $(\nabla\lambda)^0$ (where for the undistorted skyrmion lattice no rotations occur).

where A is the area of the domain. In the last approximation we used that a periodic function superimposed with a smooth increase can be approximated by its average value times the increasing function. Required for this approximation is that the periodicity of the periodic function is small compared to the length scale on which the increasing function varies. Thus, from this calculation we obtain

$$\int d^2 r\, \hat{\boldsymbol{B}} \cdot [\boldsymbol{r} \times \boldsymbol{f}(\lambda(\boldsymbol{r}))] \approx \frac{A}{4\pi} \hat{\boldsymbol{B}} \cdot \left[\nabla\lambda \times \partial_\lambda \int d^2 r\, \boldsymbol{f}\right]. \tag{10.30}$$

Because we consider a rigid skyrmion lattice, where $\boldsymbol{v}_d$ is constant across the domain, it is essential to take the derivative with respect to λ for a fixed drift velocity, i.e. $\frac{\partial}{\partial\lambda}\boldsymbol{f}\big|_{\boldsymbol{v}_d}$. Since the sum of all contributing forces, Eq. (9.16), vanishes, $\sum_\alpha \boldsymbol{f}^\alpha(\lambda, \boldsymbol{v}_d) = 0$, it is of course $\frac{d}{d\lambda}\sum_\alpha \boldsymbol{f}^\alpha = 0$, but $\frac{\partial}{\partial\lambda}\sum_\alpha \boldsymbol{f}^\alpha\big|_{\boldsymbol{v}_d}$ is finite. Furthermore, as in the last Sections, we have neglected all terms that are odd in $\boldsymbol{r}$ in Eq. (10.30), which vanish for symmetrically shaped domains.

Another contribution comes from the time derivatives $\partial_t \hat{\boldsymbol{\Omega}}$ in Eq. (8.12). Within our ansatz:

$$\partial_t \hat{\boldsymbol{\Omega}} = \partial_t\phi\, \partial_\phi \hat{\boldsymbol{\Omega}} - (\boldsymbol{v}_d \cdot \nabla)\hat{\boldsymbol{\Omega}}. \tag{10.31}$$

The term $(\boldsymbol{v}_d \cdot \nabla)\hat{\boldsymbol{\Omega}}$ leads to contributions of the types discussed above, but $\partial_t\phi\, \partial_\phi \hat{\boldsymbol{\Omega}}$ induces additional torques. When multiplying $\partial_t\phi\, \partial_\phi \hat{\boldsymbol{\Omega}}$ with the generator of the rotation mode, $\partial_\phi \hat{\boldsymbol{\Omega}}$ of Eq. (10.28), one immediately obtains terms that are quadratic in $\Delta\boldsymbol{r}$ and that are independent of $\nabla\lambda$ like $\alpha\, \partial_t\phi \int d^2 r M[(\hat{\boldsymbol{B}}[\Delta\boldsymbol{r} \times \nabla])\boldsymbol{\Omega}]^2$. This term is describes the friction torque per volume when a domain is rotating with an angular velocity $\partial_t\phi$. For a rotating domain, the local rotation velocity grows linearly with the distance from the center of the rotating domain. Therefore, also the friction forces increase linearly with the distance from the center. From this follows that terms like $\alpha\, \partial_t\phi \int M[(\hat{\boldsymbol{B}}[\Delta\boldsymbol{r} \times \nabla])\boldsymbol{\Omega}]^2/A$ grow also linear with the area of the domain A, as expected.

Finally, a type of rotational torques originates from the coupling of the magnetic lattice to the underlying atomic lattice. As discussed above, it accounts for the fact that the skyrmion lattice has a preferred orientation with respect to the atomic lattice without an applied current or gradients. The corresponding torque per unit cell is given by

$$\mathcal{T}_L \approx -\chi \sin(6\phi) \tag{10.32}$$

Note that we have to consider this term, because it is the leading contribution arising to zeroth order in $\nabla\lambda$ and $\boldsymbol{v}_s$, despite the fact that it does not scale with the size of the domain as the other terms.

In total, we obtain an equation for the acting torques which have to balance each other:

$$0 = \mathcal{T}_L + \mathcal{T}_G + \mathcal{T}_D + \mathcal{T}_{\text{pin}}, \tag{10.33}$$

where the torques $\mathcal{T}_G$, $\mathcal{T}_D$, and $\mathcal{T}_{\text{pin}}$ are given by:

$$\mathcal{T}_G = \frac{A}{4\pi}\nabla\lambda \cdot \left[\frac{\partial(\mathcal{G}\boldsymbol{v}_s)}{\partial\lambda} - \frac{\partial\mathcal{G}}{\partial\lambda}\boldsymbol{v}_d\right], \tag{10.34a}$$

$$\mathcal{T}_D = -\frac{A\tilde{\alpha}\mathcal{D}}{2\pi}\partial_t\phi - \frac{A}{4\pi}\nabla\lambda \cdot \left[\hat{\boldsymbol{B}} \times \left(\frac{\partial(\mathcal{D}\tilde{\beta}\boldsymbol{v}_s)}{\partial\lambda} - \frac{\partial(\mathcal{D}\tilde{\alpha})}{\partial\lambda}\boldsymbol{v}_d\right)\right], \tag{10.34b}$$

$$\mathcal{T}_{\text{pin}} = \frac{A}{4\pi}\nabla\lambda \cdot [\hat{\boldsymbol{B}} \times \hat{\boldsymbol{v}}_d]\frac{\partial F_{\text{pin}}}{\partial\lambda}, \quad F_{\text{pin}} \equiv |\boldsymbol{F}_{\text{pin}}|. \tag{10.34c}$$

Eq. (10.33) describes how a rotational torque around the magnetic field axis is created by the applied current. Note that the contributing torques linear in $\nabla\lambda$ are all of the form $(\nabla\lambda)^T \cdot \mathcal{M} \cdot \boldsymbol{v}$, where $\mathcal{M}$ denotes a 3×3 matrix and $\boldsymbol{v}$ a velocity. For example, neglecting the possible λ-dependence of $\boldsymbol{v}_s$, for the torque $\mathcal{T}_\mathcal{G}$ due to the Magnus force one finds $\boldsymbol{v} = \boldsymbol{v}_s - \boldsymbol{v}_d$ and $\mathcal{M} = \frac{A}{4\pi}\frac{\partial\mathcal{G}}{\partial\lambda}\mathbb{1}$ with the 3×3 unit matrix $\mathbb{1}$. Actually, the structure of the gradient-induced torques is mainly fixed by the symmetries of the skyrmion lattice. To see this, let us for simplicity consider a magnetic field in $\hat{\boldsymbol{z}}$ direction. The sixfold rotation symmetry of the skyrmion lattice around the magnetic field direction (which corresponds here to the $\hat{\boldsymbol{z}}$ axis) reduces the 3×3 matrix $\mathcal{M}$ for all contributions to an effective 2×2 matrix $\widetilde{\mathcal{M}}$ in the xy plane, which is of the form $\widetilde{\mathcal{M}}_{ij} \sim c_1\,\delta_{ij} + c_2\,\epsilon_{ij}$ with parameters c_1 and c_2. Furthermore, the magnetic structure and the magnetic field is invariant under the combined symmetry of time-reversal and a rotation by π around an $\langle 100 \rangle$ axis in the xy-plane. From this follows that matrix $\widetilde{\mathcal{M}}_{ij}$ has to be proportional to δ_{ij} (ϵ_{ij}) for the reactive (dissipative) torques.

From above equations it is clear that for a given $\nabla\lambda$ the strength of the torques depends on one hand on the λ dependence of the parameters $\mathcal{G}$, $\mathcal{D}$, $\tilde{\alpha}$, $\tilde{\beta}$, $\boldsymbol{v}_s$, and F_{pin}, and on the other on the relative orientation between the drift velocity and the applied current. In the limit $\boldsymbol{v}_d = 0$, the torque arising from the Magnus force does not contribute if the current and the gradient are perpendicular to each other, and is largest for a parallel configuration. For the dissipative torques $\mathcal{T}_D$ it is the other way around. They contribute most when gradient and current are perpendicular to each other. This corresponds to the situation sketched in Fig. 10.16, when regarding the red (green) arrows as the Magnus (dissipative) forces. For a finite $\boldsymbol{v}_d$, this simple picture does not apply as, for example, the torque due to the Magnus forces almost vanishes in the limit $\boldsymbol{v}_d \approx \boldsymbol{v}_s$.

Eq. (10.33) is of the following structure:

$$\sin 6\phi = -\gamma\,\partial_t\phi + \nabla\lambda \cdot \boldsymbol{V_s}, \tag{10.35}$$

where

$$\gamma = \frac{A\tilde{\alpha}\mathcal{D}}{2\pi\chi}. \tag{10.36}$$

To obtain the vector $\boldsymbol{V_s} = \boldsymbol{V_s}[\boldsymbol{v}_s]$ one has to first solve Eq. (9.16) for $\boldsymbol{v}_d$ as a function of $\boldsymbol{v}_s$. Inserting $\boldsymbol{v}_d$ into Eq. (10.33) and dividing Eq. (10.33) by $-\chi$ one obtains $\boldsymbol{V_s}$ by comparison of Eqs. (10.32)–(10.35). In Chapter 9, we discussed that a closed solution for $\boldsymbol{v}_d$ is not possible as long as $\boldsymbol{F}_{\mathrm{pin}}$ is not known. However, assuming that we have already expressed $\boldsymbol{v}_d$ as a function of $\boldsymbol{v}_s$, then $\boldsymbol{V_s}$ is given by:

$$\boldsymbol{V_s}[\boldsymbol{v}_s] = \frac{A}{4\pi\chi}\left\{\left[\frac{\partial(\mathcal{G}\boldsymbol{v}_s)}{\partial\lambda} - \frac{\partial\mathcal{G}}{\partial\lambda}\boldsymbol{v}_d\right] - \left[\hat{\boldsymbol{B}} \times \left(\frac{\partial(\mathcal{D}\tilde{\beta}\boldsymbol{v}_s)}{\partial\lambda} - \frac{\partial(\mathcal{D}\tilde{\alpha})}{\partial\lambda}\boldsymbol{v}_d\right)\right] + [\hat{\boldsymbol{B}} \times \hat{\boldsymbol{v}}_d]\frac{\partial F_{\mathrm{pin}}}{\partial\lambda}\right\} \tag{10.37}$$

The vector $\boldsymbol{V_s}$ contains all information about the coupling of the current to the small gradients, and it includes contributions from the Magnus, the dissipative and the pinning forces. Note that $\boldsymbol{V_s}$ is proportional to the area A of the domain as is γ, and for $\boldsymbol{v}_s = 0$ we get $\boldsymbol{V_s}[0] = 0$. Eq. (10.35) is for fixed γ, $\boldsymbol{V_s}$, and $\nabla\lambda$ a simple differential equation in time, for which a closed solution exists.

First of all, one observes that if $\boldsymbol{V_s}$ and $\nabla\lambda$ are perpendicular to each other, Eq. (10.35) is solved by $\phi = 0$, and no rotation occurs. This will be discussed further below. Furthermore, for $j < j_c$, when pinning forces cancel all reactive and dissipative forces, the solution of Eq. (10.35) is trivial. Neither a motion nor a rotation of the skyrmion lattice
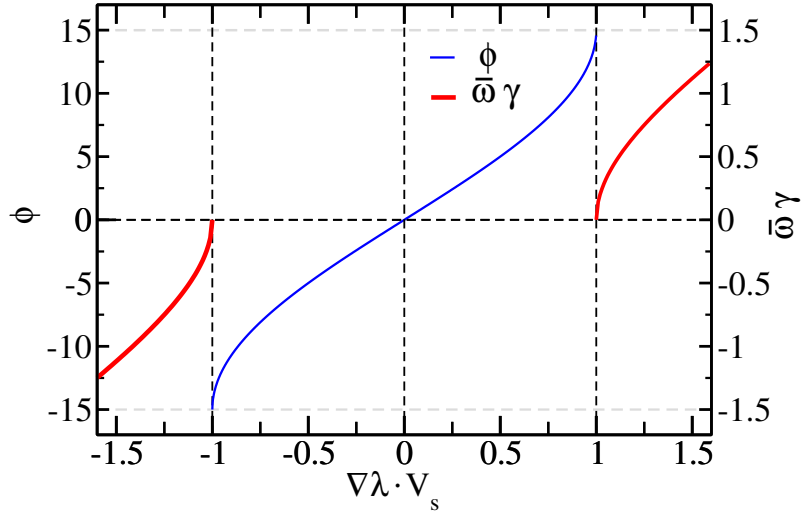
Figure 10.17: Rotation angle ϕ (in units of 1°) and angular velocity $\bar{\omega}$ times the prefactor γ as a function of $\nabla\lambda \cdot \boldsymbol{V_s}$. We published this Figure in Ref. [71].

occur, *i.e.* $\boldsymbol{V_s} = 0$ and $\phi = 0$ within our theory. As mentioned already, even below j_c a slow creep motion might occur. Whether creep also leads to rotations is unclear. The recent experiments seem, however, to exclude pronounced rotations due to creep, since the observed onset of the rotation is rather sharp [10], see panel (A) of Fig. 10.15.

For $j > j_c$, the domains move, and $\boldsymbol{V_s}$ will generally be finite. In this case, the size of $\nabla\lambda \cdot \boldsymbol{V_s}$ determines whether a rotation by a finite angle or a continuous rotation will set in. In the following, we discuss Eq. (10.35) from different perspectives. First, we consider a fixed $\boldsymbol{V_s}$ and γ, and analyze it for various strengths of the gradient. Then we discuss its dependence on the strength of the current as well as the different relative orientations of currents and gradients. Afterwards, we consider the domain size dependence. Finally, we compare our theory to the present experimental situation and suggest new experiments to further explore the coupling of magnetism and currents.

Dependence on size of gradients: For $|\nabla\lambda \cdot \boldsymbol{V_s}| < 1$, a solution of Eq. (10.35) is given by

$$\phi = \frac{1}{6}\arcsin(\nabla\lambda \cdot \boldsymbol{V_s}), \tag{10.38}$$

which shows that the gradient induces a rotation by a finite angle (*i.e.* $\partial_t \phi = 0$). For increasing $\nabla\lambda$ (and $\nabla\lambda \cdot \boldsymbol{V_s} \neq 0$) the rotation angle increases up to the maximal possible value of $\pi/12 = 15°$. For $|\nabla\lambda \cdot \boldsymbol{V_s}| > 1$, the domain rotates with the average angular velocity

$$\bar{\omega} = \frac{\sqrt{(\nabla\lambda \cdot \boldsymbol{V_s})^2 - 1}}{\gamma}, \tag{10.39}$$

and Eq. (10.35) is solved by

$$\phi(t) = \frac{1}{3}\arctan\left[\frac{1 + \gamma\bar{\omega}\tan(3\bar{\omega}t)}{\sqrt{1 + \gamma^2\bar{\omega}^2}}\right]. \tag{10.40}$$

In Fig. 10.17, the rotation angle ϕ and the average angular velocity $\bar{\omega}$ are plotted as a function of $\nabla\lambda \cdot \boldsymbol{V_s}$. The solution for the rotation angle ϕ, Eq. (10.40), as a function of
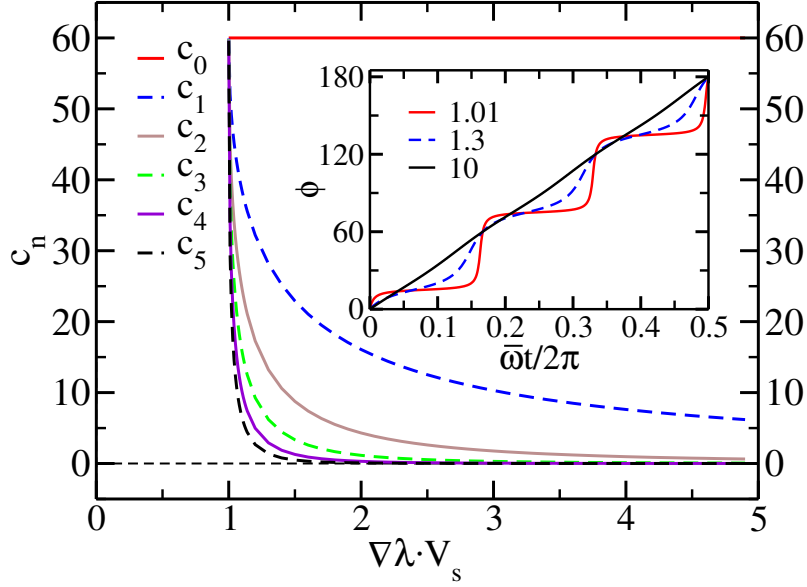
Figure 10.18: Inset: Rotation angle (in units of $1°$) as a function of time for three different strengths of $\nabla\lambda \cdot \boldsymbol{V_s} > 1$. When increasing $\nabla\lambda \cdot \boldsymbol{V_s}$, the rotation gets more and more harmonic. This can also be seen by considering the Fourier coefficients of $\partial_t\phi$ given by $c_n = |\int_0^{2\pi/6\bar\omega} \partial_t\phi e^{in6\bar\omega t}\, dt|$ shown in the main panel as a function of $\nabla\lambda \cdot \boldsymbol{V_s}$. We published this Figure in Ref. [71].

time is shown in the inset of Fig. 10.18 for different strengths of $\nabla\lambda \cdot \boldsymbol{V_s}$. Just above the threshold, $\nabla\lambda \cdot \boldsymbol{V_s} \gtrsim 1$, the rotation is not homogeneous. It is slowed down close to an angle of $15°$ (plus multiples of $60°$). In the limit $|\nabla\lambda \cdot \boldsymbol{V_s}| \gg 1$, the average angular velocity $\bar\omega \approx (\nabla\lambda \cdot \boldsymbol{V_s})/\gamma$ becomes independent of the domain size, as both γ and $\boldsymbol{V_s}$ are linear in the area A of the domain. In that limit, the domain rotates uniformly with $\phi = \bar\omega t$. In the main plot of Fig. 10.18, the modulus of the Fourier components of $\partial_t\phi$, $|c_n| = |\int e^{i6\bar\omega nt}\partial_t\phi\, dt|$ as a function of $\nabla\lambda \cdot \boldsymbol{V_s}$ is shown. At the threshold $\nabla\lambda \cdot \boldsymbol{V_s} = 1$, all Fourier components contribute equally to $\partial_t\phi$, whereas for larger gradients the rotation gets more uniform. The reason for plotting the Fourier components of $\partial_t\phi$ is that it might be possible to measure them in experiments. For instance, exploiting the emergent electric field $\boldsymbol{E}^e$, which can be measured in a Hall experiment [80] as discussed above, contains a contribution proportional to $\partial_t\phi$ for continuously rotating domains.

To check whether the velocity at the boundary of a domain $v_{\rm b}$ arising from the rotation still remains small for fixed $\bar\omega$ and with $v_{\rm b} = \bar\omega\, r_d$, where r_d is the radius of the domain, we estimate

$$v_{\rm b} = \bar\omega\, r_d \approx \frac{|\nabla\lambda \cdot \boldsymbol{V_s}|}{\gamma} r_d \ll |\boldsymbol{V_s}|\lambda/\gamma \lesssim v_s/\tilde\alpha. \tag{10.41}$$

In the penultimate inequality, we used our assumption that the gradients across the sample and therefore also across a single domain are small, $r_d |\nabla\lambda| \ll \lambda$. We expect that the velocity at the boundary of a domain $v_{\rm b}$ is typically smaller than the velocity of the domain v_d, although our estimate does not exclude that v_b might be somewhat larger than v_s or v_d. Eq. (10.41) also implies that the breakup of domains due to the rotation or other violent phenomena will probably not occur. To summarize, the solution of Eq. (10.35) for various $\nabla\lambda$ at fixed $\boldsymbol{V_s}$ is rather universal and independent of microscopic details. In the following, we discuss Eq. (10.35) for different current strengths.

Dependence on strength of current: As discussed above, for current densities below the threshold current density, $j < j_c$, we get $\boldsymbol{V_s} = 0$, and neither a motion nor a rotation of the skyrmion lattice occurs. Directly at the current threshold, when the domain just starts to move and the drift velocity is tiny ($v_d \approx 0$), $\boldsymbol{V_s}$ jumps to the finite value

$$\boldsymbol{V_s}|_{v_s=v_{\text{pin}}} = -\frac{A}{4\pi\chi} \left[\left(-\frac{\partial \mathcal{G} \boldsymbol{v}_s}{\partial \lambda} + \frac{\mathcal{G}\boldsymbol{v}_s}{F_{\text{pin}}} \frac{\partial F_{\text{pin}}}{\partial \lambda} \right) + \hat{\boldsymbol{B}} \times \left(\frac{\partial \mathcal{D}\tilde{\beta}\boldsymbol{v}_s}{\partial \lambda} - \frac{\mathcal{D}\tilde{\beta}\boldsymbol{v}_s}{F_{\text{pin}}} \frac{\partial F_{\text{pin}}}{\partial \lambda} \right) \right]. \quad (10.42)$$

The jump is independent of the two damping constants α, α', and their gradients (see Fig. 10.20) as $v_d \approx 0$ at the depinning transition. This jump of $\boldsymbol{V_s}$ leads to a jump of the rotation angle if $|\nabla\lambda \cdot \boldsymbol{V_s}| < 1$. Otherwise, for $|\nabla\lambda \cdot \boldsymbol{V_s}| > 1$ a continuous rotation sets in immediately. However, the behavior of $\nabla\lambda \cdot \boldsymbol{V_s}$ as a function of $\boldsymbol{v}_s$ is complex. Upon increasing the current, $\nabla\lambda \cdot \boldsymbol{V_s}$ can either increase, decrease or even change its sign, depending on the direction of $\nabla\lambda$ and on the fact which of the forces changes most strongly upon varying λ.

Motivated by the experiments dicussed in the previous Section we now study the case of a temperature gradient, *i.e.* $\lambda = t$. For our numerical calculations we assume that the temperature dependence of the pinning force $\boldsymbol{F}_{\text{pin}} = -4\pi M v_{\text{pin}} f(v_d/v_{\text{pin}})$ arises only from the temperature dependence of the magnetization M. The latter we obtain from the Ginzburg-Landau theory as well as the temperature dependence of the other parameters $\mathcal{G}$, $\mathcal{D}$, and $\mathcal{D}'$, see Fig. 9.2. This assumption is based on the experimental observation [80] that the critical current is almost temperature independent, at least for a certain range of temperatures.

Moreover, we first assume that all damping constants are temperature independent, and that the temperature gradients are independent of the applied current as well, but these two assumptions are relaxed below. In this case, a typical result for the rotation angle and the angular velocity of a skyrmion domain as a function of $\boldsymbol{v}_s$ in the presence of a temperature gradient is shown in Fig. 10.19. In the left (right) panel of the Figure, the temperature gradient is applied parallel (perpendicular) to $\boldsymbol{v}_s$, and the rotation angle ϕ decreases (increases) after the initial jump. In the parallel configuration, the rotation angle rises again for larger values of $\boldsymbol{v}_s$. When the rotation angle reaches its maximal value of $15°$, the continuous rotation sets in. Within the assumption that all damping parameters are temperature independent, the qualitative shape of these curve appears to be rather independent of the precise values of the various parameters.

In the experiments of Ref. [10], described in the previous Section, the temperature gradients are induced by the currents and are therefore not independent of the current strength. As can be seen from Fig. 10.15, the temperature gradients grow quadratically with v_s. In Fig. 10.20, we take this extra effect into account, and plot the rotation angle for small current densities (blue thin curves) again for the parallel (left panel) and perpendicular (right panel) configuration of $\nabla\lambda$ and $\boldsymbol{v}_s$. This does not lead to any qualitative changes (note the different scale on the x axis). However, one can obtain qualitatively different results when including a small temperature dependence of the Gilbert damping α. This is illustrated by the thick green curves in Fig. 10.20. In that case, we obtain that after the initial jump the rotation angle increases for both the parallel and perpendicular configuration. The latter can reproduce qualitatively the experimentally observed behavior, as discussed below. To sum up, the behavior of ϕ and $\bar{\omega}$ as a function of the strength of the current for fixed $\nabla\lambda$ is much more complex than the dependence on $\nabla\lambda$ for fixed $\boldsymbol{V_s}$. Furthermore, it depends very sensitively on the details of the theory.
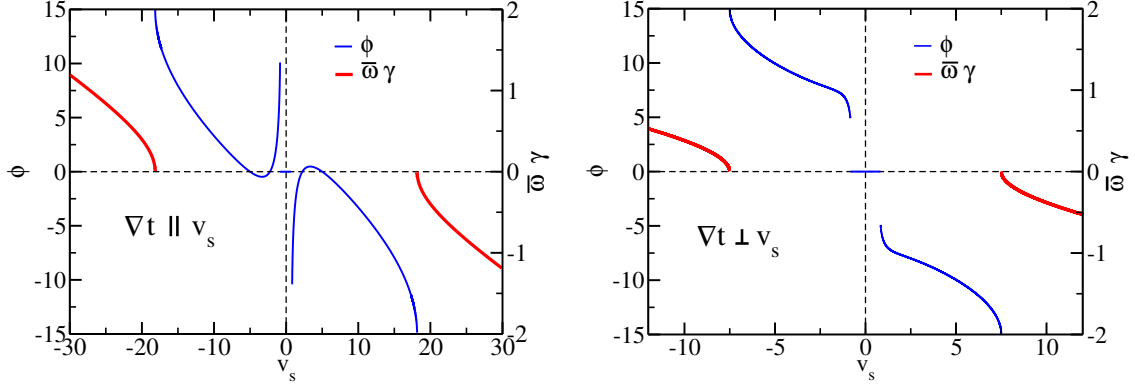
Figure 10.19: Rotation angle ϕ (in units of $1°$) and angular velocity $\bar{\omega}\gamma$ as a function of v_s for a temperature gradient parallel ($\nabla t \| \boldsymbol{v}_s$, $\nabla t = (-0.1, 0, 0)^T$, left panel) and perpendicular ($\nabla t \perp \boldsymbol{v}_s$, $\nabla t = (0, -0.05, 0)^T$, right panel) to the current for the parameters $\alpha = 0.2$, $\beta = 0.45$, $\alpha' = 0.01$, $\beta' = 0.2$, $A/\chi = 200$, $t = -1$, $\boldsymbol{B} = (0, 0, 1/\sqrt{2})^T$, $v_{\rm pin} = 1$, and $f = 1$. For both geometries one observes a jump of ϕ at $v_s \approx v_{\rm pin}$ from zero to a finite rotation angle. After the initial jump the rotation angle increases for the perpendicular configuration (right panel), while for the parallel arrangement (left panel) first a drop and then an increase up to the maximal angle of $15°$ occurs. For larger v_s, a continuous rotation characterized by the angular velocity $\bar{\omega}$ sets in for both configurations. For the calculation we assumed that the damping parameters and $v_{\rm pin}$ are independent of t. We published this Figure in Ref. [71].
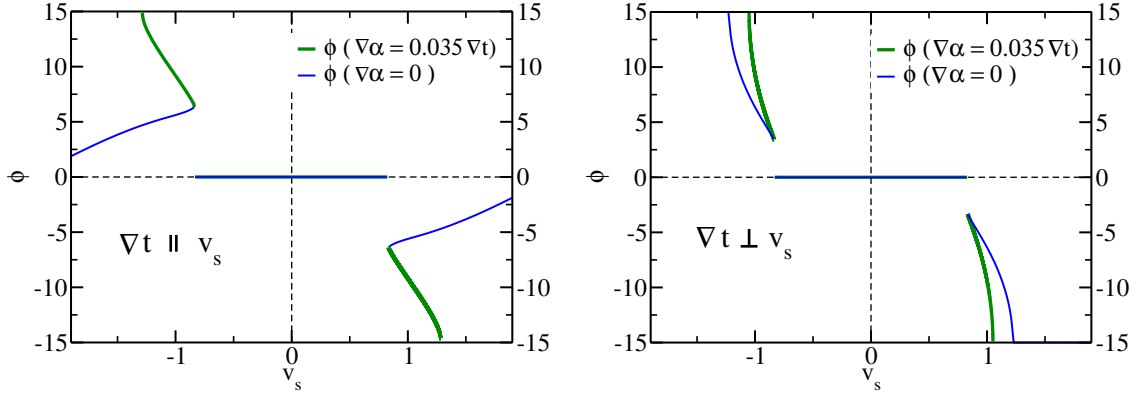
Figure 10.20: Rotation angle ϕ (in units of $1°$) as a function of v_s for a temperature gradient parallel ($\nabla t \| \boldsymbol{v}_s$, left panel) and perpendicular ($\nabla t \perp \boldsymbol{v}_s$, right panel) to the current. The parameters are the same as in Fig. 10.19 with two exceptions. First, we have taken into account that in the experiments of Ref. [10] the temperature gradient grows with the square of the applied current, $\nabla t = (-0.1 v_s^2, 0, 0)^T$ and $\nabla t = (0, -0.05 v_s^2, 0)^T$, for current parallel and perpendicular to $\boldsymbol{v}_s$, respectively. Second, for the thin blue curve we assumed (as in Fig. 10.19) that the damping constants are independent of t, while for the thick green curve a weak temperature dependence of the damping constant α, $\nabla \alpha = 0.035 \nabla t$, was assumed. This parameter has been chosen to reflect the experimental observation, see Fig. 10.23. For even stronger currents (not measured experimentally and not shown in the figure), the size of the torque drops again, and a finite rotation angle is obtained for $1.57 \lesssim v_s \lesssim 2.53$ in the parallel configuration with the temperature-dependent damping constant α. We published this Figure in Ref. [71].

Dependence on the relative orientation of the current and the gradient: The rotational torques on the system depend strongly on the relative orientation of the gradient and the current, as shown in Figs. 10.19 and 10.20. The reason for this is that one probes different physical mechanisms for different relative orientations between gradient and current. Above we discussed this already for the simple case of a static domain without pinning forces. In general, however, the situation is more complex. All directional information is encoded in the function $\boldsymbol{V_s}[\boldsymbol{v_s}]$ which contains unfortunately a rather large number of unknown parameters like the functional form of the pinning forces and their dependence on λ, or the size and the λ-dependence of the damping constants. Therefore, in the following we discuss only a few limiting cases, as a drastically simplified picture occurs in regimes when only two forces dominate in Eq. (9.16). Remember that to obtain $\boldsymbol{V_s}[\boldsymbol{v_s}]$ one has to first solve Eq. (9.16) for $\boldsymbol{v_d}$ as described above. We will consider first the limit, where the strength of the applied current density is slightly above the threshold current, and later a situation, where the applied current density is large.

Close to the depinning transistion, the Magnus force is of the same order as the pinning force, while the two dissipative forces are typically much smaller. Eq. (9.16) implies that $\hat{\boldsymbol{v}}_d$ can be expressed by

$$\hat{\boldsymbol{v}}_d = \frac{\mathcal{G}}{F_{\text{pin}}} \hat{\boldsymbol{B}} \times (\boldsymbol{v}_s - \boldsymbol{v}_d), \tag{10.43}$$

and thus $\hat{\boldsymbol{v}}_d$ is in particular parallel to $\hat{\boldsymbol{B}} \times (\boldsymbol{v}_s - \boldsymbol{v}_d)$. When inserting this result into Eq. (10.34c) we obtain that for an λ-independent $\boldsymbol{v}_s$ both the reactive rotational coupling vector and the rotational pinning vector become proportional to $\nabla\lambda \cdot (\boldsymbol{v}_s - \boldsymbol{v}_d)$. Despite the fact that the particular prefactors of $\mathcal{T}_{\text{pin}}$ and $\mathcal{T}_{\mathcal{G}}$ contributing to $\boldsymbol{V_s}$ are still complicated, the ratio of the component of $\boldsymbol{V_s}$ parallel $(\boldsymbol{V_{s\parallel}})$ and perpendicular $(\boldsymbol{V_{s\perp}})$ to $\boldsymbol{v}_s$ is independent of the details and depends only on the direction in which the skyrmion lattice drifts:

$$\frac{\boldsymbol{V_{s\parallel}}}{\boldsymbol{V_{s\perp}}} \approx \frac{(\boldsymbol{v}_s - \boldsymbol{v}_d)_{\parallel}}{(\boldsymbol{v}_s - \boldsymbol{v}_d)_{\perp}} = \frac{v_s - v_{d\parallel}}{-v_{d\perp}} \tag{10.44}$$

To evaluate the last expression further, let us project Eq. (10.43) onto $(\hat{\boldsymbol{v}}_d \times \hat{\boldsymbol{B}})$ which leads to $0 = \hat{\boldsymbol{v}}_d \cdot (\boldsymbol{v}_s - \boldsymbol{v}_d)$, and thus $\hat{\boldsymbol{v}}_d \cdot \boldsymbol{v}_s = v_d$. With this we obtain

$$v_{d\parallel} = \boldsymbol{v}_d \cdot \hat{\boldsymbol{v}}_s = \frac{v_d}{v_s} \hat{\boldsymbol{v}}_d \cdot \boldsymbol{v}_s = \frac{v_d^2}{v_s}. \tag{10.45}$$

As a consequence it follows that

$$v_s = \frac{v_d^2}{v_{d\parallel}} = \frac{v_{d\perp}^2 + v_{d\parallel}^2}{v_{d\parallel}} = \frac{v_{d\perp}^2}{v_{d\parallel}} + v_{d\parallel} \tag{10.46}$$

and finally when inserting Eq. (10.46) into Eq. (10.43) we can express $\boldsymbol{V_{s\parallel}}/\boldsymbol{V_{s\perp}}$ just by the parallel and perpendicular components of $\boldsymbol{v}_d$:

$$\frac{\boldsymbol{V_{s\parallel}}}{\boldsymbol{V_{s\perp}}} \approx \frac{(\boldsymbol{v}_s - \boldsymbol{v}_d)_{\parallel}}{(\boldsymbol{v}_s - \boldsymbol{v}_d)_{\perp}} = -\frac{v_{d\perp}}{v_{d\parallel}}. \tag{10.47}$$

This ratio $\boldsymbol{V_{s\parallel}}/\boldsymbol{V_{s\perp}}$ is plotted versus $-v_{d\perp}/v_{d\parallel}$ as a function of the current v_s for different strengths of the damping constants in Fig. 10.21. Note that in the limit of small damping (blue line in the Figure) Eq. (10.47) is fulfilled.

In principle, this ratio can be experimentally determined in different ways. One way to obtain the ratio $\boldsymbol{V_{s\parallel}}/\boldsymbol{V_{s\perp}}$ would be to measure the rotation angle or the angular velocity
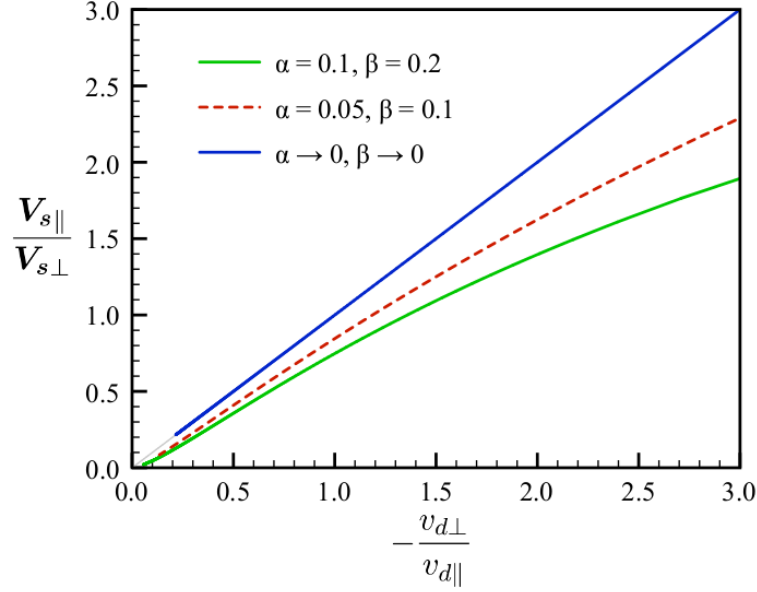
Figure 10.21: Ratio $V_{s\parallel}/V_{s\perp}$ versus $-v_{d\perp}/v_{d\parallel}$ as a function of v_s for different strengths of the damping parameters α and β (here assumed to be independent of t). The other parameters are $\boldsymbol{v}_s = v_s\,(1,0,0)^T$, $t = -1$, $\boldsymbol{B} = \sqrt{-t/2}\,(0,0,1)^T$, $\alpha' = 0$, $\beta' = 0$, and $f = 1$.

for $\nabla\lambda$ parallel and perpendicular to the current. From these quantities one can calculate $\boldsymbol{V}_{s\parallel}/\boldsymbol{V}_{s\perp}$ directly by using Eq. (10.38) or Eq. (10.39), respectively. Since $\arcsin x \approx x$ for $x \ll 1$, for small angles this ratio is just given by the ratio of the two rotation angles. Another way to obtain $\boldsymbol{V}_{s\parallel}/\boldsymbol{V}_{s\perp}$ is to find the relative orientation of the gradient $\nabla\lambda$ and the current $\boldsymbol{v}_s$, where all rotations vanish, $\nabla\lambda \cdot \boldsymbol{V}_s = 0$. When defining this relative orientation between $\nabla\lambda$ and $\boldsymbol{v}_s$ by the angle ϕ_m, we obtain

$$\frac{\boldsymbol{V}_{s\parallel}}{\boldsymbol{V}_{s\perp}} = \frac{1}{\tan\phi_m}. \tag{10.48}$$

Using Eq. (10.47) the ratio $\boldsymbol{V}_{s\parallel}/\boldsymbol{V}_{s\perp}$ allows to determine the ratio $v_{d\perp}/v_{d\parallel}$ quantitatively. Together with the independent measurement of $v_{d\parallel}$ in the Hall effect exploiting the emergent electric field [80], one obtains the complete information on the drift motion by combining the results of both experiments.

In the limit of large currents, $v_s \gg v_{\text{pin}}$, we expect that pinning forces can be neglected. In this case, we can follow a similar procedure as above, and use Eq. (9.16) to show that $(\tilde{\beta}\boldsymbol{v}_s - \tilde{\alpha}\boldsymbol{v}_d)$ is parallel to $\hat{\boldsymbol{B}} \times (\boldsymbol{v}_s - \boldsymbol{v}_d)$, and therefore $\boldsymbol{V}_s$ is parallel to $\hat{\boldsymbol{B}} \times (\boldsymbol{v}_s - \boldsymbol{v}_d)$. Using Eq. (9.22) and neglecting the possible λ-dependence of v_s we obtain to linear order in $\tilde{\beta}$ and $\tilde{\alpha}$ for $\boldsymbol{V}_s$:

$$\begin{aligned}
\boldsymbol{V}_s &= -\frac{A}{4\pi\chi}\left(\hat{\boldsymbol{B}} \times \boldsymbol{v}_s\right)\left((\tilde{\beta} - \tilde{\alpha})\frac{\partial\mathcal{G}}{\partial\lambda}\frac{\mathcal{D}}{\mathcal{G}} + \frac{\partial\mathcal{D}(\tilde{\beta} - \tilde{\alpha})}{\partial\lambda}\right) \\
&= -\frac{A}{4\pi\chi}\left(\hat{\boldsymbol{B}} \times \boldsymbol{v}_s\right)\frac{1}{\mathcal{G}}\frac{\partial}{\partial\lambda}\left(\mathcal{D}\mathcal{G}(\tilde{\beta} - \tilde{\alpha})\right).
\end{aligned} \tag{10.49}$$

As expected, this expression is proportional to $\tilde{\beta} - \tilde{\alpha}$, and therefore no torques do occur in a Galilean invariant system. From Eq. (10.49) it follows that for large currents the rotation

occurs mainly for gradients perpendicular to $\boldsymbol{v}_s$. This is consistent with the result that for large currents the Magnus force (being proportional to $(\boldsymbol{v}_s - \boldsymbol{v}_d)$) almost vanishes, because the skyrmions move mainly parallel to the current and $\boldsymbol{v}_s \approx \boldsymbol{v}_d$, as discussed previously. Furthermore, this is consistent with the behavior of the rotation angle and the angular velocity shown in Fig. 10.19. Although we use a two times smaller gradient for the perpendicular configuration in this plot, we nevertheless obtain that the value of v_s, where the continuous rotation sets, is much smaller than in the parallel configuration.

Domain size dependence and angular distribution: So far we discussed the physics of Eq. (10.35) for one domain. In a real system, there are in general many domains present with a certain distribution of domain sizes A. Since both $\boldsymbol{V_s}$ and γ depend linearly on A, the rotation angle and the angular velocity will in general depend on the domain size and therefore on the distribution of domains. As discussed above, only for $|\nabla\lambda \cdot \boldsymbol{V_s}| \gg 1$, the angular velocity $\bar{\omega}$ becomes independent of the domain size and all domains rotate approximately with the same angular velocity. For smaller values of $|\nabla\lambda \cdot \boldsymbol{V_s}|$, the distribution of domain sizes $P_d(A)$ leads to a distribution of rotation angles $P_\phi = P_\phi^s + P_\phi^r$ which is the sum of the rotation angle distribution for the static domains, P_ϕ^s, and the continuously rotating domains, P_ϕ^r. For the static domains only angles up to $15°$ are possible, and we obtain P_ϕ^s from $P_d(A)$ and Eq. (10.38):

$$
\begin{aligned}
P_\phi^s &= \int_0^{A_c} dA\, P_d(A)\, \delta\left(\phi - \frac{\arcsin(A/A_c)}{6}\right) \\
&= 6A_c \cos(6\phi)\, P_d(A_c \sin(6\phi)) \quad \text{for } 0 \le \phi \le \frac{\pi}{12}\ (= 15°),
\end{aligned}
\tag{10.50}
$$

where $A_c = A/(|\nabla\lambda \cdot \boldsymbol{V_s}|)$ is the size of a "critical" domain which just starts to rotate continuously. The angular distribution of the continuously rotating domains, P_ϕ^r, is also non-trivial, because the angular velocity $\partial_t\phi$ of a rotating domain is slowed down close to $\phi = 15°$ (plus multiples of $60°$), when the counter-forces due to the atomic lattice are strongest, see inset of Fig. 10.18. It can be calculated from a distribution of domain sizes $P_d(A)$ and the angular distribution $p_\phi^r(A)$ of a single domain. We obtain

$$
P_\phi^r = \int_{A_c}^{\infty} dA\, P_d(A)\, p_\phi^r(A),
\tag{10.51a}
$$

$$
p_\phi^r(A) = \frac{1}{T} \int_0^T \delta(\phi - \phi(t)) dt = \frac{1}{T\partial_t\phi}\bigg|_{\phi(t)=\phi} = \frac{3}{\pi}\frac{\sqrt{A^2 - A_c^2}}{A - A_c \sin 6\phi},
\tag{10.51b}
$$

where $T = 2\pi/(6\bar{\omega})$. The total distribution $P_\phi = P_\phi^s + P_\phi^r$ is normalized to 1, *i.e.* $\int_0^{2\pi/6} P_\phi\, d\phi = 1$. Furthermore, P_ϕ is smooth for $\phi > 0$, even though both P_ϕ^s and P_ϕ^r are non-analytic at $\phi = 15°$. In Fig. 10.22, we plot the total angular distribution P_ϕ of the rotation angle for the skyrmion lattice assuming the domain distribution $P_d(A) = e^{-A/A_0}A/A_0^2$ for various values of A_0/A_c. It can be clearly seen from the Figure that a distribution of domain sizes leads to a distribution of rotation angles. This implies that in the neutron scattering data one would expect to see aside from the rotation of the Bragg spots also a broadening of those.

As explained, it is possible to calculate the distribution of rotation angles for a given distribution of domain sizes. Of course, it is also possible to invert these above equations, *i.e.* to extract the distribution of domain sizes from the angular distribution P_ϕ which, in principle, can be obtained with elastic neutron scattering by measuring the scattering
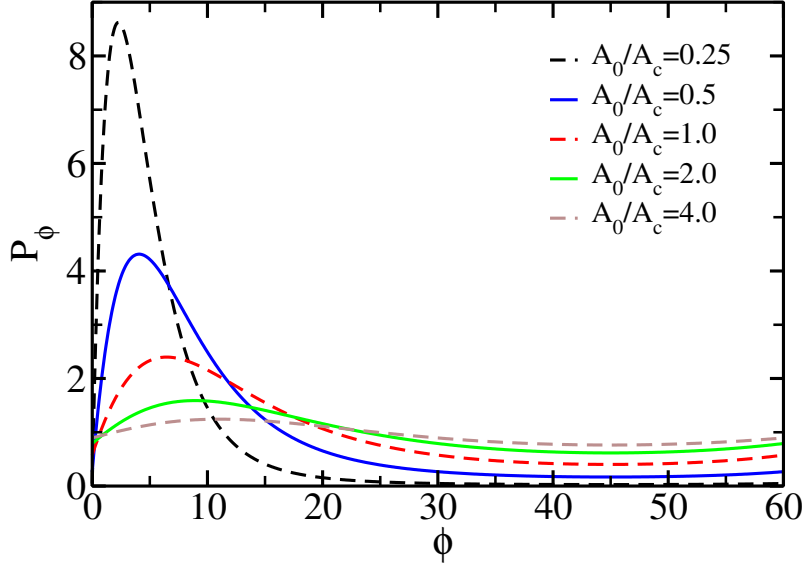
Figure 10.22: Angular distribution P_ϕ of the rotation angle of the skyrmion lattice for various values of $A_0/A_c \propto |\nabla\lambda|$. Here, we assumed a distribution of domain sizes of the form $P_d(A) = e^{-A/A_0} A/A_0^2$. To the total smooth angular momentum distribution P_ϕ contribute both the static and the continuously rotating domains. While static domains contribute only for $0 \leq \phi \leq 15°$, rotating domains with $A > A_c$ contribute to all angles. We published this Figure in Ref. [71].

intensity as a function of the angle. For instance, in the regime, where most of the domains do not rotate continuously, one can extract the distribution of domain sizes by using Eq. (10.50) and plotting $P_\phi/\cos 6\phi$ as a function of $\sin 6\phi$. In particular, one also obtains the behavior of A_c as a function of $\nabla\lambda$ and the current by comparing angular distributions for different strength of the current or the gradient

Comparison to experiments: In the experiments of Ref. [10], only a temperature gradient was applied in the direction of the current. The perpendicular configuration and other gradients like magnetic field gradients have not been studied so far. For a full quantitative comparison of theory and experiment it would be desirable to have data, where the applied current as well as both the strength and the direction of the gradients are changed independently. Note that in the experiments of Ref. [10] the temperature gradient was induced by the current, and they are therefore not independent of each other, see Fig. 10.15. At present, such data is, however, not available. Therefore, we restrict ourselves to a few qualitative observations. In our theory, we obtain a critical current density above which a rotation sets in, as in the experiments, compare Figs. 10.15, 10.19, and 10.20. Furthermore, according to our theory we expect a jump of the rotation angle at j_c which depends on the domain size. This seems consistent with the observed rather abrupt increase of the rotation angle at j_c, especially when taking into account that the experimental results are based on a distribution of domain sizes. For even larger current densities, a slower increase of the rotation angle was observed in the experiments. For temperature-independent damping constants α, α', β, and β', however, the extended Landau-Lifshitz-Gilbert equation predicts a decrease after the initial jump. Nonetheless, for a weak temperature-dependent Gilbert damping α we can describe the experimentally
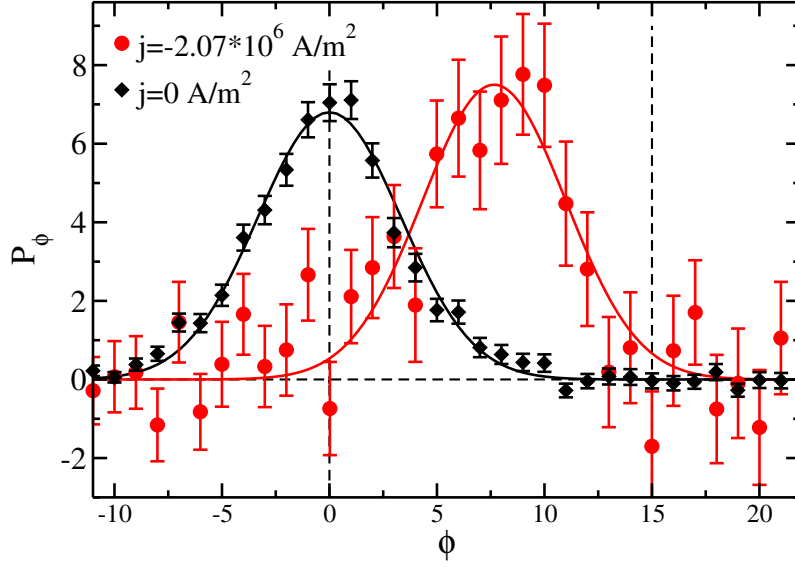
Figure 10.23: To study the angular distribution P_ϕ of the scattering intensity we have re-analyzed the data of Ref. [10]. Here, we show P_ϕ normalized to 1 for $T = 27.4$ K and currents of strength $j = 0$ (black diamonds) and $j \approx -2.07 \cdot 10^6$ A/m^2 (red circles). The lines are Gaussian fits serving as a guide to the eye. Note that the distribution of angles extends up the maximally possible rotation angle of 15° which suggests that some of the larger domains are close to (or are already) continuously rotating with a finite angular velocity for this parameter range. We published this Figure in Ref. [71].

observed behavior, compare Figs. 10.15 and 10.20. In Fig. 10.20, we also accounted for the quadratic current dependence of the temperature gradient arising from the resistive heating in the sample.

To adress the question whether some larger domains are already continuously rotating in the existing experiments, we observe again that average rotation angles up to 10° – rather close to the maximally possible value of 15° for static domains – have already been observed, see Fig. 10.15. This suggests that continuously rotating domains are either already present in the system, or may be reached by using slightly larger currents or temperature gradients. To examine this aspect further we have investigated the angular distribution of the scattering pattern, re-analyzing the experimental data of Ref. [10]. In Fig. 10.23, we show the azimuthal intensity distribution with and without an applied current. One observes that for zero current the intensity distribution is substantially broadened due to demagnetization effects, as explained previously. This effect can be avoided by using thin samples, where only the central part is illuminated [67], as discussed in Chapter 5. However, for the existing data this implies that a quantitative analysis of P_ϕ is not possible. Concerning the interesting question, whether continuously rotating domains are already present in the data, we observe that the azimuthal intensity distribution for the rotation angle with the applied current density of $j \approx -2.07 \cdot 10^6$ A/m^2 extends up just to 15°, Fig. 10.23. Therefore, from the present data we can neither claim nor exclude that continuously rotating domains already exist for this set of data. Nevertheless, slightly larger current densities or gradients should be sufficient to create those.

However, in principle, the investigation of the angular distribution of the neutron scattering only provides an indirect evidence for the expected continuous rotation of the

skyrmion lattice. To observe the continuous rotation of the skyrmion lattice directly one can, for example, exploit the emergent electric field as discussed above. Here, it would be interesting to observe higher harmonics in the Hall signal which are expected to appear close to the threshold, where continuous rotations set in, see Fig. 10.18.

To summarize, in this Section we developed a theory for the rotation of the skyrmion lattice due to currents and gradients. We have shown that the rotational torques can be controlled both by the strength and the direction of field gradients or temperature gradients in combination with electric currents. We have also shown that the current-induced torques react very sensitively on the relative strengths of the various forces and on the variations of these forces with respect to temperature or magnetic field. While we studied these aspects of the theory in detail, many other questions remain open. An important question is, for example, to identify the leading damping mechanisms and their dependence on temperature and field. Furthermore, a deeper understanding of the pinning forces and their interplay with damping and the motion of magnetic textures is required to control spin-torque effects. We expect that future rotation experiments will provide valuable information. Quantitatively, we only studied the role of temperature or magnetic field gradients, but other options like macroscopic variations of a sample cross section leading to gradients in the current density are possible, too. Also, changes in the chemical composition, like a gradient in doping or strain in the sample, can induce gradients. Furthermore, while we applied our theory to skyrmion lattices, our theoretical approaches can be used for other complex magnetic textures, too, and our results should also have ramifications for other setups [99, 138]. In the future, it might also be interesting to substitute the electrical current by, for example, pure spin currents or thermal currents to manipulate skyrmion lattices (*e.g.* in insulators). We expect that also in such systems the investigation of rotational motion driven by gradients will give useful insight in the control of magnetism beyond thermal equilibrium.

In the next Chapter of this Thesis, we will briefly present some analogies of the skyrmion lattice and the vortext lattice of a type-II superconductor.

11 Skyrmion Lattice vs. Vortex Lattice of a Type-II Superconductor

In this Section, we compare the skyrmion lattice and its properties to the vortex lattice of a type-II superconductor. Therefore, we first briefly review the vortex lattice state which was theoretically predicted in 1957 by A. A. Abrikosov [143] and first observed in 1964 by D. Cribier *et al.* using neutron diffraction [144] and then by U. Essman and H. Träuble in 1967 [145] using electron microscopy. Later, in 2003, A. A. Abrikosov together with V. L. Ginzburg and A. J. Leggett were awarded the Nobel prize in Physics "for pioneering contributions to the theory of superconductors and superfluids".

In view of this long and rich history of superconductors in combination with five Nobel prizes since their discovery, a lot of information on superconductors can be found in the literature. Here, we will therefore focus on some aspects which are appropriate for our analogies to the skyrmion lattice.

In a superconductor, the formation of a superconducting condensate consisting of Cooper pairs leads to a disappearance of the resistance and to the Meissner effect. The so-called type-I superconductors show a complete Meissner effect, *i.e.* that an applied magnetic field (smaller than the critical field, $B < B_c$) is fully expelled from the superconducting region. Above the critical field, $B > B_c$, superconductivity is destroyed.

However, most known superconductors, in particular the high-temperature superconductors, are of type II. In type-II superconductors, there exists an interval for the magnetic field strength $B_{c1} < B < B_{c2}$, where vortex tubes of quantized magnetic flux $\Phi = h/(2e)$ penetrate the superconductor.

As in the case of magnetism, superconductivity can phenomenologically be described by a Ginzburg-Landau theory [146]. Here, the complex order parameter is given by $\boldsymbol{\Psi}(\boldsymbol{r}) = |\boldsymbol{\Psi}|e^{i\phi}$, consisting of an amplitude $|\boldsymbol{\Psi}|$ and a phase ϕ. It can be interpreted as the macroscopic wave function at the postion $\boldsymbol{r}$ of the superconducting condensate, and $|\boldsymbol{\Psi}(\boldsymbol{r})|^2$ represents the density of the Cooper pairs. In the normal phase above T_c, the order parameter is invariant under the gauge transformation $\phi \to \phi'$. However, in the superconducting state, *i.e.* below T_c, the gauge symmetry of the order parameter is spontaneously broken, and the system takes a special value of ϕ. A. A. Abrikosov showed that in a type-II superconductor with $B_{c1} < B < B_{c2}$ the order parameter obeys a vortex lattice solution. It vanishes at the vortex cores which, in general, form a triangular lattice in the plane perpendicular to the applied magnetic field. These are exactly the points, where the magnetic field penetrates the sample, see left panel of Fig. 11.1. Furthermore, the phase of the order parameter changes by multiples of 2π when following a closed contour around one of these lattice points.

Concerning general aspects, the skyrmion lattice and the vortex lattice share a lot of similarities. Both can be described phenomenologically in terms of a Ginzburg-Landau
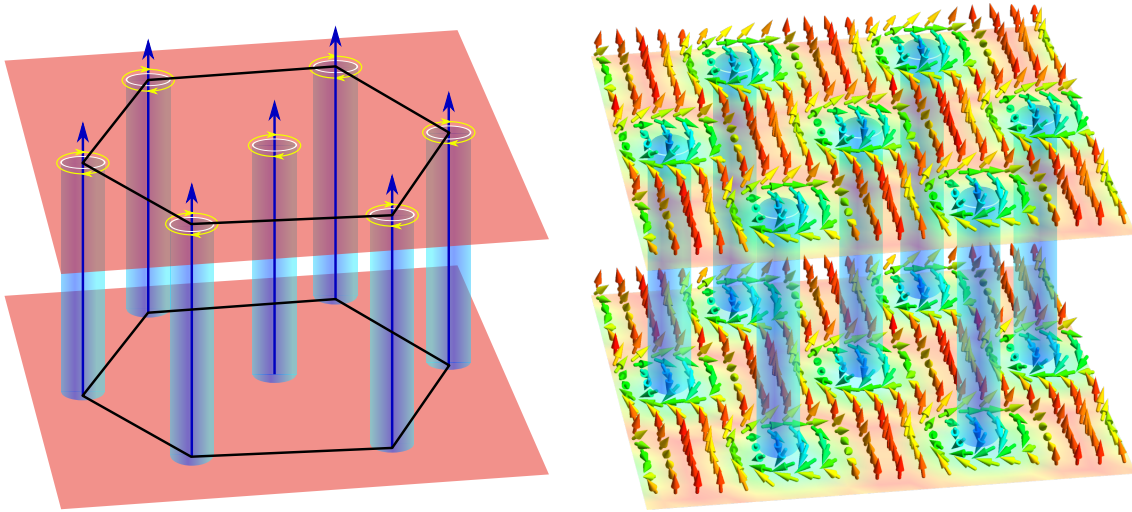
Figure 11.1: Left panel: sketch of a vortex lattice in a superconductor. Right panel: sketch of the skyrmion lattice.

theory. The corresponding solution is a triangular lattice of skyrmions or vortices in the direction perpendicular to the applied magnetic field. Along the direction of the magnetic field, both structures are translationally invariant, leading actually to vortex tubes and skyrmion tubes, respectively, as sketched in Fig 11.1. Also, both configurations are topologically stable. In the case of the vortex lattice, the winding of the phase of the order parameter is quantized to multiples of 2π while going around a vortex core, *i.e.* topological order is described by the homotopy group $\pi_1(S_1) = \mathbb{Z}$. In the case of the skyrmion lattice, the topological order is described the homotopy group $\pi_2(S_2) = \mathbb{Z}$, and it is the winding number of the magnetization direction that is quantized. In contrast to a vortex, where the order parameter vanishes in the center and varies on a length scale which is usually much smaller than the distance of two vortices, the magnetization in the skyrmion lattice is smooth and remains always finite [1]. Furthermore, in Chapter 9 we introduced an alternative, intuitive picture for the skyrmion lattice, where we considered it as an array of circulating dissipationless spin currents around the skyrmions with a quantized winding number. In comparison, in a vortex lattice, there are dissipationless charge currents flowing around the quantized vortices. They occur due to gradients in the phase of the order parameter, whereas the dissipationless spin currents in the skyrmion lattice are due to gradients in the spin orientation. One main difference between the two pictures is that in superconductors the total charge is a conserved quantity. In the case of the skyrmion lattice, the spin is, however, not a conserved quantity. Therefore, and due to further dissipative forces acting on the skyrmions [124], this intuitive picture for the skyrmion lattice is not complete, as mentioned in Chapter 9.

When applying an electric current to the two systems (without a thermal gradient), they also share a few similarities, but their current-induced dynamics are different. For the skyrmion lattice we have seen that, in the presence of a current, different kinds of forces act on the skyrmion lattice, namely Magnus forces, dissipative forces, and pinning forces due to disorder and the underlying atomic lattice. Furthermore, we discussed in Chapters 7 and 9 that for small current densities, $j < j_c$, the skyrmion lattice is pinned. Above the critical current density it gets unpinned and starts to move. For $j \gg j_c$, pinning forces can be neglected and the drift velocity becomes proportional to the applied

current. For a vortex lattice, the same type of forces act on the vortices and they follow essentially the same equation of motions, Eq. (9.16). This means that also the vortex lattice is pinned below a critical current density, $j < j_c$, determined by the strength of the pinning forces, and starts to move for $j > j_c$ [81–83]. Note that in Chapter 4.3, where we phenomenologically discussed the pinning physics for the skyrmion lattice, we exploited the knowlegde from the pinning physics of the vortex lattice case which has been studied in the literature [83]. Although the structure of the pinning forces are expected to be similar in both lattices, the precise form will, however, differ in the case of the skyrmion lattice due to its smooth and non-vanishing magnetization.

Nonetheless, the dynamics of vortices and skyrmions and therefore the direction of their drift velocities are different. For the skyrmion lattice, we have shown that the drift velocity becomes proportional to the applied current for $j \gg j_c$, where pinning forces can be neglected. Therefore, skyrmions move mainly parallel to the current, since the contribution of the Magnus force is almost canceled, *i.e.* $\boldsymbol{v}_d \approx \boldsymbol{v}_s$ with corrections of the order of $\alpha D/|G|$. Moreover, we showed in Chapter 7 that a moving skyrmion lattice induces an emergent electric field. Due to the dominantly parallel motion of the skyrmion lattice with respect to the applied current, the relative speed of the spin current is reduced which leads to a large emergent electric field in perpendicular direction. In contrast, for vortices dissipation dominates [135], *i.e.* $\mathcal{D}\alpha \gg \mathcal{G}$. This implies that the motion of superconducting vortices is dominantly in the direction of the Magnus force, *i.e.* perpendicular to the current. Furthermore, the change in the Hall signal due to the electric field, which results from the motion of the vortex lattice, is much smaller [83, 135].

Concerning the rotations, for skyrmions they either occur due to a distortion of the skyrmion lattice or due to a non-uniform applied spin current, as we have discussed in the previous Chapter. For the vortex lattice the situation is similar. The current-induced rotation caused by distortions due to *disorder* has been analyzed for vortex lattices in superconductors [81]. Note, however, that this is a different mechanism to obtain distortions which we did not discuss in this Thesis in the case of the skyrmion lattice. Those rotations by a finite angle, which originate in disorder-induced distortions of the vortex lattice, have been observed experimentally measuring the alternating current response of superconductors [147]. In the skyrmion lattice, so far only rotations due to non-uniform spin currents have been observed experimentally, where a temperature gradient was used to induce a gradient in the spin currents, as discussed in Sec. 10.3. Actually, also in the vortex lattice a current-induced rotation due to a non-uniform applied current was observed [148]. However, since charge is a conserved quantity, this is more difficult to realize than for skyrmions. The reason for this is that one does not obtain easily a gradient in the applied electric current by tuning some external parameters like the applied magnetic field or temperature. Therefore, in Ref. [148] the authors had to create a gradient in the current density itself to induce the rotation of the vortex lattice. Experimentally, they realized the gradient in the current density by taking a sample of the shape of a disk and they injected the current at the center of a disk while removing it at the perimeter such that the radial current density decayed as 1/radius.

We conclude this Chapter by summarizing some aspects of the vortex lattice and the skyrmion lattice in Table 11.1.

Compare	Vortex lattice	Skyrmion lattice
Order parameter	macroscopic wavefunction $\boldsymbol{\Psi}$ of superconducting condensate	direction of magnetization $\hat{\boldsymbol{\Omega}}$
Dissipationless	charge current	spin current
Around	vortices with quantized winding of phase	skyrmions with quantized winding number
Due to gradients	in the phase	in the spin-orientation
Conservation	of charge	no conservation of spin (due to spin-orbit coupling)
Motion mainly	perpendicular to current	parallel to current
Rotation	of undistorted vortex lattice: due to charge conservation not so easy to realize	of undistorted skyrmion lattice: realization, *e.g.*, via temperature or magnetic field gradients

Table 11.1: Comparison of some aspects of the vortex and the skyrmion lattice.

12 Conclusion

In this Thesis, we have studied a new type of magnetic order – the skyrmion lattice – which was discovered in 2009 [1] and has by now been observed in a wide range of cubic, chiral materials including insulators [42, 43], doped semiconductors [39] and good metals [1, 41]. In the first Part, we have examined the equilibrium properties of the topologically stable magnetic whirl-lines and discussed the Ginzburg-Landau theory for the skyrmion lattice. We have reviewed that in bulk materials the skyrmion lattice phase is stabilized by Gaussian fluctuations and briefly mentioned that it is much more stable in thin films [44, 45]. From this theory it is expected that the skyrmion lattice occurs in any material with B20 symmetry, which would be ferromagnetic in the absence of spin-orbit coupling, in the presence of a small magnetic field. Moreover, we have considered the effects of the underlying crystalline lattice and pinning due to disorder. In agreement with the experiments we have confirmed the long-range crystalline nature of the skyrmion lattice [67].

In the second Part of this Thesis, we have investigated the interplay between an electric current and a magnetic texture, focussing again on the skyrmion crystal. We discussed that electrons traversing a spatially or temporally inhomogeneous magnetization configuration pick up a Berry phase which, rewritten as an Aharonov-Bohm phase arising from emergent magnetic and electric fields, leads to an effective Lorentz force acting on the electrons. To describe the response of the skyrmion lattice to the applied current, we described the evolution of the magnetic structure by the standard Landau-Lifshitz-Gilbert equation extended by a new damping mechanism recently proposed [8, 9]. The theoretically predicted current-induced motion [129] was experimentally detected exploiting the emergent electric field on the conduction electron. Using Faraday's law of induction [80] this allowed to detect the motion of the skyrmion lattice by simple transport measurements.

Furthermore, we have analyzed the experimentally observed rotation of the skyrmion lattice by a finite angle [10]. We have discussed different rotation mechanisms and developed a theory by generalizing the Thiele method for the rotational degree of freedom. In the last Section of Chapter 10, we predicted a continuous rotation of the skyrmion lattice with a finite angular velocity [71]. We also suggested experiments which probably allow to detect the continuous rotation. We are looking forward to the experiments (already in planning stage) that will test our prediction and will hopefully be performed in the near future.

To conclude, our observations on the current-induced dynamics of chiral magnetic structures, in particular skyrmions, in combination with the ultra-low threshold current density of $j \sim 10^6$ A/m^2 above which it is possible to manipulate the skyrmion lattice, indicate that chiral magnets and systems with nontrivial topological properties are ideally suited to advance the general understanding of spin-transfer torques effects by investigating the coupling of electric, thermal or spin currents to magnetic textures.

Part III

Appendices

A Ginzburg-Landau Terms for B20 Structures

In this Appendix, we give an overview of symmetry-allowed terms in the free energy functional F for B20 materials like MnSi. The space group of MnSi is $P2_1 3$ which consists of threefold rotation axes in the $\langle 111 \rangle$ direction and of twofold $\langle 100 \rangle$ screw axes, as discussed in Section 3.1. All terms appearing in the Ginzburg-Landau theory for B20 materials should be invariant under these transformations. In general, for a periodic magnetic structure, all terms contributing to the Ginzburg-Landau free energy functional can be written in the following form:

$$\gamma_{QR}^{(i)} \sum_{\boldsymbol{q}_j, j=1,...N} f_{QR}^{(i)}(\boldsymbol{q}_1, ..., \boldsymbol{q}_N, \boldsymbol{m}_{\boldsymbol{q}_1}, ..., \boldsymbol{m}_{\boldsymbol{q}_N}, \boldsymbol{m}_{\boldsymbol{q}_1}^*, ..., \boldsymbol{m}_{\boldsymbol{q}_N}^*), \tag{A.1}$$

where $N \in \mathbb{N}_0$, f_{QR} is a function of the arguments $\boldsymbol{q}_1, \ldots, \boldsymbol{q}_N, \boldsymbol{m}_{\boldsymbol{q}_1}, \ldots, \boldsymbol{m}_{\boldsymbol{q}_N}, \boldsymbol{m}_{\boldsymbol{q}_1}^*, \ldots, \boldsymbol{m}_{\boldsymbol{q}_N}^*$ (note that $\boldsymbol{m}_{\boldsymbol{q}}^* = \boldsymbol{m}_{-\boldsymbol{q}}$), and $\gamma_{QR}^{(i)}$ is a complex prefactor that is independent of those arguments. By the index "Q" we denote the number of derivatives appearing in the corresponding term if expressed in real space (or equivalently the power of $\boldsymbol{q}$ vectors), and by the index "R" we denote the power of $\boldsymbol{m}_{\boldsymbol{q}}$'s for the corresponding term. For example, the Dzyaloshinskii-Moriya term $\int d^3 r \, \boldsymbol{M} \cdot (\nabla \times \boldsymbol{M})$, which in Fourier space is proportional to $\sum_{\boldsymbol{q}} \boldsymbol{m}_{\boldsymbol{q}}^* (\boldsymbol{q} \times \boldsymbol{m}_{\boldsymbol{q}})$, contains one derivative and two factors of $\boldsymbol{m}_{\boldsymbol{q}}$, i.e. $Q = 1$ and $R = 2$ (note that for $N = 1$ we write $\boldsymbol{q}$ instead of $\boldsymbol{q}_1$). Finally, the index "(i)" numbers serially the different terms.

As discussed in Chapter 4, the magnetic structures in chiral magnets develop on length scales determined by the strength of the small spin-orbit coupling λ_{so}, and thus each derivative contributes with a power of λ_{so}. However, to order the different terms properly according to their power in spin-orbit coupling strength one has to consider how exactly these terms arise, because their prefactors might also contain additional factors of λ_{so}. Here, we list the symmetry-allowed terms for $N = 1$ and $R = 2$ according to their number of derivatives, i.e. their Q value. Up to $Q = 6$ we obtain:

- $Q = 0$:

$$f_{22}^{(1)} = (\boldsymbol{m}_{\boldsymbol{q}} \cdot \boldsymbol{m}_{-\boldsymbol{q}}) \tag{A.2}$$

- $Q = 1$:

$$f_{12}^{(1)} = \boldsymbol{m}_{\boldsymbol{q}} \cdot (\boldsymbol{q} \times \boldsymbol{m}_{-\boldsymbol{q}}) \tag{A.3}$$

- $Q = 2$:

$$f_{22}^{(1)} = \boldsymbol{q}^2 \left(\boldsymbol{m_q} \cdot \boldsymbol{m_{-q}} \right) \tag{A.4}$$

$$f_{22}^{(2)} = q_x^2 \, m_{\boldsymbol{q}}^x m_{-\boldsymbol{q}}^x + q_y^2 \, m_{\boldsymbol{q}}^y m_{-\boldsymbol{q}}^y + q_z^2 \, m_{\boldsymbol{q}}^z m_{-\boldsymbol{q}}^z \tag{A.5}$$

$$f_{22}^{(3)} = q_x^2 \, m_{\boldsymbol{q}}^y m_{-\boldsymbol{q}}^y + \text{c.p.} \tag{A.6}$$

$$f_{22}^{(4)} = q_x q_y \left(m_{\boldsymbol{q}}^x m_{-\boldsymbol{q}}^y + m_{-\boldsymbol{q}}^x m_{\boldsymbol{q}}^y \right) + \text{c.p.} \tag{A.7}$$

- $Q = 3$:

$$f_{32}^{(1)} = \boldsymbol{q}^2 \left(\boldsymbol{m_q} \cdot (\boldsymbol{q} \times \boldsymbol{m_{-q}}) \right) \tag{A.8}$$

$$f_{32}^{(2)} = \epsilon_{ijk} \, q_i^3 m_{\boldsymbol{q}}^j m_{-\boldsymbol{q}}^k \tag{A.9}$$

$$f_{32}^{(3)} = q_x^2 \, q_z \left(m_{\boldsymbol{q}}^x m_{-\boldsymbol{q}}^y - m_{-\boldsymbol{q}}^x m_{\boldsymbol{q}}^y \right) + \text{c.p.} \tag{A.10}$$

- $Q = 4$:

$$f_{42}^{(1)} = (q_x^4 + q_y^4 + q_z^4) \left(\boldsymbol{m_q} \cdot \boldsymbol{m_{-q}} \right) \tag{A.11}$$

$$f_{42}^{(2)} = (q_x^2 q_y^2 + q_y^2 q_z^2 + q_z^2 q_x^2) \left(\boldsymbol{m_q} \cdot \boldsymbol{m_{-q}} \right) \tag{A.12}$$

$$f_{42}^{(3)} = q_x^4 \, m_{\boldsymbol{q}}^x m_{-\boldsymbol{q}}^x + q_y^4 \, m_{\boldsymbol{q}}^y m_{-\boldsymbol{q}}^y + q_z^4 \, m_{\boldsymbol{q}}^z m_{-\boldsymbol{q}}^z \tag{A.13}$$

$$f_{42}^{(4)} = q_x^4 \, m_{\boldsymbol{q}}^y m_{-\boldsymbol{q}}^y + \text{c.p.} \tag{A.14}$$

$$f_{42}^{(5)} = q_x^3 q_y \left(m_{\boldsymbol{q}}^x m_{-\boldsymbol{q}}^y + m_{-\boldsymbol{q}}^x m_{\boldsymbol{q}}^y \right) + \text{c.p.} \tag{A.15}$$

$$f_{42}^{(6)} = q_x^3 q_z \left(m_{\boldsymbol{q}}^x m_{-\boldsymbol{q}}^z + m_{-\boldsymbol{q}}^x m_{\boldsymbol{q}}^z \right) + \text{c.p.} \tag{A.16}$$

$$f_{42}^{(7)} = q_x^2 q_y^2 \, m_{\boldsymbol{q}}^x m_{-\boldsymbol{q}}^x + \text{c.p.} \tag{A.17}$$

$$f_{42}^{(8)} = q_x^2 q_z^2 \, m_{\boldsymbol{q}}^x m_{-\boldsymbol{q}}^x + \text{c.p.} \tag{A.18}$$

$$f_{42}^{(9)} = q_x^2 q_y q_z \left(m_{\boldsymbol{q}}^y m_{-\boldsymbol{q}}^z + m_{-\boldsymbol{q}}^y m_{\boldsymbol{q}}^z \right) + \text{c.p.} \tag{A.19}$$

Note that by combining $f_{42}^{(1)}$ and $f_{42}^{(2)}$ one obtains also the term $\boldsymbol{q}^4 \left(\boldsymbol{m_q} \cdot \boldsymbol{m_{-q}} \right) = (\boldsymbol{q} \cdot \boldsymbol{q})^2 \left(\boldsymbol{m_q} \cdot \boldsymbol{m_{-q}} \right)$.

- $Q = 5$:

$$f_{52}^{(1)} = \boldsymbol{q}^4 \left(\boldsymbol{m_q} \cdot (\boldsymbol{q} \times \boldsymbol{m_{-q}}) \right) \tag{A.20}$$

$$f_{52}^{(2)} = \epsilon_{ijk} \, q_i^5 \, m_{\boldsymbol{q}}^j m_{-\boldsymbol{q}}^k \tag{A.21}$$

$$f_{52}^{(3)} = q_x^4 \, q_z \left(m_{\boldsymbol{q}}^x m_{-\boldsymbol{q}}^y - m_{-\boldsymbol{q}}^x m_{\boldsymbol{q}}^y \right) + \text{c.p.} \tag{A.22}$$

$$f_{52}^{(4)} = q_x^3 \, q_y^2 \left(m_{\boldsymbol{q}}^y m_{-\boldsymbol{q}}^z - m_{-\boldsymbol{q}}^y m_{\boldsymbol{q}}^z \right) + \text{c.p.} \tag{A.23}$$

$$f_{52}^{(5)} = q_x^3 \, q_z^2 \left(m_{\boldsymbol{q}}^y m_{-\boldsymbol{q}}^z - m_{-\boldsymbol{q}}^y m_{\boldsymbol{q}}^z \right) + \text{c.p.} \tag{A.24}$$

$$f_{52}^{(6)} = q_x^2 \, q_y^2 q_z \left(m_{\boldsymbol{q}}^x m_{-\boldsymbol{q}}^y - m_{-\boldsymbol{q}}^x m_{\boldsymbol{q}}^y \right) + \text{c.p.} \tag{A.25}$$

$$\tag{A.26}$$

- $Q = 6$:

$$f_{62}^{(1)} = (q_x^6 + q_y^6 + q_z^6)\,(\boldsymbol{m_q} \cdot \boldsymbol{m_{-q}}) \tag{A.27}$$

$$f_{62}^{(2)} = (q_x^4 q_y^2 + q_y^4 q_z^2 + q_z^4 q_x^2)\,(\boldsymbol{m_q} \cdot \boldsymbol{m_{-q}}) \tag{A.28}$$

$$f_{62}^{(3)} = (q_x^4 q_z^2 + q_y^4 q_x^2 + q_z^4 q_y^2)\,(\boldsymbol{m_q} \cdot \boldsymbol{m_{-q}}) \tag{A.29}$$

$$f_{62}^{(4)} = q_x^2 q_y^2 q_z^2\,(\boldsymbol{m_q} \cdot \boldsymbol{m_{-q}}) \tag{A.30}$$

$$f_{62}^{(5)} = q_x^6\, m_{\boldsymbol{q}}^x m_{-\boldsymbol{q}}^x + q_y^6\, m_{\boldsymbol{q}}^y m_{-\boldsymbol{q}}^y + q_z^6\, m_{\boldsymbol{q}}^z m_{-\boldsymbol{q}}^z \tag{A.31}$$

$$f_{62}^{(6)} = q_x^6\, m_{\boldsymbol{q}}^y m_{-\boldsymbol{q}}^y + \text{c.p.} \tag{A.32}$$

$$f_{62}^{(7)} = q_x^5 q_y\, (m_{\boldsymbol{q}}^x m_{-\boldsymbol{q}}^y + m_{-\boldsymbol{q}}^x m_{\boldsymbol{q}}^y) + \text{c.p.} \tag{A.33}$$

$$f_{62}^{(8)} = q_x^5 q_z\, (m_{\boldsymbol{q}}^x m_{-\boldsymbol{q}}^z + m_{-\boldsymbol{q}}^x m_{\boldsymbol{q}}^z) + \text{c.p.} \tag{A.34}$$

$$f_{62}^{(9)} = q_x^4 q_y^2\, m_{\boldsymbol{q}}^x m_{-\boldsymbol{q}}^x + \text{c.p.} \tag{A.35}$$

$$f_{62}^{(10)} = q_x^4 q_y^2\, m_{\boldsymbol{q}}^y m_{-\boldsymbol{q}}^y + \text{c.p.} \tag{A.36}$$

$$f_{62}^{(11)} = q_x^4 q_z^2\, m_{\boldsymbol{q}}^x m_{-\boldsymbol{q}}^x + \text{c.p.} \tag{A.37}$$

$$f_{62}^{(12)} = q_x^4 q_z^2\, m_{\boldsymbol{q}}^y m_{-\boldsymbol{q}}^y + \text{c.p.} \tag{A.38}$$

$$f_{62}^{(13)} = q_x^4 q_y q_z\, (m_{\boldsymbol{q}}^y m_{-\boldsymbol{q}}^z + m_{-\boldsymbol{q}}^y m_{\boldsymbol{q}}^z) + \text{c.p.} \tag{A.39}$$

$$f_{62}^{(14)} = q_x^3 q_y^3\, (m_{\boldsymbol{q}}^x m_{-\boldsymbol{q}}^y + m_{-\boldsymbol{q}}^x m_{\boldsymbol{q}}^y) + \text{c.p.} \tag{A.40}$$

$$f_{62}^{(15)} = q_x^3 q_y^2 q_z\, (m_{\boldsymbol{q}}^x m_{-\boldsymbol{q}}^z + m_{-\boldsymbol{q}}^x m_{\boldsymbol{q}}^z) + \text{c.p.} \tag{A.41}$$

$$f_{62}^{(16)} = q_x^3 q_y q_z^2\, (m_{\boldsymbol{q}}^x m_{-\boldsymbol{q}}^y + m_{-\boldsymbol{q}}^x m_{\boldsymbol{q}}^y) + \text{c.p.} \tag{A.42}$$

Note that combining $f_{62}^{(1)}$, $f_{62}^{(2)}$, $f_{62}^{(3)}$, and $f_{62}^{(4)}$ leads also to the term $\boldsymbol{q}^6\,(\boldsymbol{m_q} \cdot \boldsymbol{m_{-q}}) = (\boldsymbol{q} \cdot \boldsymbol{q})^3\,(\boldsymbol{m_q} \cdot \boldsymbol{m_{-q}})$.

In the above list "c.p." denotes cyclic permutation of the indices x, y, and z. Finally, note that for example the terms F_L of Eq. (4.26) and F_D of Eq. (4.27), which we used to orient and distort the skyrmion lattice, are represented in this list by $f_{62}^{(1)}$ and $f_{22}^{(3)}$, respectively.

B Derivations of the Landau-Lifshitz-Gilbert Equation

In this Appendix, we will derive the LLG equation first for the very simple case of a single spin without damping, and second we derive it from a variational principle. Microscopic derivations of the Landau-Lifshitz-Gilbert equation, Eq. (8.1), can be found, for example, in Refs. [125, 127, 149]. The approach used in Ref. [125] is based on a functional formulation of the Keldysh formalism. In another approach [127], the authors use imaginary-time methods to calculate α and β.

B.1 Derivation of the LLG Equation for a Single Spin without Damping

Let us consider a single spin with a normalized magnetic moment in a magnetic field $\boldsymbol{B}$, as in Sec. 8.1. The Hamiltonian operator is given by

$$\hat{H} = -\gamma \boldsymbol{B} \cdot \hat{\boldsymbol{S}}, \tag{B.1}$$

where $\hat{\boldsymbol{S}}$ is the spin operator. The gyromagnetic ratio γ of a particle is the proportionality factor between its magnetic moment $\boldsymbol{M}$ and the expectation value of its spin $\langle \hat{\boldsymbol{S}} \rangle$, $i.e.$

$$\boldsymbol{m} = \gamma \langle \hat{\boldsymbol{S}} \rangle. \tag{B.2}$$

For a particle with charge q, the gyromagnetic ratio is given by the product of its dimensionless gyromagnetic factor g (g-factor) and its magneton $\mu = q\hbar/(2m)$ divided by $\hbar$:

$$\gamma = \frac{g\mu}{\hbar} = \frac{gq}{2m}. \tag{B.3}$$

Thus, γ is characteristic for every type of particle, and in particular it can have different signs. For example, the gyromagnetic ratio of an electron (proton) is given by $\gamma_{\mathrm{e}} \approx -1.76 \cdot 10^{11} \ \mathrm{s}^{-1}\mathrm{T}^{-1}$ ($\gamma_{\mathrm{p}} \approx 2.675 \cdot 10^{8} \ \mathrm{s}^{-1}\mathrm{T}^{-1}$). Despite the sign of γ, the energy of the system given by $-\boldsymbol{B} \cdot \boldsymbol{m}$ is lowest when the magnetic moment $\boldsymbol{m}$ aligns in the direction of the external magnetic field $\boldsymbol{B}$.

The Heisenberg equation of motion for the spin operator follows from

$$\partial_t \hat{S}_j = -i \, [\hat{S}_j, \hat{H}] = -i \, [\hat{S}_j, -\gamma \boldsymbol{B} \cdot \hat{\boldsymbol{S}}] = +i \, \gamma B_i \, [\hat{S}_j, \hat{S}_i] = i \, \gamma B_i (i \, \epsilon_{jik} \hat{S}_k) = \gamma \big(\hat{\boldsymbol{S}} \times \boldsymbol{B} \big)_j,$$

and thus we obtain

$$\partial_t \hat{\boldsymbol{S}} = \gamma \hat{\boldsymbol{S}} \times \boldsymbol{B}. \tag{B.4}$$

The equation of motion for the magnetization, which is also called Bloch equation, is therefore given by

$$\partial_t \boldsymbol{m} = \gamma \boldsymbol{m} \times \boldsymbol{B}. \tag{B.5}$$

The above equation, however, depends on the sign of γ, implying that in particular the sign of the charge q determines whether the magnetic moment precesses clockwise or counterclockwise around the magnetic field. Therefore, when considering the itinerant magnetism due to electrons, we adopt a negative prefactor in front of $\boldsymbol{m} \times \boldsymbol{B}$. By rescaling we therefore obtain

$$\partial_t \boldsymbol{m} = -\boldsymbol{m} \times \boldsymbol{B}, \tag{B.6}$$

which reproduces Eq. (8.4) of the main text.

A damping term does not conserve the energy, and therefore it cannot be described within a simple Hamiltonian picture. In Chapter 8, we have already motivated the form of the standard Gilbert damping term $\alpha\, \hat{\boldsymbol{m}} \times \partial_t \hat{\boldsymbol{m}}$. The signs of damping terms are fixed by the condition that during the time evolution the energy is reduced, and thus the magnetization aligns parallel to the magnetic field, as discussed in Chapter 8. Finally, when including the Gilbert damping term to Eq. (B.6) we reproduce Eq. (8.5) of the main text:

$$\frac{d\boldsymbol{m}}{dt} = -\boldsymbol{m} \times \boldsymbol{B} + \alpha\, \boldsymbol{m} \times \frac{d\boldsymbol{m}}{dt}, \tag{B.7}$$

where $\alpha > 0$.

B.2   Derivation of the LLG Equation from a Variational Principle

The Landau-Lifshitz-Gilbert equation may be derived from the variational principle [126] for a constant magnetization amplitude M at least up to a surface term discussed below. Here, we will derive the LLG given in Eq. (8.11) as in Ref. [129] including the new damping term. As the LLG equation contains damping terms, *i.e.* the energy is not conserved, it is not sufficient to derive it just from an action functional $\mathcal{A}[\hat{\boldsymbol{\Omega}}]$. However, when introducing also a dissipation fuctional $\mathcal{R}[\hat{\boldsymbol{\Omega}}]$, the LLG is obtained by calculating the variations according to the following formula:

$$\frac{\delta \mathcal{A}[\hat{\boldsymbol{\Omega}}]}{\delta \hat{\boldsymbol{\Omega}}(\boldsymbol{r},t)} = \frac{\delta \mathcal{R}[\hat{\boldsymbol{\Omega}}]}{\delta(\partial_t \hat{\boldsymbol{\Omega}}(\boldsymbol{r},t))}\,. \tag{B.8}$$

In this formula, the dissipation functional $\mathcal{R}[\hat{\boldsymbol{\Omega}}]$ is given by

$$\mathcal{R}[\hat{\boldsymbol{\Omega}}] = \mathcal{R}^{\alpha}[\hat{\boldsymbol{\Omega}}] + \mathcal{R}^{\alpha'}[\hat{\boldsymbol{\Omega}}] \tag{B.9a}$$

$$\mathcal{R}^{\alpha}[\hat{\boldsymbol{\Omega}}] = \frac{\alpha}{2} \int dt \int_V d^3r \left[\left(\partial_t + \frac{\beta}{\alpha}\boldsymbol{v}_s \cdot \nabla\right)\hat{\boldsymbol{\Omega}}(\boldsymbol{r},t)\right]^2, \tag{B.9b}$$

$$\mathcal{R}^{\alpha'}[\hat{\boldsymbol{\Omega}}] = \frac{\alpha'}{2} \int dt \int_V d^3r \left[\hat{\boldsymbol{\Omega}}(\boldsymbol{r},t) \cdot \left(\partial_i \hat{\boldsymbol{\Omega}}(\boldsymbol{r},t) \times \left(\partial_t + \frac{\beta'}{\alpha'}\boldsymbol{v}_s \cdot \nabla\right)\hat{\boldsymbol{\Omega}}(\boldsymbol{r},t)\right)\right]^2, \tag{B.9c}$$

while the action functional $\mathcal{A}$ is given by

$$\mathcal{A}[\hat{\boldsymbol{\Omega}}] = \int dt \left\{\int_V d^3r\, \boldsymbol{A}(\hat{\boldsymbol{\Omega}}(\boldsymbol{r},t)) \cdot \left(\partial_t + \boldsymbol{v}_s \cdot \nabla\right)\hat{\boldsymbol{\Omega}}(\boldsymbol{r},t) - \frac{1}{M}F[\hat{\boldsymbol{\Omega}}(\boldsymbol{r},t)]\right\}. \tag{B.10}$$

Here, $\boldsymbol{A}(\hat{\boldsymbol{\Omega}}(\boldsymbol{r},t))$ is the vector potential associated with the topological Berry phase term according to a magnetic field of a monopole, *i.e.* $\nabla_{\hat{\boldsymbol{\Omega}}} \times \boldsymbol{A} = \hat{\boldsymbol{\Omega}}$, where $\nabla_{\hat{\boldsymbol{\Omega}}} =$

$(\partial_{\Omega_x}, \partial_{\Omega_y}, \partial_{\Omega_z})^T$. This vector potential cannot be defined without singularities as for a singularity-free $\boldsymbol{A}$ we obtain $\mathrm{div}\,(\nabla \times \boldsymbol{A}) = 0$. However, we get

$$\int_V d^3r \,\mathrm{div}\,\left(\nabla_{\hat{\boldsymbol{\Omega}}} \times \boldsymbol{A}\right) = \int_{\partial V} \left(\nabla_{\hat{\boldsymbol{\Omega}}} \times \boldsymbol{A}\right) \cdot d\boldsymbol{\sigma} = \int_{\partial V} \hat{\boldsymbol{\Omega}} \cdot d\boldsymbol{\sigma} = 4\pi. \tag{B.11}$$

In spherical coordinates, *i.e.* $\hat{\boldsymbol{\Omega}}(r, \theta, \phi) = r(\sin\theta\cos\phi, \sin\theta\sin\phi, \cos\theta)^T$, a parametrization of $\boldsymbol{A}$ is given by (see *e.g.* [150]):

$$\boldsymbol{A}(r, \theta, \phi) = \frac{1 - \cos\theta}{r\sin\theta}\,\hat{\boldsymbol{e}}_\phi \quad \text{with} \quad \hat{\boldsymbol{e}}_\phi = (-\sin\phi, \cos\phi, 0)^T. \tag{B.12}$$

It is singular for $\theta = \pi$ and reduces on the unit sphere, $|\hat{\boldsymbol{\Omega}}| = r = 1$, to $\boldsymbol{A}(\theta, \phi) = (1 - \cos\theta)/\sin\theta\,\hat{\boldsymbol{e}}_\phi$. To show that Eq. (B.8) leads to the LLG equation we will calculate the variations of Eq. (B.8) explicitly , starting with the right hand side.

The variation of the dissipation functional with respect to $\partial_t\hat{\boldsymbol{\Omega}}(\boldsymbol{r}, t)$ is given by

$$\frac{\delta\mathcal{R}[\hat{\boldsymbol{\Omega}}]}{\delta(\partial_t\hat{\boldsymbol{\Omega}}(\boldsymbol{r}, t))} = \frac{\delta\mathcal{R}^\alpha[\hat{\boldsymbol{\Omega}}]}{\delta(\partial_t\hat{\boldsymbol{\Omega}}(\boldsymbol{r}, t))} + \frac{\delta\mathcal{R}^{\alpha'}[\hat{\boldsymbol{\Omega}}]}{\delta(\partial_t\hat{\boldsymbol{\Omega}}(\boldsymbol{r}, t))}, \tag{B.13a}$$

$$\frac{\delta\mathcal{R}^\alpha[\hat{\boldsymbol{\Omega}}]}{\delta(\partial_t\hat{\boldsymbol{\Omega}}(\boldsymbol{r}, t))} = \alpha\left(\partial_t + \frac{\beta}{\alpha}\boldsymbol{v}_s \cdot \nabla\right)\hat{\boldsymbol{\Omega}}(\boldsymbol{r}, t), \tag{B.13b}$$

$$\frac{\delta\mathcal{R}^{\alpha'}[\hat{\boldsymbol{\Omega}}]}{\delta(\partial_t\hat{\boldsymbol{\Omega}}(\boldsymbol{r}, t))} = \alpha'\left[\hat{\boldsymbol{\Omega}}(\boldsymbol{r}, t) \cdot \left(\partial_i\hat{\boldsymbol{\Omega}}(\boldsymbol{r}, t) \times (\partial_t + \frac{\beta'}{\alpha'}\boldsymbol{v}_s \cdot \nabla)\hat{\boldsymbol{\Omega}}(\boldsymbol{r}, t))\right]\left(\hat{\boldsymbol{\Omega}}(\boldsymbol{r}, t) \times \partial_i\hat{\boldsymbol{\Omega}}(\boldsymbol{r}, t)\right), \tag{B.13c}$$

which reproduces both damping terms on the right hand side of Eq. (8.11). Because the variation of the action functional is more subtle, we will present the detailed calculation. The action functional $\mathcal{A}[\hat{\boldsymbol{\Omega}}]$ contains the Ginzburg-Landau free energy functional and the time- and the space-dependent Berry phase terms. Therefore, we divide it into three parts:

$$\mathcal{A}[\hat{\boldsymbol{\Omega}}] = \int dt \left\{ \int_V d^3r\,\boldsymbol{A}(\hat{\boldsymbol{\Omega}}(\boldsymbol{r}, t)) \cdot (\partial_t + \boldsymbol{v}_s \cdot \nabla)\,\hat{\boldsymbol{\Omega}}(\boldsymbol{r}, t) - \frac{1}{M}F[\hat{\boldsymbol{\Omega}}(\boldsymbol{r}, t)] \right\}$$
$$\equiv \left(\mathcal{A}^{(t)}[\hat{\boldsymbol{\Omega}}(\boldsymbol{r}, t)] + \mathcal{A}^{(\nabla)}[\hat{\boldsymbol{\Omega}}(\boldsymbol{r}, t)] + \mathcal{A}^{(F)}[\hat{\boldsymbol{\Omega}}(\boldsymbol{r}, t)]\right) \tag{B.14}$$

with

$$\mathcal{A}^{(t)}[\hat{\boldsymbol{\Omega}}(\boldsymbol{r}, t)] = \int dt \int_V d^3r\,\boldsymbol{A}(\hat{\boldsymbol{\Omega}}(\boldsymbol{r}, t)) \cdot \partial_t\hat{\boldsymbol{\Omega}}(\boldsymbol{r}, t), \tag{B.15a}$$

$$\mathcal{A}^{(\nabla)}[\hat{\boldsymbol{\Omega}}(\boldsymbol{r}, t)] = \int dt \int_V d^3r\,\boldsymbol{A}(\hat{\boldsymbol{\Omega}}(\boldsymbol{r}, t)) \cdot (\boldsymbol{v}_s\nabla)\,\hat{\boldsymbol{\Omega}}(\boldsymbol{r}, t), \tag{B.15b}$$

$$\mathcal{A}^{(F)}[\hat{\boldsymbol{\Omega}}(\boldsymbol{r}, t)] = -\int dt\,\frac{1}{M}F[\hat{\boldsymbol{\Omega}}(\boldsymbol{r}, t)]. \tag{B.15c}$$

Let us start by considering the variational derivative of $\mathcal{A}^{(t)}[\hat{\boldsymbol{\Omega}}(\boldsymbol{x}, t)]$ which is defined by:

$$\frac{\delta\mathcal{A}^{(t)}[\hat{\boldsymbol{\Omega}}(\boldsymbol{x}, t)]}{\delta\Omega_j(\boldsymbol{y}, t')} = \lim_{\epsilon \to 0} \frac{1}{\epsilon}\left(\mathcal{A}^{(t)}[\hat{\boldsymbol{\Omega}}(\boldsymbol{x}, t) + \epsilon\,\hat{e}_j\delta(\boldsymbol{x} - \boldsymbol{y}, t - t')] - \mathcal{A}^{(t)}[\hat{\boldsymbol{\Omega}}(\boldsymbol{x}, t)]\right) \tag{B.16}$$

with a variation in the direction of $\hat{e}_j$. To ensure that $\hat{\boldsymbol{\Omega}}(\boldsymbol{x}, t) + \epsilon\,\hat{e}_j\delta(\boldsymbol{x} - \boldsymbol{y}, t - t')$ is normalized to linear order in ϵ, one can only consider directions $\hat{e}_j$ with $\hat{e}_j \perp \hat{\boldsymbol{\Omega}}(\boldsymbol{x}, t)$,

which is equivalent to the condition that $\hat{\boldsymbol{\Omega}}$ varies only in the tangent space of the sphere. Hence, we obtain:

$$
\frac{\delta \mathcal{A}^{(t)}[\hat{\boldsymbol{\Omega}}(\boldsymbol{x}, t)]}{\delta \hat{\Omega}_j(\boldsymbol{y}, t')}
$$

$$
= \lim_{\epsilon \to 0} \frac{1}{\epsilon} \left[\int_V d^3x \int dt \left(\partial_t \left(\hat{\boldsymbol{\Omega}}(\boldsymbol{x}, t) + \epsilon\, \hat{e}_j \delta(\boldsymbol{x} - \boldsymbol{y}, t - t') \right)_k \right.\right.
$$
$$
\left.\left. \cdot A_k \left[\hat{\boldsymbol{\Omega}}(\boldsymbol{x}, t) + \epsilon\, \hat{e}_j \delta(\boldsymbol{x} - \boldsymbol{y}, t - t') \right] - \partial_t \Omega_k(\boldsymbol{x}, t) \cdot A_k[\hat{\boldsymbol{\Omega}}(\boldsymbol{x}, t)] \right) \right]
$$

$$
= \lim_{\epsilon \to 0} \frac{1}{\epsilon} \left[\int_V d^3x \int dt \left(\partial_t \Omega_k(\boldsymbol{x}, t) \left(A_k \left[\hat{\boldsymbol{\Omega}}(\boldsymbol{x}, t) + \epsilon\, \hat{e}_j \delta(\boldsymbol{x} - \boldsymbol{y}, t - t') \right] - A_k[\hat{\boldsymbol{\Omega}}(\boldsymbol{x}, t)] \right) \right.\right.
$$
$$
\left.\left. + \epsilon\, \delta_{jk} \frac{\partial \delta(\boldsymbol{x} - \boldsymbol{y}, t - t')}{\partial t} A_k \left[\hat{\boldsymbol{\Omega}}(\boldsymbol{x}, t) + \epsilon\, \hat{e}_j \delta(\boldsymbol{x} - \boldsymbol{y}, t - t') \right] \right) \right]
$$

$$
= \int_V d^3x \int dt\, \partial_t \Omega_k(\boldsymbol{x}, t) \lim_{\epsilon \to 0} \frac{1}{\epsilon} \left(A_k \left[\hat{\boldsymbol{\Omega}}(\boldsymbol{x}, t) + \epsilon\, \hat{e}_j \delta(\boldsymbol{x} - \boldsymbol{y}, t - t') \right] - A_k[\hat{\boldsymbol{\Omega}}(\boldsymbol{x}, t)] \right)
$$
$$
+ \lim_{\epsilon \to 0} \int_V d^3x \int dt \left(\frac{\partial \delta(\boldsymbol{x} - \boldsymbol{y}, t - t')}{\partial t} A_j \left[\hat{\boldsymbol{\Omega}}(\boldsymbol{x}, t) + \epsilon\, \hat{e}_j \delta(\boldsymbol{x} - \boldsymbol{y}, t - t') \right] \right)
$$

$$
= \int_V d^3x \int dt\, \partial_t \Omega_k(\boldsymbol{x}, t)\, \delta(\boldsymbol{x} - \boldsymbol{y}, t - t') \frac{\partial A_k[\hat{\boldsymbol{\Omega}}(\boldsymbol{x}, t)]}{\partial \Omega_j} + \frac{\partial \delta(\boldsymbol{x} - \boldsymbol{y}, t - t')}{\partial t} A_j[\hat{\boldsymbol{\Omega}}(\boldsymbol{x}, t)]
$$

$$
\stackrel{\text{p.i.}}{=} \left(\partial_t \Omega_k(\boldsymbol{x}, t) \left. \frac{\partial A_k[\hat{\boldsymbol{\Omega}}(\boldsymbol{x}, t)]}{\partial \Omega_j} \right|_{\boldsymbol{x}=\boldsymbol{y}, t=t'} - \int_V d^3x \int dt \delta(\boldsymbol{x} - \boldsymbol{y}, t - t') \frac{\partial A_j[\hat{\boldsymbol{\Omega}}(\boldsymbol{x}, t)]}{\partial t} \right)
$$
$$
+ \left(A_j[\hat{\boldsymbol{\Omega}}(\boldsymbol{y}, t_2)]\delta(t_2 - t') - A_j[\hat{\boldsymbol{\Omega}}(\boldsymbol{y}, t_1)]\delta(t_1 - t') \right)
$$

$$
=: \mathrm{MT}_j^{(t)} + \mathrm{BT}_j^{(t)}.
$$

Here, "p.i." denotes partial integration, t_1 and t_2 are the limits of the time integral, and the abbrevation "MT" denotes the main term, while "BT" denotes the boundary term. The boundary term $\mathrm{BT}_j^{(t)}$ vanishes due to the usual Lagrangian formalism which allows only for variations that leave the configuration at the initial and final time invariant. The main term $\mathrm{MT}_j^{(t)}$ can be simplified further as follows:

$$
\mathrm{MT}_j^{(t)} = \partial_t \Omega_k(\boldsymbol{x}, t) \left. \frac{\partial A_k[\hat{\boldsymbol{\Omega}}(\boldsymbol{x}, t)]}{\partial \Omega_j} \right|_{\boldsymbol{x}=\boldsymbol{y}, t=t'} - \int_V d^3x \int dt\, \delta(\boldsymbol{x} - \boldsymbol{y}, t - t') \frac{\partial A_j[\hat{\boldsymbol{\Omega}}(\boldsymbol{x}, t)]}{\partial t}
$$

$$
= \left(\partial_t \Omega_k(\boldsymbol{x}, t) \frac{\partial A_k[\hat{\boldsymbol{\Omega}}(\boldsymbol{x}, t)]}{\partial \Omega_j} - \frac{\partial A_j[\hat{\boldsymbol{\Omega}}(\boldsymbol{x}, t)]}{\partial t} \right)\Bigg|_{\boldsymbol{x}=\boldsymbol{y}, t=t'}
$$

$$
= \partial_t \Omega_k(\boldsymbol{x}, t) \left(\frac{\partial A_k[\hat{\boldsymbol{\Omega}}(\boldsymbol{x}, t)]}{\partial \Omega_j} - \frac{\partial A_j[\hat{\boldsymbol{\Omega}}(\boldsymbol{x}, t)]}{\partial \Omega_k} \right)\Bigg|_{\boldsymbol{x}=\boldsymbol{y}, t=t'}
$$

$$
= \partial_t \Omega_k(\boldsymbol{x}, t) (\delta_{ja}\delta_{kb} - \delta_{jb}\delta_{ka}) \left. \frac{\partial A_b[\hat{\boldsymbol{\Omega}}(\boldsymbol{x}, t)]}{\partial \hat{\boldsymbol{\Omega}}_a} \right|_{\boldsymbol{x}=\boldsymbol{y}, t=t'}
$$

$$
= \epsilon_{jkm}\, \epsilon_{mab}\, \partial_t \Omega_k(\boldsymbol{x}, t) \left. \frac{\partial A_b[\hat{\boldsymbol{\Omega}}(\boldsymbol{x}, t)]}{\partial \hat{\boldsymbol{\Omega}}_a} \right|_{\boldsymbol{x}=\boldsymbol{y}, t=t'}
$$

$$
= \epsilon_{jkm}\, \partial_t \Omega_k(\boldsymbol{x}, t) \left(\nabla_{\hat{\boldsymbol{\Omega}}} \times \boldsymbol{A}[\hat{\boldsymbol{\Omega}}(\boldsymbol{x}, t)] \right)_m \Bigg|_{\boldsymbol{x}=\boldsymbol{y}, t=t'}
$$

Thus, for the main term $\mathrm{MT}_j^{(t)}$ we obtain:

$$\begin{aligned}
\mathrm{MT}_j^{(t)} &= \epsilon_{jkm}\frac{\partial \Omega_k(\boldsymbol{x},t)}{\partial t}\,\Omega(\boldsymbol{x},t)_m\bigg|_{\boldsymbol{x}=\boldsymbol{y},t=t'} \\
&= \left(\frac{\partial \hat{\boldsymbol{\Omega}}(\boldsymbol{y},t')}{\partial t'}\times\hat{\boldsymbol{\Omega}}(\boldsymbol{y},t')\right)_j,
\end{aligned}$$

(B.17)

where we used the relation $\nabla_{\hat{\boldsymbol{\Omega}}}\times\boldsymbol{A}=\hat{\boldsymbol{\Omega}}$. Let us now consider the variational derivative of $\mathcal{A}^{(\nabla)}[\hat{\boldsymbol{\Omega}}(\boldsymbol{x},t)]$. By definition we obtain

$$\frac{\delta\mathcal{A}^{(\nabla)}[\hat{\boldsymbol{\Omega}}(\boldsymbol{x},t)]}{\delta\hat{\boldsymbol{\Omega}}_j(\boldsymbol{y},t')}=\lim_{\epsilon\to 0}\frac{1}{\epsilon}\left(\mathcal{A}^{(\nabla)}[\hat{\boldsymbol{\Omega}}(\boldsymbol{x},t)+\epsilon\,\hat{e}_j\delta(\boldsymbol{x}-\boldsymbol{y},t-t')]-\mathcal{A}^{(\nabla)}[\hat{\boldsymbol{\Omega}}(\boldsymbol{x},t)]\right)$$

(B.18)

with $\hat{e}_j\perp\hat{\boldsymbol{\Omega}}(\boldsymbol{x},t)$ as in the case of $\mathcal{A}^{(t)}$. By an analog straightforward calculation we get:

$$\begin{aligned}
&\frac{\delta\mathcal{A}^{(\nabla)}[\hat{\boldsymbol{\Omega}}(\boldsymbol{x},t)]}{\delta\hat{\boldsymbol{\Omega}}_j(\boldsymbol{y},t')} \\
&=\lim_{\epsilon\to 0}\frac{1}{\epsilon}\left[\int_V d^3x\int dt\left((\boldsymbol{v}_s\cdot\nabla)\left(\hat{\boldsymbol{\Omega}}(\boldsymbol{x},t)+\epsilon\,\hat{e}_j\delta(\boldsymbol{x}-\boldsymbol{y},t-t')\right)\right.\right. \\
&\qquad\qquad\left.\left. A_k[\hat{\boldsymbol{\Omega}}(\boldsymbol{x},t)+\epsilon\,\hat{e}_j\delta(\boldsymbol{x}-\boldsymbol{y},t-t')]-(\boldsymbol{v}_s\cdot\nabla)\Omega_k(\boldsymbol{x},t)\,A_k[\hat{\boldsymbol{\Omega}}(\boldsymbol{x},t)]\right)\right] \\
&=\lim_{\epsilon\to 0}\frac{1}{\epsilon}\left[\int_V d^3x\int dt\left((\boldsymbol{v}_s\cdot\nabla)\Omega_k(\boldsymbol{x},t)\left(A_k[\hat{\boldsymbol{\Omega}}(\boldsymbol{x},t)+\epsilon\,\hat{e}_j\delta(\boldsymbol{x}-\boldsymbol{y},t-t')]-A_k[\hat{\boldsymbol{\Omega}}(\boldsymbol{x},t)]\right)\right.\right. \\
&\qquad\qquad\left.\left. +\epsilon\,\delta_{jk}(\boldsymbol{v}_s\cdot\nabla)\delta(\boldsymbol{x}-\boldsymbol{y},t-t')\,A_k[\hat{\boldsymbol{\Omega}}(\boldsymbol{x},t)+\epsilon\,\hat{e}_j\delta(\boldsymbol{x}-\boldsymbol{y},t-t')]\right)\right] \\
&=\int_V d^3x\int dt\,(\boldsymbol{v}_s\cdot\nabla)\Omega_k(\boldsymbol{x},t)\lim_{\epsilon\to 0}\frac{1}{\epsilon}\left(A_k[\hat{\boldsymbol{\Omega}}(\boldsymbol{x},t)+\epsilon\,\hat{e}_j\delta(\boldsymbol{x}-\boldsymbol{y},t-t')]-A_k[\hat{\boldsymbol{\Omega}}(\boldsymbol{x},t)]\right) \\
&\qquad +\lim_{\epsilon\to 0}\int_V d^3x\int dt\left((\boldsymbol{v}_s\cdot\nabla)\delta(\boldsymbol{x}-\boldsymbol{y},t-t')\,A_j[\hat{\boldsymbol{\Omega}}(\boldsymbol{x},t)+\epsilon\,\hat{e}_j\delta(\boldsymbol{x}-\boldsymbol{y},t-t')]\right) \\
&=\int_V d^3x\int dt\,(\boldsymbol{v}_s\cdot\nabla)\Omega_k(\boldsymbol{x},t)\delta(\boldsymbol{x}-\boldsymbol{y},t-t')\frac{\partial A_k[\hat{\boldsymbol{\Omega}}(\boldsymbol{x},t)]}{\partial\Omega_j} \\
&\qquad +\int_V d^3x\int dt\,(\boldsymbol{v}_s\cdot\nabla)\delta(\boldsymbol{x}-\boldsymbol{y},t-t')A_j[\hat{\boldsymbol{\Omega}}(\boldsymbol{x},t)] \\
&\stackrel{\text{p.i.}}{=}\left[(\boldsymbol{v}_s\cdot\nabla)\Omega_k(\boldsymbol{x},t)\cdot\frac{\partial A_k[\hat{\boldsymbol{\Omega}}(\boldsymbol{x},t)]}{\partial\Omega_j}\bigg|_{\boldsymbol{x}=\boldsymbol{y},t=t'}\right. \\
&\qquad\left. -\int_V d^3x\int dt\,\delta(\boldsymbol{x}-\boldsymbol{y},t-t')(\boldsymbol{v}_s\cdot\nabla)A_j[\hat{\boldsymbol{\Omega}}(\boldsymbol{x},t)]\right] \\
&\qquad +\int dt\int_{S(V)}d\sigma^{(x)}\,\delta(\boldsymbol{x}-\boldsymbol{y},t-t')A_j[\hat{\boldsymbol{\Omega}}(\boldsymbol{x},t)](\boldsymbol{v}_s\cdot\boldsymbol{\nu}) \\
&=:\mathrm{MT}_j^{(\nabla)}+\mathrm{BT}_j^{(\nabla)}.
\end{aligned}$$

where $d\sigma^{(x)}$ is the area element, and $\boldsymbol{\nu}$ is the outer normal unit vector on the surface $S(V)$ of the volume V, i.e. $d\boldsymbol{\sigma}^{(x)}=\boldsymbol{\nu}\,d\sigma^{(x)}$. Note that the superscript "x" implies the integration over $\boldsymbol{x}$, but not $\boldsymbol{y}$.

Similar to the calculation for $\mathcal{A}^{(t)}$ we get for the main term $\mathrm{MT}^{(\nabla)}$:

$$
\begin{aligned}
\mathrm{MT}_j^{(\nabla)} &= [(\boldsymbol{v}_s \nabla)\Omega_k(\boldsymbol{x},t)] \left. \frac{\partial A_k[\hat{\boldsymbol{\Omega}}(\boldsymbol{x},t)]}{\partial \Omega_j} \right|_{\boldsymbol{x}=\boldsymbol{y},t=t'} \\
&\qquad - \int_V d^3x \int dt \, \delta(\boldsymbol{x}-\boldsymbol{y},t-t')(\boldsymbol{v}_s \cdot \nabla)A_j[\hat{\boldsymbol{\Omega}}(\boldsymbol{x},t)] \\
&= \left([(\boldsymbol{v}_s \cdot \nabla)\Omega_k(\boldsymbol{x},t)] \frac{\partial A_k[\hat{\boldsymbol{\Omega}}(\boldsymbol{x},t)]}{\partial \Omega_j} - (\boldsymbol{v}_s \cdot \nabla)A_j[\hat{\boldsymbol{\Omega}}(\boldsymbol{x},t)] \right)\Bigg|_{\boldsymbol{x}=\boldsymbol{y},t=t'} \\
&= [(\boldsymbol{v}_s \cdot \nabla)\Omega_k(\boldsymbol{x},t)] \left(\frac{\partial A_k[\hat{\boldsymbol{\Omega}}(\boldsymbol{x},t)]}{\partial \Omega_j} - \frac{\partial A_j[\hat{\boldsymbol{\Omega}}(\boldsymbol{x},t)]}{\partial \Omega_k} \right)\Bigg|_{\boldsymbol{x}=\boldsymbol{y},t=t'} \\
&= [(\boldsymbol{v}_s \cdot \nabla)\Omega_k(\boldsymbol{x},t)] \, (\delta_{ja}\delta_{kb} - \delta_{jb}\delta_{ka})\frac{\partial A_b[\hat{\boldsymbol{\Omega}}(\boldsymbol{x},t)]}{\partial \hat{\Omega}_a}\Bigg|_{\boldsymbol{x}=\boldsymbol{y},t=t'} \\
&= [(\boldsymbol{v}_s \cdot \nabla)\Omega_k(\boldsymbol{x},t)] \, \epsilon_{jkm}\epsilon_{mab} \frac{\partial A_b[\hat{\boldsymbol{\Omega}}(\boldsymbol{x},t)]}{\partial \hat{\Omega}_a}\Bigg|_{\boldsymbol{x}=\boldsymbol{y},t=t'} \\
&= [(\boldsymbol{v}_s \cdot \nabla)\Omega_k(\boldsymbol{x},t)] \, \epsilon_{jkm} \left(\nabla_{\hat{\boldsymbol{\Omega}}} \times \boldsymbol{A}[\hat{\boldsymbol{\Omega}}(\boldsymbol{x},t)] \right)_m \Bigg|_{\boldsymbol{x}=\boldsymbol{y},t=t'} \\
&= \epsilon_{jkm} [(\boldsymbol{v}_s \cdot \nabla)\Omega_k(\boldsymbol{x},t)] \, \Omega(\boldsymbol{x},t)_m \Bigg|_{\boldsymbol{x}=\boldsymbol{y},t=t'} \\
&= \left(\left[(\boldsymbol{v}_s \cdot \nabla)\hat{\boldsymbol{\Omega}}(\boldsymbol{y},t') \right] \times \hat{\boldsymbol{\Omega}}(\boldsymbol{y},t') \right)_j .
\end{aligned}
$$

Concerning the boundary term, we perform the time integration, and we are left with

$$
\begin{aligned}
\mathrm{BT}_j^{(\nabla)} &= \int dt \int_{S(V)} d\sigma^{(x)} \, \delta(\boldsymbol{x}-\boldsymbol{y},t-t')A_j[\hat{\boldsymbol{\Omega}}(\boldsymbol{x},t)](\boldsymbol{v}_s \cdot \boldsymbol{\nu}) \\
&= \int_{S(V)} d\sigma^{(x)} \, \delta(\boldsymbol{x}-\boldsymbol{y})A_j[\hat{\boldsymbol{\Omega}}(\boldsymbol{x},t')](\boldsymbol{v}_s \cdot \boldsymbol{\nu}).
\end{aligned}
\tag{B.19}
$$

The role of this boundary term is discussed in Appendix C.2. To sum up, for the three terms $\mathcal{A}^{(t)}$, $\mathcal{A}^{(\nabla)}$, and $\mathcal{A}^{(F)}$ we get:

$$
\frac{\delta \mathcal{A}^{(t)}[\hat{\boldsymbol{\Omega}}(\boldsymbol{r},t)]}{\delta \Omega_j(\boldsymbol{y},t')} = \left(\frac{\partial \hat{\boldsymbol{\Omega}}(\boldsymbol{y},t')}{\partial t'} \times \hat{\boldsymbol{\Omega}}(\boldsymbol{y},t') \right)_j, \tag{B.20a}
$$

$$
\frac{\delta \mathcal{A}^{(\nabla)}[\hat{\boldsymbol{\Omega}}(\boldsymbol{r},t)]}{\delta \Omega_j(\boldsymbol{y},t')} = \left(\left[(\boldsymbol{v}_s \cdot \nabla)\hat{\boldsymbol{\Omega}}(\boldsymbol{y},t') \right] \times \hat{\boldsymbol{\Omega}}(\boldsymbol{y},t') \right)_j
$$
$$
+ \int_{S(V)} d\sigma^{(x)} \, \delta(\boldsymbol{r}-\boldsymbol{y})A_j[\hat{\boldsymbol{\Omega}}(\boldsymbol{r},t')](\boldsymbol{v}_s \cdot \boldsymbol{\nu}), \tag{B.20b}
$$

$$
\frac{\delta \mathcal{A}^{(F)}[\hat{\boldsymbol{\Omega}}(\boldsymbol{r},t)]}{\delta \Omega_j(\boldsymbol{y},t')} =: \frac{1}{M} \frac{\delta F[\hat{\boldsymbol{\Omega}}(\boldsymbol{r},t')]}{\delta \hat{\boldsymbol{\Omega}}(\boldsymbol{y},t')}, \tag{B.20c}
$$

where in the last equation we considered the functional $F[\hat{\boldsymbol{\Omega}}]$ at a fixed time t' to eliminate the time integral. Exchanging $\boldsymbol{r}$, $\boldsymbol{y}$ and t, t' we get:

$$
\begin{aligned}
\frac{\delta \mathcal{A}[\hat{\boldsymbol{\Omega}}]}{\delta \hat{\boldsymbol{\Omega}}(\boldsymbol{r},t)} &= -\hat{\boldsymbol{\Omega}}(\boldsymbol{r},t) \times (\partial_t + \boldsymbol{v}_s \cdot \nabla)\,\hat{\boldsymbol{\Omega}}(\boldsymbol{r},t) - \frac{1}{M} \frac{\delta F[\hat{\boldsymbol{\Omega}}]}{\delta \hat{\boldsymbol{\Omega}}(\boldsymbol{r},t)} \\
&\qquad\qquad\qquad + \int_{S(V)} d\sigma^{(y)} \, \delta(\boldsymbol{y}-\boldsymbol{r})A_j[\hat{\boldsymbol{\Omega}}(\boldsymbol{y},t)](\boldsymbol{v}_s \cdot \boldsymbol{\nu}). \quad \text{(B.21)}
\end{aligned}
$$

Combining Eqs. (B.8), (B.9a), (B.9b), (B.9c), (B.21), and neglecting the boundary term we obtain Eq. (8.11) of the main text:

$$-\frac{1}{M}\frac{\delta F}{\delta \hat{\boldsymbol{\Omega}}} = \hat{\boldsymbol{\Omega}} \times (\partial_t + \boldsymbol{v}_s \cdot \nabla)\,\hat{\boldsymbol{\Omega}} + \alpha\Big(\partial_t + \frac{\beta}{\alpha}\boldsymbol{v}_s \cdot \nabla\Big)\hat{\boldsymbol{\Omega}}$$

$$+ \hat{\boldsymbol{\Omega}} \times \alpha'\Big[\hat{\boldsymbol{\Omega}} \cdot \big(\partial_i\hat{\boldsymbol{\Omega}} \times (\partial_t + \frac{\beta'}{\alpha'}\boldsymbol{v}_s \cdot \nabla)\hat{\boldsymbol{\Omega}}\big)\Big]\partial_i\hat{\boldsymbol{\Omega}}. \quad (B.22)$$

C Numerics for the Skyrmion Phase and an Alternative Approach

In this Appendix, we discuss the numerics we use to obtain the magnetization structure for the skyrmion phase. Parts of it can be found in Refs. [70, 129]. Furthermore, we show that alternative approaches for the drift velocity as well as for the rotation angle lead to the same results as obtained in the main text.

C.1   Numerics for the Skyrmion Lattice in Equilibrium

To obtain the magnetization structure $\boldsymbol{M}(\boldsymbol{r})$ in the skyrmion lattice phase we employ the following mean-field approximation. We minimize the free energy functional with the ansatz of Eq. (4.14), and we include in the sum only the three smallest reciprocal lattice vectors $\boldsymbol{q}_j$ if not stated otherwise. In particular, in Chapter 5 we also have included higher-order modes. As we have indicated in Section 4.3, and as was confirmed in Chapter 5, the superposition of the three lowest modes is quite a good approximation, because higher-order terms contribute at most a few percent to the total magnetization. Furthermore, the effects of thermal fluctuations are not included in our numerical calculations. As discussed in the main text, they are crucial for stabilizing the skyrmion lattice in competition to the conical phase, but when considering the skyrmion phase (at least not too close to the phase transition) they lead only to a small renormalization of prefactors [1].

When neglecting higher-order modes, in our numerical calculations we approximate the magnetic texture in total by 27 real parameters μ_i, $i = 1, \ldots, 27$, consisting of the uniform magnetization $\boldsymbol{M}_f$, two reciprocal lattice vectors $\boldsymbol{q}_1$, $\boldsymbol{q}_2$ (with $\boldsymbol{q}_3 = -\boldsymbol{q}_1 - \boldsymbol{q}_2$) and three complex Fourier modes $\boldsymbol{m}_{\boldsymbol{q}_j} = \boldsymbol{m}_{\boldsymbol{q}_j}^{(r)} + i\,\boldsymbol{m}_{\boldsymbol{q}_j}^{(i)}$, $j = 1, 2, 3$, with the real $\boldsymbol{m}_{\boldsymbol{q}_j}^{(r)}$ and imaginary part $\boldsymbol{m}_{\boldsymbol{q}_j}^{(i)}$. This yields $3 + 2 \cdot 3 + 3 \cdot 3 \cdot 2 = 27$ parameters. Therefore, our ansatz for the magnetization in the skyrmion phase is given by

$$\boldsymbol{M}(\boldsymbol{r}) = \boldsymbol{M}_f + \sum_{\boldsymbol{q}_j \in \tilde{L}_R} \boldsymbol{m}_{\boldsymbol{q}_j}\, e^{i\boldsymbol{q}_j \cdot \boldsymbol{r}}, \tag{C.1}$$

with $\tilde{L}_R = \{\pm\boldsymbol{q}_1, \pm\boldsymbol{q}_2, \pm\boldsymbol{q}_3\}$ which reproduces Eq. (4.14) of the main text when taking only the the lowest Fourier modes into account.

C.2   Alternative Approach

In order to obtain the acting forces and the drift velocity as well as the rotation angle and the acting torques, we projected the LLG equation onto the translational and rotational modes, respectively.

To check this approach and substantiate its validity, we confirmed that an alternative derivation without the explicit projection onto the corresponding mode leads to the same results [70, 129]. Here, we will first introduce the method, and then discuss the motion and the rotation separately.

Within our numerics the magnetic texture is described by a certain finite number of time-dependent variables u_j $(j = 1, \ldots, n)$, i.e. $\hat{\mathbf{\Omega}}(\boldsymbol{r}, t) = \hat{\mathbf{\Omega}}(\boldsymbol{r}, u_1(t), \ldots, u_n(t))$. In the static case, $u_i = \mu_i$, $i = 1, \ldots, 27$, but for a moving magnetic texture also the drift characterizes the system, and we have to take it into account as discussed below. An alternative approach is to directly derive effective equations of motions for these variables. Starting from the LLG equation we multiply Eq. (8.10) by $\left(\hat{\mathbf{\Omega}} \times \frac{\partial \hat{\mathbf{\Omega}}}{\partial u_j}\right)$ and then integrate over a volume V. Using the fact that $\hat{\mathbf{\Omega}}$ is normalized, $\hat{\mathbf{\Omega}}$ is perpendicular to its derivatives, $\hat{\mathbf{\Omega}} \cdot \frac{\partial \hat{\mathbf{\Omega}}}{\partial u_j} = 0$, so that we obtain the following n linear coupled differential equations of first order in time:

$$\int_V d^3r \left(\hat{\mathbf{\Omega}} \times \frac{\partial \hat{\mathbf{\Omega}}}{\partial u_j}\right) \cdot (\partial_t + (\boldsymbol{v}_s \cdot \nabla)) \hat{\mathbf{\Omega}} - \frac{1}{|\boldsymbol{M}|} \frac{\partial F}{\partial u_j} = \int_V d^3r \, \alpha \left(\partial_t + \frac{\beta}{\alpha}(\boldsymbol{v}_s \cdot \nabla)\right) \hat{\mathbf{\Omega}} \cdot \frac{\partial \hat{\mathbf{\Omega}}}{\partial u_j}$$
$$- \int_V d^3r \alpha' \left[\hat{\mathbf{\Omega}} \cdot \left(\partial_i \hat{\mathbf{\Omega}} \times \left(\partial_t + \frac{\beta'}{\alpha'}(\boldsymbol{v}_s \cdot \nabla)\right)\hat{\mathbf{\Omega}}\right)\right] \cdot \partial_i \hat{\mathbf{\Omega}} \cdot \left(\hat{\mathbf{\Omega}} \times \frac{\partial \hat{\mathbf{\Omega}}}{\partial u_j}\right). \quad \text{(C.2)}$$

C.2.1 Equations of Motion from a Variational Principle

In principle, it is possible to derive these effective equations of motion from the variational principle

$$\frac{\delta \mathcal{A}[\hat{\mathbf{\Omega}}]}{\delta u_j(s)} = \frac{\delta \mathcal{R}[\hat{\mathbf{\Omega}}, \partial_t \hat{\mathbf{\Omega}}]}{\delta(\partial_t u_j(s))}. \quad \text{(C.3)}$$

However, in this case we will obtain a "boundary term" that occured already in Appendix B, which one has to neglect to obtain Eq. (C.2). Further discussing this "boundary term" we show that this contribution will not necessarily result in a surface term, but might also contribute to the bulk value. This subtle issue is discussed in more detail below.

To obtain the effective equations of motion from the variatonal principle, we assume $n = 1$ without loss of generality, and set $u_1(t) = u(t)$. As an intermediate step, let us first calculate

$$\frac{\partial}{\partial \dot{u}}\left(\partial_t \hat{\mathbf{\Omega}}(\boldsymbol{x}, u)\right)\bigg|_u = \frac{\partial}{\partial \dot{u}}\left(\frac{\partial \hat{\mathbf{\Omega}}(\boldsymbol{x}, u)}{\partial u}\dot{u}\right)\bigg|_u = \frac{\partial \hat{\mathbf{\Omega}}(\boldsymbol{x}, u)}{\partial u}. \quad \text{(C.4)}$$

Moreover, we use the following lemma for an arbitrary sufficiently smooth function $F(t)$ depending on t. If F depends on a parameter $u = u(t)$ such that $F(t) = F(u(t))$, then

$$\frac{\delta F(t')}{\delta u(t)} = \frac{\partial F(u)}{\partial u}\delta(t' - t). \quad \text{(C.5)}$$

Applying this lemma we obtain

$$\frac{\delta \hat{\mathbf{\Omega}}(\boldsymbol{y}, t')}{\delta u(t)} = \frac{\partial \hat{\mathbf{\Omega}}(\boldsymbol{y}, u)}{\partial u}\delta(t' - t) \quad \text{and} \quad \frac{\delta(\partial_t \hat{\mathbf{\Omega}}(\boldsymbol{y}, t'))}{\delta \dot{u}(t)}\bigg|_u = \frac{\partial(\partial_t \hat{\mathbf{\Omega}}(\boldsymbol{y}, u, \dot{u}))}{\partial \dot{u}}\bigg|_u \cdot \delta(t' - t). \quad \text{(C.6)}$$

Thus, we get:

$$
\begin{aligned}
0 &= \int_V d^3y \int dt \frac{\delta\mathcal{A}[\hat{\boldsymbol{\Omega}}(\boldsymbol{x},t)]}{\delta\hat{\boldsymbol{\Omega}}(\boldsymbol{y},t')}\,\delta(t-t')\overbrace{\left(\frac{\partial\hat{\boldsymbol{\Omega}}(\boldsymbol{y},t)}{\partial u} - \frac{\partial(\partial_t\hat{\boldsymbol{\Omega}}(\boldsymbol{y},t))}{\partial\dot{u}}\bigg|_u\right)}^{=0} \\
&= \int_V d^3y \int dt \frac{\delta\mathcal{A}[\hat{\boldsymbol{\Omega}}(\boldsymbol{x},t)]}{\delta\hat{\boldsymbol{\Omega}}(\boldsymbol{y},t')}\left(\frac{\delta\hat{\boldsymbol{\Omega}}(\boldsymbol{y},t')}{\delta u(t)} - \frac{\delta(\partial_t\hat{\boldsymbol{\Omega}}(\boldsymbol{y},t'))}{\delta\dot{u}(t)}\bigg|_u\right) \\
&= \int_V d^3y \int dt \frac{\delta\mathcal{A}[\hat{\boldsymbol{\Omega}}(\boldsymbol{x},t)]}{\delta\hat{\boldsymbol{\Omega}}(\boldsymbol{y},t')}\frac{\delta\hat{\boldsymbol{\Omega}}(\boldsymbol{y},t')}{\delta u(t)} - \int_V d^3y \int dt \frac{\delta\mathcal{R}[\hat{\boldsymbol{\Omega}}(\boldsymbol{y},t),\partial_t\hat{\boldsymbol{\Omega}}(\boldsymbol{x},t)]}{\delta(\partial_t\hat{\boldsymbol{\Omega}}(\boldsymbol{y},t))}\frac{\delta(\partial_t\hat{\boldsymbol{\Omega}}(\boldsymbol{y},t'))}{\delta\dot{u}(t)}\bigg|_u \\
&= \frac{\delta\mathcal{A}[\hat{\boldsymbol{\Omega}}(\boldsymbol{x},t)]}{\delta u(t)} - \frac{\delta\mathcal{R}[\hat{\boldsymbol{\Omega}}(\boldsymbol{x},t),\partial_t\hat{\boldsymbol{\Omega}}(\boldsymbol{x},t)]}{\delta\dot{u}(t)}\,,
\end{aligned}
$$

where in the penultimate line we applied Eq. (B.8). Hence, neglecting the boundary term appearing in Eq. (B.21) we have shown that u_j solves Eq. (C.2). However, within this proof the role of the "boundary term" is somehow concealed. To get a better understanding of this additional term, we will consider the variation of the action with respect to the variational parameter u explicitly. Applying the chain rule leads to

$$
\frac{\delta\mathcal{A}[\hat{\boldsymbol{\Omega}}(\boldsymbol{x},t)]}{\delta u_j(s)} = \int_V d^3y \int dt' \frac{\delta\mathcal{A}[\hat{\boldsymbol{\Omega}}(\boldsymbol{x},t)]}{\delta\hat{\boldsymbol{\Omega}}_j(\boldsymbol{y},t')}\bigg|_{\hat{\boldsymbol{\Omega}}=\hat{\boldsymbol{\Omega}}(u)}\frac{\delta\hat{\boldsymbol{\Omega}}_j(\boldsymbol{y},t')}{\delta u(s)}\,. \tag{C.7}
$$

Using above lemma we obtain

$$
\frac{\delta\Omega_j(\boldsymbol{y},t')}{\delta u(s)} = \frac{\partial\Omega_j(\boldsymbol{y},u)}{\partial u}\delta(s-t')\,, \tag{C.8}
$$

and inserting the result of Eq. (B.21) we get

$$
\begin{aligned}
\frac{\delta\mathcal{A}[\hat{\boldsymbol{\Omega}}(\boldsymbol{x},t)]}{\delta u(s)} &= \int_V d^3y \int dt'\bigg[-\left(\hat{\boldsymbol{\Omega}}(\boldsymbol{y},t')\times(\partial_t+\boldsymbol{v}_s\cdot\nabla)\,\hat{\boldsymbol{\Omega}}(\boldsymbol{y},t')\right)_j - \frac{1}{M}\frac{\delta F[\hat{\boldsymbol{\Omega}}]}{\delta\hat{\boldsymbol{\Omega}}_j(\boldsymbol{y},t')} \\
&\quad + \int_{S(V)} d\sigma^{(y')}\delta(\boldsymbol{y}'-\boldsymbol{y})A_j[\hat{\boldsymbol{\Omega}}(\boldsymbol{y}',t')](\boldsymbol{v}_s\cdot\boldsymbol{\nu})\bigg]\frac{\partial\Omega_j(\boldsymbol{y},t')}{\partial u}\delta(s-t')\bigg|_{\hat{\boldsymbol{\Omega}}=\hat{\boldsymbol{\Omega}}(\boldsymbol{y},u)} \\
&= -\int_V d^3y\left(\hat{\boldsymbol{\Omega}}(\boldsymbol{y},s)\times(\partial_t+\boldsymbol{v}_s\cdot\nabla)\,\hat{\boldsymbol{\Omega}}(\boldsymbol{y},s)\right)\frac{\partial\Omega_j(\boldsymbol{y},s)}{\partial u} - \frac{1}{M}\frac{\partial F[\hat{\boldsymbol{\Omega}}]}{\partial u} \\
&\quad + \int_V d^3y\left(\int_{S(V)} d\sigma^{(y')}\delta(\boldsymbol{y}'-\boldsymbol{y})A_j[\hat{\boldsymbol{\Omega}}(\boldsymbol{y}',s)](\boldsymbol{v}_s\cdot\boldsymbol{\nu})\right)\cdot\frac{\partial\Omega_j(\boldsymbol{y},s)}{\partial u}\bigg|_{\hat{\boldsymbol{\Omega}}=\hat{\boldsymbol{\Omega}}(\boldsymbol{y},u)}
\end{aligned}
$$

where $\boldsymbol{\nu}$ is the outward pointing unit normal vector of the surface $S(V)$ of the integration volume V. The boundary term may be simplified further to

$$
\begin{aligned}
&\int_{S(V)} d\sigma^{(y')}\int_V d^3y \frac{\partial\Omega_j(\boldsymbol{y},s)}{\partial u}\delta(\boldsymbol{y}'-\boldsymbol{y})A_j[\hat{\boldsymbol{\Omega}}(\boldsymbol{y}',s)](\boldsymbol{v}_s\cdot\boldsymbol{\nu}) \\
&= \int_{S(V)} d\sigma^{(y')}\frac{\partial\Omega_j(\boldsymbol{y},s)}{\partial u}A_j[\hat{\boldsymbol{\Omega}}(\boldsymbol{y}',s)]\underbrace{(\boldsymbol{v}_s\cdot\boldsymbol{\nu})}_{=v_{s_i}\hat{e}_i\cdot\boldsymbol{\nu}}\,,
\end{aligned}
$$

applying Gauss' theorem yields

$$= \int_V d^3y' \, v_{s_i} \frac{d}{dy_i'} \left(\frac{\partial \Omega_j(\boldsymbol{y}', s)}{\partial u} A_j[\hat{\boldsymbol{\Omega}}(\boldsymbol{x}, s)] \right),$$

and renaming of variables leads to

$$= \int_V d^3x \, (\boldsymbol{v}_s \cdot \nabla) \left(\frac{\partial \Omega_j(\boldsymbol{x}, s)}{\partial u} A_j[\hat{\boldsymbol{\Omega}}(\boldsymbol{x}, s)] \right).$$

A technical problem to further evaluate this term is the explicit appearance of the vector potential $A[\hat{\boldsymbol{\Omega}}(\boldsymbol{x}, s)]$ which cannot be written in a coordinate invariant form (see Appendix B). To sum up, we get:

$$\frac{\delta \mathcal{A}[\hat{\boldsymbol{\Omega}}(\boldsymbol{x}, t)]}{\delta u_j(s)} = \int_V d^3y \left(\hat{\boldsymbol{\Omega}}(\boldsymbol{y}, s) \times \frac{\partial \hat{\boldsymbol{\Omega}}(\boldsymbol{y}, s)}{\partial u_j} \right) \cdot (\partial_t + (\boldsymbol{v}_s \cdot \nabla)) \hat{\boldsymbol{\Omega}} - \frac{1}{M} \frac{\partial F[\hat{\boldsymbol{\Omega}}(\boldsymbol{x}, s)]}{\partial u_j}$$
$$+ \int_V d^3y \, (\boldsymbol{v}_s \cdot \nabla) \left(\frac{\partial \Omega_k(\boldsymbol{y}, s)}{\partial u_j} A_k[\hat{\boldsymbol{\Omega}}(\boldsymbol{y}, s)] \right). \quad \text{(C.9)}$$

In the absence of the last term on the right hand side, this reproduces the equations of motion, together with the damping terms arising from $\delta \mathcal{R}[\hat{\boldsymbol{\Omega}}, \partial_t \hat{\boldsymbol{\Omega}}] / \delta(\partial_t u_j(s))$. As one may derive the equations of motion directly from of Eq. (8.11), we claim that this third term is an artifact of the choice of the action functional. At first glance, it seems that the additional term is just a boundary term and will not play a crucial role compared to the bulk terms. However, if one first calculates the action functional in terms of the variational parameters u_j and then, in a second step, takes the derivative with respect to the dynamical variables u_j, this may lead to wrong results, as can be seen from the following example.

In spherical coordinates, $\mathcal{A}^{(\nabla)}[\hat{\boldsymbol{\Omega}}(\boldsymbol{x}, t)]$ with $\hat{\boldsymbol{\Omega}}(\boldsymbol{x}, t) = \hat{\boldsymbol{e}}_r(\theta(\boldsymbol{x}, t), \phi(\boldsymbol{x}, t))$ is given by

$$\mathcal{A}^{(\nabla)}[\hat{\boldsymbol{\Omega}}(\boldsymbol{x}, t)] = \int dt \int_V d^3x \, \boldsymbol{A}(\hat{\boldsymbol{\Omega}}(\boldsymbol{x}, t)) \cdot (\boldsymbol{v}_s \cdot \nabla) \hat{\boldsymbol{\Omega}}(\boldsymbol{x}, t)$$
$$= \int dt \int_V d^3x \, (1 - \cos(\theta))(\boldsymbol{v}_s \cdot \nabla) \phi \quad \text{(C.10)}$$
$$\equiv \int dt \, E_{\text{SST}},$$

where the last two lines define E_{SST}. As an example, let us consider the simplest case of a helix. To be concrete, we consider the case of zero applied magnetic field, $\boldsymbol{B} = 0$, the abscence of damping, and we do not include pinning physics or anisotropy terms from the atomic lattice. In this case, a helix with a $\boldsymbol{q}$ vector in an arbitrary direction that is drifting with the direction and velocity of $\boldsymbol{v}_s$ solves the Landau-Lifshitz-Gilbert equation. Without loss of generality, we consider a helix in z-direction given by

$$\hat{\boldsymbol{\Omega}}(\boldsymbol{x}, t) = \cos\left[q(z + \varphi_z(t))\right] \hat{\boldsymbol{x}} + \sin\left[q(z + \varphi_z(t))\right] \hat{\boldsymbol{y}}, \quad \text{(C.11)}$$

where $\varphi_z = \boldsymbol{v}_{s_z} t$. For a normalized $\boldsymbol{q}$ vector we have $q = 1$, but for clarity we write here

q instead of 1. A comparison of Eq. (C.11) and $\hat{\boldsymbol{\Omega}}(\boldsymbol{x}, t) = \hat{\boldsymbol{e}}_r(\theta, \phi)$ leads to

$$\cos(\theta) \stackrel{!}{=} 0 \qquad\qquad \Rightarrow \quad \theta = \frac{\pi}{2} + n\pi, \quad n \in Z$$

$$\sin(\theta)\cos(\phi) \stackrel{!}{=} \cos(qz + \varphi_z(t)) \quad \Rightarrow \quad \phi = qz + \varphi_z(t) + 2\pi m, \quad m \in Z$$

$$\wedge \quad \sin(\theta) = 1 \quad \Rightarrow \quad \theta = \frac{\pi}{2} + 2\pi n, \quad n \in Z$$

$$\sin(\theta)\sin(\phi) \stackrel{!}{=} \sin(qz + \varphi_z(t)) \quad \Rightarrow \quad \phi = qz + \varphi_z(t) + 2\pi m, \quad m \in Z$$

$$\wedge \quad \sin(\theta) = 1 \quad \Rightarrow \quad \theta = \frac{\pi}{2} + 2\pi n, \quad n \in Z$$

Inserting the angles θ and ϕ in the formula for E_{SST} we obtain

$$\begin{aligned} E_{\mathrm{STT}}[\hat{\boldsymbol{\Omega}}] &= \int_V d^3x \, (\boldsymbol{v}_s \cdot \nabla) \, (qz + \varphi_z(t)) \\ &= \int_V d^3x \, v_{s_z} \, q = \int_V d^3x \, \boldsymbol{v}_s \cdot \boldsymbol{q} \quad \text{with} \quad \boldsymbol{q} = (0, 0, 1)^T. \end{aligned} \tag{C.12}$$

Note that this is no longer a surface term. This term rather suggests that for a helix there is a simple linear coupling of the direction of the applied current and the $\boldsymbol{q}$ vector which might lead to a re-orientation of the helix when a current is applied. However, such a term is not allowed by symmetry. The reason for this is that the magnetic structure of the helix remains invariant under a rotation of 180° around an axis perpendicular to the $\boldsymbol{q}$ direction. However, the term $\boldsymbol{v}_s \cdot \boldsymbol{q}$ and therefore also E_{STT} change sign under this transformation which implies that the "energy" E_{STT} does not respect the symmetries of the helix. Moreover, note that a re-orientation of the $\boldsymbol{q}$ vector of the helix due to an applied current has not been observed experimentally so far.

This simple example illustrates that first calculating the action and then taking the derivative with respect to the variables may lead to wrong terms in the equation of motions. To conclude, the correct way of deriving the equations of motion is the way described above Eq. (C.2) or from the variational principle neglecting the additional "boundary term".

C.2.2   Motion of the Skyrmion Lattice

When applying a sufficiently strong current to the system, we have seen in Chapter 7 and Chapter 9 that the skyrmion lattice will move. In this representation, the drift solution, *i.e.* the solution that comprises the motion of the skyrmion lattice, can be written to linear order in the applied current as

$$\hat{\boldsymbol{\Omega}}(\boldsymbol{r}, t) = \hat{\boldsymbol{\Omega}}(\boldsymbol{r} - \boldsymbol{v}_d t, \{u_i\}), \tag{C.13}$$

where $\boldsymbol{v}_d$ is the drift velocity of the magnetic structure.

In Section 9.2, we have already derived the equation for the drift velocity while applying the Thiele method, *i.e.* projecting Eq. (8.12) onto the generator of the translational mode $\hat{\boldsymbol{G}}^i_{\mathrm{trans}}\hat{\boldsymbol{\Omega}} = \partial_i\hat{\boldsymbol{\Omega}}$. Starting from Eq. (8.10) we have first taken the cross product with $\hat{\boldsymbol{\Omega}}$, then multiplied Eq. (8.10) by $\partial_i\hat{\boldsymbol{\Omega}}$, and finally integrated the resulting terms over a volume.

On the other hand, to obtain the drift velocity from the alternative approach with the equations of motion for the dynamical variables, we first multiplied Eq. (8.10) by $\left(\hat{\boldsymbol{\Omega}} \times \frac{\partial\hat{\boldsymbol{\Omega}}}{\partial u_i}\right)$ and then integrate over a volume V. In that case, $\boldsymbol{u} = (\boldsymbol{\varphi}, \boldsymbol{\mu})$, *i.e.* $u_i = \varphi_i$ for $i = 1, 2, 3$ with $\boldsymbol{\varphi} = \boldsymbol{v}_d t$. In the "static limit", where $\dot{u}_j = 0$ for all variables except $\boldsymbol{\varphi}$, we obtain

$$\partial_t\hat{\boldsymbol{\Omega}} = \frac{\partial\hat{\boldsymbol{\Omega}}}{\partial\varphi_j} \cdot \dot{\varphi}_j = -\frac{\partial\hat{\boldsymbol{\Omega}}}{\partial r_j} \cdot \dot{\varphi}_j = -(\dot{\boldsymbol{\varphi}} \cdot \nabla)\,\hat{\boldsymbol{\Omega}} = -(\boldsymbol{v}_d \cdot \nabla)\,\hat{\boldsymbol{\Omega}}. \tag{C.14}$$

Since

$$\frac{\partial(\partial_t\hat{\boldsymbol{\Omega}})}{\partial\dot{\varphi}_j} = \frac{\partial\hat{\boldsymbol{\Omega}}}{\partial\varphi_j} = -\partial_i\hat{\boldsymbol{\Omega}} \tag{C.15}$$

it is obvious that in the "static limit" both approaches are equivalent and lead to the same results.

C.2.3 Rotation of the Skyrmion Lattice

To obtain the rotation angle and the acting torques, we projected the LLG equation onto the rotational mode around the axis $\hat{\boldsymbol{n}}$ perpendicular to the skyrmion lattice plane which, for an undistorted skyrmion lattice, is aligned along the direction of the magnetic field. To check this approach and substantiate its validity, we confirmed that the alternative derivation with the equation of motions for the variational parameters leads to the same results. We checked this explicitly for the rotational torques due to the lattice distortions [70, 129] (see Section 10.2). Here, we present the results of the alternative approach. As explained above, we describe the skyrmion lattice by $N = 27$ variational parameters u_i, $i = 1, \ldots, N$, that are determined by minimizing the free energy functional. We expect that a small spin-polarized current will change the ground state values smoothly. To determine the change δu_i of the variational parameters due to a current $\boldsymbol{v}_s$ in linear order of v_s, we calculate the N equations of motions for u_i up to linear order in v_s:

$$\boldsymbol{P}_{R,i}(\boldsymbol{v}_s - \boldsymbol{v}_d) + \boldsymbol{P}_{D,i}(\beta\boldsymbol{v}_s - \alpha\boldsymbol{v}_d) + \boldsymbol{P}_{D',i}(\beta'\boldsymbol{v}_s - \alpha'\boldsymbol{v}_d) = f''_{ij}\delta u_j, \tag{C.16}$$

where the generalized reactive and dissipative coupling vectors, $\boldsymbol{P}_{R,i}$, $\boldsymbol{P}_{D,i}$, $\boldsymbol{P}_{D',i}$, and the stiffness matrix f''_{ij} are given by:

$$(\boldsymbol{P}_{R,i})_n = \int_{\text{UC}} d^2r \left(\hat{\boldsymbol{\Omega}} \times \partial_n\hat{\boldsymbol{\Omega}}\right)\frac{\partial\hat{\boldsymbol{\Omega}}}{\partial u_i}, \tag{C.17a}$$

$$(\boldsymbol{P}_{D,i})_n = \int_{\text{UC}} d^2r \, \partial_n\hat{\boldsymbol{\Omega}}\frac{\partial\hat{\boldsymbol{\Omega}}}{\partial u_i}, \tag{C.17b}$$

$$(\boldsymbol{P}_{D',i})_n = \int_{\text{UC}} d^2r \left(\hat{\boldsymbol{\Omega}} \times [\hat{\boldsymbol{\Omega}} \cdot (\partial_j\hat{\boldsymbol{\Omega}} \times \partial_n\hat{\boldsymbol{\Omega}})]\partial_j\hat{\boldsymbol{\Omega}} \cdot\right)\frac{\partial\hat{\boldsymbol{\Omega}}}{\partial u_i}, \tag{C.17c}$$

$$f''_{ij} = \int_{\text{UC}} d^2r \frac{\partial\hat{\boldsymbol{\Omega}}}{\partial u_i}\frac{\partial\boldsymbol{H}_{\text{eff}}}{\partial u_j} = -\frac{1}{M}\int_{\text{UC}} d^2r \frac{\partial^2 F}{\partial u_i\partial u_j}. \tag{C.17d}$$

To calculate the right hand side of Eq. (C.16) we used that the effective magnetic field $\boldsymbol{H}_{\text{eff}}$ vanishes in equilibrium. Hence, we expand $\boldsymbol{H}_{\text{eff}}$ to linear order in the deviations δu_i. Since the rotational coupling vectors on the left hand side of Eq. (C.16) are linear in v_s, we calculate the rotational coupling vectors with the equilibrium magnetization texture $\boldsymbol{M}(\boldsymbol{r})$ of the skyrmion lattice obtained from the free energy functional of Eq. (4.9) together with Eqs. (4.26) and (4.27). Note that these rotational coupling vectors are, in contrast to the main text, defined without the factor M, but instead there is a factor $1/M$ on the right hand side of the equation. In the case of a constant magnetization amplitude, *i.e.* when the LLG equation is valid in the strict sense, multiplying Eq. (C.16) by M will, of course, lead to equivalent results. As in the last Chapters, we consider symmetrically shaped domains, and therefore neglect terms in the integrand that are linear in the coordinate $\boldsymbol{r}$ arising from derivatives with respect to the reciprocal lattice vectors $\boldsymbol{q}_j$.

Eq. (C.16) is basically of the form $f''_{ij}\delta u_j = c_j$. Thus, in order to obtain the deviations δu_i of the variational parameters we have to invert the stiffness matrix $(f''_{ij})_{ij} \equiv \mathcal{F}''$

which is a Hermitian 27×27 matrix. Hence, $\mathcal{F}''$ can be diagonalized and has only real eigenvalues. However, it has zero eigenvalues which stem from Goldstone modes. Two of them correspond to the translational modes, and in the case of a rotationally invariant skyrmion lattice the stiffness matrix $\mathcal{F}''$ contains another zero eigenvalue corresponding to the rotational mode, denoted by $\boldsymbol{m}_{\mathrm{rot}}$ in the following. However, neither the Berry phase nor the dissipation terms couple to the rotation mode, *i.e.* $\boldsymbol{m}_{\mathrm{rot}} \cdot \boldsymbol{c} = 0$. For the rotationally invariant case, we can then solve for the deviations δu_i by inverting the matrix and projecting out the zero modes. In this case we obtain that the lengths of the $\boldsymbol{q}$ vectors are almost constant under the influence of the current, and the sixfold rotation symmetry basically remains intact, but the plane of the three $\boldsymbol{q}$ vectors tilts slightly.

When including anisotropy terms to the free energy functional that break the rotational symmetry, as in Section 10.2, the eigenvalue of the stiffness matrix corresponding to the rotational mode (still denoted by $\boldsymbol{m}_{\mathrm{rot}}$) is no longer zero, but remains small as the anisotropy terms are small. The basic idea of choosing the corresponding anisotropy terms to lowest order in spin-orbit coupling is therefore that one term, F_L, is needed to orient the skyrmion lattice with respect to the atomic lattice in the skyrmion lattice plane, which then leads to this finite eigenvalue. Moreover, we need another anisotropy term, F_D, that leads to a finite overlap of the rotational mode and $\boldsymbol{c}$, which consists of the Berry phase and the dissipation terms. This overlap is linear in γ_D and $|\boldsymbol{v}_s|$, but depends only barely on γ_L. Note that the terms F_L and F_D have already been introduced and discussed in Section 4.3. When including these terms and calculating the current-induced distortions of the ground state variables, we obtain again that the lengths of the $\boldsymbol{q}$ vectors are almost constant under the influence of the current and that the threefold rotation symmetry basically remains intact. As before, the plane of the three $\boldsymbol{q}$ vectors tilts slightly. However, we also observe a rotation of the $\boldsymbol{q}$ vectors. To calculate the rotation angle $\delta\phi$, we have to express it in the changes of the magnetic texture parameterized by the deviations δu_i of the variational parameters. Since the rotation depends on the relative change of the $\boldsymbol{q}$ vectors, for small rotation angles $\delta\phi$ we get $\delta\boldsymbol{q}_i = (\partial\boldsymbol{q}_i/\partial\phi)\,\delta\phi$ which can be solved for $\delta\phi$ by multiplying it with $(\partial\boldsymbol{q}_i/\partial\phi)$ and summing over the index i. Thus, as an alternative expression for the rotation angle we obtain:

$$\delta\phi = \frac{\sum_i \delta\boldsymbol{q}_i \cdot \frac{\partial\boldsymbol{q}_i}{\partial\phi}}{\sum_i \frac{\partial\boldsymbol{q}_i}{\partial\phi} \cdot \frac{\partial\boldsymbol{q}_i}{\partial\phi}}, \tag{C.18}$$

where we obtain the deviations $\delta\boldsymbol{q}_i$ by solving Eq. (C.16), and we determine the drift velocity $\boldsymbol{v}_d$ from the equation of forces, Eq. (9.16). To conclude, Eq. (C.18) and Eq. (10.13) lead to identical results (provided the magnetization amplitude is constant). We have checked this analytically as well as numerically for the torques due to lattice distortions [70, 129], with the results for the rotation angle being discussed in Section 10.2. Thereby we confirmed the validity of our extended Thiele approach in the present context for the rotational motion.

Bibliography

[1] S. Mühlbauer, *et al.* "Skyrmion lattice in a chiral magnet." Science **323**, 915 (2009).

[2] J. C. Maxwell. "A Dynamical Theory of the Electromagnetic Field." Phil. Trans. R. Soc. Lond. **155**, 459 (1865).

[3] G. Binasch, P. Grünberg, F. Saurenbach, and W. Zinn. "Enhanced magnetoresistance in layered magnetic structures with antiferromagnetic interlayer exchange." Phys. Rev. B **39**, 4828 (1989).

[4] M. N. Baibich, *et al.* "Giant Magnetoresistance of (001)Fe/(001)Cr Magnetic Superlattices." Phys. Rev. Lett. **61**, 2472 (1988).

[5] J. C. Slonczewski. "Current-driven excitation of magnetic multilayer." J. Magn. Magn. Mat. **159**, L1 (1996).

[6] L. Berger. "Emission of spin waves by a magnetic multilayer traversed by a current." Phys. Rev. B **54**, 9353 (1996).

[7] S. S. P. Parkin, M. Hayashi, and L. Thomas. "Magnetic Domain-Wall Racetrack Memory." Science **320**, 190 (2008).

[8] S. Zhang and S. S.-L. Zhang. "Generalization of the Landau-Lifshitz-Gilbert Equation for Conducting Ferromagnets." Phys. Rev. Lett. **102**, 086601 (2009).

[9] J. Zang, M. Mostovoy, J. H. Han, and N. Nagaosa. "Dynamics of Skyrmion Crystals in Metallic Thin Films." Phys. Rev. Lett. **107**, 136804 (2011).

[10] F. Jonietz, *et al.* "Spin Transfer Torques in MnSi at Ultra-low Current Densities." Science **330**, 1648 (2010).

[11] T. H. R. Skyrme. "A Non-Linear Field Theory." Proc. R. Soc. A **260**, 127 (1961).

[12] T. H. R. Skyrme. "A unified field theory of mesons and baryons." Nucl. Phys. **31**, 556 (1962).

[13] I. Klebanov. "Nuclear matter in the skyrme model." Nucl. Phys. B **262**, 133 (1985).

[14] M. Kugler and S. Shrikman. "A new skyrmion crystal." Phys. Lett. B **208**, 491 (1988).

[15] L. Castellejo, *et al.* "Dense skyrmion systems." Nucl. Phys. A **501**, 801 (1989).

[16] S. L. Sondhi, A. Karlhede, S. A. Kivelson, and E. H. Rezayi. "Skyrmions and the crossover from the integer to fractional quantum Hall effect at small Zeeman energies." Phys. Rev. B **47**, 16419 (1993).

[17] L. Brey, H. A. Fertig, R. Côté, and A. H. MacDonald. "Skyrme Crystal in a Two-Dimensional Electron Gas." Phys. Rev. Lett. **75**, 2562 (1995).

[18] C. Timm, S. M. Girvin, and H. A. Fertig. "Skyrmion lattice melting in the quantum Hall system." Phys. Rev. B **58**, 10634 (1998).

[19] A. G. Green. "Quantum-critical dynamics of the Skyrmion lattice." Phys. Rev. B **61**, R16299 (2000).

[20] W. Desrat, *et al.* "Resistively Detected Nuclear Magnetic Resonance in the Quantum Hall Regime: Possible Evidence for a Skyrme Crystal." Phys. Rev. Lett. **88**, 256807 (2002).

[21] G. Gervais, *et al.* "Evidence for Skyrmion Crystallization from NMR Relaxation Experiments." Phys. Rev. Lett. **94**, 196803 (2005).

[22] Y. Gallais, *et al.* "Soft Spin Wave near $\nu = 1$: Evidence for a Magnetic Instability in Skyrmion Systems." Phys. Rev. Lett. **100**, 086806 (2008).

[23] U. Al Khawaja and H. Stoof. "Skyrmions in a ferromagnetic Bose-Einstein condensate." Nature **411**, 918 (2001).

[24] H. M. Price and N. R. Cooper. "Skyrmion-antiskyrmion pairs in ultracold atomic gases." Phys. Rev. A **83**, 061605 (2011).

[25] D. C. Wright and N. D. Mermin. "Crystalline liquids: the blue phases." Rev. Mod. Phys. **61**, 385 (1989).

[26] A. N. Bogdanov, U. K. Rößler, and A. A. Shestakov. "Skyrmions in nematic liquid crystals." Phys. Rev. E **67**, 016602 (2003).

[27] A. Malozemoff and J. Slonczewski. *Magnetic domain walls in bubble materials.* Applied solid state science: Supplement (Academic Press, 1979). ISBN 9780120029518.

[28] X. Yu, *et al.* "Magnetic stripes and skyrmions with helicity reversals." Proceedings of the National Academy of Sciences **109**, 8856–8860 (2012).

[29] A. N. Bogdanov and D. A. Yablonskii. "Thermodynamically stable "vortices" in magnetically ordered crystals. The mixed state of magnets." Sov. Phys. JETP **68**, 101 (1989).

[30] A. N. Bogdanov and A. Hubert. "Thermodynamically stable magnetic vortex states in magnetic crystals." J. Magn. Magn. Mater. **138**, 255 (1994).

[31] A. N. Bogdanov. "New localized solutions of the nonlinear field-equations." Sov. Phys. JETP **62**, 247 (1995).

[32] B. Binz and A. Vishwanath. "Theory of helical spin crystals: Phases, textures, and properties." Phys. Rev. B **74**, 214408 (2006).

[33] B. Binz and A. Vishwanath. "Chirality induced anomalous-Hall effect in helical spin crystals." Phys. B **403**, 1336 (2008).

[34] S. D. Yi, S. Onoda, N. Nagaosa, and J. H. Han. "Skyrmions and anomalous Hall effect in a Dzyaloshinskii-Moriya spiral magnet." Phys. Rev. B **80**, 054416 (2009).

[35] J. H. Han, *et al.* "Skyrmion lattice in a two-dimensional chiral magnet." Phys. Rev. B **82**, 094429 (2010).

[36] B. Binz, A. Vishwanath, and V. Aji. "Theory of the Helical Spin Crystal: A Candidate for the Partially Ordered State of MnSi." Phys. Rev. Lett. **96**, 207202 (2006).

[37] I. Fischer, N. Shah, and A. Rosch. "Crystalline phases in chiral ferromagnets: Destabilization of helical order." Phys. Rev. B **77**, 024415 (2008).

[38] U. K. Rößler, A. N. Bogdanov, and C. Pfleiderer. "Spontaneous skyrmion ground states in magnetic metals." Nature **442**, 797 (2006).

[39] W. Münzer, *et al.* "Skyrmion lattice in the doped semiconductor $Fe_{1-x}Co_xSi$." Phys. Rev. B **81**, 041203 (2010).

[40] A. Neubauer, *et al.* "Topological Hall Effect in the *A* Phase of MnSi." Phys. Rev. Lett. **102**, 186602 (2009).

[41] C. Pfleiderer, *et al.* "Skyrmion lattices in metallic and semiconducting B20 transition metal compounds." J. Phys.: Condens. Matter **22**, 164207 (2010).

[42] S. Seki, X. Z. Yu, S. Ishiwata, and Y. Tokura. "Observation of Skyrmions in a Multiferroic Material." Science **336**, 198 (2012).

[43] T. Adams, *et al.* "Long wavelength helimagnetic order and skyrmion lattice phase in Cu_2OSeO_3." arXiv:1204.3597v1 (2012).

[44] X. Z. Yu, *et al.* "Real-Space Observation of a Two-Dimensional Skyrmion Crystal." Nature **465**, 901 (2010).

[45] X. Z. Yu, *et al.* "Near room-temperature formation of a skyrmion crystal in thin-films of the helimagnet FeGe." Nat. Mat. **10**, 106 (2011).

[46] Y. Tokura *et al.*, presentation at German March Meeting, Dresden (2011).

[47] C. Pfleiderer, G. J. McMullan, S. R. Julian, and G. G. Lonzarich. "Magnetic quantum phase transition in MnSi under hydrostatic pressure." Phys. Rev. B **55**, 8330 (1997).

[48] C. Pfleiderer, S. R. Julian, and G. G. Lonzarich. "Non-Fermi liquid nature of the normal state of itinerant-electron ferromagnets." Nature **414**, 427 (2001).

[49] C. Pfleiderer. "The non-Fermi liquid puzzle of MnSi at high pressure." Phys. B **328**, 100 (2003).

[50] C. Pfleiderer, *et al.* "Non-Fermi liquid Metal without Quantum Criticality." Science **316**, 1871 (2007).

[51] C. Pfleiderer, *et al.* "Partial magnetic order in the non-Fermi liquid phase of MnSi." Nature **427**, 227 (2004).

[52] C. Thessieu, C. Pfleiderer, A. N. Stepanov, and J. Flouquet. "Field dependence of the magnetic quantum phase transition in MnSi." J. Phys.: Condens. Matter **9**, 6677 (1997).

[53] Y. Ishikawa, G. Shirane, J. A. Tarvin, and M. Kohgi. "Magnetic excitations in the weak itinerant ferromagnet MnSi." Phys. Rev. B **16**, 4956 (1977).

[54] Y. Ishikawa and M. Arai. "Magnetic phase diagram of MnSi near critical temperature studied by neutron small angle scattering." J. Phys. Soc. Jpn. **53**, 2726 (1984).

[55] P. Båk and M. Jensen. "Theory of helical magnetic structures and phase transitions in MnSi and FeGe." J. Phys. C: Solid State **13**, L881 (1980).

[56] O. Nakanishi, A. Yanase, A. Hasegawa, and M. Kataoka. "The origin of the helical spin density wave in MnSi." Sol. St. Comm. **35**, 995 (1980).

[57] M. L. Plumer and M. B. Walker. "Wavevector and spin reorientation in MnSi." J. Phys. C: Solid State Physics **14**, 4689 (1981).

[58] M. Kataoka and O. Nakanishi. "Helical Spin Density Wave Due to Antisymmetric Exchange Interaction." J. Phys. Soc. Jpn. **50**, 3888 (1981).

[59] I. E. Dzyaloshinskii. "A Thermodynamic theory of weak ferromagnetism of Antiferromagnets." J. Phys. Chem. Sol. **4**, 241 (1958).

[60] T. Moriya. "Anisotropic Superexchange Interaction and Weak Ferromagnetism." Phys. Rev. **120**, 91 (1960).

[61] Y. Ishikawa, K. Tajima, D. Bloch, and M. Roth. "Helical spin structure in manganese silicide MnSi." Sol. St. Comm. **19**, 525 (1976).

[62] L. D. Landau and E. M. Lifshitz. *Electrodynamics of continuous media.* Second edition (Pergamon Press, Oxford, 1984). ISBN 0750626348.

[63] B. Lebech, *et al.* "Magnetic phase diagram of MnSi." J. Magn. Magn. Mat. **140**, 119 (1995).

[64] C. Pfleiderer, D. Reznik, L. Pintschovius, and J. Haug. "Magnetic Field and Pressure Dependence of Small Angle Neutron Scattering in MnSi." Phys. Rev. Lett. **99**, 156406 (2007).

[65] B. Lebech. *Magnetic ordering in nearly ferromagnetic antiferromagnetic helices*, p. 167 (World Scientific, Singapore, 1993).

[66] S. V. Grigoriev, *et al.* "Field-induced reorientation of the spin helix in MnSi near T_c." Phys. Rev. B **73**, 224440 (2006).

[67] T. Adams, *et al.* "Long-Range Crystalline Nature of the Skyrmion Lattice in MnSi." Phys. Rev. Lett. **107**, 217206 (2011).

[68] R. Georgii, *et al.* "MIRA–A flexible instrument for VCN." Phys. B **397**, 150 (2007).

[69] S. Heinze, *et al.* "Spontaneous atomic-scale magnetic skyrmion lattice in two dimensions." Nat. Phys. **7**, 713 (2011).

[70] K. Everschor, M. Garst, R. A. Duine, and A. Rosch. "Current-induced rotational torques in the skyrmion lattice phase of chiral magnets." Phys. Rev. B **84**, 064401 (2011).

[71] K. Everschor, *et al.* "Rotating skyrmion lattices by spin torques and field or temperature gradients." arXiv:1204.5051v1 (2012).

[72] J. W. Negele and H. Orland. *Quantum Many-Particle Systems.* Frontiers in Physics (Addison-Wesley, Reading, MA, 1988).

[73] F. Schwabel. *Statistische Mechanik* (Springer, 2006).

[74] P. M. Chaikin and T. C. Lubensky. *Principles of Condensed Matter Physics* (Cambridge University Press, 1995).

[75] Y. A. Izyumov. "Modulated or long periodic magnetic structures of crystals." Sov. Phys. Usp. **27**, 845 (1984).

[76] S. A. Brazovskii. "Phase transition of an isotropic system to a nonuniform state." Sov. Phys. JETP **41**, 85 (1975).

[77] J. Schmalian and M. Turlakov. "Quantum Phase Transitions of Magnetic Rotons." Phys. Rev. Lett. **93**, 036405 (2004).

[78] Adams, T. and Mühlbauer, S. and Bauer, A. and Neubauer, A. and Georgii, R. and Pfleiderer, C., submitted for publication.

[79] Tim Adams, presentation at German March Meeting, Berlin (2012).

[80] T. Schulz, *et al.* "Emergent electrodynamics of skyrmions in a chiral magnet." Nat. Phys. **8**, 301 (2012).

[81] A. Schmid and W. Hauger. "On the Theory of Vortex Motion in an Inhomogeneous Superconducting Film." J. Low Temp. Phys. **11**, 667 (1973).

[82] A. I. Larkin and Y. N. Ovchinnikov. "Electrodynamics of inhomogeneous type-II superconductors." Sov. Phys. JETP **38**, 854 (1974).

[83] G. Blatter, *et al.* "Vortices in high-temperature superconductors." Rev. Mod. Phys. **66**, 1125 (1994).

[84] A. Bauer, *et al.* "Quantum phase transitions in single-crystal $Mn_{1-x}Fe_xSi$ and $Mn_{1-x}Co_xSi$: Crystal growth, magnetization, ac susceptibility, and specific heat." Phys. Rev. B **82**, 064404 (2010).

[85] M. Janoschek, *et al.* "Helimagnon bands as universal excitations of chiral magnets." Phys. Rev. B **81**, 214436 (2010).

[86] B. Roessli, P. Böni, W. E. Fischer, and Y. Endoh. "Chiral Fluctuations in MnSi above the Curie Temperature." Phys. Rev. Lett. **88**, 237204 (2002).

[87] F. Semadeni, *et al.* "Direct observation of spin-flip excitations in MnSi." Phys. B **267**, 248 (1999).

[88] G. Shirane, S. M. Shapiro, and J. M. Tranquada. *Neutron Scattering with a Triple-Axis Spectrometer – Basic Techniques* (Cambridge University Press, Cambridge, England, 2002).

[89] S. Datta and B. Das. "Electronic analog of the electro-optic modulator." Appl. Phys. Lett. **56**, 665 (1989).

[90] J. Grollier, *et al.* "Switching a spin valve back and forth by current-induced domain wall motion." Appl. Phys. Lett. **83**, 509 (2003).

[91] M. Tsoi, R. E. Fontana, and S. S. P. Parkin. "Magnetic domain wall motion triggered by an electric current." Appl. Phys. Lett. **83**, 2617 (2003).

[92] G. S. D. Beach, *et al.* "Dynamics of field-driven domain-wall propagation in ferromagnetic nanowires." Nat. Mater. **4**, 741 (2005).

[93] M. Hayashi, *et al.* "Direct observation of the coherent precession of magnetic domain walls propagating along permalloy nanowires." Nat. Phys. **3**, 21 (2007).

[94] D. C. Ralph and M. D. Stiles. "Spin transfer torques." J. Magn. Magn. Mater. **320**, 1190 (2008).

[95] M. Tsoi, *et al.* "Excitation of a Magnetic Multilayer by an Electric Current." Phys. Rev. Lett. **80**, 4281 (1998).

[96] E. B. Myers, *et al.* "Current-induced switching of domains in magnetic multilayer devices." Science **285**, 867 (1999).

[97] S. I. Kiselev, *et al.* "Microwave oscillations of a nanomagnet driven by a spin-polarized current." Nature **425**, 380 (2003).

[98] O. Boulle, *et al.* "Shaped angular dependence of the spin-transfer torque and microwave generation without magnetic field." Nat. Phys. **3**, 492 (2007).

[99] V. S. Pribiag, *et al.* "Magnetic vortex oscillator driven by d.c. spin-polarized current." Nat. Phys. **3**, 498 (2007).

[100] A. A. Thiele. "Steady-State Motion of Magnetic Domains." Phys. Rev. Lett. **30**, 230 (1973).

[101] J. Xiao, A. Zangwill, and M. D. Stiles. "Spin-transfer torque for continuously variable magnetization." Phys. Rev. B **73**, 054428 (2006).

[102] S. Pancharatnam. "Generalized Theory of Interference, and Its Applications. Part I. Coherent Pencils." Proc. Indian Acad. Sci. A **44**, 247 (1956).

[103] M. V. Berry. "Quantal Phase Factors Accompanying Adiabatic Changes." Proc. R. Soc. Lond. A **392**, 45 (1984).

[104] J. Ye, *et al.* "Berry Phase Theory of the Anomalous Hall Effect: Application to Colossal Magnetoresistance Manganites." Phys. Rev. Lett. **83**, 3737 (1999).

[105] G. Tatara, *et al.* "Spin torque and force due to current for general spin textures." J. Phys. Soc. Jpn. **76**, 054707 (2007).

[106] P. Bruno, V. K. Dugaev, and M. Taillefumier. "Topological Hall Effect and Berry Phase in Magnetic Nanostructures." Phys. Rev. Lett. **93**, 096806 (2004).

[107] M. Onoda, G. Tatara, and N. Nagaosa. "Anomalous Hall Effect and Skyrmion Number in Real and Momentum Spaces." J. Phys. Soc. Jpn. **73**, 2624 (2004).

[108] Y. Taguchi, *et al.* "Spin Chirality, Berry Phase, and Anomalous Hall Effect in a Frustrated Ferromagnet." Science **30**, 2573 (2001).

[109] C. Pfleiderer and A. Rosch. "Single skyrmions spotted." Nature **465**, 880 (2010).

[110] G. E. Volovik. "Linear momentum in ferromagnets." J. Phys. C: Solid State Physics **20**, L83 (1987).

[111] S. A. Yang, *et al.* "Universal Electromotive Force Induced by Domain Wall Motion." Phys. Rev. Lett. **102**, 067201 (2009).

[112] P. N. Hai, *et al.* "Electromotive force and huge magnetoresistance in magnetic tunnel junctions." Nature **458**, 489 (2009).

[113] S. E. Barnes and S. Maekawa. "Generalization of Faraday's Law to Include Nonconservative Spin Forces." Phys. Rev. Lett. **98** (2007).

[114] B. Binz and A. Vishwanath. "Theoretical proposal predicting anomalous magnetoresistance and quadratic Hall effect in the partially ordered state of MnSi." J. Magn. Magn. Mater. **310**, 1062 (2007).

[115] M. Lee, *et al.* "Unusual Hall Effect Anomaly in MnSi under Pressure." Phys. Rev. Lett. **102**, 186601 (2009).

[116] N. Nagaosa. "Anomalous Hall Effect—A New Perspective—." J. Phys. Soc. Jpn. **75**, 042001 (2006).

[117] R. Karplus and J. M. Luttinger. "Hall Effect in Ferromagnetics." Phys. Rev. **95**, 1154 (1954).

[118] J. Smit. "The spontaneous hall effect in ferromagnetics II." Physica **24**, 39 (1958).

[119] N. Nagaosa, *et al.* "Anomalous Hall effect." Rev. Mod. Phys. **82**, 1539 (2010).

[120] M. Lee, Y. Onose, Y. Tokura, and N. P. Ong. "Hidden constant in the anomalous Hall effect of high-purity magnet MnSi." Phys. Rev. B **75**, 172403 (2007).

[121] A. Neubauer, Diploma Thesis, Technische Universität München (2006).

[122] M. Yamanouchi, D. Chiba, F. Matsukura, and H. Ohno. "Current-induced domain-wall switching in a ferromagnetic semiconductor structure." Nature **428**, 539 (2004).

[123] S. Brazovskii and T. Nattermann. "Pinning and sliding of driven elastic systems: from domain walls to charge density waves." Adv. Phys. **53**, 177 (2004).

[124] S. Zhang and Z. Li. "Roles of Nonequilibrium Conduction Electrons on the Magnetization Dynamics of Ferromagnets." Phys. Rev. Lett. **93**, 127204 (2004).

[125] R. A. Duine, A. S. Núñez, J. Sinova, and A. H. MacDonald. "Functional Keldysh theory of spin torques." Phys. Rev. B **75**, 214420 (2007).

[126] M. E. Lucassen, H. J. van Driel, C. Morais Smith, and R. A. Duine. "Current-driven and field-driven domain walls at nonzero temperature." Phys. Rev. B **79** (2009).

[127] H. Kohno, G. Tatara, and J. Shibata. "Microscopic Calculation of Spin Torques in Disordered Ferromagnets." J. Phys. Soc. Jpn. **75**, 113706 (2006).

[128] K. Goto, H. Katsura, and N. Nagaosa. "Current-induced dynamics of spiral magnet." arXiv:0807.2901 (2008).

[129] K. Everschor, Diploma Thesis, Universität zu Köln (2009).

[130] Y. B. Bazaliy, B. A. Jones, and S.-C. Zhang. "Modification of the Landau-Lifshitz equation in the presence of a spin-polarized current in colossal- and giant-magnetoresistive materials." Phys. Rev. B **57**, R3213 (1998).

[131] J. He, Z. Li, and S. Zhang. "Current-driven vortex domain wall dynamics by micromagnetic simulations." Phys. Rev. B **73**, 184408 (2006).

[132] R. A. Duine. "Effects of nonadiabaticity on the voltage generated by a moving domain wall." Phys. Rev. B **79**, 014407 (2009).

[133] S. E. Barnes and S. Maekawa. "Current-Spin Coupling for Ferromagnetic Domain Walls in Fine Wires." Phys. Rev. Lett. **95** (2005).

[134] Y. Tserkovnyak, A. Brataas, G. E. W. Bauer, and B. I. Halperin. "Nonlocal magnetization dynamics in ferromagnetic heterostructures." Rev. Mod. Phys. **77**, 1375 (2005).

[135] N. B. Kopnin. "Vortex dynamics and mutual friction in superconductors and Fermi superfluids." Rep. Prog. Phys. **65**, 1633 (2002).

[136] T. Nattermann, S. Stepanow, L.-H. Tang, and H. Leschhorn. "Dynamics of interface depinning in a disordered medium." J. Phys. II France **2**, 1483 (1992).

[137] E. M. Forgan, *et al.* "Measurement of Vortex Motion in a Type-II Superconductor: A Novel Use of the Neutron Spin-Echo Technique." Phys. Rev. Lett. **85**, 3488 (2000).

[138] A. V. Khvalkovskiy, *et al.* "Vortex oscillations induced by spin-polarized current in a magnetic nanopillar: Analytical versus micromagnetic calculations." Phys. Rev. B **80**, 140401 (2009).

[139] K. Y. Guslienko, R. H. Heredero, and O. Chubykalo-Fesenko. "Nonlinear gyrotropic vortex dynamics in ferromagnetic dots." Phys. Rev. B **82**, 014402 (2010).

[140] Y. Tserkovnyak, A. Brataas, and G. E. W. Bauer. "Theory of current-driven magnetization dynamics in inhomogeneous ferromagnets." J. Magn. Magn. Mater. **320**, 1282 (2008).

[141] M. Date, K. Okuda, and K. Kadowaki. "Electron Spin Resonance in the Itinerant-Electron Helical Magnet MnSi." J. Phys. Soc. Jpn. **42**, 1555 (1977).

[142] S. Brown, Ph.D. thesis, University of Cambridge (1990).

[143] A. A. Abrikosov. "On the Magnetic Properties of Superconductors of the Second Group." Sov. Phys. JETP **5**, 1174 (1957).

[144] D. Cribier, B. Jacrot, L. Madhav Rao, and B. Farnoux. "Mise en evidence par diffraction de neutrons d'une structure periodique du champ magnetique dans le niobium supraconducteur." Phys. Lett. **9**, 106 (1964).

[145] U. Essmann and H. Trauble. "The direct observation of individual flux lines in type II superconductors." Phys. Lett. **24A**, 526 (1967).

[146] V. L. Ginzburg and L. D. Landau. "On the theory of superconductivity." JETP Lett. **20**, 1064 (1950).

[147] A. T. Fiory. "Quantum Interference Effects of a Moving Vortex Lattice in Al Films." Phys. Rev. Lett. **27**, 501 (1971).

[148] D. López, *et al.* "Spatially Resolved Dynamic Correlation in the Vortex State of High Temperature Superconductors." Phys. Rev. Lett. **82**, 1277 (1999).

[149] I. Garate, K. Gilmore, M. D. Stiles, and A. H. MacDonald. "Nonadiabatic spin-transfer torque in real materials." Phys. Rev. B **79**, 104416 (2009).

[150] A. Altland and B. Simons. *Condensed Matter Field Theory* (Cambridge University Press, 2006).

Danksagung

Part IV

Anhänge gemäß Prüfungsordnung

Erklärung

Ich versichere, dass ich die von mir vorgelegte Dissertation selbständig angefertigt, die benutzten Quellen und Hilfsmittel vollständig angegeben und die Stellen der Arbeit – einschließlich Tabellen, Karten und Abbildungen –, die anderen Werken im Wortlaut oder dem Sinn nach entnommen sind, in jedem Einzelfall als Entlehnung kenntlich gemacht habe; dass diese Dissertation noch keiner anderen Fakultät oder Universität zur Prüfung vorgelegen hat; dass sie – abgesehen von unten angegebenen Teilpublikationen – noch nicht veröffentlicht worden ist sowie, dass ich eine solche Veröffentlichung vor Abschluss des Promotionsverfahrens nicht vornehmen werde. Die Bestimmungen der Promotionsordnung sind mir bekannt. Die von mir vorgelegte Dissertation ist von Prof. Dr. Achim Rosch betreut worden.

Teilpublikationen

- K. Everschor, M. Garst, B. Binz, F. Jonietz, S. Mühlbauer, C. Pfleiderer, and A. Rosch; *Rotating skyrmion lattices by spin torques and field or temperature gradients*, arXiv:1204.5051v1 (2012).

- T. Schulz, R. Ritz, A. Bauer, M. Halder, M. Wagner, C. Franz, C. Pfleiderer, K. Everschor, M. Garst, and A. Rosch; *Emergent electrodynamics of skyrmions in a chiral magnet*, Nature Physics **8**, 301 (2012).

- T. Adams, S. Mühlbauer, C. Pfleiderer, F. Jonietz, A. Bauer, A. Neubauer, R. Georgii, P. Böni, U. Keiderling, K. Everschor, M. Garst, and A. Rosch; *Long-range crystalline nature of the skyrmion lattice in MnSi*, Phys. Rev. Lett. **107**, 217206 (2011)

- K. Everschor, M. Garst, R. A. Duine, and A. Rosch; *Current-induced rotational torques in the skyrmion lattice phase of chiral magnets*, Phys. Rev. B **84**, 064401 (2011).

- F. Jonietz, S. Mühlbauer, C. Pfleiderer, A. Neubauer, W. Münzer, A. Bauer, T. Adams, R. Georgii, P. Böni, R. A. Duine, K. Everschor, M. Garst, and A. Rosch; *Spin Transfer Torques in MnSi at Ultralow Current Densities*, Science **330**, 1648 (2010).

- K. Everschor; Diploma Thesis: *Manipulating Magnetic Structures in Chiral Metals by Currents* (2009).

Lebenslauf

Persönliche Daten

Name	Karin Everschor
Geburtsdatum	12.04.1984
Geburtsort	Köln
Familienstand	ledig
Staatsangehörigkeit	deutsch

Schulbildung

1990 - 1994	Katholische Grundschule, Alzeyerstraße, Köln
1994 - 2003	Dreikönigsgymnasium, Köln
Juni 2003	Abitur

Hochschulstudium

2003 - 2008	Studium der Mathematik an der Universität zu Köln
2003 - 2009	Studium der Physik an der Universität zu Köln
Sept. 2005	Vordiplom in Physik und Vordiplom in Mathematik
Okt. 2005 - Feb. 2006	Auslandssemester an der Universität von Mailand, Italien
April 2007 - Juni 2012	Mitglied der Bonn-Cologne-Graduate School
Juli 2008	Diplom in Mathematik
Juni 2009	Diplom in Physik
Juli 2009 - Juni 2012	Promotionsstudium am Institut für Theoretische Physik der Universität zu Köln, Tag der mündlichen Prüfung 21.06.2012
Jan. 2010 - Juni 2012	Stipendiatin der Deutschen Telekom Stiftung
Okt. 2010 - Dez. 2010	Auslandsaufenthalt in der Arbeitsgruppe von Herrn Prof. Dr. Allan MacDonald an der Universität von Austin, Texas

Arbeitsverhältnisse

04.04.2005 - 30.09.2005	Studentische Hilfskraft am Zentrum für angewandte Informatik der Universität zu Köln
02.10.2006 - 31.01.2007	Studentische Hilfskraft am Institut für Theoretische Physik der Universität zu Köln
02.04.2007 - 13.07.2007	Studentische Hilfskraft am Institut für Theoretische Physik der Universität zu Köln
15.10.2007 - 15.02.2008	Studentische Hilfskraft am Institut für Theoretische Physik der Universität zu Köln
01.07.2008 - 30.06.2009	Studentische Hilfskraft am Institut für Theoretische Physik der Universität zu Köln
01.07.2009 - 31.12.2009	Wissenschaftliche Mitarbeiterin am Institut für Theoretische Physik der Universität zu Köln
01.01.2010 - 30.06.2012	Wissenschaftliche Hilfskraft am Institut für Theoretische Physik der Universität zu Köln
Seit 01.07.2012	Wissenschaftliche Mitarbeiterin an der Technischen Universität in München - Lehrstuhl für Experimentalphysik 3 (E21)